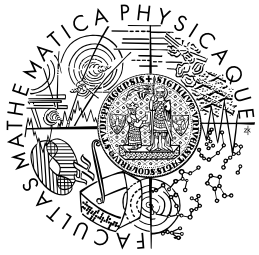

FACULTY
OF MATHEMATICS
AND PHYSICS
Charles University

DOCTORAL THESIS

Vojtěch Patočka

Maxwell-type viscoelasticity in small and large deformations of planetary mantles

Department of Geophysics

Supervisor of the doctoral thesis: prof. RNDr. Ondřej Čadek, CSc.
Study programme: Physics
Study branch: Geophysics

Prague 2018

I declare that I carried out this doctoral thesis independently, and only with the cited sources, literature and other professional sources.

I understand that my work relates to the rights and obligations under the Act No. 121/2000 Sb., the Copyright Act, as amended, in particular the fact that the Charles University has the right to conclude a license agreement on the use of this work as a school work pursuant to Section 60 subsection 1 of the Copyright Act.

In Prague, 22. 2. 2018 Patočka Vojtěch

Title: Maxwell-type viscoelasticity in small and large deformations of planetary mantles

Author: Mgr. RNDr. Vojtěch Patočka

Department: Department of Geophysics

Supervisor: prof. RNDr. Ondřej Čadek, CSc., Department of Geophysics

Abstract: A present limitation of global-scale simulations of planetary interiors is that they assume a purely viscous or viscoplastic flow law for solid rock, i.e. elasticity is ignored. This is not a good assumption in the cold and strong outermost mantle layer known as the lithosphere, which seems to maintain its elastic properties even on time scales corresponding to the geological processes of subduction or sedimentation. Here we overcome such simplification and present a numerical tool for modelling visco-elasto-plastic mantle convection. The most promising new feature of the resulting models is related to the ability of viscoelastic materials to remember deformation experienced in the past. Thus, the growing viscoelastic lithosphere of a cooling planet, when subject to internal or surface loading, can store information about its thickness at the time of loading. This phenomena is consistent with datasets of the effective elastic thicknesses determined in flexure studies and we label it here as the "stress memory effect". Attention is also paid to the theoretical foundations of viscoelasticity. We review the approaches that are commonly used to formulate Maxwell-type constitutive equations and thoroughly analyze the condition of material objectivity in a search for objective stress rate that fits Maxwell's original idea the best. While the main focus of the thesis lies in the field of large deformations, small deformations of planetary mantles are addressed too. We solve the traditional problem of glacial isostatic adjustment on a rotating Earth and analyze the accompanying changes in the rotational, gravitational and elastic energy of the planet.

Keywords: Viscoelasticity, Maxwell fluid, Numerical modelling

Název: Viskoelasticita Maxwellova typu v malých i velkých deformacích plášťů terrestrických planet

Autor: Mgr. RNDr. Vojtěch Patočka

Katedra: Katedra geofyziky

Vedoucí disertační práce: prof. RNDr. Ondřej Čadek, CSc., Katedra geofyziky

Abstrakt: Současná limitace globálních simulací plášťů terrestrických planet spočívá v tom, že uvažují čistě viskózní nebo visko-plastické tečení plášťových hornin, a tedy zanedbávají jejich elasticitu. Tato aproximace není vyhovující ve studené a pevné svrchní vrstvě pláště, známé jako litosféra, která si uchovává elastické vlastnosti i na časových škálách odpovídajícíh geologickým procesům subdukce a sedimentace. V této práci překonáváme toto zjednodušení a představujeme numerický nástroj pro modelování visko-elasto-plastické plášťové konvekce. Zajímavá vlastnost našich simulací pramení ze schopnosti viskoelastického materiálu pamatovat si prodělanou deformaci. A tak postupně mohutnějící litosféra chladnoucí planety, vystavená vnitřím nebo povrchovým zátěžím, ukládá informaci o své tloušťce v okamžiku zátěže. Tento jev je v souladu s hodnotami efektivní elastické tloušťky získanými v rámci měření flexe litosféry, a my jej zde označujeme jako "napěťová paměť materiálu". Pozornost je věnována i teoretickým základům viskoelasticity. Shrnujeme přístupy, které lze použít při formulaci konstitutivní rovnice Maxwellova typu, a důkladně analyzujeme podmínku materiálové objektivity za cílem nalezení objektivní tenzorové derivace, která odpovídá původní Maxwellově myšlence nejlépe. Zatímco těžiště práce spočívá v oblasti velkých deformací, malé deformace planetárních plášťů jsou adresovány také. Řešíme tradiční úlohu postglaciálního výzdvihu na rotující Zemi a analyzujeme změny v rotační, gravitační a elastické energii tělesa, ke kterým při tom dochází.

Klíčová slova: Viskoelasticita, Maxwellova tekutina, Numerické modelování

I am grateful for the years spent at the Department of Geophysics in Prague. First of all, I owe many thanks to Prof. Ondřej Čadek, whose open doors I was welcome to enter for numerous discussions. He inspired me with his enthusiasm for geophysics and interesting ideas, and at the same time granted me the scientific freedom so necessary to enjoy research. Among the many others who build a warm and home-like environment at our department I name Doc. Čížková, Prof. Martinec, Dr. Souček, and Dr. Hanyk, who provided scientific and moral support whenever needed. I also appreciated my office mates Kačka, Ľubica, Míša, and Celeste, and the kilograms of tea that we shared.

One year of my PhD took place at ETH Zürich. I am thankful to Prof. Paul Tackley for hosting me and for introducing me to his code StagYY. I was very happy to meet the young and international Geophysical Fluid Dynamics group. My friendship with some of its members lasts until today and in the present connected world I believe it can last forever. To mention some, doctors Jain, Lichtenberg, Lourenco, and Rozel will always be in my memory with their karaoke singing and I hope that they are able to perform horizontal dancing for decades to come.

In the unstable seas of academia one often needs some anchors, not to mention a good meal. I am indebted to my parents and my girlfriend Alice for providing these.

The Charles University is acknowledged for supporting my studies through grants SVV260327/2016 and SVV260447/2017, and my stay at ETH Zürich was sponsored by the Sciex project No. 13.250. I also acknowledge Cambridge University Press and Annual Reviews of Geophysics for providing figures used in the Introduction of this thesis.

Contents

Introduction **3**
0.1 The lithosphere as an elastic plate . . . 5
0.2 Elastic deformation in mantle convection . . . 9
0.3 Structure and goals of this thesis . . . 12

1 Maxwell viscoelastic fluid **14**
1.1 Material frame-indifference . . . 16
1.2 Objective tensor rates . . . 25
1.3 Maximization of entropy production . . . 32
1.A Change of frame: moving polar coordinates . . . 39
1.B Convected and corotated frames: simple shearing . . . 41

2 Small deformations of viscoelastic mantle **45**
2.1 Eulerian formulation of the governing equations . . . 45
2.2 Energy balance of GIA on a rotating Earth . . . 49
2.2.1 Introduction . . . 50
2.2.2 Governing equations . . . 52
2.2.3 Numerical implementation . . . 54
2.2.4 Energy balance of a rotating Earth . . . 59
2.2.4.1 Alternative formula for the gravitational energy . 59
2.2.4.2 Energy balance of GIA for a non-rotating Earth . 63
2.2.4.3 Energy balance of a damped Chandler wobble . . 64
2.2.4.4 Energy balance of GIA for a rotating Earth . . . 66
2.2.4.5 Energy balance as a tool for testing GIA models . 69
2.2.5 Conclusions . . . 71
2.A Energy balance and the rate of mechanical work . . . 74
2.A.1 Term 1 . . . 75
2.A.2 Term 2 . . . 77
2.A.3 Term 3 . . . 78
2.A.4 Auxiliary formulae for gravitational and centrifugal potential 78
2.A.5 Term 4 . . . 80
2.A.6 Term 5 . . . 81
2.A.7 Term 6 . . . 82
2.A.8 Remark . . . 82
2.B Second order correction to LLE . . . 83

3 Stress memory effect in viscoelastic stagnant lid convection **85**
3.1 Introduction . . . 86
3.2 Governing equations and numerical methods . . . 87
3.2.1 Governing equations . . . 88
3.2.2 Maxwell viscoelastic rheology . . . 88
3.2.3 Numerical implementation . . . 90
3.3 Rising cylinder (RC models) . . . 92
3.3.1 Model setup . . . 92

3.3.2 Results: topography above a rising cylinder 93
3.4 Thermal convection (TC models) 96
3.4.1 Model setup 96
3.4.2 Results: free-slip surface 97
3.4.3 Results: free surface 99
3.4.4 Robustness of the results 104
3.5 Discussion 105
3.A Benchmark tests 107
3.A.1 Thermal convection of an isoviscous Maxwell fluid 107
3.A.2 Recovery of the original shape of an elastic slab 108
3.B Subgrid oscillations of stress 110

4 Spontaneous initiation of subduction in mantle convection models with elasticity and a free surface 112
4.1 Introduction 112
4.2 Model setup 114
4.3 Results: small-scale convection 119
4.3.1 Influence of elasticity and a free surface on the critical value of yield stress 119
4.3.2 Short-term fluctuations and locked convection cells 123
4.3.3 Role of the initial temperature perturbation 126
4.4 Results: global-scale convection 128
4.4.1 Plume-induced subduction 128
4.5 Discussion 131
4.6 Conclusions 133

Conclusions and perspectives 134

Bibliography 138

List of Figures 147

List of Tables 149

Introduction

"*Elastic materials deform when a force is applied and return to their original shape when the force is removed. Almost all solid materials, including essentially all rocks at relatively low temperatures and pressures, behave elastically when the applied forces are not too large.*" – Turcotte & Schubert (2002)

"*Thus a block of pitch may be so hard that you cannot make a dent in it by striking it with your knuckles; and yet it will in the course of time flatten itself by its weight, and glide downhill like a stream of water*"
– James Clerk Maxwell, from Theory of Heat (1871)

The rheological behaviour of the lithosphere has long been contentious in geodynamics. The approaches developed over the years have essentially two end-members that are mutually contrasting, one treating the lithosphere as an elastic solid and the other as a highly viscous fluid.

Several observations directly confirm that the surface plates constituting the lithosphere are very rigid. Many geological structures in the continental crust have survived longer than 1 Gyr without flowing away and the linearity and constant separation of transform faults proves that the oceanic plates strongly resist to any intra-plate flow. In fact, this is a fundamental postulate of plate tectonics (e.g. Turcotte & Schubert, 2002). At the same time, the lithosphere is observed to bend under imposed loads and its topography can often be fitted by the curvature of a flexed elastic plate. Thickness of such theoretical plate is referred to as the effective (or equivalent) "elastic thickness" of the lithosphere.

For this reason, modelling the lithosphere as an elastic solid has traditionally played an important role in geodynamics, particularly when response to surface loading and unloading is investigated. These flexure studies, however, also suggest that the lithosphere relaxes with time, meaning that it cannot be purely elastic. It is best illustrated by the general disagreement between seismic thickness of the lithosphere, as indicated by the depth of the low-velocity zone (e.g. Shapiro & Ritzwoller, 2002), and the elastic thickness observed at long time scales, the latter being much smaller. Moreover, there is evidence for a decrease of effective elastic thickness of oceanic lithosphere with the age of imposed surface loads. An insightful review by Watts et al. (2013) employs a large dataset of topographic and gravity measurements to support and quantify these geophysical observations. In Section 0.1 we repeat some of the conclusions presented by Watts et al. (2013) and discuss them in the context of viscoelastic rheologies.

In numerical experiments of mantle convection the approach is different, since convection is intrinsically associated with fluid-like behaviour. The dominant type of creep mechanism in the upper and lower mantle is still debated (e.g. Ranalli, 1995; Schaeffer et al., 2016), but both major candidates – the diffusion

and dislocation creep – can be described by temperature and pressure dependent viscous flow laws. For present day temperatures of terrestrial planets one obtains large viscosity contrasts with these flow laws, resulting in a mantle that convects below a highly viscous stagnant lid (Solomatov, 1995). The rheological behaviour of the outer thermal boundary layer (the lid, more generally the lithosphere) is then not of primary importance. Its internal deformation has little effect on the overall thermal evolution, layering of convection, convective vigor, the shape of plumes, or other typically addressed features.

When plastic yielding is introduced, more tectonic regimes can be obtained in thermal convection models. Namely, the mobile lid regime, similar to plate tectonics on Earth (Tackley, 2000), and episodic lid regime, which could apply to Venus (Armann & Tackley, 2012; Rozel, 2012). Lithosphere-scale shear zones develop in these regimes due to plastic yielding, splitting the lid into plates which then subduct. Most of the deformation is accommodated within boundaries of the plates, that is, within some localized shear zones. In plate-like regimes the rheology of the lithosphere is more important, as it controls the shape of subducted slabs during their descent (e.g. Čížková et al., 2007), which in turn affects slab penetration through the transition zone (e.g. Tagawa et al., 2007), and thus also the overall convection pattern. Nevertheless, elasticity is still only rarely considered in global-scale numerical models of mobile and episodic lid regimes. In regional-scale models the behaviour of subducting slabs is under closer scrutiny and visco-elasto-plastic rheology is more common.

The basic premise of this thesis is that essentially all materials show viscoelastic properties: their short term response is elastic or elasto-brittle and when loaded for sufficient time the elastic strains are accommodated by a dissipative mechanism, gradually diminishing the stored elastic strain energy. The key question to ask is what the "sufficient time" is for a given material and given spatial scale, as recognized already by Maxwell (1871): "In the case of a viscous fluid it is time which is required, and if enough time is given, the very smallest force will produce a sensible effect, such as would require a very large force if suddenly applied. Thus a block of pitch may be so hard that you cannot make a dent in it by striking it with your knuckles; and yet it will in the course of time flatten itself by its weight, and glide downhill like a stream of water." (adopted from Málek & Rajagopal, 2005).

In the case of lithosphere the time needed for it to behave "like a stream of water" is extremely large: it can preserve elastic energy even on geological time scales, examples of which are given in Section 0.1. While this alone advocates for considering elasticity in mantle convection modelling, there is also another aspect. The effects of elastic deformation in regional modelling, even when short-lived, suggest a possible influence on the long-term behaviour of global-scale models. These are discussed in Section 0.2.

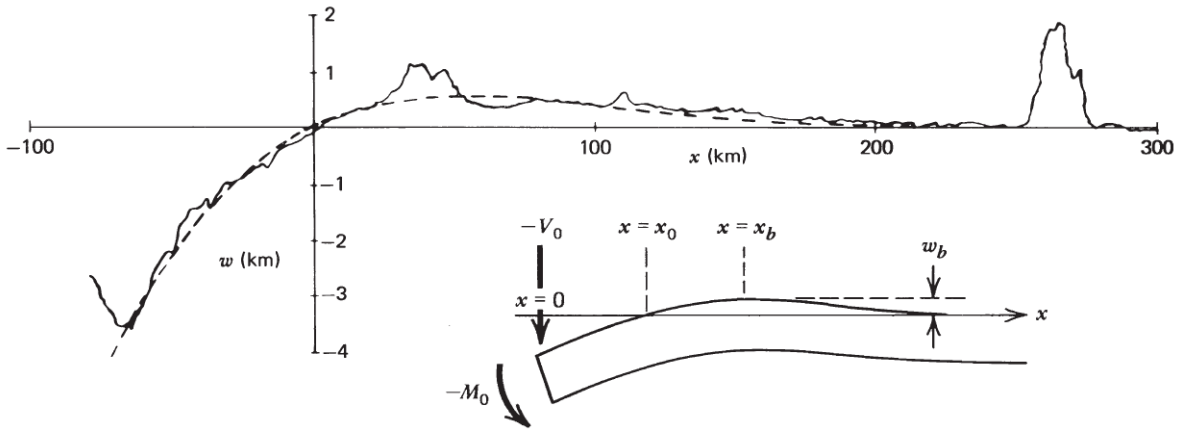

Figure 1: Comparison of a bathymetric profile across the Mariana trench (solid line) with the universal lithospheric deflection profile, that is, with the solution of the general equation for the deflection of a thin elastic plate subject to an end loading (dashed line). The scheme in the right bottom corner shows the parameters describing such situation. A plate fixed on the right side and loaded by a vertical force V_0 and a bending moment M_0 on its left edge. Distance $x_b - x_0$ is the half-width of the forebulge from which the thickness of the plate can be inferred. Adopted in modified form from section 3 of Turcotte & Schubert (2002).

0.1 The lithosphere as an elastic plate

On short time scales, there are two major types of experiments to determine the elastic properties of rocks: laboratory and seismological. In laboratory experiments the spatial scales are limited. One can measure up to meter-sized blocks of material, typically involving monoliths (well connected unfractured samples made of a single rock type). From seismology, in particular from the study of free oscillations of the Earth, we know that the mantle behaves as a continuous elastic body even on very large spatial scales, with wavelengths reaching thousands of kilometers. Such evidence does not, however, directly imply that the mantle can preserve its elastic properties on geological time scales.

A textbook example that in the lithosphere this is indeed the case can be found near the deepest part of the world's oceans – by investigating the bathymetric profile across the Mariana trench (see Fig. 1). While viscous or viscoplastic plates can also bend over time when subject to loading, such bending does not form a forebulge as observed near the Mariana trench and in other subduction zones. The formation of a forebulge is related to the way elastic rods and plates transfer bending moments throughout their lengths (for some settings a forebulge can be created and supported by viscous flow only, but a satisfying fit to the observed forebulge morphology is not obtained without elasticity – see Gurnis et al. (1996) and Hall & Gurnis (2005)). The bathymetric profile across the Mariana trench can be compared with the solution of the general equation for deflection of a thin elastic plate subject to an end loading. Measuring the half-width of observed forebulge almost directly leads to the thickness of such bent elastic plate: upon

specifying plate density, its Young's modulus, Poisson's ratio, the density of water, and the gravitational acceleration, the half-width $x_b - x_0$ can be converted to the plate thickness T_e.

For typical parameters one gets $T_e \cong 28$ kilometers for the Pacific plate subducting at the Mariana trench (Turcotte & Schubert, 2002, Fig. 3-35). This is much less than the local thickness of the oceanic lithosphere when defined as the width of the thermal boundary layer derived from a half space cooling model (e.g., Turcotte & Schubert, 2002, eq. 4-115). Thermal boundary layer is the region where temperature drops by a certain amount (relative to the initial temperature contrast, that is, relative to the difference between the temperature of the rising magma and the surface temperature of ocean floor) and so its depth corresponds to a predefined isotherm (typically around 1300 °C). With viscosity strongly dependent on temperature, it is a region where viscosity exceeds a given threshold, i.e. it is very stiff (with high resistance to flowing). The estimated thickness of the thermal boundary layer matches quite well with the depth to the channel of low seismic velocities (the astenosphere), as first observed from Rayleigh wave dispersion data by Leeds et al. (1974).

How, then, is the discrepancy between the observed T_e and the thickness of the oceanic lithosphere explained? The stresses that develop in a subducting plate easily exceed the brittle strength of rocks and part of the bending energy is released in relatively small intra-plate fractures (not to be confused with the possibly large seismic events at the interface of two plates), reducing the plate's equivalent elastic thickness in effect. Moreover, stress-dependent ductile creep may get activated in deeper parts of the slab, further releasing elastic energy into heat through viscous dissipation of the creeping material. While brittle failure is almost singular in time, ductile yielding acts gradually and reduces the lithospheric elastic strain progressively.

The slower a tectonic process is, the more time creep mechanisms have to relax elastic stresses that formed in response to lithospheric loads. Convergence rate at the Mariana trench is a few cm/year, leaving each segment of the slab loaded for several tens of Myr before it sinks into the mantle. The computed T_e value can be viewed as a measure of elastic strength which persists over the characteristic time of each process. In the case of subduction it is several tens of Myr. In principle, the slower the sinking rate of slab is, the smaller value of T_e one should expect. To our knowledge, no systematic study relates convergence rates with observed elastic thickness of subducting plates, but there is other evidence of time dependent stress relaxation in the lithosphere: the relationship between the age of a seamount and the amount of deflection it causes to the underlying seafloor. Oceanic seafloor is littered with volcanic seamounts which make ideal lithospheric loads because they are very concentrated (having large edifice height to width ratio) and form rapidly (1-2 Myr). An example of seamount chain is depicted on Fig. 2, adopted from Watts et al. (2013), the left panel showing the free-air gravity anomaly along the Louisville Ridge, and the right panel demonstrating

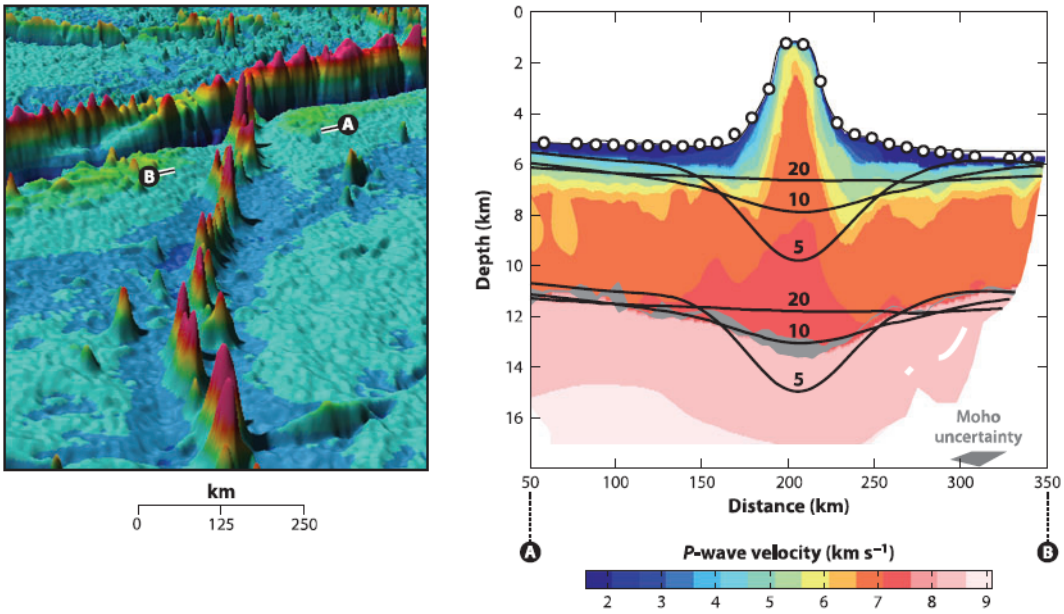

Figure 2: The crustal and upper-mantle structure along Profile AB, which intersects the crest of the Louisville Ridge seamount chain in the southwest Pacific Ocean at 27°35'S (Contreras-Reyes et al., 2010) (for perspective image of the free-air gravity anomaly along the Louisville Ridge seamount chain in the southwest Pacific Ocean see left part of the figure). The colors indicate the P-wave velocity structure derived from a seismic refraction experiment involving a shooting ship (R/V SONNE) and ocean-bottom seismometers (open symbols). The solid black lines represent the predicted flexure of the crust and upper mantle assuming a load base at a depth of 4910 m with densities of the infill, load, and mantle of $2800, 2800$, and 3400 kg m^{-3}, respectively, and effective elastic thickness, T_e, of 5, 10, and 20 km. There is an excellent fit between the observed seismically constrained depth to Moho and the calculated depth based on the predictions of a simple elastic plate (flexure model) with $T_e = 10$ km. Adopted from Watts et al. (2013).

how seismic refraction data can be used to determine the elastic thickness of the Pacific plate in that region.

In their review paper, Watts et al. (2013) collect data from many studies of flexure such as the one depicted in Fig. 2. They show that the observed elastic thickness T_e generally decreases with load age. The evidence is not very robust, for reasons discussed below, but for the moment let us assume that T_e indeed decreases with the seamount age. What implications can be made for the lithospheric rheology?

General feature of viscoelastic rheologies is that both the viscous and the elastic deformation are present when a viscoelastic body is loaded. The relationship between these two deformational components is, however, different for different viscoelastic material models. If we compare the two most fundamental ones, Maxwell model and Kelvin-Voight model (other models are often built by combining these), only the first one allows for elastic energy to be gradually dissipated by the viscous mechanism when the imposed loading is held constant. Thus, as long as erosion does not significantly reduce the size of the seamounts

over time, only the Maxwell model can explain the observed decrease of T_e with time (i.e. the decrease of elastic support with time). Note also that Kelvin-Voight material does not behave as fluid in the $t \to \infty$ limit, meaning that it can never reach hydrostatic equilibrium. This seems unlikely for planetary bodies, whose rotational bulge is often close to the hydrostatic equilibrium (see also Chapter 2). Therefore, we choose Maxwell model as the central concept of this thesis, for it is the simplest viscoelastic rheology capable of explaining the phenomena mentioned above.

While the dependence of T_e on the load age is not very robust, a more convincing feature in the large dataset assembled by Watts et al. (2013) is that the observed elastic thicknesses are related to the thermal age of the oceanic plates at the time of loading rather than to their current thermal age. When volcanic eruptions form a seamount, it causes deflection of the underlying seafloor. The amount of deflection is given by the size of the load and by the thickness of the plate at the time of eruptions. Subsequent cooling and thickening of the oceanic lithosphere has little effect on the recorded deflection of its crustal strata. In the words of Watts et al. (2013): "Accordingly, as the plate increases its age away from a mid-ocean ridge, it increases in strength, and despite a possible decrease in T_e with load age, the plate retains a memory of this strength for long periods of time". In Chapter 3 we, for the first time in the literature, demonstrate such memory effects in numerical simulations of global-scale thermal convection.

The fact that the measured elastic thicknesses primarily depend on the plate age makes it difficult to extract the relationship between T_e and load age. One needs to get rid of the plate age to obtain such relationship, e.g. by compiling a dataset that compares values of T_e under seamounts of different age, but for which the plate's thermal age at the time of loading (formation of the seamount) is the same for all the selected seamounts. Clear evidence of gradual stress relaxation is given only in individual cases, e.g. when the long-term subsidence of Ascension volcanic island is reported (Minshull et al., 2010), or similarly for the islands in French Polynesia (Watts & Zhong, 2000).

While all oceanic seamounts eventually get subducted, leaving no loads older than cca. 200 Myr, the continents are subject to a wider range of load age and so have a better potential to manifest lithospheric relaxation. Unfortunately, their thermal and mechanical evolution is much more complicated than that of the oceanic plates. It is dominated by the Wilson cycle, leaving structural inheritance which makes it complicated to isolate loads from the deformation they cause (Watts et al., 2013). Perhaps the least troubling geological structures in terms of such isolation are foreland basins. To illustrate the general procedure of determining T_e in foreland basins we adopt Fig. 3 from Watts et al. (2013), who compute the T_e value in the case of Ganges basin, loaded by the Himalayas. Watts et al. (2013) gather 86 T_e estimates from foreland basins and rim flank uplifts, portraying the flexure of Archean and Middle Proterozoic to Phanerozoic lithosphere. The main result is, similarly as for the oceanic lithosphere, that

the equivalent elastic thickness increases significantly with the plate thermal age and is much smaller than the seismic thickness of the lithosphere in each region. Dependence of T_e on load age shows even larger scatter than for the oceanic lithosphere data, providing little information about the long-term relaxation of lithospheric stresses.

To summarize, elasticity is important when lithospheric deformation is studied – both on short time scales and on geological time scales. The elastic mechanism must be complemented by a dissipative one in order to explain the difference between the computed T_e estimates and the observed seismic thicknesses of the lithosphere in various regions. Dissipation takes place both through brittle cracking and through gradual ductile creep. Moreover, the viscosity controlling the creep must be temperature dependent in order to explain the dependence of T_e on the plate's thermal age at the time of loading. It is, however, difficult to identify particular creep type because the data on T_e against the load age show a large scatter, making it hard to infer the temporal evolution of stress relaxation under the load. Despite these uncertainties, it is flexure studies that provide important constraints on the brittle/ductile transition and on the active creep mechanism in a realistic, compositionally stratified lithosphere (e.g. Afonso & Ranalli, 2004; Burov, 2010). Note that one cannot infer such rheological zonation from lab experiments only, because the experimentally determined constitutive relations for lithospheric rocks strongly depend on composition, water content and temperature, and these are not well known in the real Earth.

0.2 Elastic deformation in mantle convection

There is a certain paradox in many numerical experiments of subduction and mantle convection. While flexure studies are often taken into account – by using therein derived constraints on the brittle/ductile transition and on the active type of creep – flexure itself is often forgotten in these experiments as elasticity is ignored in them. Perhaps it is because their focus have traditionally been on the deeper dynamics rather than near the surface. Below we address a few exceptions – studies that include elastic deformation in global geodynamical simulations.

Planetary-scale thermal convection of viscoelastic medium has first been addressed long ago by Ivins et al. (1982) and Harder (1991), but the papers do not include the temperature dependence of viscosity. When it is considered, the basic mode of thermal convection becomes the stagnant lid regime, as mentioned above. The dynamic effects of elasticity on stagnant lid convection have only been investigated many years later by Beuchert & Podladchikov (2010), who employed a free-slip upper boundary condition and found mostly transient differences when comparing viscous and viscoelastic models. Some stress reduction due to elasticity was observed, but the overall effects were not very dramatic on the global-scale.

Quite recently, it was shown by Thielmann et al. (2015) that a free surface up-

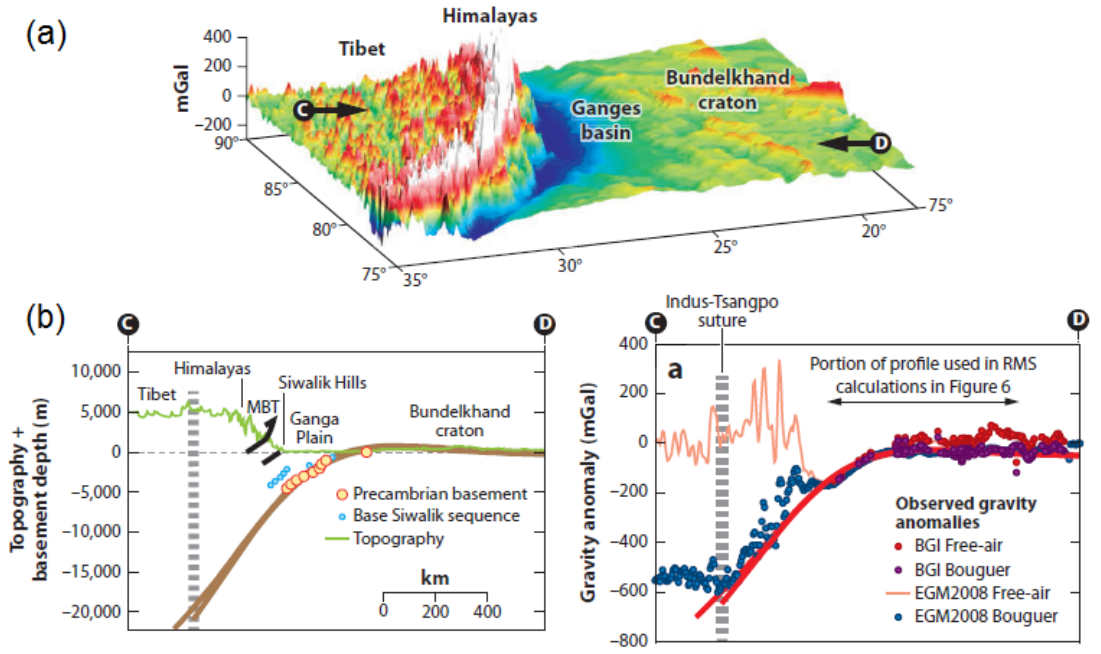

Figure 3: (a) Perspective view (from the northwest) of the EGM2008 free-air gravity anomaly field over the Himalayas and Ganges basin and the outer rise of central India. Arrows show the location of Profile CD in panel b. (b) Comparison of the observed and calculated Bouguer anomalies (right) and depth to the base of the foreland basin sequence (left) along Profile CD of northern India, the Ganges basin, the Himalayas, and Tibet. The profile intersects the Main Boundary thrust (MBT), which separates the subducting Indo-Australian plate from the overthrusting Eurasian plate, at longitude 82.4°E and latitude 28.3°N. The observed gravity anomalies are based on "point" measurements compiled by the Bureau Gravimetrique International (BGI) (*red and purple circles*) and the 2.5' × 2.5' EGM2008 combined terrestrial and satellite derived free-air gravity anomaly grid of Pavlis et al. (2008) (*thin red line*). The EGM2008 field has been converted to Bouguer gravity anomalies (*blue circles*) using a fast Fourier transform method of calculating the gravity effect of the topography up to degree and order 4 (Parker 1972), a GEBCO topographic grid, and an average crustal density of 2,650 kg m^{-3}. The calculated Bouguer gravity anomalies (*thick red lines*) and depth to the base of the foreland basin sequence (*thick brown lines*) are based on an elastic plate model with a load and infill density of 2,650 kg m^{-3}, an effective elastic thickness, T_e, of 87.5 km (best fit) and a plate break at a distance of 185, 285, and 385 km north of the MBT. The calculated Bouguer gravity anomaly has been referenced to the general level of the observed anomalies over the unflexed parts of the Bundelkhand craton, and the calculated depth to the base of the foreland basin sequence has been referenced to mean sea level. The Indus-Tsangpo suture (*thick gray dashed line*) is located 285 km north of the MBT. Adopted from Watts et al. (2013)

per boundary is necessary for the effects of elasticity to fully develop in stagnant lid convection. Similar findings were reported earlier in the context of mantle lithosphere detachment from the continental crust (Kaus & Becker, 2007). In Chapter 3, we analyze this in detail by comparing viscous and viscoelastic simulations with a free surface. A viscoelastic lithosphere is able to build topography much more quickly than a purely viscous one, resulting in a significant lithospheric stress reduction in viscoelastic models. We quantify this effect for the case of a rising cylinder and for basally heated stagnant lid convection. Moreover, we show how the stress patterns formed in the lithosphere are influenced by the fact that Maxwell material, unlike purely viscous medium, remembers the deformation it has undergone in the past. Initially thin viscoelastic lithosphere can record the pull of downwellings and the push of plumes as it grows in thickness, the respective stress patterns being "frozen" into it for times comparable with its Maxwell relaxation time. Despite the above mentioned features, most of the typical observables of interest, such as the surface heat flux, vigor of convection, or the behaviour of plumes, are little affected by considering elasticity in the overlying stagnant lid.

Global-scale simulations of plate tectonics have also only rarely been performed with rheologies that include elasticity, exceptions being the works of Moresi et al. (2002), Muhlhaus & Regenauer-Lieb (2005), and Muhlhaus et al. (2006). These pioneering studies focused mainly on the methodology, leaving little space for a systematic evaluation of the influence of viscoelastic rheology on the convective patterns. Moresi et al. (2002), who originated the method for including elasticity into a viscous flow solver which we adopt and expand in Chapter 3, also computed three simulations of mantle convection with a subducting plate, differing from each other by the Maxwell relaxation time of the plate. They investigated whether the slab would roll forward, as is typical in simulations with viscoplastic rheology (but not observed in nature very often), or roll backwards, as is often observed in nature. They found that for the intermediate value of the relaxation time the slab rolled backwards for a transient period of time, but surprisingly this feature did not appear for the highest relaxation time. They conclude that "the effect of increasing the elastic stresses in the end is to modify the manner in which the lithosphere yields. This highlights the unpredictability of complex nonlinear systems and serves as a warning that application of these simulations to modeling of plate tectonics requires considerable care and a thorough attention to data which constrain the evolution of specific plate boundaries."

Recently, Jaquet et al. (2016) found elasticity to play a significant role in the context of shear heating induced thermal softening (e.g. Thielmann & Kaus, 2012; Schmalholz & Duretz, 2015). Jaquet et al. (2016) performed regional models of lithospheric shortening with realistic crustal and upper mantle rheologies. They found that stresses build up much more slowly when strain can accumulate in the form of elastic strain. When plastic criterion is reached and strain localizes within a shear zone, the global release of the accumulated elastic strain energy

promotes shear heating and increases the strain localization in effect, helping to form a narrow and deep shear zone such as needed for the initiation of subduction. Similar thermoelastic feedback, though less dramatic, was observed earlier by Regenauer-Lieb et al. (2001) in models that include hydrated minerals. Motivated by these results, we investigate in Chapter 4 how the ability to store and release elastic energy influences the critical yield stress value needed to form a lithosphere-scale shear zone in mantle convection simulations. Diffusion creep is, apart from the elastic mechanism, coupled with either Drucker-Prager or Von-Mises plasticity in these models, with the aim to parametrize both the brittle failure and ductile yielding of the lithosphere. We perform a systematic study, aiming at statistically robust results that minimize the influence of chaoticity, intrinsic to every convection simulation with a high Rayleigh number.

0.3 Structure and goals of this thesis

Although not discussed very often in geodynamical literature, the traditional formulation of Maxwell constitutive equation violates the principle of material frame-indifference. Every constitutive relation and other physical laws should respect this principle. The traditional formulation of Maxwell rheology is only acceptable when understood as an approximation of a more complete formulation, with its range of applicability being restricted to small strains (e.g. postglacial rebound, see below). The topic has been pioneered in the fifties by Oldroyd (1950), but is recently again gaining attention as new thermodynamics based formulations of constitutive laws are being proposed. In Chapter 1, we thoroughly review the principle of material frame-indifference and bring new insights into its implications for generalizations of the traditional model.

Chapter 2 is devoted to a classical application of Maxwell rheology, in which the Earth is subject to small deformations resulting from glacial isostatic adjustment (GIA). The periodic accumulation and melting of ice loads and unloads the Earth's surface within tens to hundreds of kyr, that is, on short time scales when compared to geological processes (e.g. Peltier, 2004). Viscoelastic relaxation is crucial in explaining the postglacial rebound data. The rate at which the surface is being uplifted due to historical ice caps is an observable directly linked to the relaxation time of the lithosphere. A purely elastic Earth would predict zero present day uplift due to the already melted ice caps, because elastic models deform only when the load size is being changed. Purely viscous models, on the other hand, would predict unrealistically small uplift rates – surface loads cannot induce significant deformation of the deeper mantle when emplaced onto a non-elastic, highly viscous lithosphere. Moreover, secular drift of the rotation axis in response to GIA would be too small in a purely viscous Earth, because the readjustment of the rotational bulge would be too slow. For these reasons, viscoelastic rheology has always been a necessity in GIA modelling, with the Maxwell model being the most common, almost unanimous, choice. Computing GIA on a ro-

tating Earth becomes a delicate exercise as one has to account for the changes in Earth's rotation induced by the load induced deformation. In Chapter 2, we analyze this phenomena from an energetic point of view. We derive a diagnostic tool that can be used, within the field of small planetary deformations, to detect physically ill-posed problems, or to reveal numerically incorrect solutions to physically well-posed problems. We apply this tool to review the approximations commonly used in GIA modelling and demonstrate some of their inconsistencies.

The main goal of this thesis is to investigate the footprints of viscoelasticity in the context of mantle convection. We study how elasticity influences the surface topography and lithospheric stresses when internal loading is generated by self-consistently developed plumes and downwellings. The focus is on mantle-lithosphere interaction: how the internal dynamics impacts the deformation of a viscoelastic lithosphere and, conversely, how the elastic properties of the lithosphere affect the internal dynamics. In Chapter 3, we evaluate the response of a stagnant lid and discuss the importance of the lid thickness and its evolution in time. We perform simulations of a model Mars that is cooling down from its initially hot state and analyze the stress patterns in its thickening lithosphere. Statistically steady state, in which the lid thickness remains constant in time, is also addressed. In Chapter 4, we study the transition from a stagnant lid to plate-like mode of convection in visco-elasto-plastic models. We asses the fluctuations of lithospheric stresses that are associated with the chaotic movement of sinking and rising plumes and explore whether the expected effects of elasticity and a free surface emerge despite these fluctuations. Attention is paid to the role of viscosity profile assumed in the mantle.

1. Maxwell viscoelastic fluid

"*Mathematicians may flatter themselves that they possess new ideas which mere human language is as yet unable to express. Let them make the effort to express these ideas in appropriate words without the aid of symbols, and if they succeed they will not only lay us laymen under a lasting obligation, but, we venture to say, they will find themselves very much enlightened during the process, and will even be doubtful whether the ideas as expressed in symbols had ever quite found their way out of the equations into their minds.*" – James Clerk Maxwell

"*All the mathematical sciences are founded on relations between physical laws and laws of numbers, so that the aim of exact science is to reduce the problems of nature to the determination of quantities by operations with numbers.*"
– James Clerk Maxwell, from Faraday's Lines of Force (1856)

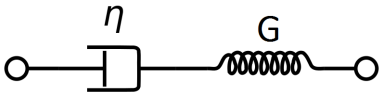

Figure 1.1: Mechanical analogue for Maxwell viscoelastic body

In this chapter we review two phenomenological[1] approaches to formulating Maxwell viscoelastic rheology. In one way or the other they both involve a spring and dashpot mechanical analogue, the spring representing elastic deformation and the dashpot representing viscous deformation. In the first approach, the traditional one, one-dimensional stress S and one-dimensional deformation Δ are introduced, and these are put into a relation that follows from the mechanical analogue. For a Maxwell body both elements are connected in series, see Fig. 1.1, meaning that stress is the same in the spring as in the dashpot, while deformation adds up:

$$\mathrm{S} = \mathrm{S}_{\mathrm{elastic}} = \mathrm{S}_{\mathrm{viscous}}; \quad \Delta = \Delta_{\mathrm{elastic}} + \Delta_{\mathrm{viscous}}\,. \tag{1.1}$$

Linear elastic behaviour can be expressed as $S_{\mathrm{elastic}} = G\Delta_{\mathrm{elastic}}$, the constant of proportion G being the shear modulus. Viscous friction law reads $S_{\mathrm{viscous}} = \eta\dot{\Delta}_{\mathrm{viscous}}$, the dot denoting time derivative and η standing for the viscosity. By computing time derivative of eq. (1.1), employing the elastic and viscous laws, and assuming the shear modulus G to be time constant, one obtains

$$\dot{\Delta} = \dot{\Delta}_{\mathrm{elastic}} + \dot{\Delta}_{\mathrm{viscous}} \quad \Rightarrow \quad \dot{\Delta} = \frac{\dot{S}_{\mathrm{elastic}}}{G} + \frac{S_{\mathrm{viscous}}}{\eta} = \frac{\dot{S}}{G} + \frac{S}{\eta}, \tag{1.2}$$

which is the classical equation for Maxwell's one-dimensional mechanical analogue.

[1]"dealing only with phenomena directly accessible to the experience and measurement without trying to interpret the phenomena in terms of ostensibly more fundamental (microscopic) physical theories" - Málek & Průša (2016)

In order to rewrite the equation into the language of continuum mechanics, one must identify $S, \dot{S}$ and $\dot{\Delta}$ in terms of some appropriate tensorial quantities that describe stress, stress rate and deformation rate of three-dimensional bodies. While the Cauchy stress tensor $\overleftrightarrow{\tau}$ and the strain-rate tensor $\mathbb{D}$, defined as the symmetric part of the velocity gradient, $2\mathbb{D} := \nabla\vec{v} + (\nabla\vec{v})^{\mathrm{T}}$, are the obvious adepts for two of these quantities, there is no straightforward counterpart for the stress rate $\dot{S}$. Even though it is sometimes overlooked in geodynamical and other literature, neither partial nor material time derivative of second-order tensors are frame-indifferent quantities, meaning that neither of these rates should appear in a self-consistent physical law.

To illustrate, let us consider an elastic body deformed to some shape, and not deforming any further (e.g. a tennis ball squeezed into a fence), watched by two observers: one registering no motion of the body at all (observer attached to the fence), and the other observer moving both translationally and rotationally with respect to the first one. Let us further assume that both observers are given a physical law, called "the constancy of stress", which has the form $\mathcal{D}\overleftrightarrow{\tau}/\mathcal{D}t = 0$, with $\mathcal{D}/\mathcal{D}t$ being the material time derivative. The stress tensor field (or any other second-order symmetric tensor field) can be visualized as a set of three-axial ellipsoids with axes aligned according to the principal directions of stress at each point. The attached observer's solution to the constancy of stress is a stress field constant in time (as he is solving $\partial\overleftrightarrow{\tau}/\partial t + 0 \cdot \nabla\overleftrightarrow{\tau} = 0$). To him, each material point of the body is fixed in space and the three-axial ellipsoid sitting on that point is also fixed, its orientation is not changing. The moving observer sees a translating and rotating body. Since there is only one stress field in the body, one should expect the moving observer's solution to the constancy of stress to be a set of three-axial ellipsoids that both follow the material particles' trajectories and also rotate with respect to the moving observer the same as the body rotates with respect to him. The moving observer's solution is, however, a set of stress ellipsoids that follow material points of the body, but their orientation is time constant with respect to him. It is because the material derivative takes account of the drift of material points during the motion (via the term $\vec{v}\cdot\nabla\overleftrightarrow{\tau}$), but it does not account for the change of orientation of the infinitesimal volume elements that contain material points (absence of corotational term). It is a valid rate for scalar quantities, which have no orientation in space, but not for quantities with orientation in space.

In Section 1.1 we discuss the principle of material frame-indifference (PMFI) in detail. Its implications for formulating Maxwell constitutive law are covered in Section 1.2. In particular, we aim to emphasize the differences in geometrical interpretations of various objective rates. Contrary to mathematically driven literature, we find one particular rate that fits the traditional derivation of Maxwell body the best, namely the lower convected rate.

Relatively recently, a new technique for producing thermodynamically consistent constitutive laws has emerged, referred to as "entropy production maxi-

mization" procedure. It is based on the work of Rajagopal & Srinivasa (2004) and summarized in Málek & Průša (2016). The procedure consists of *a priori* stating how the model material dissipates energy (i.e. produces entropy). Within this approach, the constitutive law is obtained by assuming that the body always deforms such as to maximize its entropy production while simultaneously complying with the thermodynamical constraints imposed by fundamental balance laws.

In Section 1.3 we briefly review how Maxwell viscoelastic fluid can be derived within such framework. Similarly as in the traditional approach, the underlying idea is to assume the total deformation of a viscoelastic body to be composed of two parts, one being dissipative and the other elastic. A special configuration of the considered body is introduced to distinguish these: so-called natural configuration. The natural configuration, respectively its temporal evolution, corresponds only to the dissipative part of the total deformation. The entropy production maximization technique is very different from the traditional one, but the principle of material frame-indifference is equally important within its concept. It is because the principle has to be applied when proposing a model's entropy production rate. With natural configuration involved, the proper application of PMFI is a delicate exercise, which has not been to our knowledge discussed in the literature. We pay attention to it in Section 1.3.

1.1 Material frame-indifference

In this section we adopt the conceptual approach of Martinec (2011) (see chapter 5. therein) and expand it by considering non-Cartesian frames. Such expansion will be needed in Section 1.2. Regarding key terminology we strictly follow the analysis by Liu & Sampaio (2014), who distinguish between the concepts of *frame indifference, postulate of Euclidean objectivity, principle of material frame-indifference*, and *condition of material objectivity.*

Let a body $\mathcal{B}$ be a set of material points. Motion of the body will be defined as a mapping of the body, at each time $t \in [0, \infty)$, into the Euclidean space $\mathbb{E}$,

$$\chi : \mathcal{B} \times [0, \infty) \to \mathbb{E}. \tag{1.3}$$

We will consider two observers of the body. Each observer can be understood as a *frame*, the frame allowing the observer to measure positions, distances and angles in the Euclidean space $\mathbb{E}$. Frame can be formalized as a mapping that, at a given time t, associates each point of the Euclidean space with its coordinates in the frame $\phi : \mathbb{E} \times [0, \infty) \to \mathbb{R}^3$. Motion of the body, when measured in frame ϕ, is defined as the composite mapping $\chi_\phi = \phi \circ \chi$,

$$\chi_\phi : \mathcal{B} \times [0, \infty) \to \mathbb{R}^3, \tag{1.4}$$

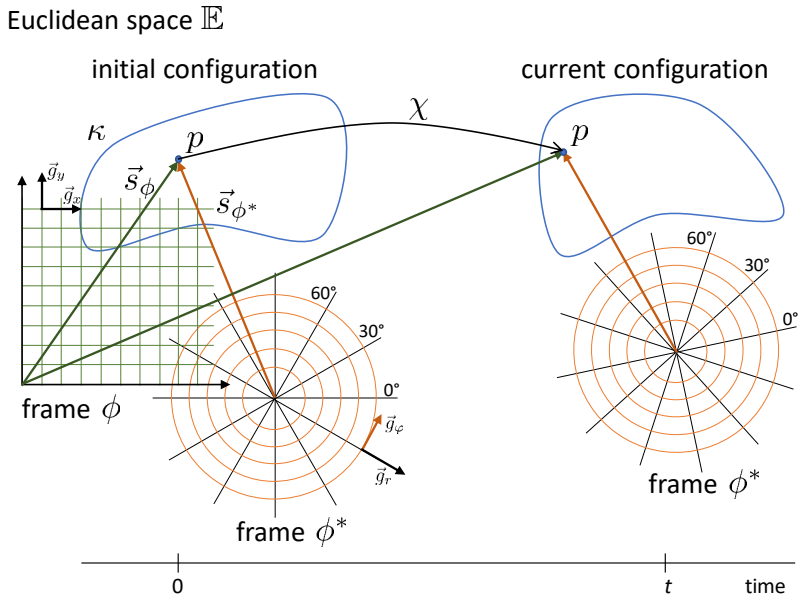

Figure 1.2: Position of particle p at times 0 and t, as viewed from fixed Cartesian frame $\phi\colon \mathbb{E}\to\mathbb{R}^3$ and from moving polar frame $\phi^*\colon \mathbb{E}\times[0,\infty)\to\mathbb{R}^3$.

where the triplets of real numbers denote the coordinates of material points' positions at time t in frame ϕ. During any motion χ, measured by two observers ϕ and ϕ^*, we can identify the position of each particle p by its coordinates $\boldsymbol{x} = \chi_\phi(p,t)$ in frame ϕ and its coordinates $\boldsymbol{x}^* = \chi_{\phi^*}(p,t)$ in frame ϕ^*. The time dependent mapping between coordinates of the same point in the Euclidean space $\mathbb{E}$ will be referred to as *change of frame*: $\boldsymbol{x}^* = \boldsymbol{x}^*(\boldsymbol{x},t)$, resp $\boldsymbol{x} = \boldsymbol{x}(\boldsymbol{x}^*,t)$. See Appendix 1.A for a worked out example.

Each frame contains an *origin*, the point with zero coordinates, and a local basis formed by vectors tangent to coordinate lines at each point (see Fig. 1.2). The local basis $\vec{e}_{i=1,2,3}$ of frame ϕ is related with the local basis $\vec{g}_{i=1,2,3}$ of frame ϕ^* via

$$\vec{g}_j(\boldsymbol{x}^*,t) = \frac{\partial x^i(\boldsymbol{x}^*,t)}{\partial x^j_*}\,\vec{e}_i(\boldsymbol{x},t) =: Q^i{}_j(\boldsymbol{x}^*,t)\,\vec{e}_i(\boldsymbol{x},t), \tag{1.5}$$

where we have defined the shifter tensor $Q^i{}_j$ and used the Einstein summation convention. The local vector bases $\vec{e}_i$ and $\vec{g}_i$ are but two different bases of the same vector space $\mathbb{V}$, which is the translational space of the Euclidean space $\mathbb{E}$.

Let us assume that each material point, at any time t, holds a scalar quantity $a\colon \mathcal{B}\times[0,\infty)\to\mathbb{R}$. The functions $a_\phi\colon \mathbb{R}^3\times[0,\infty)\to\mathbb{R}$ and $a_{\phi^*}\colon \mathbb{R}^3\times[0,\infty)\to\mathbb{R}$, defined as $a_\phi(\chi_\phi(p,t),t) := a(p,t)$, resp. $a_{\phi^*}(\chi_{\phi^*}(p,t),t) := a(p,t)$, are representations of the scalar field a in the frames ϕ and ϕ^*. Clearly, $a_{\phi^*}(\boldsymbol{x}^*,t) = a_\phi(\boldsymbol{x},t)$. We say that the scalar field a is *frame indifferent*, or objective, because for each point in the Euclidean space $\mathbb{E}$ its value is given, irrespective of the chosen frame.

Similarly, for any vector quantity $\vec{a}$ belonging to $\mathbb{V}$ we say that it is objective if $\vec{a}_{\phi^*}(\boldsymbol{x}^*,t) = \vec{a}_\phi(\boldsymbol{x},t)$. For the components of such vector field with respect to

the local bases of $\vec{e}_i$ and $\vec{g}_j$ eq. (1.5) gives

$$\begin{aligned}&\vec{a}_{\phi^*}(\boldsymbol{x}^*,t) = a^j_{\phi^*}(\boldsymbol{x}^*,t)\,\vec{g}_j(\boldsymbol{x}^*,t) = a^j_{\phi^*}(\boldsymbol{x}^*,t)\;Q^i{}_j(\boldsymbol{x}^*,t)\,\vec{e}_i(\boldsymbol{x},t)\\ =&\,\vec{a}_\phi(\boldsymbol{x},t) = a^i_\phi(\boldsymbol{x},t)\,\vec{e}_i(\boldsymbol{x},t),\end{aligned}$$

which provides the transformation properties of components of objective vectors, $a^i_\phi(\boldsymbol{x},t) = Q^i{}_j(\boldsymbol{x}^*,t)\,a^j_{\phi^*}(\boldsymbol{x}^*,t)$.

For any second-order contravariant tensor $\overleftrightarrow{a}$ belonging to $\mathbb{V}\otimes\mathbb{V}$ we get, following the same procedure,

$$\overleftrightarrow{a}_{\phi^*} = a^{kl}_{\phi^*}\,\vec{g}_k\otimes\vec{g}_l = a^{kl}_{\phi^*}\,(Q^i{}_k\,\vec{e}_i)\otimes(Q^j{}_l\,\vec{e}_j) = a^{kl}_{\phi^*}Q^i{}_kQ^j{}_l\,\vec{e}_i\otimes\vec{e}_j = \overleftrightarrow{a}_\phi = a^{ij}_\phi\,\vec{e}_i\otimes\vec{e}_j,$$

that its components transform as

$$a^{ij}_\phi(\boldsymbol{x},t) = Q^i{}_k(\boldsymbol{x}^*,t)Q^j{}_l(\boldsymbol{x}^*,t)\,a^{kl}_{\phi^*}(\boldsymbol{x}^*,t). \tag{1.6}$$

The basis of the space of all linear mappings $\mathbb{V}\to\mathbb{R}$, denoted as $\mathcal{L}(\mathbb{V})$, will be referred to as the local dual basis. It is formed by one-forms $\underline{e}^i$, resp. $\underline{g}^i$, which are defined through the relations

$$\underline{e}^i(\vec{e}_j) = \delta^i{}_j; \quad \underline{g}^i(\vec{g}_j) = \delta^i{}_j, \tag{1.7}$$

where $\delta^i{}_j$ is the Kronecker delta. In virtue of the identity

$$\delta^i{}_j = \frac{\partial x^i_*(\boldsymbol{x},t)}{\partial x^k}\frac{\partial x^k(\boldsymbol{x}^*,t)}{\partial x^j_*} \tag{1.8}$$

we see that (insert for $\delta^i{}_j$ in the second relation of eq. (1.7) and expand $\vec{g}_j$ on its left-hand side – the following then stems from the linearity of one-forms)

$$\underline{g}^i(\boldsymbol{x}^*,t) = \frac{\partial x^i_*(\boldsymbol{x},t)}{\partial x^j}\,\underline{e}^j(\boldsymbol{x},t) = \{Q^{-1}(\boldsymbol{x},t)\}^i{}_j\,\underline{e}^j(\boldsymbol{x},t), \tag{1.9}$$

where $Q^{-1}(\boldsymbol{x},t)$ is the inverse shifter tensor, $Q^i{}_k(\boldsymbol{x}^*,t)\,\{Q^{-1}(\boldsymbol{x},t)\}^k{}_j = \delta^i{}_j$. The transformation properties of one-forms, or covectors, are thus inverse when compared to those of vectors. Typical example of a one-form is the gradient of a scalar field:

$$\nabla a = \frac{\partial a_\phi(\boldsymbol{x},t)}{\partial x^i}\,\underline{e}^i(\boldsymbol{x},t) = \frac{\partial a_{\phi^*}(\boldsymbol{x}^*,t)}{\partial x^k_*}\frac{\partial x^k_*(\boldsymbol{x},t)}{\partial x^i}\,\underline{e}^i(\boldsymbol{x},t) = \frac{\partial a_{\phi^*}(\boldsymbol{x}^*,t)}{\partial x^k_*}\,\underline{g}^k(\boldsymbol{x}^*,t),$$

where we have used the chain rule in differentiating $a_\phi(\boldsymbol{x},t) = a_{\phi^*}(\boldsymbol{x}^*(\boldsymbol{x},t),t)$ to show that the components of the gradient indeed transform according to eq. (1.9), that is, $\{\nabla a_\phi(\boldsymbol{x},t)\}_i = \{Q^{-1}\}^k_i(\boldsymbol{x}^*,t)\,\{\nabla a_{\phi^*}(\boldsymbol{x}^*,t)\}_k$.

Performing the above procedure for components of an objective vector field $\vec{a}$

yields the transformation properties of the gradient of objective vector field:

$$\{\nabla \vec{a}_\phi(\boldsymbol{x},t)\}^i{}_j = Q^i{}_k(\boldsymbol{x},t)\,\{Q^{-1}(\boldsymbol{x}^*,t)\}^l{}_j\,\{\nabla \vec{a}_{\phi^*}(\boldsymbol{x}^*,t)\}^k_l, \tag{1.10}$$

where $\{\nabla \vec{a}_\phi(\boldsymbol{x},t)\}^i{}_j := \partial a^i_\phi/\partial x^j$. The shifter tensor in eq. (1.10) comes from the objectivity of the vector field, $a^i_\phi(\boldsymbol{x},t) = Q^i{}_j\, a^j_{\phi^*}(\boldsymbol{x}^*(\boldsymbol{x},t),t)$, and the inverse shifter tensor stems from the differentiation. Eq. (1.10) is equivalent to saying that the gradient of objective vector field is a second-order, right covariant mixed tensor (contravariant in its first index, covariant in the second index). Such tensors can be written as a linear combination of $\vec{e}_i \otimes \underline{e}^j$, so that $\nabla \vec{a}_\phi(\boldsymbol{x},t) = \{\nabla \vec{a}_\phi(\boldsymbol{x},t)\}^i{}_j\,\vec{e}_i \otimes \underline{e}^j$.

Not all vectors are objective. Typical examples of frame dependent vector fields are the velocity and the acceleration of a body. Velocity of a particle is the rate of change of its position vector. We will denote the position vector of particle p in frame ϕ as $\vec{s}_\phi(\boldsymbol{x},t)$, resp. $\vec{s}_{\phi^*}(\boldsymbol{x}^*,t)$ in frame ϕ^*, where $\boldsymbol{x}{=}\chi_\phi(p,t)$ and $\boldsymbol{x}^*{=}\chi_{\phi^*}(p,t)$ are the respective coordinates of point p. The position vectors are related via

$$\vec{s}_\phi(\boldsymbol{x},t) = \vec{s}_{\phi^*}(\boldsymbol{x}^*,t) + \vec{c}(t), \tag{1.11}$$

where $\vec{c}(t)$ is a vector connecting the origins of both frames. To see how the velocity of a particle, when measured in frame ϕ, is related to the velocity observed in frame ϕ^*, we must apply the material derivative $\frac{\mathcal{D}}{\mathcal{D}t} := \frac{\partial}{\partial t}\big|_{p=const}$ to eq. (1.11). First, let us express the vectors in eq. (1.11) in terms of its components in the corresponding local vector bases

$$s^i_\phi(\boldsymbol{x},t)\,\vec{e}_i(\boldsymbol{x},t) = s^j_{\phi^*}(\boldsymbol{x}^*,t)\,\vec{g}_j(\boldsymbol{x}^*,t) + \vec{c}(t). \tag{1.12}$$

Though generally not necessary, it is usually instructive to have one observer equipped with a simple Cartesian frame attached to the Euclidean space, $\phi\colon \mathbb{E} \to \mathbb{R}^3$, with its basis being identical at every point of the Euclidean space, $\vec{e}_i(\boldsymbol{x},t){=}\vec{e}_i$, and experiment only with the other observer $\phi^*\colon \mathbb{E}\times[0,\infty) \to \mathbb{R}^3$. Eq. (1.12) then reads

$$x^i(p,t)\,\vec{e}_i = s^j_{\phi^*}(\boldsymbol{x}^*(p,t),t)\,\vec{g}_j(\boldsymbol{x}^*(p,t),t) + c^k_\phi(t)\,\vec{e}_k, \tag{1.13}$$

because in the Cartesian frame components of the position vector are equal to the coordinates of the respective point, $s^i_\phi(\boldsymbol{x}(p,t),t){=}x^i(p,t)$. By applying material derivative to eq. (1.13) we get

$$v^i_\phi \vec{e}_i = \frac{\mathcal{D}s^j_{\phi^*}}{\mathcal{D}t}\,\vec{g}_j + s^j_{\phi^*}\,\frac{\partial \vec{g}_j}{\partial x^l_*}\,\frac{\mathcal{D}x^l_*}{\mathcal{D}t} + s^j_{\phi^*}\,\frac{\partial \vec{g}_j}{\partial t} + \frac{\mathrm{d}c^k_\phi}{\mathrm{d}t}\vec{e}_k, \tag{1.14}$$

where the particle's velocity in the Cartesian frame was identified, $v^i_\phi{:=}(\mathcal{D}x^i)/(\mathcal{D}t)$. The first two terms on the right-hand side of eq. (1.14) together form the velocity $\vec{v}_{\phi^*}$, with the second term correcting for the change of the local basis along the

trajectory of the particle (first term alone would equal the velocity $\vec{v}_{\phi^*}$ if the local basis of ϕ^* was spatially homogeneous). The third term is related to the relative motion of both frames (see below). The last term describes the relative velocity of the origins of both frames and does not depend on which particle p we are tracing.

By *Euclidean change of frame* we will understand a change of frame that satisfies

$$s^j_{\phi^*}(\boldsymbol{x}^*,t)\,\frac{\partial \vec{g}_j(\boldsymbol{x}^*,t)}{\partial t} = \vec{\omega}(t)\times\vec{s}_{\phi^*}(\boldsymbol{x}^*,t) \tag{1.15}$$

for all points $\boldsymbol{x}^*$ and times t. The vector $\vec{\omega}(t)$ is the relative rotation of both frames and it is dependent on time only. It can be related with the tensor

$$\Omega^i{}_j(\boldsymbol{x}^*,t) := \frac{\partial Q^i{}_k(\boldsymbol{x}^*,t)}{\partial t}\,\{Q^{-1}(\boldsymbol{x}(\boldsymbol{x}^*,t),t)\}^k{}_j\,, \tag{1.16}$$

through the relation $\Omega^i{}_j a^j = \xi_{ijk}\omega^j a^k$, valid for any vector $\vec{a}$. ξ_{ijk} denotes the Levi-Civita symbol. In other words, the change of frame is Euclidean if and only if $\Omega^i{}_j(\boldsymbol{x}^*,t)$ is antisymmetric and spatially homogeneous. In Appendix 1.A the formulae (1.14) are worked out for a particular example, explaining the meaning of each term in eq. (1.14) and discussing the properties of $\Omega^i{}_j(\boldsymbol{x}^*,t)$ for Euclidean changes of frame, for which the relative motion of frames ϕ and ϕ^* is a combination of translation and rotation only.

Note that it would not have been possible to distinguish between Euclidean and other changes of frame, had we, in the beginning, restricted ourselves only to Cartesian frames (with equal metric). Cartesian frames with equal metric are always only translated and rotated with respect to each other. For the rest of this section, however, we will consider Euclidean changes of frame only and for brevity we will thus abandon curvilinear coordinates (we return to them in Section 1.2).

For Cartesian coordinates one gets $\vec{g}_j(\boldsymbol{x}^*,t)=\vec{g}_j(t)$, $s^j_{\phi^*}(\boldsymbol{x}^*(p,t),t)=x^j_*(p,t)$, $Q^i{}_j(\boldsymbol{x}^*,t)=Q^i{}_j(t)$ and eq. (1.14) reads

$$v^i_\phi(\boldsymbol{x},t)\vec{e}_i = v^j_{\phi^*}(\boldsymbol{x}^*,t)\,\vec{g}_j(t) + \xi_{ijk}\omega_j(t)x^k_*(p,t)\,\vec{g}_i(t) + \frac{\mathrm{d}c^k_\phi(t)}{\mathrm{d}t}\,\vec{e}_k. \tag{1.17}$$

Applying material derivative again gives a relation between the accelerations of the particle, as viewed by the two observers:

$$a^i_\phi\vec{e}_i = a^j_{\phi^*}\,\vec{g}_j + v^j_{\phi^*}\frac{\partial\vec{g}_j}{\partial t} + \xi_{ijk}\frac{\mathrm{d}\omega_j}{\mathrm{d}t}x^k_*\,\vec{g}_i + \xi_{ijk}\omega^j\frac{\mathcal{D}x^k_*}{\mathcal{D}t}\,\vec{g}_i + \xi_{ijk}\omega^j x^k_*\frac{\partial\vec{g}_i}{\partial t} + \frac{\mathrm{d}^2c^k_\phi}{(\mathrm{d}t)^2}\,\vec{e}_k,$$

where $a^i_\phi := \mathcal{D}v^i_\phi/\mathcal{D}t$, resp. $a^i_{\phi^*} := \mathcal{D}v^i_{\phi^*}/\mathcal{D}t$. Since eq. (1.15) is valid for any position vector, it must be valid for any vector in general, and we can rewrite the second, fourth and fifth terms as cross products:

$$a^i_\phi\vec{e}_i = a^j_{\phi^*}\,\vec{g}_j + \vec{\omega}\times\vec{v}_{\phi^*} + \xi_{ijk}\frac{\mathrm{d}\omega_j}{\mathrm{d}t}x^k_*\,\vec{g}_i + \vec{\omega}\times\vec{v}_{\phi^*} + \vec{\omega}\times(\vec{\omega}\times\vec{s}_{\phi^*}) + \frac{\mathrm{d}^2c^k_\phi}{(\mathrm{d}t)^2}\,\vec{e}_k. \tag{1.18}$$

In direct notation, that is, without expanding the vectors into local bases, eq. (1.18) reads

$$\vec{a}_\phi = \vec{a}_{\phi^*} + 2\vec{\omega}\times\vec{v}_{\phi^*} + \frac{\mathrm{d}\vec{\omega}}{\mathrm{d}t}\times\vec{s}_{\phi^*} + \vec{\omega}\times(\vec{\omega}\times\vec{s}_{\phi^*}) + \frac{\mathrm{d}^2\vec{c}_\phi}{(\mathrm{d}t)^2}, \tag{1.19}$$

which is valid for any Euclidean change of frame. We see that the accelerations in frames ϕ and ϕ^* differ by the well known Coriolis acceleration, Euler acceleration, centrifugal acceleration, and by the relative acceleration of the frames' origins.

Once we have derived the transformation properties of objective vectors, one-forms and contravariant tensors, as well as the transformation properties of material particle's velocity and acceleration, we can discuss the transformation properties of the equation of motion. Let us assume that frame ϕ is an inertial frame. The equation of motion then acquires the form

$$\nabla\cdot\overleftrightarrow{\tau}_\phi + \vec{f}_\phi = \rho_\phi\,\vec{a}_\phi. \tag{1.20}$$

To find the equation of motion in some non-inertial frame ϕ^*, one must find the transformation properties of the density ρ_ϕ, the volumetric body force $\vec{f}_\phi$, and the Cauchy stress tensor $\overleftrightarrow{\tau}_\phi$. We agree with Liu & Sampaio (2014), that "unlike the acceleration, transformation properties of non-kinematic quantities cannot be deduced theoretically". Instead, the transformation properties of non-kinematic quantities must be postulated. The *postulate of Euclidean objectivity* says that, for any Euclidean change of frame, the density, the body force and the Cauchy stress tensor are frame indifferent, and so their components transform in the following manner:

$$\begin{aligned}\rho_\phi(\boldsymbol{x},t) = \rho_{\phi^*}(\boldsymbol{x}^*,t);\quad f^i_\phi(\boldsymbol{x},t) = Q^i{}_j(t)\,f^j_{\phi^*}(\boldsymbol{x}^*,t);\\ \tau^{ij}_\phi(\boldsymbol{x},t) = Q^i{}_k(t)\,Q^j{}_l(t)\,\tau^{kl}_{\phi^*}(\boldsymbol{x}^*,t).\end{aligned} \tag{1.21}$$

In other words, these quantities are objective scalar, vector, and contravariant tensor fields respectively. The equation of motion in a non-inertial frame ϕ^* can then be written as

$$\nabla\cdot\overleftrightarrow{\tau}_{\phi^*} + \vec{f}_{\phi^*} = \rho_{\phi^*}\,\vec{a}_{\phi^*} + \rho_{\phi^*}\,\vec{i}_{\phi^*}, \tag{1.22}$$

where $\rho_{\phi^*}\vec{i}_{\phi^*}$ are the so-called fictious forces, $\vec{i}_{\phi^*}$ being the accelerations named below eq. (1.19).

The primary focus of this chapter is on the properties of constitutive equations for the Cauchy stress tensor. We will assume a body whose stress state is determined only by the body's motion,

$$\tau^{ij}_\phi(\boldsymbol{x}(p,t),t) = \mathcal{F}^{ij}_\phi(\chi_\phi;\,p), \tag{1.23}$$

where $\mathcal{F}^{ij}_{\phi}$ is a functional that can generally depend on the entire history of the motion that the body has experienced. From the postulate of Euclidean objectivity it immediately follows that

$$\mathcal{F}^{ij}_{\phi}(\chi_\phi;\, p) = Q^i{}_k(t)\, Q^j{}_l(t)\, \mathcal{F}^{kl}_{\phi^*}(\chi_{\phi^*};\, p) = Q^i{}_k(t)\, Q^j{}_l(t)\, \mathcal{F}^{kl}_{\phi^*}(*(\chi_\phi);\, p), \tag{1.24}$$

where $*$ denotes the Euclidean change of frame $\boldsymbol{x}^*{=}\boldsymbol{x}^*(\boldsymbol{x}, t)$ of the entire history of the motion χ_ϕ. Eq. (1.24) does not yet impose any restrictions on the constitutive functional $\mathcal{F}^{ij}_{\phi}$ itself. It is a relation between two constitutive functionals $\mathcal{F}^{ij}_{\phi}$ and $\mathcal{F}^{ij}_{\phi^*}$, defining the Cauchy stress tensor for two different observers. The desired restriction comes when eq. (1.24) is combined with the *principle of material frame-indifference*, which says that the form of the constitutive equation does not depend on observer:

$$\mathcal{F}^{ij}_{\phi}(\bullet;\, p) = \mathcal{F}^{ij}_{\phi^*}(\bullet;\, p). \tag{1.25}$$

Only then one arrives at the *condition of material objectivity*:

$$\mathcal{F}^{ij}_{\phi}(\chi_\phi;\, p) = Q^i{}_k(t)\, Q^j{}_l(t)\, \mathcal{F}^{kl}_{\phi}(*(\chi_\phi);\, p), \tag{1.26}$$

where $*$ stands for any Euclidean change of frame. Eq. (1.26) is a fundamental result in constitutive theories. It is used for testing whether a suggested constitutive law is physically consistent. An intuitive way to interpret the condition of material objectivity is to consider χ_ϕ and $*(\chi_\phi)$ to be two different motions of the same body, these motions being measured in the frame ϕ. The deformation experienced by the body in these motions is, however, identical, because the motions differ only by a rigid body motion (see the definition of Euclidean changes of frame). The condition (1.26) thus says that the stress state of the material depends on the experienced deformation only.

Note that if we wanted to stay within the general framework of curvilinear coordinates, we could not write eq. (1.25)[2]. Indeed, in some textbooks it is directly eq. (1.26) that is postulated, referred to as the "principle of invariance under superimposed rigid body motions". It is because eq. (1.26) is valid for any frame, including curvilinear ones, as long as $*(\chi_\phi)$ is a motion composed of the motion χ_ϕ and some rigid body translation and rotation, measured in the frame ϕ. The shifter tensor in eq. (1.26) is, however, spatially dependent for curvilinear frames.

So far we have worked with motions defined as mappings of the body $\mathcal{B}$. The domain of such mappings was a set of material points. In real applications, this is rarely the case. Motions are usually defined with respect to some reference configuration. By a *reference configuration* of the body $\mathcal{B}$ in frame ϕ we understand a mapping $\kappa_\phi{:}\,\mathcal{B} \to \mathbb{R}^3$, which is a time independent mapping that associates each material point uniquely with a set of coordinates in the frame ϕ. Reference con-

[2]See the example in Appendix 1.A, where eq. (1.25) is not valid because frame ϕ is Cartesian and frame ϕ^* is polar.

figuration is often chosen as the initial configuration the body, $\kappa_\phi(\bullet) = \chi_\phi(\bullet, 0)$, but not necessarily. For example, when modelling small deformations of a planet, the reference configuration is usually taken as a sphere, even though the planet never was a sphere during the studied motion (see e.g. the modelling study in Chapter 2).

When κ_ϕ is used to replace the set of material points $\mathcal{B}$ by $\mathbb{R}^3$ in the definition of motion χ_ϕ, we get the traditional notion of a motion, used in practical applications:

$$\chi_{\kappa,\phi} : \mathbb{R}^3 \times [0, \infty) \to \mathbb{R}^3, \tag{1.27}$$

where $\chi_{\kappa,\phi}$ is the motion χ_ϕ with respect to the reference configuration κ_ϕ. The coordinates of material point p in the reference configuration κ_ϕ are usually denoted as $\boldsymbol{X}{=}\kappa_\phi(p)$. The coordinates of such particle throughout the motion are obtained as $\boldsymbol{x}{=}\chi_{\kappa,\phi}(\boldsymbol{X}, t)$. Distinguishing between χ_ϕ and $\chi_{\kappa,\phi}$ has important implications for constitutive theory, which was pointed out by Liu & Sampaio (2014). Constitutive functional $\mathcal{F}^{ij}_\phi$, defined for motions χ_ϕ, is not ideal for real applications. Instead, it is convenient to introduce a constitutive functional $\mathcal{F}^{ij}_{\kappa,\phi}$, defined on motions in referential description:

$$\mathcal{F}^{ij}_\phi(\chi_\phi;\, p) = \mathcal{F}^{ij}_\phi(\chi_{\kappa,\phi} \circ \kappa_\phi;\, \kappa^{-1}_\phi(\boldsymbol{X})) =: \mathcal{F}^{ij}_{\kappa,\phi}(\chi_{\kappa,\phi};\, \boldsymbol{X}). \tag{1.28}$$

The principle of material frame-indifference (1.25), when motion χ_ϕ is inserted in its both sides, implies that

$$\begin{aligned} \mathcal{F}^{ij}_{\kappa,\phi}(\chi_{\kappa,\phi};\, \boldsymbol{X}) = \mathcal{F}^{ij}_\phi(\chi_\phi;\, p) \overset{(1.25)}{=} \mathcal{F}^{ij}_{\phi^*}(\chi_\phi;\, p) = \mathcal{F}^{ij}_{\phi^*}(\chi_{\kappa,\phi}{\circ}\kappa_\phi;\, \kappa^{-1}_\phi(\boldsymbol{X})) \\ = \mathcal{F}^{ij}_{\phi^*}(\chi_{\kappa,\phi}{\circ}\kappa_\phi{\circ}\kappa^{-1}_{\phi^*}{\circ}\kappa_{\phi^*};\, \kappa^{-1}_{\phi^*}{\circ}\kappa_{\phi^*}{\circ}\kappa^{-1}_\phi(\boldsymbol{X})) = \mathcal{F}^{ij}_{\kappa^*,\phi^*}(\chi_{\kappa,\phi}{\circ}\kappa_\phi{\circ}\kappa^{-1}_{\phi^*};\, \kappa_{\phi^*}{\circ}\kappa^{-1}_\phi(\boldsymbol{X})), \end{aligned} \tag{1.29}$$

and so $\mathcal{F}^{ij}_{\kappa,\phi}(\bullet;\, \boldsymbol{X}) \neq \mathcal{F}^{ij}_{\kappa^*,\phi^*}(\bullet;\, \boldsymbol{X})$, in contrast to eq. (1.25)[3]. In the referential description, such relation is only be valid if κ_ϕ is equal to κ_{ϕ^*}, so that the joined mappings $\kappa_{\phi^*}{\circ}\kappa^{-1}_\phi$ and $\kappa_\phi{\circ}\kappa^{-1}_{\phi^*}$ are identity. For the typical scenario, in which reference configuration is chosen as the initial configuration, the condition $\kappa_\phi{=}\kappa_{\phi^*}$ means that both frames coincide at time $t{=}0$.

The condition of material objectivity can also be written in the referential description. Following a similar procedure as above, eq. (1.26) can be reformulated in terms of $\mathcal{F}^{ij}_{\kappa,\phi}$ instead of $\mathcal{F}^{ij}_\phi$:

$$\mathcal{F}^{ij}_{\kappa,\phi}(\chi_{\kappa,\phi};\, \boldsymbol{X}) = Q^i{}_k(t)\, Q^j{}_l(t)\, \mathcal{F}^{kl}_{\kappa,\phi}(\chi_{\kappa^*,\phi^*}{\circ}\kappa_{\phi^*}{\circ}\kappa^{-1}_\phi;\, \boldsymbol{X}). \tag{1.30}$$

[3]Compare eq. (1.29) with eq. (25) from Liu & Sampaio (2014). Clearly, q^* in their eq. (25) was supposed to be $\kappa_j{\circ}\kappa^{-1}_i$ and not $j{\circ}i^{-1}$. Corrected version of their original article can now be downloaded from the author's website (Liu, personal communication). We note that in view of this correction the two generally inappropriate assumptions discussed in Remark 9 of Liu & Sampaio (2014) no longer seem to cancel each other out by a "lucky coincidence": the correctness of both assumptions depends on whether or not $\kappa_j{\circ}\kappa^{-1}_i$ is identity.

Above we mentioned that the condition of material objectivity can be viewed as the equality of stress in a body experiencing two different motions, by interpreting the mappings χ_ϕ and χ_{ϕ^*} as two different motions measured in one frame ϕ (the invariance of stress under superimposed rigid body motions). By inspection of eq. (1.30) we see that in referential description this interpretation is also possible, but $\kappa_{\phi^*} \circ \kappa_\phi^{-1}$ must be identity for such interpretation to be straightforward. In other words, both such motions $\chi_{\kappa,\phi}$ and χ_{κ^*,ϕ^*} must have the same initial configuration.

In the following sections we will need transformation properties of other kinematic quantities than just the velocity and the acceleration. In the theory of solid materials, fundamental role is played by the deformation gradient:

$$\{\mathbb{F}_\phi\}^i{}_j := \frac{\partial \chi^i_{\kappa,\phi}(\boldsymbol{X},t)}{\partial X^j}; \quad \{\mathbb{F}_{\phi^*}\}^i{}_j := \frac{\partial \chi^i_{\kappa^*,\phi^*}(\boldsymbol{X}^*,t)}{\partial X^j_*}. \tag{1.31}$$

The change of frame $\boldsymbol{x} = \boldsymbol{x}(\boldsymbol{x}^*,t)$ provides a possibility to express the motion $\boldsymbol{x} = \chi_{\kappa,\phi}(\boldsymbol{X},t)$ in terms of its counterpart $\boldsymbol{x}^* = \chi_{\kappa^*,\phi^*}(\boldsymbol{X}^*,t)$, resulting in the identity $\chi_{\kappa,\phi}(\boldsymbol{X},t) = \boldsymbol{x}(\chi_{\kappa^*,\phi^*}(\boldsymbol{X}^*(\boldsymbol{X}),t),t)$, where $\boldsymbol{X}^*(\boldsymbol{X})$ is the mapping $\kappa_{\phi^*} \circ \kappa_\phi^{-1}$. By differentiating this relation we get the transformation properties of the deformation gradient

$$\{\mathbb{F}_\phi\}^i{}_j = \frac{\partial x^i(\chi_{\kappa^*,\phi^*}(\boldsymbol{X}^*(\boldsymbol{X}),t),t)}{\partial X^j} = \frac{\partial x^i(\boldsymbol{x}^*,t)}{\partial x^k_*}\,\frac{\partial \chi^k_{\kappa^*,\phi^*}(\boldsymbol{X}^*,t)}{\partial X^l_*}\,\frac{\partial X^l_*(\boldsymbol{X})}{\partial X^j}. \tag{1.32}$$

Eq. (1.32) simplifies to the traditional $\{\mathbb{F}_\phi\}^i{}_j = Q^i{}_k(t)\,\{\mathbb{F}_{\phi^*}\}^k_j$ when $\kappa_{\phi^*} \circ \kappa_\phi^{-1}$ is identity. For the inverse of the deformation gradient we analogously obtain $\{\mathbb{F}^{-1}_\phi\}^i{}_j = O^i{}_k\,\{\mathbb{F}^{-1}_{\phi^*}\}^k_l\,\{Q^{-1}(t)\}^l{}_j$, with the shifter tensor $O^i{}_j := \partial X^i/\partial X^j_*$ describing the change of frame for the reference configuration. Typically $O^i{}_j = Q^i{}_j(0)$.

In the theory of fluids, it is the velocity gradient that is of primary interest. Thanks to the identity

$$\left\{\frac{\mathcal{D}\mathbb{F}_\phi}{\mathcal{D}t}\mathbb{F}^{-1}_\phi\right\}^i{}_j = \frac{\partial^2 \chi^i_{\kappa,\phi}(\boldsymbol{X},t)}{\partial X^k \partial t}\,\frac{\partial \{\chi^{-1}_{\kappa,\phi}\}^k(\boldsymbol{x},t)}{\partial x^j} = \frac{\partial v^i_\phi(\boldsymbol{X},t)}{\partial X^k}\,\frac{\partial X^k(\boldsymbol{x},t)}{\partial x^j} = \{\nabla \vec{v}_\phi\}^i{}_j, \tag{1.33}$$

with ∇ standing for the gradient with respect to $\boldsymbol{x}$, we can use the transformation properties of the deformation gradient to infer the transformation properties of

the velocity gradient:

$$\{\nabla\vec{v}_\phi\}^i_{\ j} = \left\{\frac{\mathcal{D}\mathbb{F}_\phi}{\mathcal{D}t}\mathbb{F}_\phi^{-1}\right\}^i_{\ j} = \frac{\mathcal{D}\ (Q^i_{\ m}(t)\,\{\mathbb{F}_{\phi^*}\}^m_{\ n}\,\{O^{-1}\}^n_{\ k})}{\mathcal{D}t}O^k_{\ u}\,\{\mathbb{F}^{-1}_{\phi^*}\}^u_{\ v}\,\{Q^{-1}(t)\}^v_{\ j}$$
$$= Q^i_{\ m}(t)\frac{\mathcal{D}\{\mathbb{F}_{\phi^*}\}^m_{\ n}}{\mathcal{D}t}\{\mathbb{F}^{-1}_{\phi^*}\}^n_{\ v}\,\{Q^{-1}(t)\}^v_{\ j} + \frac{\mathrm{d}Q^i_{\ m}(t)}{\mathrm{d}t}\,\{Q^{-1}(t)\}^m_{\ j}$$
$$= Q^i_{\ m}(t)\{\nabla\vec{v}_{\phi^*}\}^m_{\ v}\,\{Q^{-1}(t)\}^v_{\ j} + \Omega^i_{\ j}(t), \tag{1.34}$$

where $O^i_{\ j}$ is no longer present as it was canceled with its inverse in both terms on the second line. Eq. (1.34) resembles the transformation properties of gradients of objective vector fields (cf. eq. (1.10)). However, since the velocity vector is not objective, there is an additional term $\Omega^i_{\ j}(t)$ in eq. (1.34), making $\nabla\vec{v}_\phi$ not objective either. The tensor $\Omega^i_{\ j}(t)$ describes the relative rotation of frames ϕ and ϕ^*.

We have defined Euclidean change of frame to be any transformation $\boldsymbol{x}^*{=}\boldsymbol{x}^*(\boldsymbol{x},t)$ for which $\Omega^i_{\ j}$ is spatially homogeneous and antisymmetric (see also Appendix 1.A). It is thus a direct consequence of eq. (1.34) that the symmetric part of the velocity gradient, $\mathbb{D}_\phi := \frac{1}{2}[\nabla\vec{v}_\phi + (\nabla\vec{v}_\phi)^{\mathrm{T}}]$, is Euclidean objective, while the complementary antisymmetric part, $\mathbb{W}_\phi := \frac{1}{2}[\nabla\vec{v}_\phi - (\nabla\vec{v}_\phi)^{\mathrm{T}}]$, is not. The symbol T is the transposition[4]. The strain-rate $\mathbb{D}_\phi$ describes the stretching of a given volume element, while the spin $\mathbb{W}_\phi$ describes the rigid body rotation of that volume element. Indeed, the measure of deformation rate $\mathbb{D}_\phi$ is independent of observer, while the observed local rigid rotation $\mathbb{W}_\phi$ differs by the relative rotation of both frames $\Omega^i_{\ j}$ from observer to observer.

1.2 Objective tensor rates

In the beginning of this chapter, the 1-D analogue of Maxwell viscoelastic fluid was introduced, leading to the equation $S = \eta\dot{\Delta} - (\eta/G)\dot{S}$. Based on this equation it was suggested that the corresponding 3-D constitutive law should be of the form

$$\tau^{ij}_\phi(\chi_{\kappa,\phi}(\boldsymbol{X},t),t) = \mathcal{F}^{ij}_{\kappa,\phi}(\chi_{\kappa,\phi};\,\boldsymbol{X}) = 2\eta_\phi\mathbb{D}^{ij}_\phi - \frac{\eta_\phi}{G_\phi}\frac{\mathcal{D}_?(\tau^{ij}_\phi)}{\mathcal{D}t}, \tag{1.35}$$

but it was unclear what stress rate to employ, since the material derivative of second-order tensors was argued to be frame dependent. In the first half of this section we use the condition of material objectivity to impose restrictions on the

[4]Note that the gradient of a vector field is a right covariant mixed tensor, while the transpose of it is a left covariant mixed tensor (covariant in its first index and contravariant in the second index), which implies that both tensors generally cannot be added together, as they are of different kind. Let us, for now, continue in the scenario in which ϕ is a Cartesian frame, where we can disregard such subtleties.

possible stress rates. While such procedure eliminates non-objective tensor rates from considerations, it does not provide a hint as to which tensor rate to actually use. In the second half of this section we use the work of Oldroyd (1950) and geometrical considerations to suggest which objective rate results in a material model that fits the traditional derivation of Maxwell body.

First, let us investigate the transformation properties of $2\eta_\phi \mathbb{D}^{ij}_\phi$. The viscosity η_ϕ is not a kinematic quantity, and its transformation properties thus cannot be derived. Instead, η_ϕ must be postulated to be objective scalar, $\eta_\phi{=}\eta_{\phi^*}$. The product $2\eta_\phi \mathbb{D}^{ij}_\phi$ is then automatically frame indifferent, because strain-rate $\mathbb{D}$ was shown to be objective in the previous section. Note that when only frame indifferent quantities are used in a constitutive law the condition of material objectivity (1.26), resp. (1.30), is automatically satisfied.

Similarly as for the viscosity, the relaxation time $t_{\mathrm{rel}}{:=}\eta_\phi/G_\phi$ must be postulated to be objective scalar, leaving the transformation properties of the second term in eq. (1.35) to be determined by the properties of the proposed stress rate. In the introduction to this chapter, we have argued by qualitative means that material derivative of second-order tensor fields is not objective. By applying $\mathcal{D}/\mathcal{D}t$ to eq. (1.6) we directly obtain its transformation properties:

$$\begin{aligned}\frac{\mathcal{D}a^{ij}_\phi(\boldsymbol{x},t)}{\mathcal{D}t} &= Q^i{}_k(t)\,Q^j{}_l(t)\,\frac{\mathcal{D}a^{kl}_{\phi^*}(\boldsymbol{x}^*,t)}{\mathcal{D}t} + \frac{\mathrm{d}Q^i{}_k(t)}{\mathrm{d}t}\,Q^j{}_l(t)\,a^{kl}_{\phi^*}(\boldsymbol{x}^*,t) + Q^i{}_k(t)\,\frac{\mathrm{d}Q^j{}_l(t)}{\mathrm{d}t}\,a^{kl}_{\phi^*}(\boldsymbol{x}^*,t) \\ &= Q^i{}_k(t)\,Q^j{}_l(t)\,\frac{\mathcal{D}a^{kl}_{\phi^*}(\boldsymbol{x}^*,t)}{\mathcal{D}t} + \Omega^i{}_k(t)\,a^{kj}_\phi(\boldsymbol{x},t) + \Omega^j{}_k(t)\,a^{ik}_\phi(\boldsymbol{x},t),\end{aligned} \tag{1.36}$$

where the objectivity of $\overrightarrow{a}$ and the definition $\Omega^i{}_j{:=}(\mathrm{d}Q^i{}_k/\mathrm{d}t)\,\{Q^{-1}\}^k_j$ are used on the second line. Eq. (1.36) shows that $\mathcal{D}\overrightarrow{a}_\phi/\mathcal{D}t$ is not an objective tensor[5], because its components do not transform according to eq. (1.6). To fix this, one needs to incorporate a quantity into the definition of the proposed time derivative, whose transformation properties could cancel out the second and third terms in eq. (1.36). Eq. (1.34) immediately suggests such quantity. Adding $-\{\nabla v_\phi\}^i{}_k\,a^{kj}_\phi$ into the definition of a tensor rate would cancel the second term and adding $-a^{ik}_\phi\,\{\nabla(v_\phi)\}^j{}_k$ would cancel the third term from eq. (1.36).

This idea can be formalized by introducing so-called "upper convected", or Oldroyd, time derivative

$$\frac{\mathcal{D}_{\mathrm{uc}}\,a^{ij}_\phi}{\mathcal{D}t} := \frac{\mathcal{D}a^{ij}_\phi}{\mathcal{D}t} - \{\nabla\vec{v}_\phi\}^i{}_k\,a^{kj}_\phi - a^{ik}_\phi\,\{\nabla\vec{v}_\phi\}^j{}_k, \tag{1.37}$$

where a^{ij}_ϕ are the components of any contravariant tensor $\overrightarrow{a}$. By combining

[5]To be fully consistent, one should thus distinguish between $\mathcal{D}_\phi(\bullet)/\mathcal{D}t$ and $\mathcal{D}_{\phi^*}(\bullet)/\mathcal{D}t$ in the definition of material time derivative. For brevity we not do so. The observer performing the derivative will always be identifiable from the subscript of the quantity being differentiated.

eqs. (1.34) and (1.36) it follows that

$$\frac{\mathcal{D}_{\mathrm{uc}}\, a_\phi^{ij}(\boldsymbol{x},t)}{\mathcal{D}t} = Q^i{}_k(t)\, Q^j{}_l(t)\, \frac{\mathcal{D}_{\mathrm{uc}}\, a_{\phi^*}^{kl}(\boldsymbol{x}^*,t)}{\mathcal{D}t}, \tag{1.38}$$

which means that the Oldroyd derivative of an objective tensor is an objective tensor (the rate is objective). Recall that the transformation properties (1.38) simply imply that

$$\frac{\mathcal{D}_{\mathrm{uc}}\, \overrightarrow{a}_\phi(\boldsymbol{x},t)}{\mathcal{D}t} = \frac{\mathcal{D}_{\mathrm{uc}}\, \overrightarrow{a}_{\phi^*}(\boldsymbol{x}^*,t)}{\mathcal{D}t}. \tag{1.39}$$

An immediate consequence is that when such rate is used in eq. (1.35), the resulting constitutive law satisfies the condition of material objectivity.

In Section 1.1 the symmetric and antisymmetric parts of the velocity gradient were introduced and called the strain-rate $\mathbb{D}_\phi$ and the spin $\mathbb{W}_\phi$ respectively. It was argued that the carrier of non-objectivity of the velocity gradient is the spin $\mathbb{W}_\phi$ (because $\Omega^i{}_j$ in eq. (1.34) is antisymmetric). In effect, it is not necessary to use the full velocity gradient when defining a stress rate to get rid of the second and third terms from eq. (1.36). The antisymmetric part $\mathbb{W}_\phi$ alone can be employed. This idea stands behind the definition of another rate, named after Jaumann:

$$\frac{\mathcal{D}_{\mathrm{Jau}}\, a_\phi^{ij}}{\mathcal{D}t} := \frac{\mathcal{D} a_\phi^{ij}}{\mathcal{D}t} - \mathbb{W}_\phi^{ik}\, a_\phi^{kj} + a_\phi^{ik}\, \mathbb{W}_\phi^{kj}, \tag{1.40}$$

where the antisymmetry of spin was used, $\mathbb{W}_\phi^{jk}{=}{-}\mathbb{W}_\phi^{kj}$. Again, by combining eqs. (1.34) and (1.36), together with the definition of spin, it can be shown that the Jaumann rate is objective.

In fact, an entire class of objective rates can be built, which the above rates belong to:

$$\frac{\mathcal{D}_{\mathrm{Old}(c)}\, a_\phi^{ij}}{\mathcal{D}t} := \frac{\mathcal{D} a_\phi^{ij}}{\mathcal{D}t} - \mathbb{W}_\phi^{ik}\, a_\phi^{kj} + a_\phi^{ik}\, \mathbb{W}_\phi^{kj} - c\,(\mathbb{D}_\phi^{ik}\, a_\phi^{kl} + a_\phi^{ik}\, \mathbb{D}_\phi^{kj}), \tag{1.41}$$

where the parameter c is usually taken to be from the interval $[-1,1]$. But it can be arbitrary, because both $\overrightarrow{a}$ and $\mathbb{D}$ are objective, so their products do not influence the transformation properties of $\mathcal{D}_{\mathrm{Old}(c)}/\mathrm{D}t$. For $c{=}1$ eq. (1.41) gives the upper convected rate, for $c{=}0$ we get the Jaumann rate, and for $c{=}{-}1$ we will refer to the rate as the lower convected rate and denote it $\mathcal{D}_{\mathrm{lc}}/\mathrm{D}t$.

A different approach that leads to formulating an objective stress rate, namely the Truesdell rate, is to perform material derivative to the second Piola-Kirchhoff stress instead of the Cauchy stress tensor. The two stresses are related through so-called Piola transformation, which is a special mapping of tensors from current to reference configuration of the body. By altering this procedure, in particular by modifying the Piola transformation in a way as to consider only the rotation tensor instead of the full deformation gradient, another objective rate is derived, named the Green-Naghdi rate. We will not discuss these two rates here, with

the exception of one remark in Appendix 1.B. Nevertheless, it is worth noting that the Truesdell rate is equal to the upper convected rate for isochoric flows and that the Green-Naghdi rate resembles the Jaumann rate, only it employs a slightly different kinematic quantity than the spin.

A fundamental insight into objective tensor rates is provided in the work of Oldroyd (1950), who analyzes the temporal evolution of second-order tensors under a very special non-Euclidean change of frame: he considers a frame that is convected with the material. In other words, the coordinate lines of such frame are "frozen" into the material and deform the same way as the body deforms. It is shown that the components of a contravariant tensor $\overrightarrow{a}$ are time constant in the convected frame if and only if the Oldroyd derivative of the tensor is zero:

$$\frac{\mathcal{D}_{\mathrm{uc}}\,\overrightarrow{a}_{\phi}}{\mathcal{D}t}=0 \quad \Rightarrow \quad a^{ij}_{\phi^*}(\boldsymbol{x}^*,t)=a^{ij}_{\phi^*}(\boldsymbol{x}^*), \tag{1.42}$$

where ϕ^* denotes the convected frame. Note that the properties of the convected frame are governed by the deformation of the body and cannot be arbitrarily chosen. It is generally a curvilinear frame with spatially heterogeneous and temporally dependent metric tensor (see below).

We do not repeat the analysis of Oldroyd here (for a modern treatment, see Gurtin et al., 2010, sections 13 and 20). Instead, the validity of (1.42) is demonstrated in Appendix 1.B on a particular example of stationary simple shearing. Eq. (1.42) is usually interpreted in the way that the natural rate of contravariant tensors is the upper convected rate. It is because the basic property one would expect from a time derivative is that when it is zero the differentiated quantity stays constant. For geometrical interpretation of the constancy of $a^{ij}_{\phi^*}(t)$ see Appendix 1.B below eq. (1.93). The natural rate of covariant tensors is the lower convected rate.

The key question to ask is whether or not there is a particular objective rate that should be used in the constitutive law for Maxwell viscoelastic fluid. Before we address this question, it is necessary to mention "raising and lowering indices" and direct notation.

For any one-form $\underline{f}{:=}f_i\,\underline{e}^i$ the Riesz representation theorem uniquely gives vector $\vec{f}$ such that $\underline{f}(\vec{v})=\vec{f}\cdot\vec{v}$ for any $\vec{v}\in\mathbb{V}$, where dot is the scalar product. No particular frame is now under consideration, so the notion of frame is omitted for this paragraph. The components of such vector $\vec{f}$ can be obtained as $f^m{=}g^{mn}f_n$, where g^{mn} is the inverse of the metric tensor $g_{mn}:=\vec{e}_m\cdot\vec{e}_n$ (the inverse defined through $g^{mn}g_{nl}{=}\delta^m_l$). Thanks to this bijection $\mathcal{L}(\mathbb{V})\leftrightarrow\mathbb{V}$ one can go from contravariant to covariant tensors and vice versa, and one traditionally distinguishes the components of contravariant, covariant and mixed tensors by upper and lower indices in tensor analysis. In fact, it is common to denote the tensors $\mathbb{A}^{ij}\,\vec{e}_i{\otimes}\vec{e}_j$, $\mathbb{A}^i_{\ j}\,\vec{e}_i{\otimes}\underline{e}^j$ and $\mathbb{A}_{ij}\,\underline{e}^i{\otimes}\underline{e}^j$, whose components are related via

$\mathbb{A}^i{}_j = g_{mj}\mathbb{A}^{im}$ and $\mathbb{A}_{ij} = g_{mj}g_{ni}\mathbb{A}^{nm}$, simply as one tensor $\mathbb{A}$ (direct notation)[6]. In direct notation, the product of two tensors $\mathbb{A}$ and $\mathbb{B}$ is denoted as $\mathbb{A}\,\mathbb{B}$, and it is defined for tensors of any kind. To illustrate, for contravariant components of the product it holds

$$\{\mathbb{A}\,\mathbb{B}\}^{ij} = \mathbb{A}^i{}_n\,\mathbb{B}^{nj} = \mathbb{A}^{in}\,\mathbb{B}^j_n = g^{kn}\,\mathbb{A}^i{}_n\,\mathbb{B}^j_k = g_{kn}\,\mathbb{A}^{in}\,\mathbb{B}^{kj}, \tag{1.43}$$

because $\vec{e}_m \cdot \vec{e}_n = g_{mn}$, while $\underline{e}^i(\vec{e}_j) = \delta^i_j$, and so if upper and lower indices meet Kronecker delta comes out, while components of the metric tensor come out in other cases. To illustrate the validity of eq. (1.43), consider

$$(\mathbb{A}^{in}\,\vec{e}_i\otimes\vec{e}_n)\cdot(\mathbb{B}^{kj}\,\vec{e}_k\otimes\vec{e}_j) = \mathbb{A}^{in}\mathbb{B}^{kj}(\vec{e}_n\cdot\vec{e}_k)\,\vec{e}_i\otimes\vec{e}_j = \mathbb{A}^{in}\mathbb{B}^{kj}g_{kn}\,\vec{e}_i\otimes\vec{e}_j$$
$$= \mathbb{A}^i{}_n\mathbb{B}^{nj}\,\vec{e}_i\otimes\vec{e}_j = \mathbb{A}^i{}_n\mathbb{B}^{kj}\,(\vec{e}_i\otimes\underline{e}^n)\cdot(\vec{e}_k\otimes\vec{e}_j) = (\mathbb{A}^i{}_n\,\vec{e}_i\otimes\underline{e}^n)\cdot(\mathbb{B}^{kj}\,\vec{e}_k\otimes\vec{e}_j).$$

The objective rates discussed above can also be written in direct notation. With the velocity gradient denoted by $\mathbb{L}_\phi$, implication (1.42) reads in direct notation as

$$\frac{\mathcal{D}\,\mathbb{A}}{\mathcal{D}t} - \mathbb{L}_\phi\,\mathbb{A} - \mathbb{A}\,\mathbb{L}_\phi^{\mathrm{T}} = 0 \quad \Rightarrow \quad \mathbb{A}^{ij}_{\phi^*}(\boldsymbol{x}^*,t) = \mathbb{A}^{ij}_{\phi^*}(\boldsymbol{x}^*), \tag{1.44}$$

where $\mathbb{A}$ is any objective tensor, and similarly it holds for the lower convected derivative that

$$\frac{\mathcal{D}\,\mathbb{A}}{\mathcal{D}t} + \mathbb{L}_\phi^{\mathrm{T}}\,\mathbb{A} + \mathbb{A}\,\mathbb{L}_\phi = 0 \quad \Rightarrow \quad \{\mathbb{A}_{\phi^*}\}_{ij}(\boldsymbol{x}^*,t) = \{\mathbb{A}_{\phi^*}\}_{ij}(\boldsymbol{x}^*). \tag{1.45}$$

Frame ϕ^* is the convected frame in both theorems. In eqs (1.44) and (1.45) the definitions of objective rates are broadened with respect to (1.37) and (1.41), because the rates are now defined for tensors of any kind. The direct notation, however, removes certain subtleties.

Geometrically, tensors are defined as linear mappings from and to $\mathbb{V}$ and $\mathcal{L}(\mathbb{V})$, depending on their kind. The gradient of a vector field is a mapping $\mathbb{V}\to\mathbb{V}$, its transpose is thus a mapping $\mathcal{L}(\mathbb{V})\to\mathcal{L}(\mathbb{V})$. Since $\mathbb{L}_\phi$ is the gradient of the velocity field, only for contravariant tensors $\overrightarrow{a}$: $\mathcal{L}(\mathbb{V})\to\mathbb{V}$ it is true that both products $(\{\mathbb{L}_\phi\}^i{}_j\,\vec{e}_i\otimes\underline{e}^j)\cdot(a^{kl}\,\vec{e}_k\otimes\vec{e}_l)$ and $(a^{ij}\,\vec{e}_i\otimes\vec{e}_j)\cdot(\{\mathbb{L}_\phi\}^k_l\,\underline{e}^l\otimes\vec{e}_k)$ are again contravariant, that is, the same tensor kind as $\overrightarrow{a}$. Similarly, only for covariant tensors $\mathbb{A}_{ij}\,\underline{e}^i\otimes\underline{e}^j$ both products $(\{\mathbb{L}_\phi\}^k_l\,\underline{e}^l\otimes\vec{e}_k)\cdot(\mathbb{A}_{ij}\,\underline{e}^i\otimes\underline{e}^j)$ and $(\mathbb{A}_{kl}\,\underline{e}^k\otimes\underline{e}^l)\cdot(\{\mathbb{L}_\phi\}^i{}_j\,\vec{e}_i\otimes\underline{e}^j)$ are again covariant. This is deeply related to the derivation of theorems (1.44) and (1.45), which are covered in most modern treaties on continuum mechanics (e.g. Gurtin et al. (2010), sections 13 and 20). In analogy to the above, one can directly guess

[6]This may not be interpreted in the way that they are one tensor. Of course, $\mathbb{A}^{ij}\,\vec{e}_i\otimes\vec{e}_j \neq \mathbb{A}^i{}_j\,\vec{e}_i\otimes\underline{e}^j \neq \mathbb{A}_{ij}\,\underline{e}^i\otimes\underline{e}^j$. Direct notation only uses the fact that a tensor equation for one kind of tensor can be rewritten for any kind of tensor, by raising or lowering indices of tensors appearing in that equation.

the natural rate for right covariant mixed tensors

$$\frac{\mathcal{D}\,\mathbb{A}}{\mathcal{D}t} - \mathbb{L}_\phi\,\mathbb{A} + \mathbb{A}\,\mathbb{L}_\phi = 0 \quad \Rightarrow \quad \{\mathbb{A}_{\phi^*}\}^i{}_j(\boldsymbol{x}^*, t) = \{\mathbb{A}_{\phi^*}\}^i{}_j(\boldsymbol{x}^*), \tag{1.46}$$

where ϕ^* is the convected frame.

The equation of motion (1.20) is by its nature a vector equation, because acceleration is a vector, and we have thus assumed the Cauchy stress tensor to be contravariant[7] throughout the text. One could thus argue that it is the upper convected rate which should be used in the definition of Maxwell viscoelastic body. On the other hand, the possibility to change tensor kinds by raising or lowering indices can be used to argue that there is no *a priori* way of determining which objective rate to use, leaving the choice to experiments. It is because both the equation of motion and the constitutive law can be written in direct notation, eradicating the differences between different tensor kinds. In other words, one can write the equation of motion in a vector form, with the contravariant components of the Cauchy stress tensor, and the constitutive law in, for instance, its covariant form, with the covariant components of the Cauchy stress, and combine both equations through raising and lowering indices. This line of thought believes that there is no reason to assume that the constitutive law should be written in terms of the contravariant components of the involved tensors, or in terms of any other particular components for that matter.

We agree with the latter only partially. In theorems (1.44), (1.45) and (1.46) the direct notation can be used only on their left hand sides. It is the constancy of the particular tensor components in the convected frame that the theorems imply, regardless of which components of $\mathbb{A}$ are used when evaluating the objective rates. To illustrate, one could use the covariant components of $\mathbb{A}$ when solving $(\mathcal{D}_{\mathrm{uc}}\mathbb{A})/(\mathcal{D}t)$ in the frame ϕ, and still it would be the contravariant components of $\mathbb{A}$ in the convected frame that would be time constant, and not the covariant components. The main point we are trying to make is that the different objective rates do have different geometrical meaning[8], and the question to ask is whether there is a particular one, whose geometrical meaning suits the idea of Maxwell viscoelastic fluid outlined in the beginning of this chapter.

Recall from eq. (1.35) that the elastic component of Maxwell viscoelastic rheology must satisfy

$$\frac{\mathcal{D}_?}{\mathcal{D}t}\left(\frac{\tau_\phi^{ij}}{2G}\right) = \mathbb{D}^{ij}_{\phi,\,\mathrm{el}}. \tag{1.47}$$

[7]Because it must return a vector and acts on normals to surfaces. Normals to surfaces are one-forms, or covectors, because they are the normalized gradients of functions that implicitly define the respective surfaces.

[8]Note that the objective rates from eq. (1.41) have a distinct geometrical meaning only for $c \in \{-1, 0, 1\}$. Using any other value of c in a proposed constitutive law for some material would thus be difficult to justify. One should always consider the geometrical meaning of the objective rate he proposes to employ in a constitutive law.

In linear elastic rheologies, stress is proportional to elastic strain with the constant of proportion equal to $2G$. By replacing $\tau_\phi^{ij}/2G$ with $\mathbb{E}^{ij}_{\phi,\,\mathrm{el}}$ in eq. (1.47) we see that the problem of finding the right objective rate is in fact equivalent to finding a measure of elastic strain $\mathbb{E}_{\phi,\,\mathrm{el}}$ for which it holds that

$$\frac{\mathcal{D}_?\,\mathbb{E}^{ij}_{\phi,\,\mathrm{el}}}{\mathcal{D}t} = \mathbb{D}^{ij}_{\phi,\,\mathrm{el}}. \tag{1.48}$$

Indeed, the problem in eq. (1.2) was in going from $\Delta_{\mathrm{elastic}}$ to its rate $\dot{\Delta}_{\mathrm{elastic}}$. One of the most common measures of strain used in continuum mechanics is the Eulerian strain tensor, defined as

$$\mathbb{E}_\phi := \frac{1}{2}\left(\mathbb{I} - \mathbb{F}_\phi^{-\mathrm{T}}\,\mathbb{F}_\phi^{-1}\right). \tag{1.49}$$

It is related to the change of distance between two infinitesimally close material points p and q, whose coordinates differ by $\mathrm{d}x^i(t) = \chi^i_\phi(p,t) - \chi^i_\phi(q,t)$, as follows:

$$\begin{aligned}\mathrm{d}s^2_\phi - \mathrm{d}S^2_\phi = g^\phi_{ij}\mathrm{d}x^i\mathrm{d}x^j - g^\phi_{ij}\mathrm{d}X^i\mathrm{d}X^j = g^\phi_{ij}\mathrm{d}x^i\mathrm{d}x^j - g^\phi_{ij}\{\mathbb{F}^{-1}_\phi\}^i{}_k\{\mathbb{F}^{-1}_\phi\}^j{}_l\mathrm{d}x^k\mathrm{d}x^l \\ = (g^\phi_{kl} - g^\phi_{ij}\{\mathbb{F}^{-1}_\phi\}^i{}_k\{\mathbb{F}^{-1}_\phi\}^j{}_l)\,\mathrm{d}x^k\mathrm{d}x^l = 2\{\mathbb{E}_\phi\}_{kl}\,\mathrm{d}x^k\mathrm{d}x^l.\end{aligned} \tag{1.50}$$

The Eulerian strain is, geometrically speaking, a covariant tensor, which can be seen both from its definition (1.49) and from eq. (1.50). Eq. (1.50) can be written also in the convected frame ϕ^*. The coordinates of material points do not change with time in the frame ϕ^*, $\mathrm{d}x^i_*(t) = \mathrm{d}X^i_*$, but the metric tensor of the frame evolves with time, and so eq. (1.50) takes the form

$$\mathrm{d}s^2 - \mathrm{d}S^2 = [g^{\phi^*}_{kl}(\boldsymbol{x}^*,t) - g^{\phi^*}_{kl}(\boldsymbol{x}^*,0)]\,\mathrm{d}X^k_*\mathrm{d}X^l_*. = 2\{\mathbb{E}_{\phi^*}(\boldsymbol{x}^*,t)\}_{kl}\,\mathrm{d}X^k_*\mathrm{d}X^l_* \tag{1.51}$$

Eq. (1.51) provides a good reason to use the lower convected rate in Maxwell viscoelastic rheology. When one demands the elastic part of the total deformation to be constant (i.e. the limiting case of purely viscous fluid, $G \to \infty$), then it is naturally the covariant components of the elastic strain that have to be constant in the convected frame. And this is ensured, for any tensor field, by setting its lower convected derivative to zero.

Coming back to eq. (1.48), we see that making the choice of the lower convected derivative is equivalent to saying that

$$\frac{\mathcal{D}_{\mathrm{lc}}\,\mathbb{E}_{\phi,\,\mathrm{el}}}{\mathcal{D}t} = \mathbb{D}_{\phi,\,\mathrm{el}}. \tag{1.52}$$

Is eq. (1.52) reasonable? It is indeed. For any deformation, the Eulerian strain tensor and the strain-rate tensor are related through the identity (e.g. Martinec, 2011, eq. 2.24):

$$\frac{\mathcal{D}\,\mathbb{E}_\phi}{\mathcal{D}t} = \mathbb{D}_\phi - \left(\mathbb{E}_\phi\mathbb{L}_\phi + \mathbb{L}_\phi^{\mathrm{T}}\,\mathbb{E}_\phi\right) \quad \Rightarrow \quad \frac{\mathcal{D}_{\mathrm{lc}}\,\mathbb{E}_\phi}{\mathcal{D}t} = \mathbb{D}_\phi, \tag{1.53}$$

where the implication follows directly from the definition of the lower convected derivative.

We are aware that the considerations above have certain drawbacks. The major one is that adding strain-rates as $\mathbb{D}_\phi = \mathbb{D}_{\phi,\mathrm{vis}} + \mathbb{D}_{\phi,\mathrm{el}}$ is disputable, which is illustrated in the next section. We do not claim that the lower convected derivative is the only one to use, the goal of our analysis is to discuss the different geometrical meaning of several objective rates in the context of the traditional derivation of Maxwell body. As far as we understand it, the traditional derivation is based on the addition of strain-rates. The identity (1.53) nicely fits into such framework.

In Chapter 3 we use the Jaumann rate in geodynamical modelling. In direct notation the Jaumann rate reads

$$\frac{\mathcal{D}_{\mathrm{Jau}}\,\mathbb{A}}{\mathcal{D}t} := \frac{\mathcal{D}\mathbb{A}}{\mathcal{D}t} - \mathbb{W}_\phi\,\mathbb{A} + \mathbb{A}\,\mathbb{W}_\phi. \tag{1.54}$$

Note that, in view of eq. (1.43), the definition (1.40) is valid only for Cartesian frames. The Jaumann rate is not the natural rate for any tensor kind. Setting this rate to zero ensures that both the covariant and the contravariant components of $\mathbb{A}$ are constant, but not in the convected frame (where this can generally never happen due to the properties of the frame's metric tensor). The components are $\mathbb{A}$ are constant in so-called corotated frame when the Jaumann rate of $\mathbb{A}$ is zero (see the worked-out example in Appendix 1.B). While such property gives the Jaumann rate a clear geometrical interpretation, it is primarily the fact that it preserves the trace of the stress tensor that makes it popular among modelers.

1.3 Maximization of entropy production

The approach used in the preceding sections was based on mechanical considerations. *A posteriori* it can be shown that the Maxwell model derived above satisfies the second law of thermodynamics, that is, entropy is produced when the body deforms. In modern literature, a reverse procedure starts to play increasingly important role in constitutive theory: first it is postulated how a model produces entropy and from that the rheology is derived.

The approach presented in this section is summarized in detail in Málek & Průša (2016). We refer the reader who is not yet familiar with the procedure to their handbook and the references therein. Here we only repeat the analysis of section 4.4.3 in Málek & Průša (2016), where viscoelastic models are derived, and comment on the inclusion of PMFI into the theory.

Similarly as in the traditional approach, the total deformation of the body is decomposed into two parts: dissipative and reversible (elastic). Contrary to the traditional approach, the idea is formalized by introducing so-called "natural configuration" of the body (see Fig. 1.3). The motion mapping the reference

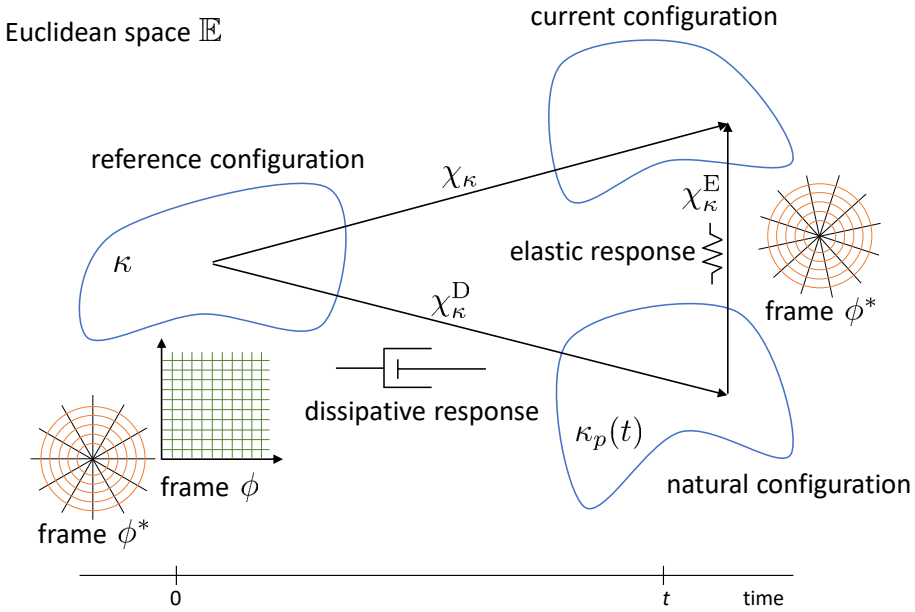

Figure 1.3: Reference, current and natural configurations associated with a viscoelastic body, as viewed from a fixed Cartesian frame ϕ and from a moving polar frame ϕ^*. For a description of the concept of change of frame see also Fig. 1.2.

configuration onto the natural configuration describes the dissipative processes. The mapping from the natural configuration to the current configuration describes the instantaneous elastic response. Every deformation of a body is driven by some loading. Had all the loading suddenly ceased to exist, the body would take the natural configuration.

To formalize this idea, the motion of the body $\boldsymbol{\chi}_{\kappa,\phi}$ is decomposed into two, $\boldsymbol{\chi}_{\kappa,\phi} = \boldsymbol{\chi}^{\mathrm{E}}_{\kappa_p(t),\phi} \circ \boldsymbol{\chi}^{\mathrm{D}}_{\kappa,\phi}$, with $\boldsymbol{\chi}^{\mathrm{D}}_{\kappa,\phi}(\boldsymbol{X},t)$ being the dissipative part of the motion, and $\boldsymbol{\chi}^{\mathrm{E}}_{\kappa_p(t),\phi}(\boldsymbol{\xi},t)$ being the elastic deformation of the natural configuration $\kappa_p(t)$. We denote the coordinates in the natural configuration by $\boldsymbol{\xi}$, $\boldsymbol{\xi}(\boldsymbol{X},t) := \boldsymbol{\chi}^{\mathrm{D}}_{\kappa,\phi}(\boldsymbol{X},t)$. For the total deformation gradient the chain rule gives

$$\mathbb{F}_\phi = \hat{\mathbb{F}}_\phi \, \tilde{\mathbb{F}}_\phi, \tag{1.55}$$

where the partial deformation gradients are defined as

$$\{\tilde{\mathbb{F}}_\phi\}^i_{\ j} := \frac{\partial \{\boldsymbol{\chi}^{\mathrm{D}}_{\kappa,\phi}(\boldsymbol{X},t)\}^i}{\partial X^j}; \quad \{\hat{\mathbb{F}}_\phi\}^i_{\ j} := \frac{\partial \{\boldsymbol{\chi}^{\mathrm{E}}_{\kappa_p(t),\phi}(\boldsymbol{\xi},t)\}^i}{\partial \xi^j}. \tag{1.56}$$

For later reference, we derive a few identities related to kinematics of media with multiple configurations. In analogy with eq. (1.33), the velocity gradient of the natural configuration is defined as

$$\tilde{\mathbb{L}}_\phi := \frac{\mathcal{D}\tilde{\mathbb{F}}_\phi}{\mathcal{D}t} \, \tilde{\mathbb{F}}^{-1}_\phi. \tag{1.57}$$

Eq. (1.55) together with the identity

$$\frac{\mathcal{D}}{\mathcal{D}t}\left(\tilde{\mathbb{F}}_\phi^{-1}\right) = -\tilde{\mathbb{F}}_\phi^{-1}\,\frac{\mathcal{D}\tilde{\mathbb{F}}_\phi}{\mathcal{D}t}\,\tilde{\mathbb{F}}_\phi^{-1} \tag{1.58}$$

yields

$$\frac{\mathcal{D}\hat{\mathbb{F}}_\phi}{\mathcal{D}t} = \frac{\mathcal{D}\mathbb{F}_\phi}{\mathcal{D}t}\,\tilde{\mathbb{F}}_\phi^{-1} + \mathbb{F}_\phi\,\frac{\mathcal{D}\tilde{\mathbb{F}}_\phi^{-1}}{\mathcal{D}t} = \mathbb{L}_\phi\,\mathbb{F}_\phi\,\tilde{\mathbb{F}}_\phi^{-1} - \mathbb{F}_\phi\,\tilde{\mathbb{F}}_\phi^{-1}\,\frac{\mathcal{D}\tilde{\mathbb{F}}_\phi}{\mathcal{D}t}\,\tilde{\mathbb{F}}_\phi^{-1} = \mathbb{L}_\phi\,\hat{\mathbb{F}}_\phi - \hat{\mathbb{F}}_\phi\,\mathbb{L}_\phi. \tag{1.59}$$

For the left Cauchy-Green tensor $\hat{\mathbb{B}}_\phi := \hat{\mathbb{F}}_\phi\,\hat{\mathbb{F}}_\phi^{\mathrm{T}}$ eq. (1.59) gives

$$\frac{\mathcal{D}\hat{\mathbb{B}}_\phi}{\mathcal{D}t} = \mathbb{L}_\phi\,\hat{\mathbb{B}}_\phi + \hat{\mathbb{B}}_\phi\,\mathbb{L}_\phi^{\mathrm{T}} - 2\hat{\mathbb{F}}_\phi\,\tilde{\mathbb{D}}_\phi\,\hat{\mathbb{F}}_\phi^{\mathrm{T}}, \tag{1.60}$$

which implies a relation for the material derivative of the trace of $\hat{\mathbb{B}}_\phi$,

$$\frac{\mathcal{D}}{\mathcal{D}t}(\mathrm{Tr}\hat{\mathbb{B}}_\phi) = 2\mathbb{D}_\phi : \hat{\mathbb{B}}_\phi - 2\hat{\mathbb{C}}_\phi : \tilde{\mathbb{D}}_\phi \tag{1.61}$$

where $\mathbb{A}{:}\mathbb{B} := \mathrm{Tr}(\mathbb{A}\mathbb{B}^{\mathrm{T}})$ and the identity $\mathrm{Tr}(\mathbb{A}\mathbb{B}) = \mathrm{Tr}(\mathbb{B}\mathbb{A})$ was used to replace the deformation gradients in the second term by the right Cauchy-Green tensor $\hat{\mathbb{C}}_\phi$. Finally, since $\mathcal{D}(\det\mathbb{A})/\mathcal{D}t = (\det\mathbb{A})\,\mathrm{Tr}(\mathcal{D}\mathbb{A}/\mathcal{D}t\,\mathbb{A}^{-1})$, for the material derivative of the logarithm of determinant of the right Cauchy-Green tensor $\hat{\mathbb{B}}$ one gets

$$\frac{\mathcal{D}}{\mathcal{D}t}(\log(\det\hat{\mathbb{B}}_\phi)) = \mathrm{Tr}\left(\frac{\mathcal{D}\hat{\mathbb{B}}_\phi}{\mathcal{D}t}\,\hat{\mathbb{B}}_\phi^{-1}\right) = 2\mathbb{I} : \mathbb{D} - 2\mathbb{I} : \tilde{\mathbb{D}}_\phi \tag{1.62}$$

Often, the only quantity that needs to be specified in the procedure by (Rajagopal & Srinivasa, 2004) is the production of entropy. For viscoelastic materials, however, the internal energy of the body must be allowed to account for stored elastic energy. The form of such storage is also to be assumed, and here the internal energy takes the following form:

$$e(s,\rho,\mathrm{Tr}\,\hat{\mathbb{B}}_\phi,\det\hat{\mathbb{B}}_\phi) = \tilde{e}(s,\rho) + \frac{G}{2\rho}\left(\mathrm{Tr}\,\hat{\mathbb{B}}_\phi - 3 - \log(\det\hat{\mathbb{B}}_\phi)\right). \tag{1.63}$$

The second term on the right hand side represents the energy stored in the elastic deformation of the natural configuration and $\tilde{e}$ is analogous of the internal energy for a simple thermodynamic system, for which it depends on entropy and volume of the system only. The quantity s is the specific entropy per unit volume. The motivation for this particular choice of storage of elastic energy comes from the theory of isotropic elastic materials (see Horgan & Saccomandi, 2004, for a list of other frequently used possibilities).

Next step in the procedure is to derive evolutionary equation for the specific entropy of the model. By applying material derivative to eq. (1.63), and

multiplying both sides by ρ, we get,

$$\begin{aligned}\rho\frac{\mathcal{D}e}{\mathcal{D}t} &= \rho\left(\frac{\partial e}{\partial s}\frac{\mathcal{D}s}{\mathcal{D}t}+\frac{\partial e}{\partial \rho}\frac{\mathcal{D}\rho}{\mathcal{D}t}+\frac{\partial e}{\partial(\operatorname{Tr}\hat{\mathbb{B}}_\phi)}\frac{\mathcal{D}(\operatorname{Tr}\hat{\mathbb{B}}_\phi)}{\mathcal{D}t}+\frac{\partial e}{\partial(\det\hat{\mathbb{B}}_\phi)}\frac{\mathcal{D}(\det\hat{\mathbb{B}}_\phi)}{\mathcal{D}t}\right)\\ &= \rho\frac{\partial\tilde{e}}{\partial s}\frac{\mathcal{D}s}{\mathcal{D}t}+\left(\rho\frac{\partial\tilde{e}}{\partial\rho}-\frac{G}{2\rho}(\operatorname{Tr}\hat{\mathbb{B}}_\phi-3-\log(\det\hat{\mathbb{B}}_\phi)\right)\frac{\mathcal{D}\rho}{\mathcal{D}t}\\ &\quad +G\left(\hat{\mathbb{B}}_\phi:\mathbb{D}_\phi-\hat{\mathbb{C}}_\phi:\tilde{\mathbb{D}}_\phi-\mathbb{D}_\phi:\mathbb{I}+\tilde{\mathbb{D}}_\phi:\mathbb{I}\right),\end{aligned}\tag{1.64}$$

where eqs (1.61) and (1.62) are used on the third line. Along with Málek & Průša (2016), we define the "pressure" as

$$p^{\mathrm{M}}_{\mathrm{th}} := \rho^2\frac{\partial e}{\partial\rho}=\rho^2\frac{\partial\tilde{e}}{\partial\rho}-\frac{G}{2}\left(\operatorname{Tr}\hat{\mathbb{B}}_\phi-3-\log(\det\hat{\mathbb{B}}_\phi)\right).\tag{1.65}$$

Note that such definition is questionable. Thermodynamic pressure is the system's resistance to changes of volume, generally defined as in eq. (1.65), but under the assumption that the internal energy e is known as a function of mutually independent state variables. In our case, $\hat{\mathbb{B}}_\phi$ describes the deformation of the natural configuration, and $\det\hat{\mathbb{B}}_\phi$ is thus inevitably related to changes of density of our medium. Since the density ρ and $\det\hat{\mathbb{B}}_\phi$ are not mutually independent state variables, we believe that the $p^{\mathrm{M}}_{\mathrm{th}}$, as defined in eq. (1.65), is not the thermodynamic pressure of the studied system. Nevertheless, by employing eq. (1.65), together with the definition of temperature, $\theta := \partial e/\partial s$, and the continuity equation, eq. (1.64) simplifies to

$$\rho\frac{\mathcal{D}e}{\mathcal{D}t}=\rho\theta\frac{\mathcal{D}s}{\mathcal{D}t}-p^{\mathrm{M}}_{\mathrm{th}}\operatorname{div}\vec{v}_\phi+G\left(\hat{\mathbb{B}}_\phi:\mathbb{D}_\phi-\hat{\mathbb{C}}_\phi:\tilde{\mathbb{D}}_\phi-\mathbb{D}_\phi:\mathbb{I}+\tilde{\mathbb{D}}_\phi:\mathbb{I}\right).\tag{1.66}$$

The temporal evolution of the specific internal energy e is, on the other hand, also governed by the standard energy balance

$$\rho\frac{\mathcal{D}e}{\mathcal{D}t}=\boldsymbol{\tau}_\phi:\mathbb{D}_\phi-\operatorname{div}\vec{j}_q,\tag{1.67}$$

where $\vec{j}_q$ is the heat flux. Internal (e.g. radioactive) heat sources are omitted. By inserting for $\rho\mathcal{D}e/\mathcal{D}t$ from eq. (1.67) into eq. (1.66) we get

$$\rho\frac{\mathcal{D}s}{\mathcal{D}t}+\operatorname{div}\frac{\vec{j}_g}{\theta}=\frac{1}{\theta}\left[\boldsymbol{\tau}_\phi{:}\mathbb{D}_\phi-\frac{\vec{j}_q{\cdot}\nabla\theta}{\theta}+p^{\mathrm{M}}_{\mathrm{th}}\operatorname{div}\vec{v}_\phi-G\left(\hat{\mathbb{B}}_\phi{:}\mathbb{D}_\phi-\hat{\mathbb{C}}_\phi{:}\tilde{\mathbb{D}}_\phi-\mathbb{D}_\phi{:}\mathbb{I}+\tilde{\mathbb{D}}_\phi{:}\mathbb{I}\right)\right],\tag{1.68}$$

where the identity $\operatorname{div}(\vec{j}_g/\theta)=(\operatorname{div}\vec{j}_q)/\theta-(\vec{j}_q{\cdot}\nabla\theta)/\theta^2$ was used in order to obtain the entropy production of the system,

$$\xi := \rho\mathcal{D}s/\mathcal{D}t+\operatorname{div}(\vec{j}_g/\theta),\tag{1.69}$$

on the left-hand side of eq. (1.68). The second law of thermodynamics states

that the entropy production is always positive, because the maximum outflux of entropy from a cooling thermodynamic system is given as $\vec{j}_q/\theta$, integrated over the surface of the system. For quasi-static processes $\rho\mathcal{D}s/\mathcal{D}t = -\mathrm{div}(\vec{j}_g/\theta)$ and the entropy production is zero.

Eq. (1.68) is valid for all materials that store elastic energy in the manner specified by eq. (1.63), regardless of their rheology. Right-hand side of eq. (1.68) is traditionally divided into terms representing mutually independent processes, each term usually expressed as a product of a thermodynamic affinity and a thermodynamic flux. For this reason, we separate the trace of the strain-rate, related to volumetric changes during deformation, from the deviatoric part of the strain-rate, which is related to isochoric shearing. The second law of thermodynamics then takes the form

$$\theta\xi = \left(\boldsymbol{\tau}_\phi^{\mathrm{d}} - G\,\hat{\mathbb{B}}_\phi^{\mathrm{d}}\right) : \mathbb{D}_\phi^{\mathrm{d}} + \left(m + p_{\mathrm{th}}^{\mathrm{M}} - \frac{G}{3}\mathrm{Tr}\hat{\mathbb{B}}_\phi + G\right)\mathrm{div}\vec{v}_\phi + G\,\hat{\mathbb{C}}_\phi^{\mathrm{d}} : \tilde{\mathbb{D}}_\phi^{\mathrm{d}} + G\left(\frac{\mathrm{Tr}\hat{\mathbb{B}}_\phi}{3} - 1\right)\mathrm{Tr}\tilde{\mathbb{D}}_\phi - \frac{\vec{j}_q\cdot\nabla\theta}{\theta} \geq 0, \quad (1.70)$$

where superscript d denotes the deviatoric part of a tensor and m is the trace of the Cauchy stress tensor $\boldsymbol{\tau}_\phi$.

One way to propose a material rheology is to derive the formula for its entropy production, as done above, and to demand each term in the formula to be positive. This can be illustrated on the example of materials with no storage of elastic energy. In such a scenario, the first term in eq. (1.70) is $\boldsymbol{\tau}_\phi^{\mathrm{d}}{:}\mathbb{D}_\phi^{\mathrm{d}}$, which can be made positive by proposing a linear relation $\boldsymbol{\tau}_\phi^{\mathrm{d}} \approx \mathbb{D}_\phi^{\mathrm{d}}$, that is, by proposing Newtonian viscous rheology $\boldsymbol{\tau}_\phi^{\mathrm{d}} = 2\eta\mathbb{D}_\phi^{\mathrm{d}}$, the constant of proportion known as viscosity, $\eta \geq 0$. The resulting entropy production term is clearly positive, because $2\eta\mathbb{D}_\phi^{\mathrm{d}}{:}\mathbb{D}_\phi^{\mathrm{d}} = 2\eta|\mathbb{D}_\phi^{\mathrm{d}}|^2$. In a way, the method by Rajagopal & Srinivasa (2004) is a generalization of such procedure. In their method, instead of inspecting eq. (1.70) and proposing relations between the thermodynamic affinities and fluxes to make each term positive, the entropy production is directly postulated as a function of the affinities. To obtain Maxwell-type fluid, Málek & Průša (2016) propose the following entropy production terms:

$$\xi(\mathbb{D}_\phi^{\mathrm{d}}, \mathrm{div}\vec{v}_\phi, \tilde{\mathbb{D}}_\phi, \nabla\theta) := \frac{1}{\theta}\left[2\eta|\mathbb{D}_\phi^{\mathrm{d}}|^2 + \frac{2\eta+3\lambda}{3}(\mathrm{div}\vec{v}_\phi)^2 + 2\eta_1\tilde{\mathbb{D}}_\phi{:}(\hat{\mathbb{C}}_\phi\tilde{\mathbb{D}}_\phi) + \kappa\frac{|\nabla\theta|^2}{\theta}\right]. \quad (1.71)$$

The constants $2\eta, (2\eta+3\lambda)/3, 2\eta_1$, and κ must all be greater than or equal to zero in order to satisfy the second law of thermodynamics in a general case. The motivation for the first two terms in eq. (1.71) comes from the theory of compressible Newtonian viscous fluid, as illustrated in the previous paragraph, and the respective constants are known as the shear and bulk viscosity. The last term in eq. (1.71) is the entropy production due to the transfer of heat, and stems from Fourier law.

As discussed at the end of this section, the third term in eq. (1.71) is motivated, so to say, by the desired outcome of the derivation. In the procedure by Rajagopal, it is the two scalar functions e and ξ that fully determine the material properties. When thermodynamic fluxes are given, the procedure assumes that each material behaves so as to maximize its entropy production for the given fluxes. To obtain the material rheology, one thus has to maximize the entropy production (1.71) with respect to the affinities $\mathbb{D}^{\mathrm{d}}_{\phi}, \mathrm{div}\vec{v}_{\phi}, \tilde{\mathbb{D}}_{\phi}, \nabla\theta$, with eq. (1.70) serving as a constraint for the maximization.

As long as the scalar functions e and ξ are objective scalars, the entropy production maximization results in constitutive laws that automatically satisfy the principle of material frame-indifference. This is a serious advantage when compared to the traditional technique. To ensure that e and ξ are objective scalars, one must investigate how the components of the kinematic quantities appearing in eq. (1.71) transform under a change of frame. To our knowledge, this is not discussed in the relatively recent literature that deals with the entropy maximization procedure within the framework including the natural configuration, that is, within the framework involving the composite deformation $\boldsymbol{\chi}_{\kappa,\phi} = \boldsymbol{\chi}^{\mathrm{E}}_{\kappa_p(t),\phi} \circ \boldsymbol{\chi}^{\mathrm{D}}_{\kappa,\phi}$.

Similarly to eq. (1.32), we can derive the transformation properties of deformation gradient $\hat{\mathbb{F}}_{\phi}$ under a change of frame, $\phi \to \phi^*$. Recall that $\hat{\mathbb{F}}_{\phi}$ describes the elastic deformation of the natural configuration, and so

$$\{\hat{\mathbb{F}}_{\phi}\}^{i}{}_{j} = \frac{\partial x^i(\chi^{\mathrm{E}}_{\kappa^*_p(t),\phi^*}(\boldsymbol{\xi}^*(\boldsymbol{\xi}),t),t)}{\partial \xi^j} = \frac{\partial x^i(\boldsymbol{x}^*,t)}{\partial x^k_*} \frac{\partial\{\chi^{\mathrm{E}}_{\kappa^*_p(t),\phi^*}(\boldsymbol{\xi}^*,t)\}^k}{\partial \xi^l_*} \frac{\partial \xi^l_*(\boldsymbol{\xi},t)}{\partial \xi^j}. \tag{1.72}$$

The important difference from eq. (1.32) is that while the reference configuration is a time independent mapping, the natural configuration evolves with time (similarly as the current configuration, see Fig. 1.3). The transformation $\boldsymbol{\xi} \to \boldsymbol{\xi}^*$ is thus identical to the transformation $\boldsymbol{x} \to \boldsymbol{x}^*$, making $\hat{\mathbb{F}}_{\phi}$ an objective contravariant tensor (unlike the common deformation gradient $\mathbb{F}_{\phi}$, which is a non-standard object).

Note that the traditional formula for the total deformation gradient, $\{\mathbb{F}_{\phi}\}^{i}{}_{j} = Q^{i}{}_{k}(t)\,\{\mathbb{F}_{\phi^*}\}^{k}_{j}$, is not applicable to the partial deformation gradient $\hat{\mathbb{F}}_{\phi}$. While one can easily restrict their considerations to changes of frame that satisfy $\boldsymbol{X}^*(\boldsymbol{X})=\boldsymbol{X}$ when discussing objectivity, it is not possible to demand that $\boldsymbol{\xi}^*(\boldsymbol{\xi},t) = \boldsymbol{\xi}$ (compare eqs (1.32) and (1.72)). Assuming $\boldsymbol{\xi}^*(\boldsymbol{\xi},t) = \boldsymbol{\xi}$ means nothing less than to demand that both frames ϕ and ϕ^* are identical at all times, prohibition any discussion of objectivity in effect. Note also that, in view of eq. (1.72), the left Cauchy-Green tensor $\hat{\mathbb{C}}_{\phi}$ is an objective tensor, and not objective scalar, as is sometimes erroneously stated (perhaps because $\{\mathbb{F}_{\phi}\}^{i}{}_{j} = Q^{i}{}_{k}(t)\,\{\mathbb{F}_{\phi^*}\}^{k}_{j}$ is erroneously assumed to hold for $\hat{\mathbb{F}}_{\phi}$).

By repeating the argument above, it can be shown that also $\tilde{\mathbb{D}}_{\phi}$ is an objective tensor. As a result, the entropy production term $2\eta_1\tilde{\mathbb{D}}_{\phi}{:}(\hat{\mathbb{C}}_{\phi}\tilde{\mathbb{D}}_{\phi})$ is an objective scalar as desired. By a coincidence, the same conclusion is reached when the

components of $\hat{\mathbb{C}}_\phi$ are incorrectly assumed to be objective scalars.

The constrained maximization of (1.71) is performed using the Lagrange multipliers, and we refer the reader to Málek & Průša (2016) for more details. It results in the following set of equations:

$$\boldsymbol{\tau}_\phi^{\mathrm{d}} - G\,\hat{\mathbb{B}}_\phi^{\mathrm{d}} = 2\eta\mathbb{D}_\phi^{\mathrm{d}} \tag{1.73}$$

$$m + p_{\mathrm{th}}^{\mathrm{M}} - \frac{G}{3}\mathrm{Tr}\hat{\mathbb{B}}_\phi + G = \frac{2\eta+3\lambda}{3}\,\mathrm{div}\vec{v}_\phi \tag{1.74}$$

$$G\left(\hat{\mathbb{C}}_\phi - \mathbb{I}\right) = 2\eta_1\hat{\mathbb{C}}_\phi\tilde{\mathbb{D}}_\phi \tag{1.75}$$

$$\vec{j}_q = -\kappa\nabla\theta \tag{1.76}$$

Upon multiplying eq. (1.75) by $\hat{\mathbb{F}}_\phi^{\mathrm{T}}$ from the right and by $\hat{\mathbb{F}}_\phi^{\mathrm{T}}$ from the left, and recalling the identity (1.60), eq. (1.75) reads

$$\frac{\mathcal{D}\hat{\mathbb{B}}_\phi}{\mathcal{D}t} - \mathbb{L}_\phi\,\hat{\mathbb{B}}_\phi - \hat{\mathbb{B}}_\phi\,\mathbb{L}_\phi^{\mathrm{T}} + G\left(\hat{\mathbb{B}}_\phi - \mathbb{I}\right) = 0, \tag{1.77}$$

which allows one to combine eqs (1.73), (1.74) and (1.77) into the constitutive relation for the Cauchy stress tensor:

$$\boldsymbol{\tau}_\phi = -p_{\mathrm{th}}^{\mathrm{M}} + 2\eta\mathbb{D}_\phi + \mathbb{S}_\phi + \lambda(\mathrm{div}\,\vec{v}_\phi)\mathbb{I} \tag{1.78a}$$

$$\frac{\eta_1}{G}\left(\frac{\mathcal{D}\mathbb{S}_\phi}{\mathcal{D}t} - \mathbb{L}_\phi\,\mathbb{S}_\phi - \mathbb{S}_\phi\,\mathbb{L}_\phi^{\mathrm{T}}\right) + \mathbb{S}_\phi = 2\eta_1\mathbb{D}_\phi, \tag{1.78b}$$

where the extra stress tensor $\mathbb{S}_\phi := G(\hat{\mathbb{B}}_\phi - \mathbb{I})$ was introduced. Málek & Průša (2016) note that eq. (1.78a) can be seen as a *compressible variant of the classical Oldroyd-B model*, developed for viscoelastic incompressible fluids by Oldroyd (1950). In our case, it is interesting to set η and λ to zero, because then eq. (1.78a) reduces to the constitutive relation for a compressible Maxwell-type viscoelastic fluid:

$$\boldsymbol{\tau}_\phi = -p_{\mathrm{th}}^{\mathrm{M}} + \mathbb{S}_\phi \tag{1.79a}$$

$$\frac{\eta_1}{G}\left(\frac{\mathcal{D}\mathbb{S}_\phi}{\mathcal{D}t} - \mathbb{L}_\phi\,\mathbb{S}_\phi - \mathbb{S}_\phi\,\mathbb{L}_\phi^{\mathrm{T}}\right) + \mathbb{S}_\phi = 2\eta_1\mathbb{D}_\phi. \tag{1.79b}$$

The resulting constitutive eq. (1.79a) contains the upper convected rate. Unlike in the traditional technique, which is based on mechanical analogues, the stress rate is a result of the performed procedure here. Seemingly, this makes the geometrical interpretations of various objective rates redundant. However, one must realize that choosing the entropy production maximization over mechanical analogues is nothing but choosing one uncertainty over the other. The upper convected derivative in eq. (1.79a) can be traced back to the entropy production term $2\eta_1\tilde{\mathbb{D}}_\phi{:}(\hat{\mathbb{C}}_\phi\tilde{\mathbb{D}}_\phi)$ in eq. (1.71). Finding a valid physical interpretation for this dissipational mechanism may be equally hard as trying to justify the upper

convected rate on geometrical grounds. Nevertheless, the maximization technique is very intriguing and various dissipational mechanisms can be expected to appear in the literature. We hope that this section shed more light on the transformation properties of $\hat{\mathbb{C}}_\phi$, $\hat{\mathbb{B}}_\phi$ and $\tilde{\mathbb{D}}_\phi$, which usually have to be considered when proposing an equation for the entropy production ξ.

1.A Change of frame: moving polar coordinates

We consider a 2-D Euclidean space with two frames, one Cartesian and the other having polar coordinates. They are related via

$$\begin{aligned} x &= r\cos\left(\varphi{+}\theta(t)\right) + c^1(t); \quad r = \sqrt{(x-c^1(t))^2+(y-c^2(t))^2}; \\ y &= r\sin\left(\varphi{+}\theta(t)\right) + c^2(t); \quad \varphi = \arctan\left(\frac{y-c^2(t)}{x-c^1(t)}\right), \end{aligned}$$

where, $\vec{c}(t)$ and $\theta(t)$ describe the relative movement of both observers. To recall the notation from the main text, $x{=}x^1, y{=}x^2, r{=}x^1_*, \varphi{=}x^2_*$. The shifter tensor $Q^i{}_j$ and its inverse are, by their definition,

$$Q(\boldsymbol{x}^*,t) = \begin{bmatrix} \frac{\partial x}{\partial r} & \frac{\partial x}{\partial \varphi} \\ \frac{\partial y}{\partial r} & \frac{\partial y}{\partial \varphi} \end{bmatrix} = \begin{bmatrix} \cos\left(\varphi{+}\theta(t)\right) & -r\sin\left(\varphi{+}\theta(t)\right) \\ \sin\left(\varphi{+}\theta(t)\right) & r\cos\left(\varphi{+}\theta(t)\right) \end{bmatrix} \tag{1.80}$$

$$Q^{-1}(\boldsymbol{x},t) = \begin{bmatrix} \frac{\partial r}{\partial x} & \frac{\partial r}{\partial y} \\ \frac{\partial \varphi}{\partial x} & \frac{\partial \varphi}{\partial y} \end{bmatrix} = \begin{bmatrix} \frac{x-c^1(t)}{\sqrt{(x-c^1(t))^2+(y-c^2(t))^2}} & \frac{y-c^2(t)}{\sqrt{(x-c^1(t))^2+(y-c^2(t))^2}} \\ \frac{c^2(t)-y}{(x-c^1(t))^2+(y-c^2(t))^2} & \frac{x-c^1(t)}{(x-c^1(t))^2+(y-c^2(t))^2} \end{bmatrix}. \tag{1.81}$$

Both matrices are indeed inverse to each other, which can be seen when the conversion $\boldsymbol{x} \to \boldsymbol{x}^*$ is performed in eq. (1.81),

$$Q^{-1} = \begin{bmatrix} \cos\left(\varphi{+}\theta(t)\right) & \sin\left(\varphi{+}\theta(t)\right) \\ -\frac{1}{r}\sin\left(\varphi{+}\theta(t)\right) & \frac{1}{r}\cos\left(\varphi{+}\theta(t)\right) \end{bmatrix}.$$

For the curvilinear local vector basis we get (cf. eq. (1.5))

$$\begin{aligned} \vec{g}_r(\boldsymbol{x}^*,t) &= \cos\left(\varphi{+}\theta(t)\right)\vec{e}_x + \sin\left(\varphi{+}\theta(t)\right)\vec{e}_y \\ \vec{g}_\varphi(\boldsymbol{x}^*,t) &= -r\sin\left(\varphi{+}\theta(t)\right)\vec{e}_x + r\cos\left(\varphi{+}\theta(t)\right)\vec{e}_y\,. \end{aligned} \tag{1.82}$$

Now, let us consider a motion of a single particle p. In the frame ϕ^* it is described as a time-dependent mapping of the particle p into the coordinate system, $\boldsymbol{x}^* = \chi_{\phi^*}(p,t)$, so for the two coordinates of the particle's trajectory we have $r{=}r(p,t)$, and $\varphi{=}\varphi(p,t)$. For the position vector, upon inserting eq. (1.5)

into eq. (1.13), the following relation holds,

$$x^i(p,t)\,\vec{e}_i = \left[Q^k{}_j(\boldsymbol{x}^*(p,t),t)\,s^j_{\phi^*}(\boldsymbol{x}^*(p,t),t) + c^k(t)\right]\vec{e}_k, \tag{1.83}$$

which leads to an alternative form of eq. (1.14):

$$v^i_\phi \vec{e}_i = \left(Q^k{}_j \frac{\mathcal{D}s^j_{\phi^*}}{\mathcal{D}t} + \frac{\partial Q^k{}_j}{\partial x^l_*}\frac{\mathcal{D}x^l_*}{\mathcal{D}t}s^j_{\phi^*} + \frac{\partial Q^k{}_j}{\partial t}s^j_{\phi^*} + \frac{\mathrm{d}c^k_\phi}{\mathrm{d}t}\right)\vec{e}_k. \tag{1.84}$$

Note that in polar coordinates the position vector has radial component only, $\vec{s}_{\phi^*}(\boldsymbol{x}^*,t) = s^1_{\phi^*}(\boldsymbol{x}^*,t)\,\vec{g}_r(\boldsymbol{x}^*,t)$, and so while $s^1_{\phi^*}$ is equal to r, the second component of the position vector $s^2_{\phi^*}$ is identically zero. We can thus simplify the first two terms in eq. (1.84):

$$v^i_\phi \vec{e}_i = \left(Q^k{}_1 \frac{\mathcal{D}r}{\mathcal{D}t} + \frac{\partial Q^k{}_1}{\partial\varphi}\frac{\mathcal{D}\varphi}{\mathcal{D}t}s^1_{\phi^*} + \frac{\partial Q^k{}_j}{\partial t}s^j_{\phi^*} + \frac{\mathrm{d}c^k_\phi}{\mathrm{d}t}\right)\vec{e}_k, \tag{1.85}$$

where the independence of Q^k_1 on r for both k=1, 2 was recognized. If we evaluate the expression and employ the relations (1.82) we get

$$v^i_\phi \vec{e}_i = \frac{\mathcal{D}r}{\mathcal{D}t}\vec{g}_r + \frac{\mathcal{D}\varphi}{\mathcal{D}t}\vec{g}_\varphi + \frac{\partial Q^k{}_j}{\partial t}s^j_{\phi^*}\vec{e}_k + \frac{\mathrm{d}c^k_\phi}{\mathrm{d}t}\vec{e}_k. \tag{1.86}$$

We see that the first sum in eq. (1.14) from the main text, $(\mathcal{D}s^j_{\phi^*}/\mathcal{D}t)\,\vec{g}_j$, is equal to $(\mathcal{D}r/\mathcal{D}t)\,\vec{g}_r$ for our particular example, which is the radial velocity of the particle. The second sum in eq. (1.14), $s^j_{\phi^*}(\partial\vec{g}_j/\partial x^l_*)(\mathcal{D}x^l_*/\mathcal{D}t)$, is equal to $(\mathcal{D}\varphi/\mathcal{D}t)\,\vec{g}_\varphi$ for our example, which is the angular velocity of the particle. The terms are thus the two components of the velocity vector $\vec{v}_{\phi^*}$. Indeed, they describe the tangent to the parametrized curve r=$r(p,t)$; φ=$\varphi(p,t)$, that is, the particle's trajectory, which is the primary definition of velocity[9].

To investigate the third sum in eq. (1.14), $s^j_{\phi^*}\frac{\partial\vec{g}_j}{\partial t}$, let us insert in eq. (1.86) for $s^j_{\phi^*}$ from eq. (1.83):

$$v^i_\phi \vec{e}_i = \frac{\mathcal{D}r}{\mathcal{D}t}\vec{g}_r + \frac{\mathcal{D}\varphi}{\mathcal{D}t}\vec{g}_\varphi + \frac{\partial Q_{kj}}{\partial t}Q^{-1}_{jl}(x^l - c^l)\vec{e}_k + \frac{\mathrm{d}c^k_\phi}{\mathrm{d}t}\vec{e}_k. \tag{1.87}$$

[9]Note that $\vec{v}_{\phi^*} \neq \frac{\mathcal{D}}{\mathcal{D}t}(s^j_{\phi^*}(\boldsymbol{x}^*,t)\,\vec{g}_j(\boldsymbol{x}^*,t))$. It is because any observer, when provided the components of the position vector (for each time t) with the task to measure the particle velocity, is generally not aware of the fact that he himself is moving (he measures the velocity with respect to his frame), and so the term $s^j_{\phi^*}(\boldsymbol{x}^*,t)\,\partial\vec{g}_j(\boldsymbol{x}^*,t)/\partial t$, discussed below, is not part of the velocity measured by the observer.

Since the product $\Omega^k_l := (\partial Q^k_j/\partial t)\,\{Q^{-1}\}^j_l$ is equal to

$$\begin{bmatrix} -\frac{\mathrm{d}\theta}{\mathrm{d}t}\sin(\varphi{+}\theta) & -\frac{\mathrm{d}\theta}{\mathrm{d}t}r\cos(\varphi{+}\theta) \\ \frac{\mathrm{d}\theta}{\mathrm{d}t}\cos(\varphi{+}\theta) & -\frac{\mathrm{d}\theta}{\mathrm{d}t}r\sin(\varphi{+}\theta) \end{bmatrix} \begin{bmatrix} \cos(\varphi{+}\theta) & \sin(\varphi{+}\theta) \\ -\frac{1}{r}\sin(\varphi{+}\theta) & \frac{1}{r}\cos(\varphi{+}\theta) \end{bmatrix} = \begin{bmatrix} 0 & -\frac{\mathrm{d}\theta}{\mathrm{d}t} \\ \frac{\mathrm{d}\theta}{\mathrm{d}t} & 0 \end{bmatrix},$$

we see that the change of frame studied in this example satisfies our definition of Euclidean change of frame, because Ω^k_l is antisymmetric and spatially homogeneous. Indeed, for any antisymmetric and homogeneous tensor Ω^k_l, the third term in eq. (1.87), resp. in eq. (1.14), can be written as $\xi_{ijk}\omega^j(x^k - c^k)\,\vec{e}_i$, which is the cross product $\vec{\omega}\times(\vec{s}_\phi - \vec{c}) = \vec{\omega}\times\vec{s}_{\phi^*}$. This term describes the relative rotation of both frames. In other words, the mutual motion of two frames that are bound by Euclidean change of frame is a combination of translation and rotation only, it is a deformationless motion. This can be confirmed by observing the metric tensor of the frame ϕ^*, $g_{mn} := \vec{g}_m \cdot \vec{g}_n$. The metric tensor is spatially dependent, but constant in time:

$$g_{mn}(\boldsymbol{x}^*, t) = \begin{bmatrix} \vec{g}_r{\cdot}\vec{g}_r & \vec{g}_r{\cdot}\vec{g}_\phi \\ \vec{g}_\phi{\cdot}\vec{g}_r & \vec{g}_\phi{\cdot}\vec{g}_\phi \end{bmatrix} = \begin{bmatrix} 1 & 0 \\ 0 & r \end{bmatrix}. \tag{1.88}$$

For the convected frame, discussed below, we cannot write $g_{mn}(\boldsymbol{x}^*, t) = g_{mn}(\boldsymbol{x}^*)$, because switching to the convected frame is not a Euclidean change of frame.

1.B Convected and corotated frames: simple shearing

Let us assume a 2-D Euclidean space with a Cartesian frame ϕ, in which simple shearing of a body is observed:

$$\left.\begin{aligned} \chi^1_{\kappa,\phi}(\boldsymbol{X}, t) &= X^1 + \alpha X_2 t \\ \chi^2_{\kappa,\phi}(\boldsymbol{X}, t) &= X^2 \end{aligned}\right\} \quad \left.\begin{aligned} v^1_\phi(\boldsymbol{x}, t) &= \alpha x_2 \\ v^2_\phi(\boldsymbol{x}, t) &= 0 \end{aligned}\right\} \quad \nabla\vec{v}_\phi = \begin{pmatrix} 0 & \alpha \\ 0 & 0 \end{pmatrix}$$

Note that $\chi^1_{\kappa,\phi}(\boldsymbol{X}, t{=}0) = X^1$ and $\chi^2_{\kappa,\phi}(\boldsymbol{X}, t{=}0) = X^2$, and so the reference configuration is the initial configuration. The strain-rate and the spin of this motion are, along with the velocity gradient, spatially homogeneous and stationary:

$$\mathbb{D}_\phi = \frac{1}{2}\left(\nabla\vec{v}_\phi + (\nabla\vec{v}_\phi)^{\mathrm{T}}\right) = \begin{pmatrix} 0 & \frac{\alpha}{2} \\ \frac{\alpha}{2} & 0 \end{pmatrix}; \quad \mathbb{W}_\phi = \frac{1}{2}\left(\nabla\vec{v}_\phi - (\nabla\vec{v}_\phi)^{\mathrm{T}}\right) = \begin{pmatrix} 0 & \frac{\alpha}{2} \\ -\frac{\alpha}{2} & 0 \end{pmatrix}.$$

Let us further assume a contravariant tensor $\overset{\leftharpoonup}{a}(\boldsymbol{x}, t) = a^{ij}_\phi(\boldsymbol{x}, t)\,\vec{e}_i{\otimes}\vec{e}_j$, whose time evolution is governed by

$$\frac{\mathcal{D}_{\mathrm{uc}}\, a^{ij}_\phi}{\mathcal{D}t} = \frac{\mathcal{D}a^{ij}_\phi}{\mathcal{D}t} - \{\nabla\vec{v}_\phi\}^i_{\ k}\, a^{kj}_\phi - a^{ik}_\phi\,\{\nabla\vec{v}_\phi\}^j_{\ k} = 0\,. \tag{1.89}$$

At the origin of the frame ($\boldsymbol{x}$=0), the observed velocity of the motion is zero and eq. (1.89) reduces to

$$\frac{\partial}{\partial t}\begin{bmatrix} a_\phi^{11} & a_\phi^{12} \\ a_\phi^{12} & a_\phi^{22} \end{bmatrix} = \begin{bmatrix} 2\alpha a_\phi^{12} & \alpha a_\phi^{22} \\ \alpha a_\phi^{22} & 0 \end{bmatrix}$$

This set of ordinary differential equations has the following solution

$$\begin{aligned} \vec{a}(\boldsymbol{x}{=}0,t) = (2\alpha^2 t^2 a_0^{22} + 2\alpha t a_0^{12} + a_0^{11})\,\vec{e}_1{\otimes}\vec{e}_1 + (\alpha t a_0^{22} + a_0^{12})\,\vec{e}_1{\otimes}\vec{e}_2 \\ +(\alpha t a_0^{22} + a_0^{12})\,\vec{e}_2{\otimes}\vec{e}_1 + a_0^{22}\,\vec{e}_2{\otimes}\vec{e}_2\,, \end{aligned} \tag{1.90}$$

where $a_0^{11}, a_0^{22}, a_0^{12}$ are the initial values of $\vec{a}$, that is, $a_\phi^{ij}(\boldsymbol{x}{=}0, t{=}0)$.

The simple shearing studied here can be also viewed from the convected frame ϕ^*, related to ϕ through a non-Euclidean change of frame $\boldsymbol{x}^*{=}\boldsymbol{x}^*(\boldsymbol{x},t)$, defined so that the coordinates of material points stay constant throughout the motion:

$$\left.\begin{aligned} x^1(\boldsymbol{x}^*,t) &= x_*^1 + \alpha x_*^2 t \\ x^2(\boldsymbol{x}^*,t) &= x_*^2 \end{aligned}\right\} \quad \begin{aligned} x_*^1(\boldsymbol{x},t) &= x^1 - \alpha x^2 t \\ x_*^2(\boldsymbol{x},t) &= x^2 \end{aligned}$$

Thus, in the convected frame the motion reads $\chi^i_{\kappa^*,\phi^*}(\boldsymbol{X}^*,t) = X^i_*$, with the reference configuration chosen to be the initial configuration. For the shifter tensor of the change of frame one gets

$$Q(\boldsymbol{x}^*,t) = \begin{bmatrix} 1 & \alpha t \\ 0 & 1 \end{bmatrix}; \quad Q^{-1}(\boldsymbol{x},t) = \begin{bmatrix} 1 & -\alpha t \\ 0 & 1 \end{bmatrix}, \tag{1.91}$$

and the local curvilinear contravariant and covariant bases reads

$$\begin{aligned} &\vec{g}_1 = \vec{e}_1; \quad \vec{g}_2 = \alpha t\vec{e}_1 + \vec{e}_2; \quad \underline{g}^1 = \underline{e}^1 - \alpha t\underline{e}^2; \quad \underline{g}^2 = \underline{e}^2 \\ &\vec{e}_1 = \vec{g}_1; \quad \vec{e}_2 = \alpha t\vec{g}_1 - \vec{g}_2; \quad \underline{e}^1 = \underline{g}^1 + \alpha t\underline{g}^2; \quad \underline{e}^2 = \underline{g}^2 \end{aligned} \tag{1.92}$$

Inserting for $\vec{e}_i$ from eq. (1.92) into the solution (1.90) gives the components of the solution in the convected frame ϕ^*:

$$\vec{a}(\boldsymbol{x}^*{=}0,t) = a_0^{11}\,\vec{g}_1{\otimes}\vec{g}_1 + a_0^{12}\,\vec{g}_1{\otimes}\vec{g}_2 + a_0^{12}\,\vec{g}_2{\otimes}\vec{g}_1 + a_0^{22}\,\vec{g}_2{\otimes}\vec{g}_2. \tag{1.93}$$

We see that the components $a^{ij}_{\phi^*}$ of the solution are constant in time. Here we have shown it only at the origin $\boldsymbol{x}^*{=}0$, but it is valid for any particle of the body.

It is instructive to analyze the geometrical meaning of the fact that $a^{ij}_{\phi^*}$ are constant in time. Any contravariant tensor field $\vec{a}$ is a mapping from the dual space $\mathcal{L}(\mathbb{V})$ to $\mathbb{V}$: $\vec{a}(\underline{n}) = \vec{w}; \quad \vec{n} \in \mathcal{L}(\mathbb{V})$, $\vec{w} \in \mathbb{V}$. Generally, it is a temporally and spatially dependent mapping. Let us consider a scalar field s and a set of parametrized curves with tangents given by a vector field $\vec{w}$, such that $\vec{a}(\nabla s) = \vec{w}$

holds at every point p at time t=0. Let us further assume that the scalar field s and the parametrized curves are frozen into the body, that is, $s(p,t)$=$s(p)$ and $w^i_{\phi^*}(p,t)$=$w^i_{\phi^*}(p)$. Then, the time-constancy of $a^{ij}_{\phi^*}$ implies that $\overleftrightarrow{a}(\nabla s) = \vec{w}$ holds at every point p and every time t throughout the motion of the body.

To inspect the meaning of the Jaumann rate, let us assume a different contravariant tensor $\overleftrightarrow{b}(\boldsymbol{x},t) = b^{ij}_\phi(\boldsymbol{x},t)\,\vec{e}_i \otimes \vec{e}_j$, whose temporal evolution is governed by

$$\frac{\mathcal{D}_{\text{Jau}}\, b^{ij}_\phi}{\mathcal{D}t} = \frac{\mathcal{D} b^{ij}_\phi}{\mathcal{D}t} - \mathbb{W}^{ik}_\phi\, b^{kj}_\phi + b^{ik}_\phi\, \mathbb{W}^{kj}_\phi = 0. \tag{1.94}$$

At the origin of the frame eq. (1.94) reduces to

$$\frac{\partial}{\partial t}\begin{bmatrix} b^{11}_\phi & b^{12}_\phi \\ b^{12}_\phi & b^{22}_\phi \end{bmatrix} = \begin{bmatrix} \alpha b^{12}_\phi & \frac{\alpha}{2}(b^{22}_\phi - b^{11}_\phi) \\ \frac{\alpha}{2}(b^{22}_\phi - b^{11}_\phi) & -\alpha b^{12}_\phi \end{bmatrix},$$

which has the following solution

$$\begin{aligned} \overleftrightarrow{b}(\boldsymbol{x}{=}0,t) &= [c_1\sin(\alpha t) - c_2\cos(\alpha t) + c_3]\,\vec{e}_1{\otimes}\vec{e}_1 + [c_1\cos(\alpha t) + c_2\sin(\alpha t)]\,\vec{e}_1{\otimes}\vec{e}_2 \\ &+ [c_1\cos(\alpha t) + c_2\sin(\alpha t)]\,\vec{e}_2{\otimes}\vec{e}_1 - [c_1\sin(\alpha t) - c_2\cos(\alpha t) - c_3]\,\vec{e}_2{\otimes}\vec{e}_2, \end{aligned} \tag{1.95}$$

where c_1, c_2, c_3 are constants that can be determined from the initial conditions $b^{ij}_\phi(\boldsymbol{x}{=}0, t{=}0) = b^{ij}_0$.

Again, there exists a frame ϕ^* in which the components of $\overleftrightarrow{b}$ are time constant. It is the corotated frame, defined as

$$\left.\begin{aligned} x^1(\boldsymbol{x}^*,t) &= \sqrt{(x^1_*)^2 + (x^2_*)^2}\,\cos\left(\tfrac{\alpha}{2}t\right) \\ x^2(\boldsymbol{x}^*,t) &= \sqrt{(x^1_*)^2 + (x^2_*)^2}\,\sin\left(\tfrac{\alpha}{2}t\right) \end{aligned}\right\} \quad \begin{aligned} x^1_*(\boldsymbol{x},t) &= \sqrt{(x^1)^2 + (x^2)^2}\,\cos\left(\tfrac{\alpha}{2}t\right) \\ x^2_*(\boldsymbol{x},t) &= -\sqrt{(x^1)^2 + (x^2)^2}\,\sin\left(\tfrac{\alpha}{2}t\right) . \end{aligned}$$

Unlike in the case of the convected frame, the corotated frame is related to the Cartesian frame ϕ via Euclidean change of frame, but it is only because we are studying homogeneous simple shearing here. The relative motion of both frames is a rotation with the angular speed of $\alpha/2$ (compare with the spin of the studied motion). For the shifter tensor we get

$$Q(\boldsymbol{x}^*,t) = \begin{bmatrix} \cos\left(\frac{\alpha}{2}t\right) & \sin\left(\frac{\alpha}{2}t\right) \\ -\sin\left(\frac{\alpha}{2}t\right) & \cos\left(\frac{\alpha}{2}t\right) \end{bmatrix}; \quad Q^{-1}(\boldsymbol{x},t) = \begin{bmatrix} \cos\left(\frac{\alpha}{2}t\right) & -\sin\left(\frac{\alpha}{2}t\right) \\ \sin\left(\frac{\alpha}{2}t\right) & \cos\left(\frac{\alpha}{2}t\right) \end{bmatrix},$$

confirming that the change of frame is a time dependent rotation, because the inverse of the shifter tensor is its transpose: $Q^{-1}(\boldsymbol{x},t) = Q^{\mathrm{T}}(t)$. The local curvi-

linear contravariant and covariant bases are related via

$$\begin{aligned}\vec{g}_1 &= \cos\left(\frac{\alpha}{2}t\right)\vec{e}_1 - \sin\left(\frac{\alpha}{2}t\right)\vec{e}_2; \quad \vec{g}_2 = \cos\left(\frac{\alpha}{2}t\right)\vec{e}_2 + \sin\left(\frac{\alpha}{2}t\right)\vec{e}_1 \\ \underline{g}^1 &= \cos\left(\frac{\alpha}{2}t\right)\underline{e}^1 - \sin\left(\frac{\alpha}{2}t\right)\underline{e}^2; \quad \underline{g}^2 = \cos\left(\frac{\alpha}{2}t\right)\underline{e}^2 + \sin\left(\frac{\alpha}{2}t\right)\underline{e}^2.\end{aligned} \tag{1.96}$$

Since both frames are orthonormal, the transformation properties of one-forms and vectors are the same. With the help of eq. (1.96) the solution (1.95) can be, after some algebraic manipulations, written in terms of its components in the corotated frame ϕ^*:

$$\overleftrightarrow{b}(\boldsymbol{x}^*{=}0,t) = (c_3 - c_2)\,\vec{g}_1{\otimes}\vec{g}_1 + c_1\,\vec{g}_1{\otimes}\vec{g}_2 + c_1\,\vec{g}_2{\otimes}\vec{g}_1 + (c_3 + c_2)\,\vec{g}_2{\otimes}\vec{g}_2, \tag{1.97}$$

which are indeed constant in time.

We conclude the example with two remarks. First, the local covariant and contravariant bases are indistinguishable in the corotated frame, cf. eq. (1.96), and so the calculations with the contravariant tensor field $\overleftrightarrow{b}$ would be the same for second-order tensors of any kind, namely for any left covariant mixed tensor field, right covariant mixed tensor field, and covariant tensor field. All the components of tensor fields are constant in the corotated frame when their temporal evolution is governed by eq. (1.94). For the convected frame and the upper convected derivative this is different: only the contravariant components of tensors are constant in the convected frame when their temporal evolution is governed by eq. (1.89) (see also the discussion below eq. (1.46) in the main text).

Second, it is instructive to repeat the procedure with the convected frame for the case of simple stretching instead of simple shearing. Simple stretching can be defined as $\chi^1_{\kappa,\phi}(\boldsymbol{X},t) = X_1\exp(\alpha_1 t)$; $\chi^2_{\kappa,\phi}(\boldsymbol{X},t) = X_2\exp(\alpha_2 t)$, and it can be shown that while setting the Oldroyd derivative of a contravariant tensor to zero leads to constancy of its components in the convected frame (they are constant along particle trajectories), setting the Truesdell rate to zero results in constant components in the Cartesian frame (again, constant along particle trajectories). In other words, the first solution satisfies $a^{ij}_{\phi^*}(\boldsymbol{x}^*,t) = a^{ij}_{\phi^*}(\boldsymbol{x}^*)$, while the latter solution can be satisfies $\overleftrightarrow{a}(p,t) = \overleftrightarrow{a}(p)$.

2. Small deformations of viscoelastic mantle

"*Any opinion as to the form in which the energy of gravitation exists in space is of great importance, and whoever can make his opinion probable will have made an enormous stride in physical speculation. The apparent universality of gravitation, and the equality of its effects on matter of all kinds are most remarkable facts, hitherto without exception; but they are purely experimental facts, liable to be corrected by a single observed exception. We cannot conceive of matter with negative inertia or mass; but we see no way of accounting for the proportionality of gravitation to mass by any legitimate method of demonstration. If we can see the tails of comets fly off in the direction opposed to the sun with an accelerated velocity, and if we believe these tails to be matter and not optical illusions or mere tracks of vibrating disturbance, then we must admit a force in that direction, and we may establish that it is caused by the sun if it always depends upon his position and distance.*" – James Clerk Maxwell, Letter to William Huggins (13 Oct 1868)

2.1 Eulerian formulation of the governing equations

Throughout the thesis we use Eulerian description of field variables, meaning that the domain of these variables is the current configuration of the body at time t. Such approach is obvious when mantle convection is addressed, see Chapters 3 and 4, but it is not very common when small deformations of a planet, for example caused by surface loads, are being computed. In such cases it is more common to use Lagrangian description of field variables, with their domain being some convenient reference configuration with a regular shape. The advantage is that symmetric domains allow for the use of fast numerical methods – in planetary science it is often assumed to be a sphere or spherical shell, allowing for the use of so-called spectral methods (decomposing field variables into spherical harmonics).

In Section 2.2, dealing with deformation of the Earth due to surface glaciers and rotation, we use the Eulerian description of variables, but still choose the computational domain to be a time constant spherical shell. This somewhat puzzling combination enables us to harvest the elegance intrinsic to the Eulerian formulation – the absence of any additional terms related to the fact that in the Lagrangian formulation the body forces are expressed at locations where they do not actually act – and at the same time to employ a spectral method. The approach has appeared in geodynamical literature several times in the past decade (e.g. Tobie et al., 2008; Golle et al., 2012; Souček et al., 2016), but the papers are mostly application driven. We carefully derive the governing equations in this

section in order to avoid any potential confusions.

Let us assume a spherical body at rest, its static pressure p_0 counteracting the gravitational forcing $\rho\boldsymbol{g}_0$, ρ being the density and $\boldsymbol{g}_0$ the gravitational acceleration (see the left panel of Fig. 2.1). When the body is subject to a conservative forcing described by potential ζ it deforms. Eulerian formulation of the equation of motion then reads

$$\nabla \cdot \boldsymbol{\tau} + \rho\boldsymbol{g}_0 - \rho\nabla\zeta = 0 \quad \text{in} \quad v(t), \tag{2.1}$$

where $\boldsymbol{\tau}$ is the Cauchy stress tensor and ζ is the potential driving deformation (e.g. centrifugal potential or perturbation of the gravitational potential due to the change of the body's shape – see Section 2.2). Eq. (2.1) is valid within the deformed body occupying the region $v(t)$. If the surface of the body is free, the boundary condition reads

$$\boldsymbol{\tau} \cdot \boldsymbol{n} = 0 \quad \text{on} \quad s^- \cap s^+, \tag{2.2}$$

where $\boldsymbol{n}$ is the outer normal vector to surfaces s^- and s^+ of the deformed body, depicted on the right panel of Fig. 2.1. If the body's deformation is driven by surface loads, the boundary condition (2.2) is replaced with $\boldsymbol{\tau}\cdot\boldsymbol{n} = (\boldsymbol{g}_0 + \nabla\zeta)\,\sigma^{\mathrm{L}}$, σ^{L} representing surface mass density of the load. In this section we further assume $\sigma^{\mathrm{L}} = 0$ for clarity. Systems described by eq. (2.1) are often referred to as hydrostatically pre-stressed bodies. The effect of the static pressure p_0, which satisfies

$$-\nabla p_0 + \rho\boldsymbol{g}_0 = 0 \quad \text{in} \quad S_0 \tag{2.3}$$

and is equal to zero elsewhere, can be subtracted by subtracting eq. (2.3) from eq. (2.1). The governing equations (2.1) and (2.2) then take the form

$$\nabla \cdot \bar{\boldsymbol{\tau}} - \rho\nabla\zeta = 0 \quad \text{in} \quad v^{\mathrm{J}}(t), \tag{2.4}$$

$$\nabla \cdot \bar{\boldsymbol{\tau}} + \rho\boldsymbol{g}_0 - \rho\nabla\zeta = 0 \quad \text{in} \quad v^{+}(t), \tag{2.5}$$

$$\bar{\boldsymbol{\tau}} \cdot \boldsymbol{n} = p_0\boldsymbol{n} \quad \text{on} \quad s^{-}(t), \tag{2.6}$$

$$\bar{\boldsymbol{\tau}} \cdot \boldsymbol{n} = 0 \quad \text{on} \quad s^{+}(t), \tag{2.7}$$

where $\bar{\boldsymbol{\tau}} := \boldsymbol{\tau} + p_0\mathcal{I}$, $\mathcal{I}$ being the identity tensor. Note that the static pressure p_0 is defined by eq. 2.3 as a positive quantity inside the sphere S_0 and zero outside that sphere. In Section 2.2 we solve, however, the following set of equations:

$$\nabla \cdot \bar{\boldsymbol{\tau}} - \rho\nabla\zeta = 0 \quad \text{in} \quad S_0, \tag{2.8}$$

$$\bar{\boldsymbol{\tau}} \cdot \boldsymbol{n} = u_r\rho\boldsymbol{g}_0 \quad \text{on} \quad \partial S_0, \tag{2.9}$$

where $\boldsymbol{e}_r$ is the outer normal to surface ∂S_0 and u_r is the radial component of the Eulerian displacement field $\boldsymbol{u}$.

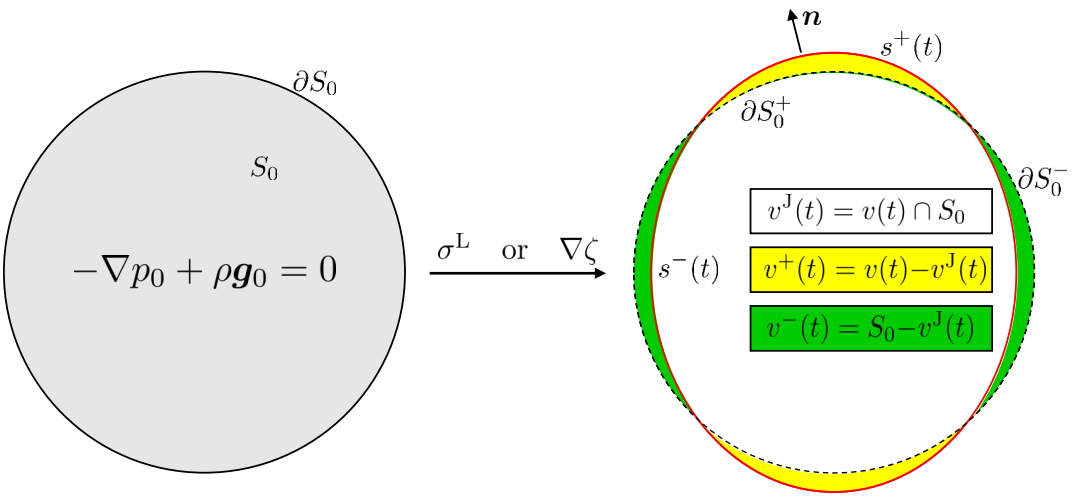

Figure 2.1: A sphere S_0 deforms and becomes volume $v(t)$ due to the acting of a surface load σ^{L} or due to a disturbing potential ζ. The surface ∂S_0 can be separated into the part ∂S_0^+ which goes up and becomes s^+ after the deformation. The other part, ∂S_0^-, descends and becomes s^- after the deformation.

To show that eqs (2.8)–(2.9) are a reasonable approximation of the original eqs (2.1)–(2.2), resp. of their equivalent eqs (2.4)–(2.7), we investigate the terms (2.5) and (2.6). Upon integrating (2.5) over the volume $v^+(t)$ and using the Gauss theorem, together with the free surface condition (2.7), we get

$$-\int_{\partial S_0^+} \bar{\boldsymbol{\tau}} \cdot \boldsymbol{e}_r \,\mathrm{d}s + \int_{v^+(t)} \rho(\boldsymbol{g}_0 - \nabla\zeta) \,\mathrm{d}v = 0. \tag{2.10}$$

The second term in eq. (2.10) can be subject to a series of approximations:

$$\int_{v^+(t)} \rho(\boldsymbol{g}_0 - \nabla\zeta) \,\mathrm{d}v \cong \int_{v^+(t)} \rho \boldsymbol{g}_0 \,\mathrm{d}v \cong \int_{\partial S_0^+} \rho \boldsymbol{g}_0 \, u_r \,\mathrm{d}s, \tag{2.11}$$

where we first assumed $\nabla\zeta \ll \boldsymbol{g}_0$ and then we expressed the volume element $\mathrm{d}v$ of $v^+(t)$ as $u_r \,\mathrm{d}s$. Note that the second step is approximative for two reasons: 1) radial variations of the integrand, $\rho\boldsymbol{g}_0$, within the volume $v^+(t)$ are neglected, and 2) the height of topography above the sphere S_0 is estimated by the value of u_r at the surface ∂S_0^+ and not at the surface s^+. Since we use Eulerian description of variables, the displacement field $\boldsymbol{u}$ taken at ∂S_0^+ represents the displacement of material particles that are at ∂S_0^+ after the deformation. It is thus only a first-order estimate of the actual topography height, which is equal to the value of u_r taken at the surface of the deformed body s^+. Eq. (2.11) together with eq. (2.10) yield

$$\int_{\partial S_0^+} (-\bar{\boldsymbol{\tau}} \cdot \boldsymbol{e}_r + \rho \boldsymbol{g}_0 \, u_r) \,\mathrm{d}s \cong 0, \tag{2.12}$$

which is the boundary condition (2.9) on ∂S_0^+. In other words, the volumetric force $\rho(\boldsymbol{g}_0 - \nabla\zeta)$ was found dynamically equivalent to the surface traction $\rho\boldsymbol{g}_0 \, u_r$, acting at the spherical surface ∂S_0^+. Also note that the approximation $\nabla\zeta \ll \boldsymbol{g}_0$

could be easily avoided by replacing $\boldsymbol{g}_0$ with $(\boldsymbol{g}_0 - \nabla\zeta)$ in eq. (2.9).

For regions with negative topography we integrate the traction in eq. (2.6) over the surface $s^-(t)$,

$$\int_{s^-(t)} p_0 \boldsymbol{n}\,\mathrm{d}s \cong \int_{s^-(t)} -\rho g_0 u_r\,\boldsymbol{n}\mathrm{d}s \cong \int_{\partial S_0^-} \rho \boldsymbol{g}_0 u_r\,\mathrm{d}s\,, \tag{2.13}$$

where in the first step the static pressure p_0 at the surface $s^-(t)$ was set equal to $-\rho g_0 u_r$, which neglects the radial variations of ρg_0 within the volume $v^-(t)$, similarly as in eq. (2.11). In the second step the surface element $\boldsymbol{n}\mathrm{d}s$ of $s^-(t)$ was approximated by the surface element of ∂S_0^-, which is a good first-order estimate. Observing eq. (2.13) directly shows that the boundary traction (2.6) is dynamically analogous to the prescribed traction (2.9) on ∂S_0^-, concluding the correspondence of eqs (2.8)–(2.9) with the set (2.4)–(2.7).

Instead of the procedure above, the same conclusions can be reached by performing the Taylor expansion of (2.2), as done in appendix to Souček et al. (2016):

$$0 = \boldsymbol{\tau}(\boldsymbol{r}_\mathrm{s}+\boldsymbol{u}) \cdot \boldsymbol{n}(\boldsymbol{r}_\mathrm{s}+\boldsymbol{u}) = (\bar{\boldsymbol{\tau}} - p_0\mathcal{I})(\boldsymbol{r}_\mathrm{s}+\boldsymbol{u}) \cdot \boldsymbol{n}(\boldsymbol{r}_\mathrm{s}+\boldsymbol{u}) \tag{2.14}$$

$$\cong \boldsymbol{n}p_0(\boldsymbol{r}_\mathrm{s}) + \bar{\boldsymbol{\tau}}(\boldsymbol{r}_\mathrm{s}) \cdot \boldsymbol{n} + \boldsymbol{u} \cdot [\nabla(p_0\boldsymbol{n})]_{\mathrm{r=r_s}} + \boldsymbol{u} \cdot [\nabla(\bar{\boldsymbol{\tau}} \cdot \boldsymbol{n})]_{\mathrm{r=r_s}} \tag{2.15}$$

$$\cong \bar{\boldsymbol{\tau}}(\boldsymbol{r}_\mathrm{s}) \cdot \boldsymbol{e}_r + \rho g_0 u_r(\boldsymbol{r}_\mathrm{s})\boldsymbol{e}_r \tag{2.16}$$

where $\boldsymbol{r}_\mathrm{s}$ is the position vector tracking the spherical surface ∂S_0, $p_0(\boldsymbol{r}_\mathrm{s})$ was recognized as zero, the normal vector $\boldsymbol{n}$ was approximated by $\boldsymbol{e}_r$, the term $\boldsymbol{u}\cdot[\nabla(p_0\boldsymbol{n})]_{\mathrm{r=r_s}}$ was approximated by $\rho g_0 u_r(\boldsymbol{r}_\mathrm{s})\boldsymbol{e}_r$, and the last term on the second line was neglected. We believe, however, that the more detailed analysis provided here may help the reader in understanding the derivations in the next section.

2.2 Energy balance of GIA on a rotating Earth

Published in Geophysical Journal International,
Volume 212(2), p. 955-975, doi: 10.1093/gji/ggx469, 2017

V. Patočka[1], O. Čadek[1] and Z. Martinec[1,2]

[1] Department of Geophysics, Faculty of Mathematics and Physics, Charles University, Prague, Czech Republic
[2] Dublin Institute for Advanced Studies, Geophysics Section, Dublin, Ireland

Summary

Understanding the feedback between the glacial isostatic adjustment (GIA) and the Earth's rotation is important for an accurate prediction of sea level changes induced by climate and tectonic processes. Here we consider a simple, four-layer incompressible Earth model, recently used for a benchmark of GIA codes to estimate the accuracy of the linearized Liouville equation (LE) and to demonstrate that models with an incomplete or missing rotational feedback violate the principle of energy conservation. First, we compute GIA on a rotating Earth by solving the equation of motion coupled with LE in its full nonlinear form. By comparing the nonlinear LE solution with the traditional linearized one, we find that the radial component of the angular velocity vector is inaccurate in the latter case, with an error exceeding 10% already after 1 kyr of evolution. To understand the cause of this discrepancy, we investigate the time evolution of different kinds of energy involved in the process. While the rotational, elastic and dissipative energies are straightforward to compute, the formula for the gravitational energy contains an integral that requires a careful, higher-order accurate evaluation of the gravitational potential perturbation. We circumvent this problem by transforming the integral into a different one, formulated in terms of displacement instead of potential. We find that the solution of the linearized LE equation does not conserve the energy, since, in the linearized case, the rate of change of the rotational energy is not equal to the power of the centrifugal force. We also compute the energy balance of GIA on a constantly rotating Earth, and demonstrate the importance of the rotational feedback in the equation of motion. The formalism derived in this study allows a detailed examination of the energy balance for a rotating, incompressible planetary body deformed by a surface load. As such, it may not only serve as a reliable tool for *a posteriori* testing of GIA numerical solutions but it can also be used in different planetary science applications.

2.2.1 Introduction

Glacial isostatic adjustment (GIA) has been investigated within the geophysical community for many decades, recently gaining attention due to the increasing precision of geodetic measurements obtained from the GRACE (Tapley et al., 2004) and GOCE (Floberghagen et al., 2011) satellite missions and the growing interest in sea level changes. The response of the Earth to surface loading was used primarily to constrain the viscosity profile of the mantle (Cathles, 2015). However, the depth to which viscosity can be inferred by measuring postglacial rebound is limited by the lateral extent of the past glaciers, leaving the lowermost mantle poorly resolved (e.g. Mitrovica & Peltier, 1991).

The motion of the rotation axis of the Earth, induced by mass redistribution that accompanies the periodic accumulation and melting of ice during glacial cycles, can be used to overcome this limitation. Assuming that the ice load history is known, lower-mantle viscosity can be constrained by fitting the observed rate of the secular drift (e.g. Sabadini et al., 1982; Wu & Peltier, 1984; Vermeersen et al., 1998; Lau et al., 2016). Also worth noting is the pioneering attempt of Nakada & Karato (2012) to infer the lower-mantle viscosity by comparing the Q-factor of the predicted Chandler wobble with the observed value (e.g. Benjamin et al., 2006).

It was only later that the perturbation of the centrifugal force, inherent to any change in the rotation vector, was also included in modelling GIA-related suite of observables. While its effect on the sea level equation has been extensively studied (e.g. Milne & Mitrovica, 1998; Mitrovica et al., 2001), its impact on the GIA-induced deformation of the Earth has only been addressed recently by Martinec & Hagedoorn (2014).

Precise computation of GIA-induced polar motion (PM) thus plays an important role in numerical simulations of postglacial rebound related phenomena. Following Munk & MacDonald (1960) it has become common to use the linearized form of the Liouville equation (LE) to obtain the PM solution. The error introduced by the linearization is not straightforward to estimate and depends on the amplitudes of the wander that the rotation axis experiences. In this paper, we couple the fully nonlinear LE (NLE) with the equations governing small deformations of a radially symmetric, self-gravitating incompressible spherical shell. By comparing the NLE solution with the linearized one we quantitatively evaluate the error due to neglecting higher-order terms in the linearized LE (LLE). In particular, we estimate the error arising from decoupling the equations for PM and the length of day (LOD) variation, which is an intrinsic property of the linearized approach. The accuracy of the LLE is tested for the Earth model M3-L70-V01 loaded with a spherical ice cap, a community benchmark by Spada et al. (2011).

Another way to assess the accuracy of the linearized solution, without having to solve the NLE, is to check whether the total energy of the Earth's model is conserved. The energy balance involves the rotational, elastic and dissipative en-

ergies, which are straightforward to evaluate, and the gravitational energy, which requires a higher-order accurate evaluation of the gravitational perturbation potential. In section 2.2.4.1 we solve this problem by deriving an equivalent integral but with the displacement in the integrand, allowing the use of a simple spectral formula for the geoid (e.g. Choblet et al., 2007).

We then compute the energy balance for various test examples relevant to GIA studies. In section 2.2.4.2 we load a non-rotating Earth with a spherical ice cap. To assess the energetic importance of free wobble, triggered by a hypothetical rapid accumulation of a surface load on a rotating Earth, we separately study this phenomenon in section 2.2.4.3. In section 2.2.4.4, we analyse the energy balance of a rotating Earth loaded with a spherical ice cap, that is, the benchmark case by Spada et al. (2011). We show that the LLE solution does not conserve the energy and discuss the consequences of this finding for the prediction of PM and LOD. In section 2.2.4.5 we consider the same surface loading, but on a constantly rotating Earth. A large deviation from the energy conservation is obtained in such case, proving the importance of including rotational feedback in GIA modelling.

All results discussed in section 2.2.4 are obtained for the four-layer, incompressible Earth model M3-L70-V01 used already in the benchmark of GIA codes (Spada et al., 2011). Although this structural model is relatively simple in comparison with recent models inferred from ice age data sets (e.g. Lau et al., 2016), it allows our predictions of PM and LOD to be compared with those in Spada et al. (2011) and the energy curves presented in section 2.2.4 to be easily reproduced.

The energy balance analysis introduced in this paper does not include the effect of compressibility. As shown by Cambiotti et al. (2010), compressibility of the real Earth can have non-negligible effect on both GIA and PM. Compressible models are more deformable than the incompressible ones, which makes the readjustment of the rotational bulge quicker, effectively reducing the GIA-induced PM. This reduction, however, depends on lower mantle viscosity and is almost negligible for values higher than 10^{22} Pa s, which are usually needed to stabilize the rotation of the Earth on geological time scales (Ricard et al., 1993).

To compute small deformations of a rotating, gravitationally pre-stressed Earth we use the Eulerian formulation of the governing equations, instead of applying the traditional Lagrangian approach (e.g. Wu & Peltier, 1982). The Eulerian formulation has appeared in the literature several times in the past decade (e.g. Tobie et al., 2008; Golle et al., 2012; Souček et al., 2016), but only for spherical shells with a constant density. We extend it for the case where the internal density is a continuous piecewise linear function and we numerically demonstrate that the solution is equivalent to the Lagrangian one. Using the Eulerian formulation we demonstrate a one-by-one correspondence between individual forces in the equation of motion and the terms describing the gravitational, rotational, elastic and dissipative energies. Such a correspondence provides a powerful tool when diagnosing a numerical solution. While the evaluation of the sum of all involved energies reveals only whether or not the solution is numerically correct, the

term-by-term correspondence can be used to directly identify a potential source of energy imbalance.

In the present paper, we do not use the normal mode theory (e.g. Peltier, 1974) or complex contour integration (e.g. Tanaka et al., 2009; Sabadini et al., 2016), as we solve all equations in the time domain, making the coupling between the equation of motion and the LE straightforward. It is worth noting that the use of the NLE does not require the amplitudes of the modelled PM to be small and the time scales on which mass redistribution occurs can be arbitrary. Our approach thus broadens the variety of processes that can be addressed compared to the traditional techniques: the linearized approach is limited to PM with small amplitudes, and the viscous quasi-fluid approximation, introduced by Lefftz et al. (1991) and Ricard et al. (1993), is valid only for mass redistribution occurring on the time scale of a few million years (see also Cambiotti et al., 2011). The rapid formation of craters and volcanoes that can subsequently shift the rotation axis of a planetary body by tens of degrees (Runcorn, 1984; Kite et al., 2009), and a number of asteroids that experience a large-amplitude wobbling (Harris, 1994), are examples of the problems that could newly be tackled with the tool we present.

2.2.2 Governing equations

We consider small deformations of a hydrostatically prestressed spherical shell with radially dependent reference density profile $\rho_0(r)$ and a homogeneous fluid core. The material of the spherical shell is assumed to behave like an incompressible Maxwell-type viscoelastic fluid. The time evolution of displacement and stress can be obtained by integrating the following set of partial differential equations (e.g. Tobie et al., 2008):

$$\nabla \cdot \boldsymbol{\tau} + \boldsymbol{f} = 0\,, \tag{2.17}$$

$$\nabla \cdot \boldsymbol{u} = 0\,, \tag{2.18}$$

$$\boldsymbol{\tau}^d - \mu(\nabla \boldsymbol{u} + (\nabla \boldsymbol{u})^{\mathrm{T}}) = -\frac{\mu}{\eta}\int_0^t \boldsymbol{\tau}^d \mathrm{d}t'\,, \tag{2.19}$$

where $\boldsymbol{\tau}$ is the Cauchy stress tensor, $\boldsymbol{\tau}^d$ is its deviatoric part, $\boldsymbol{f}$ is the body force, $\boldsymbol{u}$ is the displacement, the superscript T denotes transposition of a tensor, μ is the elastic shear modulus, η is the viscosity, and t is the time. At time t=0 the integral on the right-hand side of eq. (2.19) is zero and the spherical shell behaves like an elastic solid. Throughout the paper, we strictly use the Eulerian description of the problem. All variables are expressed as functions of the instantaneous position of the particle in the deformed body. A particle occupying the position $\boldsymbol{r}$ at time t would occupy the position $\boldsymbol{r} - \boldsymbol{u}(\boldsymbol{r}, t)$ if all forces that cause the deformation were set to zero at all times.

The body force $\boldsymbol{f}$ is given as the product of density and the negative gradient

of gravity potential. The gravity potential has three components: (i) the reference gravitational potential V_0, (ii) the centrifugal potential Ψ due to the rotation of the body, and (iii) the perturbation Φ of the gravitational potential V_0 due to the deformation of the body. V_0 is the gravitational potential of a sphere of radius a with density profile $\rho_0(r)$. Inside the sphere ($r \leq a$)

$$V_0(r) = -\frac{4\pi G}{r}\int_0^r \rho_0(r')r'^2\,\mathrm{d}r' - 4\pi G\int_r^a \rho_0(r')r'\,\mathrm{d}r', \tag{2.20}$$

where G is the universal gravitational constant. The centrifugal potential Ψ is given as

$$\Psi = \frac{1}{2}\left((\boldsymbol{\omega}\cdot\boldsymbol{r})^2 - |\boldsymbol{\omega}|^2|\boldsymbol{r}|^2\right), \tag{2.21}$$

where $\boldsymbol{\omega}$ is the angular velocity vector which has the direction of the rotation axis and the magnitude equal to the angular speed of the body.

As the sphere deforms, the initial density $\rho_0(r)$ changes to density $\rho(\boldsymbol{r},t)$ which can be expressed as a sum of density $\rho_0(r)$ and Eulerian density increment $\delta\rho(\boldsymbol{r},t)$. If the body is incompressible and the density ρ_0 is a continuous function,

$$\delta\rho(\boldsymbol{r},t) = \rho(\boldsymbol{r},t) - \rho_0(r) = \rho_0(|\boldsymbol{r}-\boldsymbol{u}(\boldsymbol{r},t)|,t) - \rho_0(r) = -\boldsymbol{u}(\boldsymbol{r},t)\cdot\nabla\rho_0(r) + O(|\boldsymbol{u}|^2), \tag{2.22}$$

where the displacement $\boldsymbol{u}$ describes the deformation of the body. The Eulerian density increment $\delta\rho$ is non-zero also at the outer surface and at the internal density interfaces where it is equal to the density jump at the respective interface. Using $\delta\rho$ we can express the perturbation potential Φ in an integral form:

$$\Phi(\boldsymbol{r},t) = -G\int_{v(t)} \frac{\delta\rho(\boldsymbol{r}',t)}{|\boldsymbol{r}-\boldsymbol{r}'|}\,\mathrm{d}v', \tag{2.23}$$

where $v(t)$ is the volume occupied by the body (including the core) at time t. Neglecting the terms $O(|\boldsymbol{u}|^2)$ and $-\delta\rho\nabla(\Phi+\Psi)$, we obtain the following expression for the body force $\boldsymbol{f}$:

$$\boldsymbol{f} = -\rho\nabla(V_0+\Phi+\Psi) \cong -(\boldsymbol{u}\cdot\nabla\rho_0)\boldsymbol{g}_0 - \rho_0\nabla\left(\Phi+\Psi\right) + \rho_0\boldsymbol{g}_0, \tag{2.24}$$

where $\boldsymbol{g}_0 = -\nabla V_0$. The laterally homogeneous and static contribution $\rho_0\boldsymbol{g}_0$ is counteracted by the hydrostatic prestress $p_0(r)$, satisfying the equation $-\nabla p_0 + \rho_0\boldsymbol{g}_0 = 0$.

Equations (2.17) – (2.19) are solved in a spherical shell with outer radius a and inner radius b. The boundary condition at the outer surface is obtained from the force equilibrium condition, taking into account the pressure due to the deformation-induced topography (e.g. Souček et al., 2016) and the presence of a surface load:

$$\boldsymbol{\tau}\cdot\boldsymbol{e}_r = \left(u_r[\rho_0]_a + \sigma^{\mathrm{L}}\right)\boldsymbol{g}_0, \tag{2.25}$$

where $\boldsymbol{e}_r$ is the radial unit vector, u_r is the radial component of displacement

$\boldsymbol{u}$, $[\rho_0]_a = \rho_0(a)$ is the density jump at the surface, and σ^{L} is the surface mass density of the prescribed surface load. A similar condition can be imposed at the bottom boundary, on Earth corresponding to the core-mantle boundary:

$$-\boldsymbol{\tau}\cdot\boldsymbol{e}_r = u_r[\rho_0]_b\,\boldsymbol{g}_0 - \rho_{\mathrm{c}}(V_0+\Phi+\Psi)\boldsymbol{e}_r, \tag{2.26}$$

where $[\rho_0]_b$ is the density jump at the bottom boundary and $-\rho_{\mathrm{c}}(V_0+\Phi+\Psi)$ is the hydrostatic pressure acting on the boundary due to the contact with a liquid core of density ρ_{c}.

To compute the temporal evolution of the angular velocity vector $\boldsymbol{\omega}$ with respect to the body-fixed Tisserand frame (Munk & MacDonald, 1960) we solve the LE with zero external torque,

$$-\boldsymbol{I}\cdot\frac{\mathrm{d}\boldsymbol{\omega}}{\mathrm{d}t} = \frac{\mathrm{d}\boldsymbol{I}}{\mathrm{d}t}\cdot\boldsymbol{\omega} + \boldsymbol{\omega}\times(\boldsymbol{I}\cdot\boldsymbol{\omega}), \tag{2.27}$$

where $\boldsymbol{I}$ is the time-dependent tensor of inertia. Equations (2.17) – (2.26) are coupled with eq. (2.27) both through the displacement field $\boldsymbol{u}$, which is needed to compute the inertia tensor $\boldsymbol{I}$, and through the centrifugal potential Ψ, which depends on the angular velocity vector $\boldsymbol{\omega}$.

2.2.3 Numerical implementation

The LE is a set of ordinary differential equations for three unknown components of vector $\boldsymbol{\omega}$ as functions of time. It can be rewritten as

$$\frac{\mathrm{d}\boldsymbol{\omega}}{\mathrm{d}t} = \mathcal{F}(\boldsymbol{I},\boldsymbol{\omega})\,, \tag{2.28}$$

where

$$\mathcal{F} = -\boldsymbol{I}^{-1}\cdot\left(\frac{\mathrm{d}\boldsymbol{I}}{\mathrm{d}t}\cdot\boldsymbol{\omega} + \boldsymbol{\omega}\times(\boldsymbol{I}\cdot\boldsymbol{\omega})\right). \tag{2.29}$$

Equation (2.28) is solved numerically using the fifth order accurate Adams-Bashforth multistep method with a time step of 10^{-3} yr. Each evaluation of $\mathcal{F}$ requires the calculation of the tensor of inertia $\boldsymbol{I}$ and its time derivative. The perturbation of the tensor of inertia is computed by MacCullagh's formula from the gravitational potential Φ and the reference density profile ρ_0 (e.g. Patočka, 2013, eqs 2.12),

$$\boldsymbol{I} = I_0\,\mathcal{I} + \sqrt{\frac{5}{\pi}}\,\frac{a^3}{6\,G}\left[\begin{pmatrix} -\Phi_{20} & 0 & 0\\ 0 & -\Phi_{20} & 0\\ 0 & 0 & 2\Phi_{20}\end{pmatrix} - \sqrt{6}\begin{pmatrix} -\mathrm{Re}\,\Phi_{22} & \mathrm{Im}\,\Phi_{22} & \mathrm{Re}\,\Phi_{21}\\ \mathrm{Im}\,\Phi_{22} & \mathrm{Re}\,\Phi_{22} & -\mathrm{Im}\,\Phi_{21}\\ \mathrm{Re}\,\Phi_{21} & -\mathrm{Im}\,\Phi_{21} & 0\end{pmatrix}\right]. \tag{2.30}$$

Here $I_0 := \frac{8}{3}\pi \int_0^a r^4 \rho_0 \mathrm{d}r$, $\mathcal{I}$ is the identity tensor, and $\Phi_{\ell m}$ are the coefficients of the spherical harmonic expansion of potential Φ,

$$\Phi(r, \vartheta, \varphi) = \sum_{\ell=0}^{\ell_{\max}} \sum_{m=-\ell}^{\ell} \Phi_{\ell m}(r) Y_{\ell m}(\vartheta, \varphi)\,, \tag{2.31}$$

where $Y_{\ell m}$ are the fully normalized spherical harmonics of degree ℓ and order m (e.g. Jones, 1985), and $\ell_{\max}$ is the cut-off degree. The potential Φ depends on the deformation of the body and we describe its calculation in the next paragraph. The term $\mathrm{d}\boldsymbol{I}/\mathrm{d}t$ is then computed numerically using the second order accurate mid-point finite difference scheme. The spectral algorithm for the numerical solution of eqs (2.17) – (2.26) for a given centrifugal potential Ψ is outlined in Tobie et al. (2008), identities needed to construct the matrix of the discretized problem are summarized in the appendix to Golle et al. (2012).

The potential Φ depends on $\boldsymbol{u}$ and vice versa. It is computed iteratively by expanding the integral (2.23) into a spherical harmonics series, while condensing topographies into surface mass densities (see eq. 35 in Choblet et al., 2007):

$$\begin{aligned}\Phi_{\ell m}(r) = \frac{-4\pi G r}{2\ell+1} \Bigg(& [\rho_0]_b \, u_{r,\ell m}(b) \left(\frac{b}{r}\right)^{\ell+2} + [\rho_0]_a \, u_{r,\ell m}(a) \left(\frac{r}{a}\right)^{\ell-1} \\ & - \int_b^r \left(\frac{r'}{r}\right)^{\ell+2} u_{r,\ell m}(r') \frac{\mathrm{d}\rho_0}{\mathrm{d}r'} \, \mathrm{d}r' - \int_r^a \left(\frac{r}{r'}\right)^{\ell-1} u_{r,\ell m}(r') \frac{\mathrm{d}\rho_0}{\mathrm{d}r'} \, \mathrm{d}r' \Bigg)\,,\end{aligned} \tag{2.32}$$

where we substituted for $\delta\rho$ from eq. (2.22) on the second line of eq. (2.32). The discretization in the radial direction is performed by the finite difference method on a staggered grid with constant spacing (e.g. Gerya & Yuen, 2003). Our approach differs from the algorithm described in Tobie et al. (2008) by employing a higher order Crank-Nicholson integration scheme for evaluating the time integral in eq. (2.19).

The accuracy of the numerical method used to solve the governing equations (2.17) - (2.26) was carefully tested against the traditional Lagrangian solution. Figure 1 shows the relative difference between the loading and tidal degree 2 Love numbers k_e^L, k_e^T, k_f^L and k_f^T, computed numerically using the method described above, and those computed semi-analytically by Spada et al. (2011) for a viscoelastic Earth model M3-L70-V01 (for description of the model, see table 3 therein). The difference is plotted as a function of the radial resolution considered in the numerical solution in which the density profile is approximated by a continuous piecewise linear function. Inspection of Fig. 1 shows that the relative error of the numerical method converges to zero with increasing resolution, decreasing below 10^{-4} when the number of equally spaced radial nodes is larger than 5000. The error does not decrease monotonically because it depends on how well the equidistant discretization matches the positions of the density interfaces. In section 2.2.4.4, we will use 460 radial grid nodes for which the error

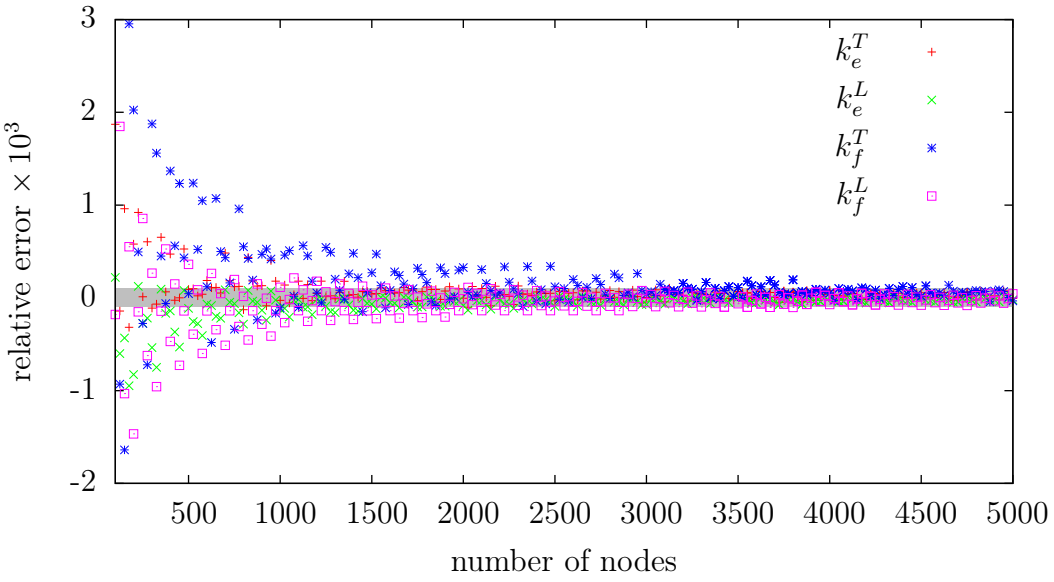

Figure 2.2: Relative error of the numerically computed tidal and loading degree 2 Love numbers k_e^T, k_f^T, k_e^L and k_f^L relative to the semi-analytically computed values by Spada et al. (2011). The subscript e denotes the instantaneous response and f is the $t\to\infty$ "fluid" limit. The shadowed region marks the domain where the relative error is smaller than 10^{-4}.

in determining the Love numbers is less than 10^{-4}. The number of radial grid nodes could be significantly smaller if we used a variable grid spacing.

Besides the computation of the Love numbers, we have also reproduced the benchmark example in Spada et al. (2011), where model M3-L70-V01 is loaded with a spherical ice cap (Spada et al., 2011, table 4), centred at the colatitude $\theta_c = 25°$ and the longitude $\lambda_c = 75°$. Our solution consists of two steps. In the first one, the model M3-L70-V01 is rotated at a constant angular velocity $\omega_0 = [0, 0, 7.292115] \times 10^{-5}\,\mathrm{s}^{-1}$ until it reaches hydrostatic equilibrium. Numerically we achieve this by integrating eqs (2.17) – (2.26) with the prescribed $\boldsymbol{\omega}_0$ and $\sigma^L \equiv 0$ over a period of 200 Myr (similar procedure was used to obtain the fluid Love numbers in Fig. 1). We will denote the hydrostatic values of the polar and equatorial moments of inertia by C and A respectively ($C{=}I_{33}^f$ and $A{=}I_{11}^f{=}I_{22}^f$). Then, at time which we formally mark as $t{=}0$, the body is suddenly loaded with a spherical ice cap. The loading instantaneously shifts the figure axis, and we adjust the vertical component of $\boldsymbol{\omega}(t{=}0)$, so that the total angular momentum is preserved in first approximation ($\boldsymbol{\omega} = \boldsymbol{\omega}_0(1 - c_{33}/C)$, where c_{33} is the change of polar moment of inertia due to the loading). The further evolution of the tensor of inertia, which in turn determines the evolution of $\boldsymbol{\omega}(t)$, is governed by both the viscoelastic relaxation under the load and the viscoelastic readjustment of the rotational bulge in response to the induced PM. For clarity of comparison with other studies, we introduce two quantities characterizing the PM – the PM

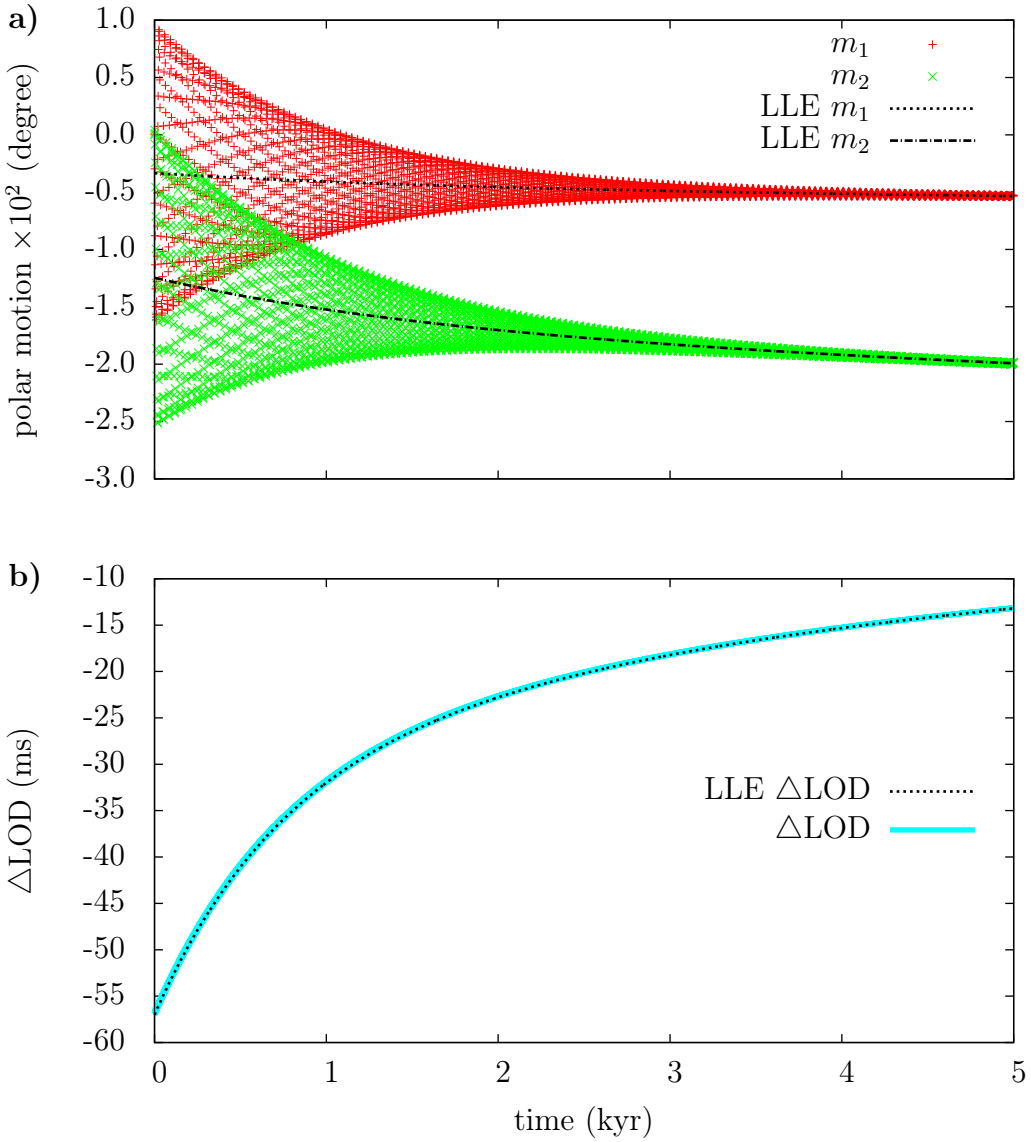

Figure 2.3: a) Polar motion induced by loading the Earth with a spherical ice cap. The coloured lines show the solution obtained by the method described in this study while the dashed black lines show the linearized solution computed in the Laplace domain and omitting the free wobble (Martinec & Hagedoorn, 2014). b) Variation of ΔLOD obtained for the same loading (blue line – our solution, dashed line – linearized solution).

vector $\boldsymbol{m}$ and the LOD variation ΔLOD:

$$\boldsymbol{\omega}(t) = \boldsymbol{\omega}_0 + |\boldsymbol{\omega}_0|\boldsymbol{m}(t)\,, \quad \Delta\mathrm{LOD}(t) = \frac{c_{33}(t)}{C}\frac{2\pi}{|\boldsymbol{\omega}_0|}\,, \tag{2.33}$$

where $c_{33}(t)$ is the time variation of I_{33} (polar moment of inertia) in response to the loading.

In Fig. 2a, we compare the PM components m_1 and m_2 computed by our method (coloured points) with those obtained using the traditional Laplace domain approach and the LLE (dashed lines, adopted from Martinec & Hagedoorn (2014)). Since our solution includes the wobbling while the LLE solution by Martinec & Hagedoorn (2014) gives only the mean position of the rotation axis, the two solutions are very different in the beginning, but they match each other once the wobbling is damped. This confirms that our code gives correct results on long time scales (i.e. greater than the damping time of Chandler wobble), and conversely, that neither the wobbling nor the linearization influences the long term evolution of the PM. A good agreement is also found for ΔLOD (Fig. 2b) where the relative difference between the two solutions is smaller than 1%.

The study by Spada et al. (2011) provides a valuable benchmark for validation of different numerical techniques to compute the PM. Nevertheless, there are two things that are worth noting because they are not explained in the original paper in sufficient details. First, in fig. 13(c) in Spada et al. (2011), the variation ΔLOD induced by the load is plotted as a positive quantity. However, since the load is imposed close to the north pole and the total mass of the Earth is conserved, the loading reduces the polar moment of inertia and the variation ΔLOD is actually negative. Second, the hydrostatic values C and A must be corrected to reproduce the benchmark results. The ΔLOD curve (Fig. 2.3b) is sensitive to the value of C, which has to be 8.0394×10^{37} kg m^2 to match the benchmark (i.e. the value given in table 1 of Spada et al. (2011)). However, to match the benchmarked PM solution (Fig. 2.3a), which is sensitive to the difference $C-A$, this difference has to be 2.6947×10^{35} kg m^2. This value corresponds to model M3-L70-V01 in the hydrostatic limit, and not to the value of $C-A$ derived from table 1 in Spada et al. (2011). Numerically we proceeded by adding a diagonal correction to our tensor of inertia, $\boldsymbol{I}^c(t{\geq}0) = \boldsymbol{I}(t) + \gamma\mathcal{I}$, where $\mathcal{I}$ is identity tensor and $\boldsymbol{I}^c$ is the corrected tensor of inertia used in our simulations. The correction γ is given as $(8.0394 - 8.17848) \times 10^{37}$ kg m^2, with 8.17848×10^{37} kg m^2 being the hydrostatic polar moment of inertia of model M3-L70-V01. We believe this information can be helpful for the future users of the benchmark.

2.2.4 Energy balance of a rotating Earth

The conservation of energy for a rotating self-gravitating viscoelastic body can be expressed as

$$E_{\rm rot} + E_{\rm el} + E_{\rm diss} + E_{\rm grav} = \text{const}\,, \tag{2.34}$$

where the terms on the left-hand side are the rotational, elastic, dissipative and gravitational energies, respectively. The kinetic energy associated with the rate of deformation is not considered, since the inertia term in the equation of motion (2.17) is neglected. The rotational energy $E_{\rm rot}$ can be computed using the standard formula

$$E_{\rm rot} = \frac{1}{2}\boldsymbol{\omega}\cdot\boldsymbol{I}\cdot\boldsymbol{\omega}. \tag{2.35}$$

The elastic energy $E_{\rm el}$ stored in the body and the viscous dissipation rate $\dot{E}_{\rm diss}$ can be expressed as (cf. Joseph, 2013, p. 50)

$$E_{\rm el} = \int_{v(t)} \frac{\boldsymbol{\tau}^d : \boldsymbol{\tau}^d}{4\mu}\,{\rm d}v \cong \int_{{\rm S}_a-{\rm S}_b} \frac{\boldsymbol{\tau}^d : \boldsymbol{\tau}^d}{4\mu}\,{\rm d}v\,, \tag{2.36}$$

$$\dot{E}_{\rm diss} = \int_{v(t)} \frac{\boldsymbol{\tau}^d : \boldsymbol{\tau}^d}{2\eta}\,{\rm d}v \cong \int_{{\rm S}_a-{\rm S}_b} \frac{\boldsymbol{\tau}^d : \boldsymbol{\tau}^d}{2\eta}\,{\rm d}v\,, \tag{2.37}$$

where $\boldsymbol{\tau}^d : \boldsymbol{\tau}^d \equiv \tau^d_{ij}\,\tau^d_{ij}$ in Cartesian components and ${\rm S}_a - {\rm S}_b$ denotes the spherical shell of outer radius a and inner radius b. The integration over the core is omitted since the core is assumed to be filled with inviscid liquid. Finally, the gravitational potential energy is given by

$$E_{\rm grav} = \frac{1}{2}\int_{v(t)} \rho\,(V_0 + \Phi)\,{\rm d}v\,. \tag{2.38}$$

2.2.4.1 Alternative formula for the gravitational energy

The computation of the gravitational energy is a delicate exercise which requires a careful evaluation of topographic and volumetric contributions to integral (2.38). In this section we derive a formula for the gravitational energy which is easy to implement and, as we will demonstrate in section 2.2.4.4, it is sufficiently accurate if the deformation is small. We first derive the formula for a model with a finite number of layers of constant densities, and then we extend it to a model with a continuous density profile. For the derivation we will assume that the surface load density $\sigma^{\rm L}$ is equal to zero. For a non-zero surface load density the problem can be converted into a problem with zero surface load density by using a modified radial displacement $u_r^{\rm mod}(a) = u_r(a) + \sigma^{\rm L}/[\rho_0]_a$.

For the sake of clarity of exposition, we consider a multilayer (N-layer) sphere. The N-layered sphere is composed of N spheres ${\rm S}_i$ with radii r_i, $i = 1, 2, ...N$, where $r_1 = a$ and $r_N = b$ are respectively the radii of the outer and inner boundary

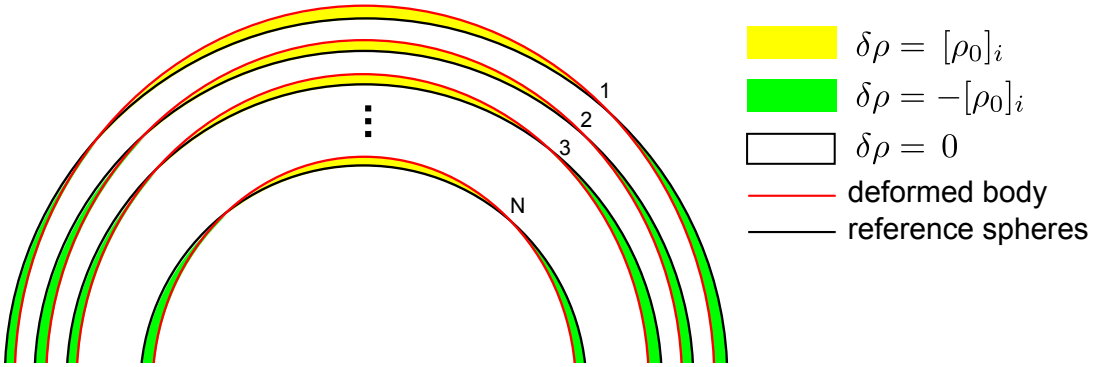

Figure 2.4: Deformation of N-layer sphere. Black lines show boundaries of the reference spherical shells with constant densities, red lines show the interfaces of the deformed body. In regions where the deformation produces a positive topography, the Eulerian density increment is equal to $[\rho_0]_i$, $i=1,2,...,N$, while in regions where the topography is negative, the density increment is equal to $-[\rho_0]_i$.

of the spherical shell considered in Section 2. The density $\rho_0(r)$ of the sphere is a piecewise constant function with density jumps $[\rho_0]_i$ at radii r_i (taken positive if the density increases with depth). When the body is deformed, each sphere S_i transforms into an aspherical object v_i and the density changes by

$$\delta\rho(\boldsymbol{r},t) = \rho_0(|\boldsymbol{r}-\boldsymbol{u}(\boldsymbol{r},t)|,t)-\rho_0(r) = \begin{cases} 0, & |r-r_i|\geq|u_r(\boldsymbol{r},t)| \quad \forall i \in \{1,2,\ldots,N\} \\ [\rho_0]_i, & u_r(\boldsymbol{r},t)>0 \quad \wedge \quad |r-r_i|<|u_r(\boldsymbol{r},t)| \\ -[\rho_0]_i, & u_r(\boldsymbol{r},t)<0 \quad \wedge \quad |r-r_i|<|u_r(\boldsymbol{r},t)| \end{cases} \tag{2.39}$$

where the three possibilities given on the right are illustrated in Fig. 3. The volume integral in eq. (2.38) can then be rewritten as

$$\int_{v(t)} \rho\,(V_0+\Phi)\,\mathrm{d}v = \sum_{i=1}^{N}[\rho_0]_i \int_{v_i} (V_0+\Phi)\,\mathrm{d}v. \tag{2.40}$$

On the right-hand side of this equation, we obtain a sum of N integrals over N homogeneous bodies which have no internal boundaries, occupy the volumes v_i and have the densities $[\rho_0]_i$. Each volume v_i can be expressed in terms of the spherical volume S_i and the volume h_i induced by the deformation (see the yellow and green regions in Fig. 3). The volume h_i is taken with a positive sign if it is above the sphere S_i (yellow regions) and with a negative sign if it is inside the sphere (green regions). The total volume of h_i at each interface (the sum of the yellow and green domain) is zero due to the incompressibility of the body. The gravitational energy can then be rewritten using S_i and h_i as follows:

$$E_{\mathrm{grav}} = \frac{1}{2}\sum_{i=1}^{N}[\rho_0]_i \int_{h_i} (V_0+\Phi)\,\mathrm{d}v + \frac{1}{2}\sum_{i=1}^{N}[\rho_0]_i \int_{\mathrm{S}_i} (V_0+\Phi)\,\mathrm{d}v. \tag{2.41}$$

The gravitational potential $V_0+\Phi$ can be split into N parts, $V_0+\Phi = \sum_{i=1}^{N}(V_0^i+\Phi^i)$, where V_0^i is the potential of the homogeneous sphere S_i of density

$[\rho_0]_i$ and Φ^i is the perturbation due to the aspherical shape of the i-th interface:

$$V_0^i(r) = -G[\rho_0]_i \int_{\mathrm{S}_i} \frac{1}{|\boldsymbol{r} - \boldsymbol{r}'|}\,\mathrm{d}v, \quad \Phi^i(\boldsymbol{r}) = -G[\rho_0]_i \int_{h_i} \frac{1}{|\boldsymbol{r} - \boldsymbol{r}'|}\,\mathrm{d}v. \tag{2.42}$$

In the following, we take advantage of the well-known fact that the gravitational energy of a body A in the gravitational field of a body B is the same as the gravitational energy of body B in the gravitational field of body A. By applying this general rule to eq. (2.42) we obtain the following relations:

$$[\rho_0]_i \int_{\mathrm{S}_i} \Phi^j\,\mathrm{d}v = [\rho_0]_j \int_{h_j} V_0^i\,\mathrm{d}v, \tag{2.43}$$

valid for any $i, j = 1, ..., N$. Using eq. (2.43) we can link the first and the second sum on the right-hand side of eq. (2.41):

$$\sum_{i=1}^{N}[\rho_0]_i \int_{\mathrm{S}_i} \Phi\,\mathrm{d}v = \sum_{i=1}^{N}[\rho_0]_i \int_{\mathrm{S}_i} \sum_{j=1}^{N} \Phi^j\,\mathrm{d}v = \sum_{j=1}^{N}[\rho_0]_j \int_{h_j} \sum_{i=1}^{N} V_0^i\,\mathrm{d}v = \sum_{i=1}^{N}[\rho_0]_i \int_{h_i} V_0\,\mathrm{d}v. \tag{2.44}$$

Substituting (2.44) into (2.41) gives the alternative formula for the gravitational energy E_{grav} of the body:

$$E_{\mathrm{grav}} = E_{\mathrm{grav}}^0 + \sum_{i=1}^{N} E_{\mathrm{grav}}^i, \tag{2.45}$$

where E_{grav}^0 is the gravitational energy of the undeformed N-layer sphere

$$E_{\mathrm{grav}}^0 = \frac{1}{2}\sum_{i=1}^{N}[\rho_0]_i \int_{\mathrm{S}_i} V_0\,\mathrm{d}v = 2\pi \int_0^a \rho_0(r) V_0(r) r^2\,\mathrm{d}r\,, \tag{2.46}$$

and

$$E_{\mathrm{grav}}^i = [\rho_0]_i \int_{h_i} \left(V_0 + \frac{1}{2}\Phi\right)\mathrm{d}v\,. \tag{2.47}$$

Since the deformation is small, the topography of the ith interface (defined here as the deviation from a sphere) can be approximated by the radial component of the displacement vector at the interface. Equation (2.47) then takes the form

$$E_{\mathrm{grav}}^i \cong [\rho_0]_i \int_{\partial \mathrm{S}_i} \int_{r_i}^{r_i + u_r(r_i,\vartheta,\varphi)} \left(V_0 + \frac{1}{2}\Phi\right)\mathrm{d}r\,\mathrm{d}s\,, \tag{2.48}$$

where $\partial \mathrm{S}_i$ denotes the surface of the sphere of radius r_i, $\mathrm{d}s$ is the element of $\partial \mathrm{S}_i$, and ϑ and φ are the spherical angular coordinates. The integral in eq. (2.48) can be simplified by expanding V_0 in a Taylor series and setting $\Phi(r, \vartheta, \varphi) \cong$

$\Phi(r_i, \vartheta, \varphi)$:

$$E^i_{\text{grav}} \cong [\rho_0]_i \int_{\partial \mathrm{S}_i} \int_{r_i}^{r_i + u_r(r_i,\vartheta,\varphi)} \left(V_0(r_i) + g_0(r_i)(r - r_i) + \frac{1}{2}\Phi(r_i, \vartheta, \varphi) \right) \mathrm{d}r \, \mathrm{d}s \,. \tag{2.49}$$

Integration of eq. (2.49) over the radius gives

$$E^i_{\text{grav}} \cong \frac{1}{2}[\rho_0]_i \int_{\partial \mathrm{S}_i} \left(g_0 u_r^2 + \Phi u_r \right) \, \mathrm{d}s \,, \tag{2.50}$$

where we used that $\int_{\partial \mathrm{S}_i} u_r \mathrm{d}s = 0$ for an incompressible body.

The surface integral in eq. (2.50) can be easily evaluated in spectral domain. Representing quantities u_r and Φ in terms of spherical harmonic expansions, eq. (2.31), and invoking the orthonormality of the spherical harmonic basis $\{Y_{\ell m}\}$, we obtain

$$E_{\text{grav}} \cong E^0_{\text{grav}} + \frac{1}{2} \sum_{i=1}^{N} [\rho_0]_i \, r_i^2 \sum_{\ell=0}^{\ell_{\max}} \sum_{m=-\ell}^{\ell} \left(g_0(r_i) |u_{r,\ell m}(r_i)|^2 + u_{r,\ell m}(r_i) \Phi^*_{\ell m}(r_i) \right) , \tag{2.51}$$

where * denotes complex conjugation. The rotational potential is described by spherical harmonics of degrees 0 and 2. Since degree 0 has no effect on the deformation of an incompressible body, we will only consider the terms with $\ell = 2$ and $|m| \leq 2$.

The formula (2.51), derived for a layered density model, can be generalized to the case of a continuous density profile. Replacing the density jumps $[\rho_0]_i$ in eq. (2.47) by $(-\mathrm{d}\rho_0(r)/\mathrm{d}r)\,\mathrm{d}r$ and the sum in eq. (2.45) by an integral, and following the analogous procedure as above, we get the formula

$$\begin{aligned} E_{\text{grav}} \cong E^0_{\text{grav}} + \frac{1}{2} \Bigg(& [\rho_0]_a \int_{\partial \mathrm{S}_a} \left(g_0 u_r^2 + u_r \Phi \right) \mathrm{d}s + [\rho_0]_b \int_{\partial \mathrm{S}_b} \left(g_0 u_r^2 + u_r \Phi \right) \mathrm{d}s \\ & - \int_b^a \frac{\mathrm{d}\rho_0}{\mathrm{d}r} \int_{\partial \mathrm{S}_r} \left(g_0 u_r^2 + u_r \Phi \right) \mathrm{d}s \, \mathrm{d}r \Bigg) , \end{aligned} \tag{2.52}$$

where $\partial \mathrm{S}_r$ denotes the surface of the sphere with radius r.

Equation (2.52) allows us to compute the gravitational energy using the quantities obtained by solving the governing equations in a regular computational domain $\mathrm{S}_a - \mathrm{S}_b$, that is, in the spherical shell of outer radius a and inner radius b. The radial displacement u_r needed to evaluate the integrals in eq. (2.52) is obtained as the solution to eqs (2.17) – (2.19), (2.25) and (2.26), with the gravitational potential Φ being computed iteratively from ρ_0 and u_r via eq. (2.32), that is, using the traditional "condensation" method (e.g. Choblet et al., 2007). If the deformation is small, the Eulerian and Lagrangian approaches give the same displacement (see Fig. 2.8b in section 2.2.4.4). Therefore, the formula for the gravitational energy derived here can be used regardless which of the approaches is chosen to evaluate the deformation.

Note, however, that a direct application of the condensation method to the energy integral (2.38) leads to an incorrect result. In order to demonstrate this, we will assume, for simplicity, that the density ρ is constant throughout the body. Equation (2.38) can then be expressed as the sum of two integrals over the sphere S_a and two integrals over the domain h_a representing the irregular shape of the body ($h_a \equiv h_1$ in the notation used above):

$$E_{\mathrm{grav}} = \frac{\rho}{2}\left(\int_{\mathrm{S}_a} V_0 \,\mathrm{d}v + \int_{\mathrm{S}_a} \Phi \,\mathrm{d}v + \int_{h_a} V_0 \,\mathrm{d}v + \int_{h_a} \Phi \,\mathrm{d}v\right) . \tag{2.53}$$

The first integral corresponds to E^0_{grav} (cf. eq. 2.46). The second integral can be evaluated by expanding Φ into spherical harmonics. Due to the orthogonality of the spherical harmonic functions, only Φ_{00} has non-zero contribution to the integral. In the simplified formula (2.32), which is based on the condensation technique, there is no coupling among coefficients of different degrees and orders. According to that formula, Φ_{00} is a function of $u_{r,00}$ only, and, since $u_{r,00}$ is zero for an incompressible body, the second integral vanishes. Condensing the volumetric density ρ into surface mass density $\rho u_r(a)$ in the last two integrals then gives

$$E_{\mathrm{grav}} = E^0_{\mathrm{grav}} + \frac{\rho}{2}\left(V_0(a)\int_{\partial \mathrm{S}_a} u_r \,\mathrm{d}s + \int_{\partial \mathrm{S}_a} \Phi u_r \,\mathrm{d}s\right) = E^0_{\mathrm{grav}} + \frac{\rho}{2}\int_{\partial \mathrm{S}_a} \Phi u_r \,\mathrm{d}s\,, \tag{2.54}$$

while the correct solution is (eq. 2.52 with $[\rho_0]_a = \rho$, $[\rho_0]_b = 0$ and $\mathrm{d}\rho_0/\mathrm{d}r = 0$)

$$E_{\mathrm{grav}} = E^0_{\mathrm{grav}} + \frac{\rho}{2}\int_{\partial \mathrm{S}_a} \left(g_0 u_r^2 + \Phi u_r\right) \,\mathrm{d}s\,. \tag{2.55}$$

In other words, the second and third integrals in eq. (2.53) have been incorrectly evaluated as zero, giving the wrong solution (2.54). In this section we have shown that both integrals are in fact non-zero, they are equally important, and together yield the contribution with $g_0 u_r^2$ in the integrand. The advantage of our formula for the gravitational energy is that it does not require the computation of Φ_{00}, which is a non-zero quantity inside the sphere S_a if evaluated exactly.

In Appendix 2.A we derive other formulae that can be helpful in assessing the energy balance of a deforming body, based on evaluating the power of individual forces in the equation of motion (2.17).

2.2.4.2 Energy balance of GIA for a non-rotating Earth

We first evaluate the energy balance for a non-rotating Earth with internal structure given by model M3-L70-V01, loaded at time t=0 with a spherical ice cap as described in Spada et al. (2011). In this case, the body has a perfectly spherical shape prior to the loading ($\rho = \rho_0$, $\Phi = \Psi = 0$, $\boldsymbol{u} = 0$, $\boldsymbol{\tau}^d = 0$). No elastic energy is stored and the gravitational energy reaches the absolute minimum. Since the total mass of the imposed surface load is zero, the loading is associated

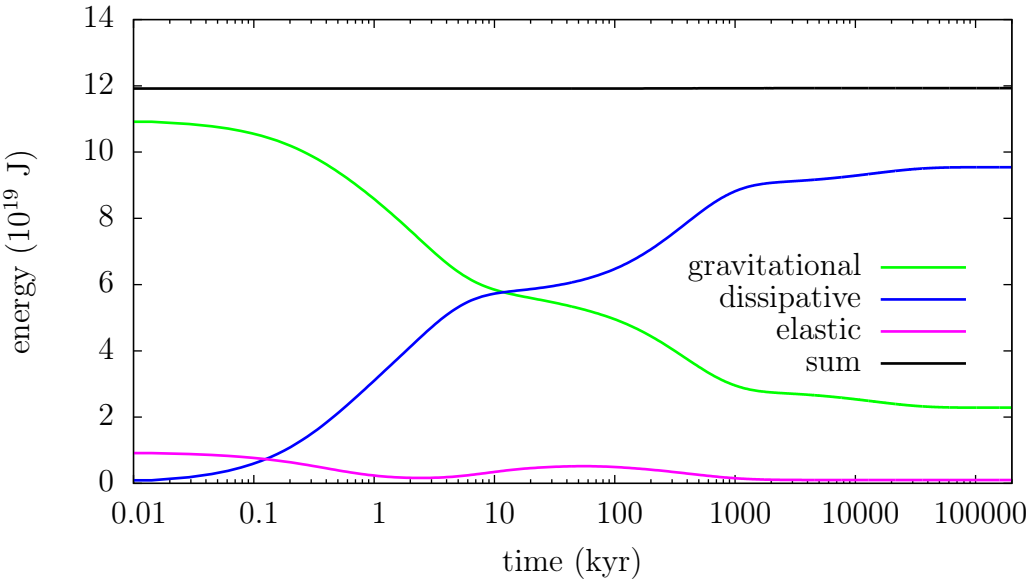

Figure 2.5: Time evolution of the gravitational (green), dissipative (blue) and elastic (magenta) energy for non-rotating Earth model M3-L70-V01, loaded with a spherical ice cap (for details, see Spada et al., 2011). The variation of the gravitational energy is plotted with respect to the gravitational energy E^0_{grav} of the undeformed body. The sum of the three energies is shown by a black line.

with a redistribution of mass at the surface of the body. This, although partially compensated by the instantaneous elastic deformation of the model due to the loading, results in shape changes and thus in an increase of the gravitational energy (Fig. 2.5, green curve). At the same time the elastic energy (plotted in magenta) rises to a value that is about ten times smaller than the increase in the gravitational energy. With increasing time, the system returns to equilibrium – the gravitational energy decreases and is dissipated in heat (blue curve in Fig. 2.5).

Since the uppermost layer in model M3-L70-V01 is purely elastic, the final equilibrium state is non-hydrostatic and the values of the elastic and gravitational energies at time $t \to \infty$ are non-zero. The elastic energy does not decrease monotonically, showing a local maximum at $t \cong 50$ kyr. This maximum is a consequence of a complex interplay between the elastic lithosphere, in which the stored elastic energy monotonically increases in time, and the deeper mantle layers, where the elastic energy behaves non-monotonically, until it finally returns to zero in the hydrostatic equilibrium. During the whole evolution, the sum of the three considered energies is constant (black line in Fig. 2.5).

2.2.4.3 Energy balance of a damped Chandler wobble

We consider the Earth model M3-L70-V01 rotating with constant angular velocity $\boldsymbol{\omega}_0 = [0, 0, 7.292115] \times 10^{-5}\,\text{s}^{-1}$. The Earth is initially in equilibrium and has an oblate spheroidal shape. At time t=0, the direction of the rotational vector is suddenly changed so that the angle between the figure axis and the rotational

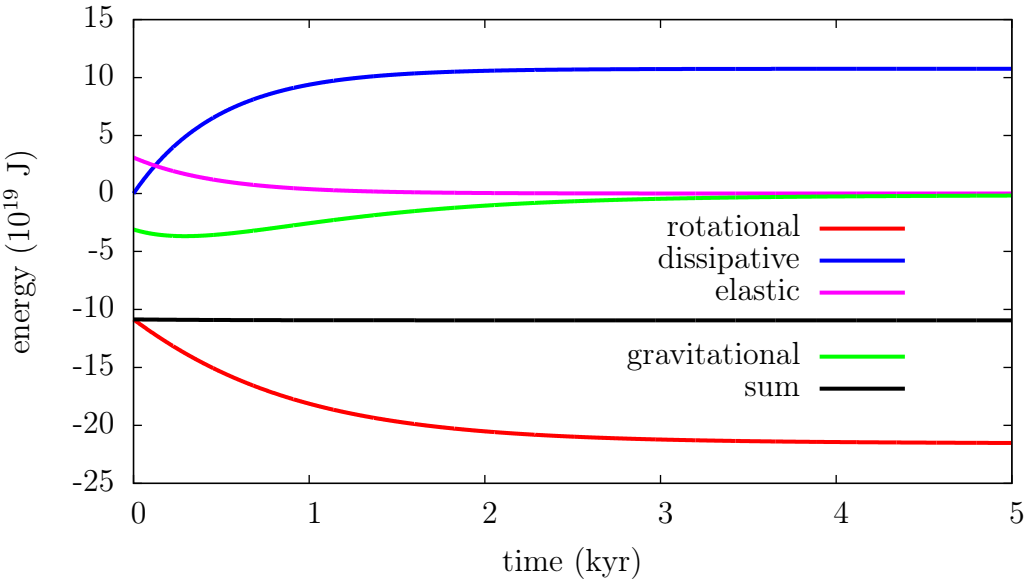

Figure 2.6: Time evolution of different types of energy for wobbling model M3-L70-V01. The variations of energy are plotted with respect to the initial equilibrium state in which the rotational vector is parallel to the main axis of the body. The wobble is induced by changing the direction of the rotational vector by 2.69×10^{-2} degrees at time t=0.

vector is 2.69×10^{-2} degrees, which is approximately the same as the angle by which figure axis is shifted in the benchmark example in Spada et al. (2011) – see Fig. 2.3a for comparison. This change induces a periodic motion ("wobble") of the axis of rotation, which is gradually damped due to dissipation. After a few thousands of years, the axis of rotation returns to its initial position, but the final rotational speed is smaller than the initial one since a part of the rotational energy is transformed to heat (note that the angular momentum is not conserved when shifting the axis at time t=0).

The time evolution of the individual types of energies associated with the above process is shown in Fig. 2.6. All energies are plotted with respect to the initial equilibrium state. In this state (corresponding to $t < 0$), the elastic energy is non-zero only in the uppermost, purely elastic layer. The abrupt change of the rotational vector at t=0 induces an instantaneous elastic deformation of the whole body (except the liquid core) and the total elastic energy increases. Since the deformation acts to reduce the flattening, both the gravitational and rotational energies decrease at t=0. The rotational energy (red curve in Fig. 2.6) further decreases with increasing time as it is dissipated through viscous deformation (blue curve). The variations in the gravitational and elastic energies (green and magenta curves, respectively) significantly contribute to the global energy budget only in the beginning of evolution. For $t \to \infty$, both curves converge to negative values which are close to zero, suggesting that the gravitational and elastic energies in the final equilibrium state are slightly smaller than those in the initial equilibrium state. This difference is associated with the change of flattening due

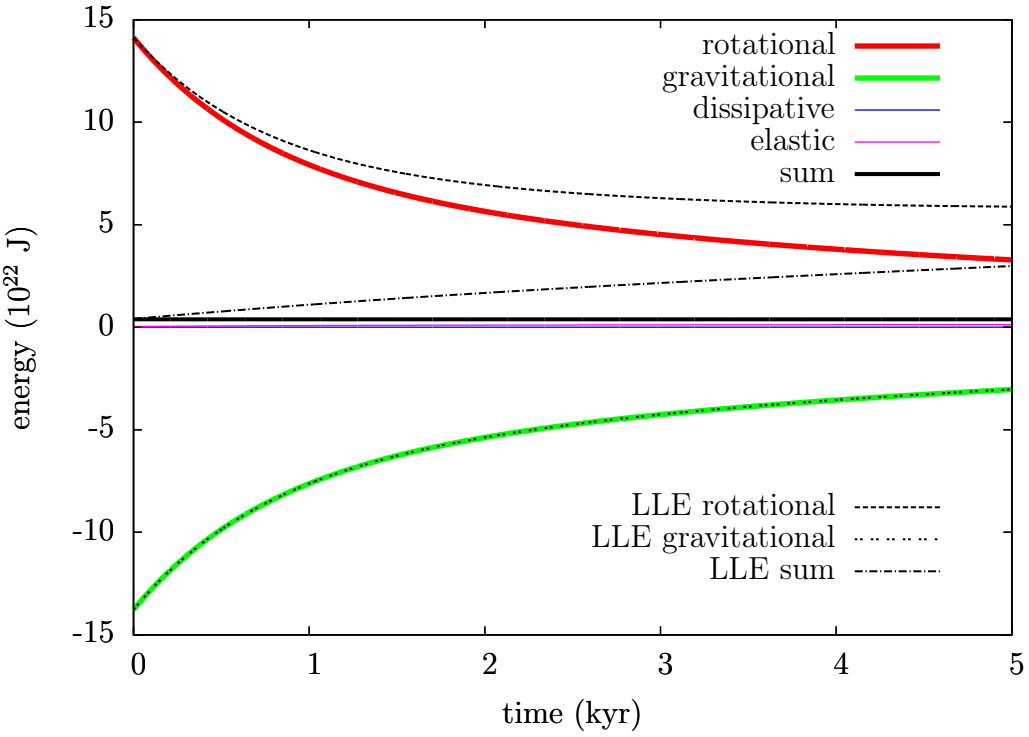

Figure 2.7: Time evolution of different types of energy for rotating model M3-L70-V01 loaded with an ice cap at t=0 (for details, see Spada et al., 2011). The variations of energy are plotted with respect to the initial equilibrium state in which the rotational vector is parallel to the main axis of the body. The results obtained using the NLE are represented by coloured lines while the LLE solution is plotted in black.

to the decrease in the rotational speed.

2.2.4.4 Energy balance of GIA for a rotating Earth

The setting of this numerical experiment corresponds to the benchmark case adopted from Spada et al. (2011), which was already discussed in section 2.2.3 (cf. Figs 2.2 and 2.3). The rotating Earth model M3-L70-V01, initially in equilibrium state, is suddenly loaded with an ice cap. The loading and the associated deformation induce a PM (Fig. 2.3a) and changes in the rotational speed (Fig. 2.3b), which are accompanied by large variations in the rotational and gravitational energy (Fig. 2.7, red and green curves, respectively). The amplitudes of these variations are of the order of $10^{22} - 10^{23}$ J and they are three orders of magnitude larger than the variations in the elastic (magenta) and dissipative (blue) energy (cf. also Figs 2.5 and 2.6). During the whole evolution, the sum of all energies is constant (full black line).

So far we have discussed the results computed using the NLE. In Fig. 2.7 the variations of the gravitational and rotational energy obtained using the LLE are shown by dashed and dotted black lines, respectively. While the curve for the gravitational energy coincides almost exactly with that obtained using the NLE, the accuracy in determining the rotational energy decreases with increasing time,

resulting in a relative error of almost 100% after 5 kyr. Consequently, the total energy of the system (dashed black line) is not conserved for the LLE solution.

As demonstrated in Fig. 7a, the large error in evaluating the rotational energy is associated with determining the component m_3, which is significantly larger than the value obtained using the NLE, in contrast to components m_1 and m_2, which are determined with high accuracy (see Fig. 2.3a). Figure 2.8b shows that the predicted degree 2 shape of the Earth does not depend on whether we use the NLE or LLE, suggesting that the displacement obtained using the LLE is only slightly affected by the error in m_3. This explains the good agreement obtained for the gravitational energy which is a function of the radial component of displacement (see eq. 2.52) and, unlike the rotational energy, does not depend directly on m_3.

Note that the difference between the NLE and LLE solution for m_3 is not related to the free wobble, as illustrated by the green line in Fig. 2.8a. The line represents a case in which the ice cap is being imposed only gradually onto the surface of the Earth, over the period of 5 yr, significantly reducing the amplitude of the induced wobble but leading to the same long term behaviour as for the instantaneous loading.

In the light of the results presented in section 2.2.3, the large error in component m_3 obtained using the LLE may be viewed as surprising. As demonstrated in Fig. 2.3b, both the NLE and LLE predict the same LOD variation ΔLOD given by eq. 2.33 (right), but m_3 computed as $m_3 = -c_{33}/C$ is still significantly affected by the neglect of the nonlinear terms in the LE (Fig. 7a). To explain this apparent paradox, we start from the formula (9.2.3) in Munk & MacDonald (1960)

$$\frac{\Delta\mathrm{LOD}}{\mathrm{LOD}} = -m_3 = \frac{c_{33}}{C}\,, \tag{2.56}$$

and we describe the simplifications that were used in its derivation. The first equality in eq. (2.56) can be derived by linearization of the exact formula for ΔLOD:

$$\frac{\Delta\mathrm{LOD}}{\mathrm{LOD}} = \frac{2\pi\omega^{-1} - 2\pi\omega_0^{-1}}{2\pi\omega_0^{-1}} = \frac{\omega_0 - \omega}{\omega} \cong \frac{\omega_0 - \omega}{\omega_0} = 1 - \sqrt{m_1^2 + m_2^2 + (1+m_3)^2}\,. \tag{2.57}$$

Using the binomial theorem and neglecting the higher-order terms, we obtain

$$\frac{\Delta\mathrm{LOD}}{\mathrm{LOD}} \cong -m_3 + \tfrac{1}{2}\left(m_1^2 + m_2^2 + m_3^2\right)\,, \tag{2.58}$$

which, after neglecting the quadratic terms, gives the first equality in eq. (2.56). The second equality in eq. (2.56) comes from the LLE for component m_3. In Appendix 2.B we derive the following higher-order approximation:

$$-m_3 + \frac{1}{2}(m_1^2 + m_2^2 + m_3^2) \cong \frac{c_{33}}{C}\,. \tag{2.59}$$

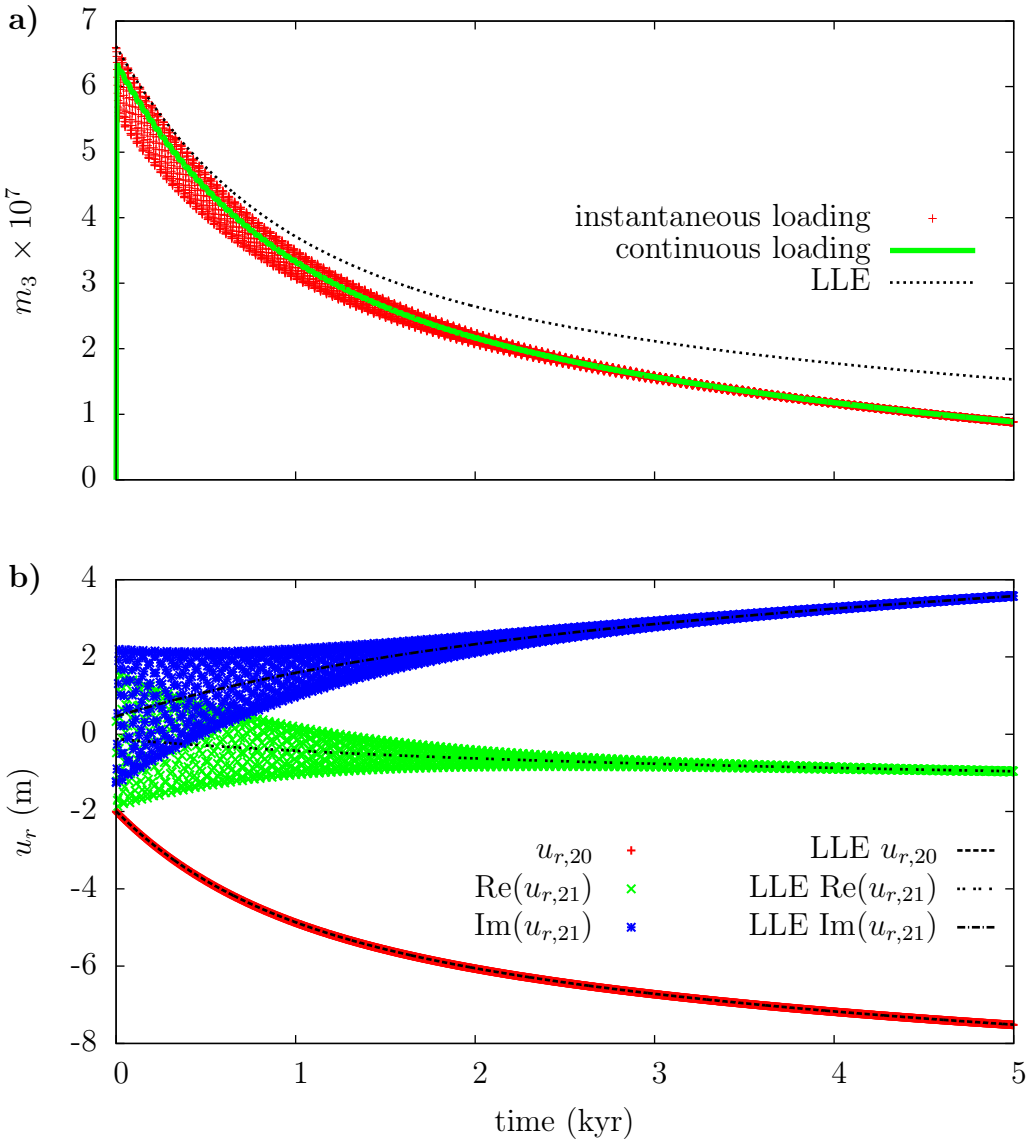

Figure 2.8: a) Time evolution of m_3 for the studied benchmark case (cf. Fig. 2.3). Red points depict our NLE solution, dashed line is the LLE solution. Green line shows our solution when the spherical ice cap is imposed on the surface of the Earth only gradually (over the period of 5 yr). b) Displacement components $u_{r,20}$ and $u_{r,21}$ relative to the hydrostatic equilibrium for the same case as above (continuous loading is omitted for clarity of the figure).

Combining eq. (2.59) with eq. (2.58) yields a more accurate version of the original equation (2.56):

$$\frac{\Delta \mathrm{LOD}}{\mathrm{LOD}} \cong -m_3 + \frac{1}{2}(m_1^2 + m_2^2 + m_3^2) \cong \frac{c_{33}}{C}\,. \tag{2.60}$$

The definition of ΔLOD in eq. (2.33) thus includes second-order accurate evaluation of the LOD variation, while the equation $m_3 = -c_{33}/C$ is only first-order accurate, which explains the disagreement between the LLE and NLE solutions in Fig. 2.8a.

The fact that the m_3 component of the rotation vector is affected by a large error does not invalidate the results of previous studies using the LLE solution. As demonstrated above, the traditional equation for $\triangle$LOD, eq. (2.33), used in these studies, is more accurate than the linearized equation for m_3 and it gives the same LOD variation as the NLE equation (Fig. 2.3b), provided that excursions of the rotation axis are small.

Our numerical tests (not presented in this paper) suggest that the shift of the rotation axis must be larger than 1 degree for the nonlinearity to significantly (by at least a few percent) affect the resulting PM and LOD. The ice cap considered here is rather small and, since the characteristic time of equatorial bulge readjustment is inversely proportional to the size of the load (Ricard et al., 1993), several Myr would be needed to shift the pole by 1 degree. If we considered an unrealistic, ten times larger ice cap, the equatorial bulge readjustment would occur faster and the linearized PM and LOD solutions would differ from the nonlinear one by few percent already after about 200 kyr.

2.2.4.5 Energy balance as a tool for testing GIA models

The rotational feedback in the equation of motion has not been considered in a number of papers dealing with modelling of GIA on the Earth (for details, see Introduction in Martinec & Hagedoorn, 2014). While such approximation is justifiable for the displacement component of degree 2 order 0 ($u_{r,20}$ has nearly identical evolution with and without the feedback), the displacement component of degree 2 and order 1 behaves in time completely differently for the two cases. A long term evolution of $u_{r,21}$ is governed by the balance between the viscoelastic relaxation of the model under the load and the viscoelastic readjustment of the equatorial bulge. For a homogeneous model, these two mechanisms perfectly cancel out each other for all times, as pointed out by Munk & MacDonald (1960), Section 6.4, and Wu & Peltier (1984). The effect of the rotational feedback has been recently discussed by Martinec & Hagedoorn (2014), who demonstrated that it may have a significant impact on the prediction of $u_{r,21}$ and sea level change. It should be emphasized that including the variations of the centrifugal potential into the field equations governing GIA-induced deformation of the Earth differs from including them into the gravity appearing in the sea level equation (i.e. the

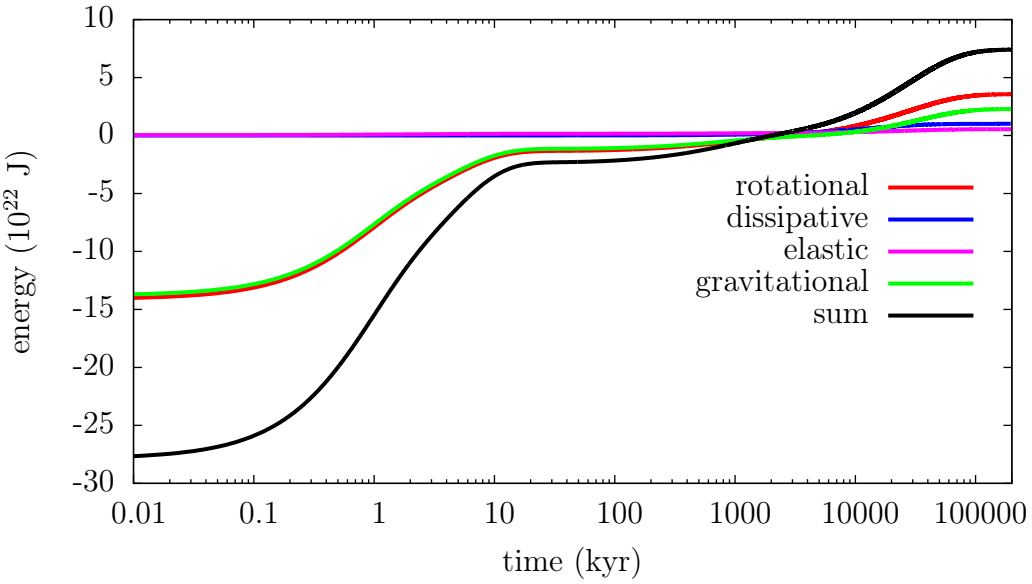

Figure 2.9: Time evolution of different types of energy for a rotating model M3-L70-V01 loaded with a spherical ice cap at t=0 (for details, see Spada et al., 2011). The rotation of the model is kept constant throughout the simulation.

rotational feedback on the sea level equation), which has already been addressed in the previous studies (e.g. Milne & Mitrovica, 1998; Peltier, 1998) and which is not a focus of our work.

Fig. 2.9 shows the time evolution of different types of energy when the rotation of the Earth is held constant, that is, the LE is not being solved at all. Fig. 2.10 compares the rotational and gravitational energies for the cases with and without the rotational feedback in the equation of motion, respectively. We can see that the gravitational energies do not differ significantly. This can be explained by the quadratic dependence of the gravitational energy on the radial component of the displacement (cf. eq. (2.51)). While the hydrostatic value of $u_{r,20}$ reaches thousands of metres, the hydrostatic value of $u_{r,21}$ is equal to zero. Since the deformation induced by the ice cap reaches only few metres (Fig. 2.8b), the change of the gravitational energy of the rotating body is dominated by the change of $u_{r,20}$. In addition, as discussed above, $u_{r,20}(t)$ is not affected by the rotational feedback significantly.

The rotational energies, on the other hand, differ significantly for the two cases. With the rotational feedback in the equation of motion, the rotational energy evolves in time with the opposite sign than the gravitational energy in order to conserve the total energy. Without considering the rotational feedback (i.e. $\boldsymbol{\omega}(t) = \boldsymbol{\omega}_0$), the rotational energy evolves in time similarly to the gravitational energy. This is because the increment of $(\boldsymbol{\omega}_0 \cdot \boldsymbol{I} \cdot \boldsymbol{\omega}_0)/2$ has, similarly to the change of the gravitational energy, a positive linear dependence on the change of $u_{r,20}$ (see MacCullagh's formula for c_{33} and insert for Φ_{20} from eq. (2.32)).

The detailed analysis of individual terms in the energy balance is given in Appendix A. Fig. 2.11 shows the results of such analysis for the two simulations

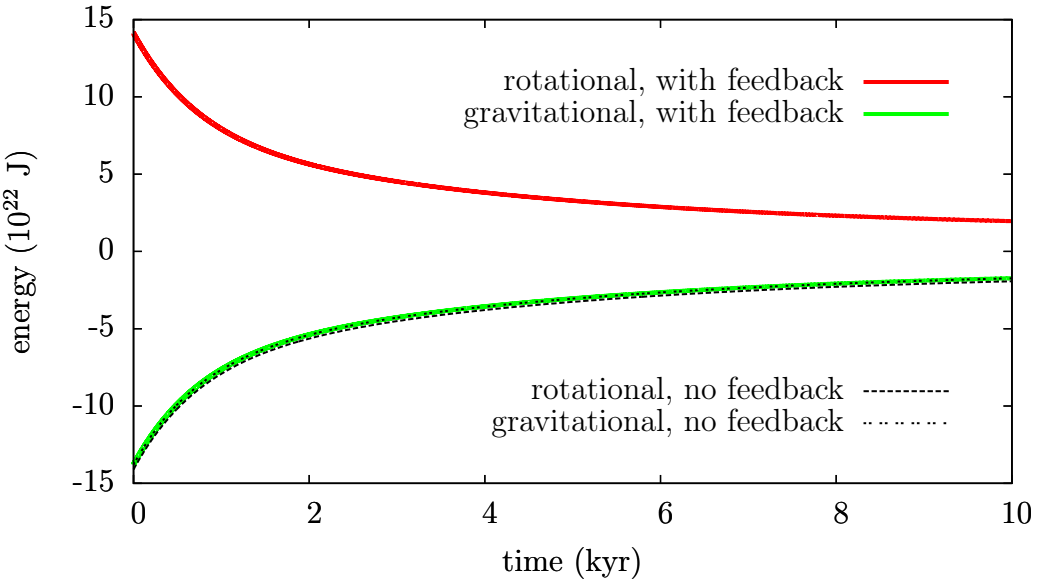

Figure 2.10: Comparison of time evolutions of the rotational and gravitational energies from Figures 2.7 and 2.9. The energies from Fig. 2.7 are in colour, dashed black lines show the curves from Fig. 2.9.

shown in Figs 2.7 and 2.9, for which the total energy of the Earth's model is not conserved. We can see that the energy imbalance is associated with the rotational energy, that is, the power of the centrifugal force is not equal to the rate of change of rotational energy.

Another example of the application of the energy analysis given in Appendix A is related to the NLE solution presented in Sections 2.2.3 and 2.2.4.4. We run a numerical experiment where the original time step of 1×10^{-3} yr is made coarser as 5×10^{-2} yr. The results are shown in Fig. 2.12a. Inspecting Fig. 2.12a we can see that not all the powers match the corresponding rates of energies. Again, it is the rotational energy that is not balanced. Hence, time step of 5×10^{-2} yr is too coarse in this case, which causes that the Liouville equation, but not eqs (1)-(3), is violated. In the parallel numerical experiment, the original spatial discretization of 460 radial nodes is reduced to 40 nodes only. Eqs (1)-(3) are now violated which is seen from the fact that the forces depending on the spatial derivatives of field variables do not match their corresponding energies.

We hope that such *a posteriori* diagnostic of numerical solutions may be of interest also in other applications. For instance, in the case where the LE is employed for determining the Q-factor of the Chandler wobble, as suggested by Nakada & Karato (2012), the solution is numerically very sensitive to time-stepping. An independent test of the solution could thus prove helpful.

2.2.5 Conclusions

In this paper, the temporal evolution of rotational, elastic, dissipative and gravitational energies is studied in the context of GIA. We have derived spectral

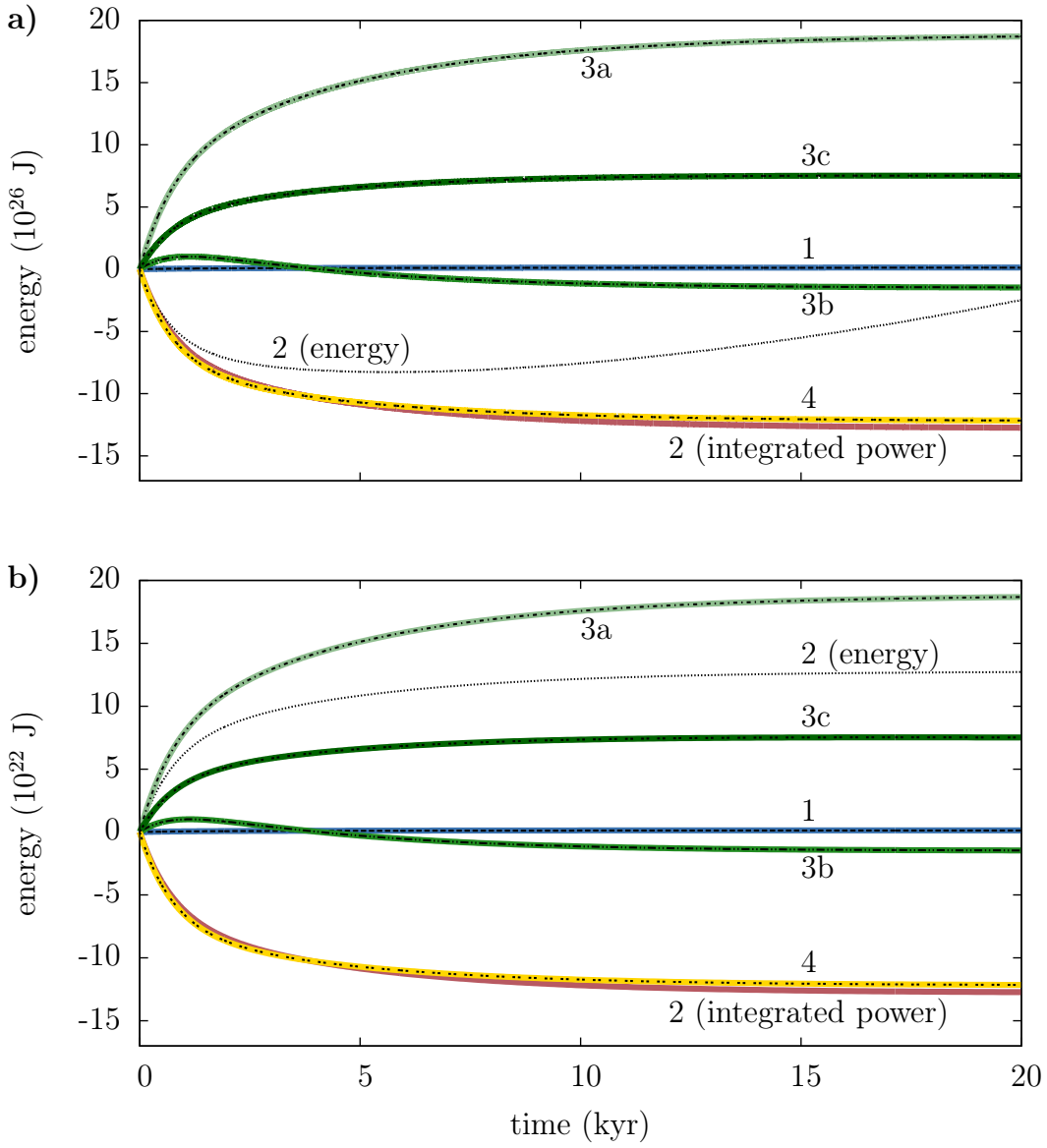

Figure 2.11: The energy integrals given in section 2.2.4 (black lines) and their equivalents obtained by integrating the rate of mechanical work over the computational domain and time (coloured lines). Two cases are considered: (a) the rotational feedback is computed using the linearized Liouville equation (cf. Fig. 2.7), and (b) the rotational feedback is completely omitted (cf. Fig. 2.9). The numbers have the following meaning: 1 - dissipated energy (dashed black and blue lines); 2 - rotational energy (dotted black and red lines); 3 and 4 - contributions to gravitational energy (dashed-dotted and green and yellow lines). For more details, see Appendix A and Fig. 2.13.

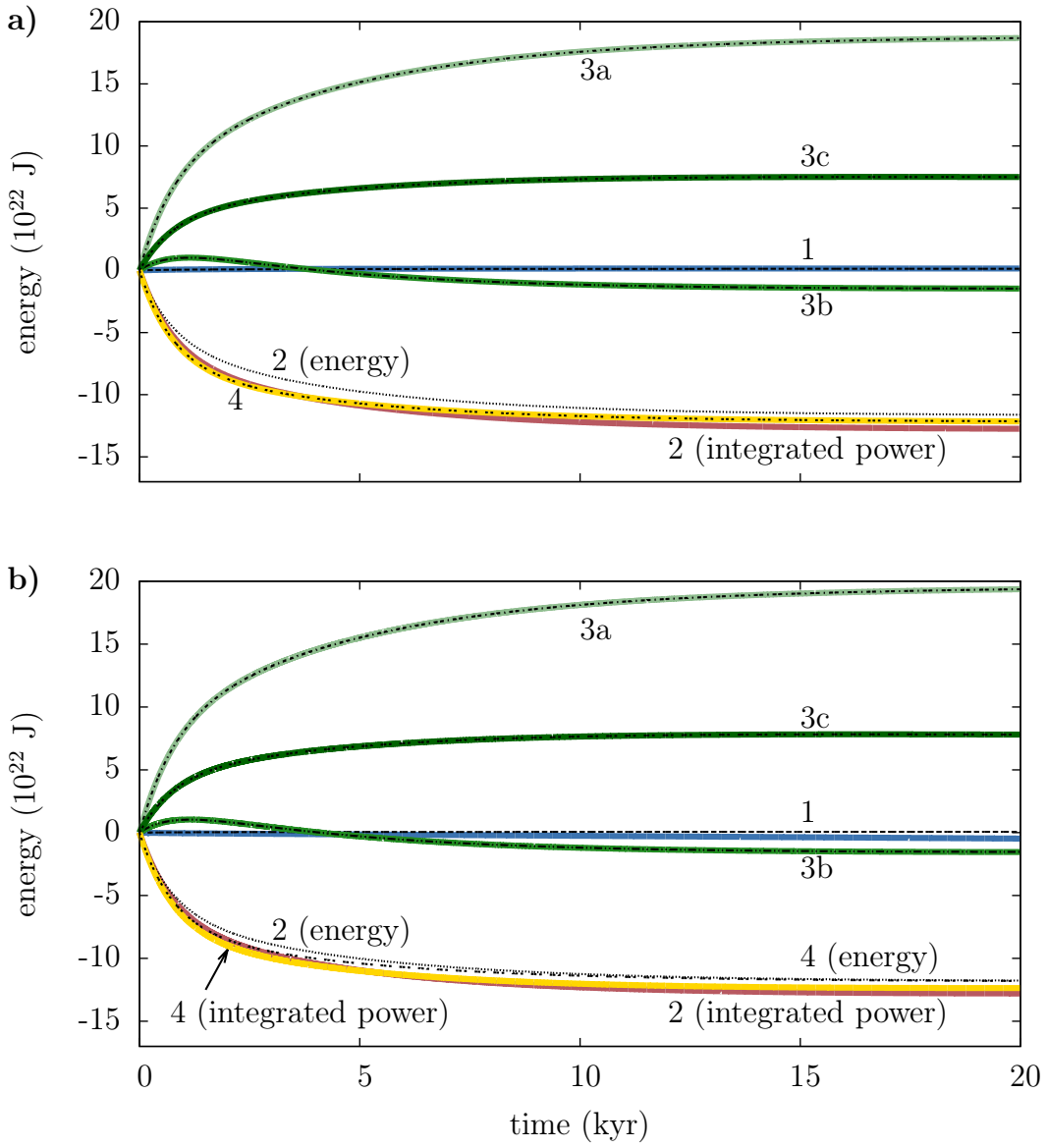

Figure 2.12: Panel (a) shows the case when the governing equations are solved using a too large time step, while panel (b) illustrates the effect of coarse radial discretization. The types of curves and the meaning of the numbers are the same as in Fig. 2.11.

formulae for computing the energies, overcoming the difficulty associated with the use of a simplified expression for the perturbation of gravitational potential. The energy evolution is then computed for several examples, demonstrating the importance of rotational and gravitational energies in the resulting balance. Viscous dissipation is proven relevant only for the damping of the Chandler wobble. By summing all energies for a rotating Earth loaded with a spherical ice cap, we show that the LLE is energetically inconsistent – the error resulting from an inaccurate evaluation of the m_3 component of rotation vector. Careful evaluation of the energy balance for a rotating Earth loaded with an ice cap shows that the omission of the rotational feedback in the momentum equation leads to a significant violation of the energy conservation law, with both rotational and gravitational energy increasing in time on a time scale typical of the Earth's glacial cycle. This finding underlines the importance of proper implementation of rotation variations in GIA modelling.

Throughout the study we strictly use the Eulerian formulation for computing the deformation of the planet, and solve the governing equations directly in time domain. The equivalence with the Lagrangian formulation and Laplace domain approach (normal mode theory) is demonstrated numerically by comparing the Love numbers. The evaluation of the mechanical work of individual forces considered in the Eulerian formulation provides a versatile numerical tool, which can be used to verify solutions to the problems dealing with small deformations of planetary bodies.

Acknowledgments

This work has been supported by the Charles University grant SVV 260447/2017. We thank Volker Klemann and an anonymous reviewer for helpful comments that improved the manuscript.

2.A Energy balance and the rate of mechanical work

The energies given in section 2.2.4 can be matched with the rates of mechanical work done by individual terms in the momentum eq. (2.17),

$$\nabla \cdot \boldsymbol{\tau} - (\boldsymbol{u} \cdot \nabla \rho_0)\, \boldsymbol{g}_0 - \rho_0 \nabla(\Phi + \Psi) + \rho_0 \boldsymbol{g}_0 = 0\,, \tag{2.61}$$

where we substituted for the body force from eq. (2.24). Multiplication of eq. (2.61) by the velocity vector, application of the tensor identity $(\nabla\cdot\boldsymbol{\tau})\cdot\boldsymbol{v} = \nabla\cdot(\boldsymbol{\tau}\cdot\boldsymbol{v}) - \boldsymbol{\tau} : \nabla\boldsymbol{v}$ and subsequent integration over the regular computational domain S_a–S_b gives

the balance equation of the rate of mechanical work:

$$\int_{\mathrm{S}_a\text{–}\mathrm{S}_b}\Big(-\boldsymbol{\tau}:\nabla\boldsymbol{v}+\nabla\cdot(\boldsymbol{\tau}\cdot\boldsymbol{v})-(\boldsymbol{u}\cdot\nabla\rho_0)\boldsymbol{g}_0\cdot\boldsymbol{v}-(\rho_0\nabla\Phi)\cdot\boldsymbol{v}-(\rho_0\nabla\Psi)\cdot\boldsymbol{v}+\rho_0\boldsymbol{g}_0\cdot\boldsymbol{v}\Big)\,\mathrm{d}v=0\,. \tag{2.62}$$

We now evaluate the integrals of the individual terms in eq. (2.62) to better understand the relationship between the mechanical work and the different types of energy discussed in the main text. The resulting expressions can be used as an alternative to the energy integrals given in section 2.2.4 and demonstrate the equivalence of the two approaches through a numerical test (Fig. 2.13).

In the following, we consider that $\boldsymbol{v}\cong\partial\boldsymbol{u}/\partial t$ under the assumption of small deformations. In Appendices 2.A.4 – 2.A.6 we use two modifications of the Reynolds transport theorem (e.g. Gurtin, 1982, p. 91, eq. 8):

$$\frac{\mathrm{d}}{\mathrm{d}t}\int_{v(t)}\rho f\,\mathrm{d}v=\int_{v(t)}\rho\frac{\mathcal{D}f}{\mathcal{D}t}\,\mathrm{d}v\,, \tag{2.63}$$

where $v(t)$ is the total volume of the deformed body at time t and $\mathcal{D}/\mathcal{D}t$ denotes the material derivative,

$$\frac{\mathcal{D}}{\mathcal{D}t}=\frac{\partial}{\partial t}+\boldsymbol{v}\cdot\nabla\,. \tag{2.64}$$

2.A.1 Term $-\boldsymbol{\tau}:\nabla\boldsymbol{v}$

Since the body is incompressible (trace of $\nabla\boldsymbol{v}$ is zero) and the Cauchy stress tensor is symmetric, $\boldsymbol{\tau}:\nabla\boldsymbol{v}$ can be rewritten as

$$\boldsymbol{\tau}:\nabla\boldsymbol{v}=\boldsymbol{\tau}^d:\tfrac{1}{2}\big(\nabla\boldsymbol{v}+(\nabla\boldsymbol{v})^{\mathrm{T}}\big)\,. \tag{2.65}$$

The strain rate $\frac{1}{2}\big(\nabla\boldsymbol{v}+(\nabla\boldsymbol{v})^{\mathrm{T}}\big)$ can be expressed from the constitutive equation (2.19):

$$\tfrac{1}{2}\big(\nabla\boldsymbol{v}+(\nabla\boldsymbol{v})^{\mathrm{T}}\big)\cong\frac{\partial}{\partial t}\Big[\tfrac{1}{2}\big(\nabla\boldsymbol{u}+(\nabla\boldsymbol{u})^{\mathrm{T}}\big)\Big]=\frac{1}{2\mu}\frac{\partial\boldsymbol{\tau}^d}{\partial t}+\frac{\boldsymbol{\tau}^d}{2\eta}\,. \tag{2.66}$$

The integral of $\boldsymbol{\tau}:\nabla\boldsymbol{v}$ then takes the form

$$\int_{\mathrm{S}_a\text{–}\mathrm{S}_b}\boldsymbol{\tau}:\nabla\boldsymbol{v}\,\mathrm{d}v\cong\int_{\mathrm{S}_a\text{–}\mathrm{S}_b}\left[\frac{\boldsymbol{\tau}^d:\boldsymbol{\tau}^d}{2\eta}+\frac{\boldsymbol{\tau}^d}{2\mu}:\frac{\partial\boldsymbol{\tau}^d}{\partial t}\right]\mathrm{d}v=\int_{\mathrm{S}_a\text{–}\mathrm{S}_b}\frac{\boldsymbol{\tau}^d:\boldsymbol{\tau}^d}{2\eta}\,\mathrm{d}v+\frac{\mathrm{d}}{\mathrm{d}t}\int_{\mathrm{S}_a\text{–}\mathrm{S}_b}\frac{\boldsymbol{\tau}^d:\boldsymbol{\tau}^d}{4\mu}\,\mathrm{d}v\,. \tag{2.67}$$

Assuming that the liquid core is inviscid and neglecting the dissipation and elastic energy within the small volumes corresponding to topographic anomalies, we can replace the integrals over $\mathrm{S}_a-\mathrm{S}_b$ on the right-hand side of eq. (2.67) by integrals over $v(t)$, resulting in the relation:

$$\int_{\mathrm{S}_a\text{–}\mathrm{S}_b}\boldsymbol{\tau}:\nabla\boldsymbol{v}\,\mathrm{d}v\cong\int_{v(t)}\frac{\boldsymbol{\tau}^d:\boldsymbol{\tau}^d}{2\eta}+\frac{\mathrm{d}}{\mathrm{d}t}\int_{v(t)}\frac{\boldsymbol{\tau}^d:\boldsymbol{\tau}^d}{4\mu}\,\mathrm{d}v=\dot{E}_{\mathrm{diss}}+\dot{E}_{\mathrm{el}}\,, \tag{2.68}$$

a)

Rates of energies		Powers
$\frac{\mathrm{d}}{\mathrm{d}t}\left(\int_{\mathrm{S}_a-\mathrm{S}_b}\frac{\boldsymbol{\tau}^d:\boldsymbol{\tau}^d}{4\mu}\,\mathrm{d}v\right)+\int_{\mathrm{S}_a-\mathrm{S}_b}\frac{\boldsymbol{\tau}^d:\boldsymbol{\tau}^d}{2\eta}\,\mathrm{d}v$	1	$-\int_{\mathrm{S}_a-\mathrm{S}_b}\boldsymbol{\tau}:\nabla\boldsymbol{v}\,\mathrm{d}v$
$+\frac{\mathrm{d}}{\mathrm{d}t}\left(\frac{1}{2}\boldsymbol{\omega}\cdot\boldsymbol{I}\cdot\boldsymbol{\omega}\right)$	2	$-\int_{\mathrm{S}_a-\mathrm{S}_b}\rho_0\nabla\Psi\cdot\boldsymbol{v}\,\mathrm{d}v-\int_{\partial\mathrm{S}_b}(\rho_c\Psi\boldsymbol{v})\cdot\boldsymbol{e}_r\,\mathrm{d}s$
$+\frac{\mathrm{d}}{\mathrm{d}t}\left(\frac{1}{2}[\rho_0]_a\int_{\partial\mathrm{S}_a}g_0u_r^2\,\mathrm{d}s\right)+\frac{1}{2}[\rho_0]_b\int_{\partial\mathrm{S}_b}g_0u_r^2\,\mathrm{d}s$	3a,b	$\int_{\partial\mathrm{S}_a}\boldsymbol{v}\cdot\boldsymbol{\tau}\cdot\boldsymbol{e}_r\,\mathrm{d}s-\int_{\partial\mathrm{S}_b}\boldsymbol{v}\cdot(\boldsymbol{\tau}+p_c\mathcal{I})\cdot\boldsymbol{e}_r\,\mathrm{d}s$
$-\frac{\mathrm{d}}{\mathrm{d}t}\left(\frac{1}{2}\int_b^a\frac{\mathrm{d}\rho_0}{\mathrm{d}r}\int_{\partial\mathrm{S}_i}g_0u_r^2\,\mathrm{d}s\,\mathrm{d}r\right)$	3c	$-\int_{\mathrm{S}_a-\mathrm{S}_b}(\boldsymbol{u}\cdot\nabla\rho_0)\,\boldsymbol{g}_0\cdot\boldsymbol{v}\,\mathrm{d}v$
$+\frac{\mathrm{d}}{\mathrm{d}t}\left(\frac{1}{2}\sum_{i=a,b}[\rho_0]_i\int_{\partial\mathrm{S}_i}u_r\Phi\mathrm{d}s-\frac{1}{2}\int_b^a\frac{\mathrm{d}\rho_0}{\mathrm{d}r}\int_{\partial\mathrm{S}_r}u_r\Phi\,\mathrm{d}s\,\mathrm{d}r,\right)$	4	$-\int_{\mathrm{S}_a-\mathrm{S}_b}\rho_0\nabla\Phi\cdot\boldsymbol{v}\,\mathrm{d}v-\int_{\partial\mathrm{S}_b}(\rho_c\Phi\boldsymbol{v})\cdot\boldsymbol{e}_r\,\mathrm{d}s$

b)

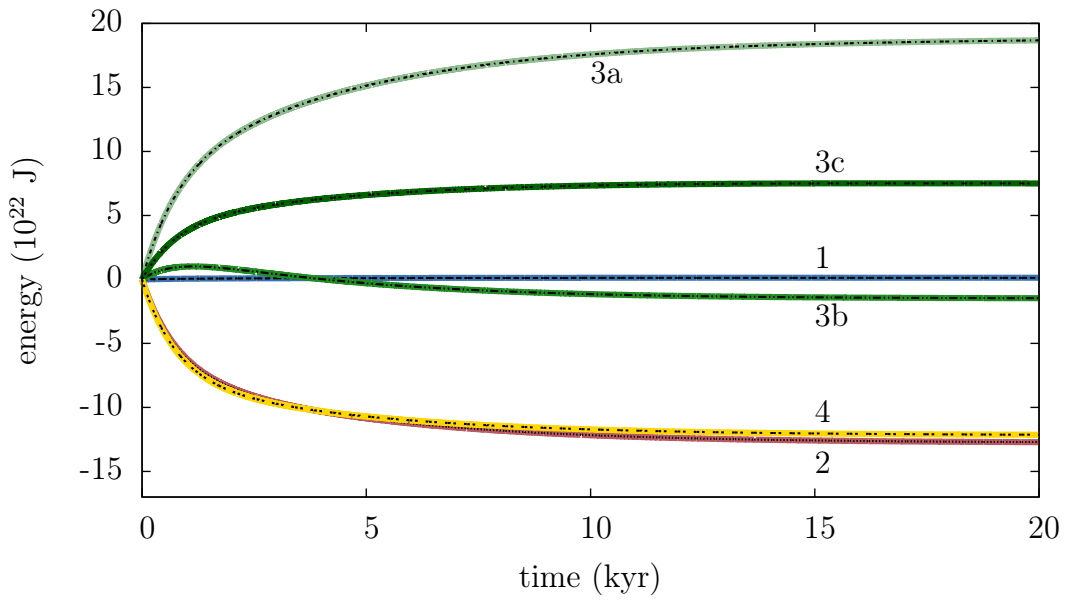

Figure 2.13: (a) Time derivatives of the energy integrals given in Section 2.2.4 (left) and their equivalents obtained by evaluating the rate of mechanical work over the computational domain (right). The numbers 1 and 2 correspond to deformation (blue) and rotational (red) powers, respectively. The gravitational power is split into individual terms derived in section 2.2.4.1. Number 3 (green) denotes the contributions due to the deformation in a reference gravitational field of potential V_0 while number 4 (yellow) corresponds to the power associated with incremental gravitational potential Φ. (b) Numerical test of the formulae in panel a performed for the benchmark case by Spada et al. (2011) (see also Sections 2.2.3 and 2.2.4.4). The coloured curves, obtained by time integration of the power formulae given in panel (a) (right), match the black curves computed directly from the corresponding energy formula. The colours and the numbers correspond to those in panel (a).

where we used eqs (2.36) and (2.37) from section 2.2.4. Equation (2.68) suggests that the power represented by the term $\boldsymbol{\tau} : \nabla \boldsymbol{v}$ is dissipated as heat or stored as elastic deformation energy in the body. For numerical validation of the relationship 2.68, see Fig. 2.13b, curve 1.

2.A.2 Term $\nabla \cdot (\boldsymbol{\tau} \cdot \boldsymbol{v})$

The volume integral of $\nabla \cdot (\boldsymbol{\tau} \cdot \boldsymbol{v})$ can be transformed into a surface integral using the Gauss theorem:

$$\int_{\mathrm{S}_a - \mathrm{S}_b} \nabla \cdot (\boldsymbol{\tau} \cdot \boldsymbol{v}) \, \mathrm{d}v = \int_{\partial \mathrm{S}_a} \boldsymbol{v} \cdot \boldsymbol{\tau} \cdot \boldsymbol{e}_r \, \mathrm{d}s - \int_{\partial \mathrm{S}_b} \boldsymbol{v} \cdot \boldsymbol{\tau} \cdot \boldsymbol{e}_r \, \mathrm{d}s \,. \tag{2.69}$$

Evaluating $\boldsymbol{\tau} \cdot \boldsymbol{e}_r$ from boundary conditions (2.25) and (2.26) and omitting the term σ^{L} (see the remark in the beginning of section 2.2.4.1), we obtain

$$\int_{\mathrm{S}_a - \mathrm{S}_b} \nabla \cdot (\boldsymbol{\tau} \cdot \boldsymbol{v}) \, \mathrm{d}v = \int_{\partial \mathrm{S}_a} \boldsymbol{v} \cdot (u_r [\rho_0]_a \boldsymbol{g}_0) \, \mathrm{d}s + \int_{\partial \mathrm{S}_b} \boldsymbol{v} \cdot (u_r [\rho_0]_b \boldsymbol{g}_0 + p_{\mathrm{c}} \boldsymbol{e}_r) \, \mathrm{d}s \,, \tag{2.70}$$

where p_{c} is the pressure in the core, $p_{\mathrm{c}} = -\rho_{\mathrm{c}}(V_0 + \Phi + \Psi)$. The first surface integral on the right-hand side of eq. (2.70) can be modified as

$$\begin{aligned} \int_{\partial \mathrm{S}_a} \boldsymbol{v} \cdot (u_r [\rho_0]_a \boldsymbol{g}_0) \, \mathrm{d}s &\cong \int_{\partial \mathrm{S}_a} \frac{\partial \boldsymbol{u}}{\partial t} \cdot (u_r [\rho_0]_a \boldsymbol{g}_0) \, \mathrm{d}s \\ &= -[\rho_0]_a \, g_0(a) \int_{\partial \mathrm{S}_a} \frac{1}{2} \frac{\partial u_r^2}{\partial t} \, \mathrm{d}s = -\frac{1}{2} [\rho_0]_a \, g_0(a) \frac{\mathrm{d}}{\mathrm{d}t} \int_{\partial \mathrm{S}_a} u_r^2 \, \mathrm{d}s \,. \end{aligned} \tag{2.71}$$

Analogously,

$$\int_{\partial \mathrm{S}_b} \boldsymbol{v} \cdot (u_r [\rho_0]_b \boldsymbol{g}_0) \, \mathrm{d}s \cong -\frac{1}{2} [\rho_0]_b \, g_0(b) \frac{\mathrm{d}}{\mathrm{d}t} \int_{\partial \mathrm{S}_b} u_r^2 \, \mathrm{d}s \,. \tag{2.72}$$

To summarize,

$$\int_{\mathrm{S}_a - \mathrm{S}_b} \nabla \cdot (\boldsymbol{\tau} \cdot \boldsymbol{v}) \, \mathrm{d}v = -\frac{1}{2} \frac{\mathrm{d}}{\mathrm{d}t} \left([\rho_0]_a \, g_0(a) \int_{\partial \mathrm{S}_a} u_r^2 \, \mathrm{d}s + [\rho_0]_b \, g_0(b) \int_{\partial \mathrm{S}_b} u_r^2 \, \mathrm{d}s \right) + \int_{\partial \mathrm{S}_b} p_{\mathrm{c}} \boldsymbol{v} \cdot \boldsymbol{e}_r \, \mathrm{d}s \,, \tag{2.73}$$

or, in terms of surface integrals

$$\begin{aligned} \int_{\partial \mathrm{S}_a} \boldsymbol{v} \cdot \boldsymbol{\tau} \cdot \boldsymbol{e}_r \, \mathrm{d}s - \int_{\partial \mathrm{S}_b} \boldsymbol{v} \cdot (\boldsymbol{\tau} + p_{\mathrm{c}} \mathcal{I}) \cdot \boldsymbol{e}_r \, \mathrm{d}s = \\ - \frac{1}{2} \frac{\mathrm{d}}{\mathrm{d}t} \left([\rho_0]_a \, g_0(a) \int_{\partial \mathrm{S}_a} u_r^2 \, \mathrm{d}s + [\rho_0]_b \, g_0(b) \int_{\partial \mathrm{S}_b} u_r^2 \, \mathrm{d}s \right) . \end{aligned} \tag{2.74}$$

where $\mathcal{I}$ is the identity tensor. Comparison of eq. (2.73) with eq. (2.52) suggests that the integral of $\nabla \cdot (\boldsymbol{\tau} \cdot \boldsymbol{v})$ over the computation domain corresponds to the changes of the gravitational energy due to the deformations of boundaries in the

gravitational field of potential V_0. For the numerical confirmation of eq. (2.74), see Fig. 2.13b, curves 3a,b.

It is worth noting that the integral of $\nabla \cdot (\boldsymbol{\tau} \cdot \boldsymbol{v})$ over the whole body $v(t)$ would be zero. Using the Gauss theorem and considering that the real surface is stress-free, we obtain

$$\int_{v(t)} \nabla \cdot (\boldsymbol{\tau} \cdot \boldsymbol{v}) \, \mathrm{d}v = \int_{\partial \mathrm{S}} \boldsymbol{v} \cdot \boldsymbol{\tau} \cdot \boldsymbol{n} \, \mathrm{d}s = 0 \,, \tag{2.75}$$

where ∂S now denotes the surface of the deformed body and $\boldsymbol{n}$ is the normal to the surface (see also Appendix 2.A.7).

2.A.3 Term $-(\boldsymbol{u} \cdot \nabla \rho_0)\, \boldsymbol{g}_0 \cdot \boldsymbol{v}$

Considering that $\boldsymbol{v} \cong \partial \boldsymbol{u}/\partial t$, $\boldsymbol{g}_0 = -g_0 \boldsymbol{e}_r$ and the functions g_0 and ρ_0 do not depend on time, we obtain

$$\begin{aligned} &- \int_{\mathrm{S}_a - \mathrm{S}_b} (\boldsymbol{u} \cdot \nabla \rho_0)\, \boldsymbol{g}_0 \cdot \boldsymbol{v} \, \mathrm{d}v \cong \int_{\mathrm{S}_a - \mathrm{S}_b} u_r \frac{\partial u_r}{\partial t} \frac{\mathrm{d}\rho_0}{\mathrm{d}r} \, g_0 \, \mathrm{d}v \\ &= \frac{1}{2} \frac{\mathrm{d}}{\mathrm{d}t} \int_{\mathrm{S}_a - \mathrm{S}_b} u_r^2 g_0 \frac{\mathrm{d}\rho_0}{\mathrm{d}r} \, \mathrm{d}v = \frac{1}{2} \frac{\mathrm{d}}{\mathrm{d}t} \int_b^a \frac{\mathrm{d}\rho_0}{\mathrm{d}r} \int_{\partial \mathrm{S}_r} g_0 u_r^2 \, \mathrm{d}s \, \mathrm{d}r \,, \end{aligned} \tag{2.76}$$

where the resulting integral can be identified with the rate of change of the gravitational energy due to volumetric density changes in the gravitational field of potential V_0 (cf. the last integral in eq. (2.52); for the numerical comparison, see Fig. 2.13b, curve 3c).

2.A.4 Auxiliary formulae for gravitational and centrifugal potential

Before we proceed to the remaining terms in eq. (2.62) we derive two auxiliary formulae for the gravitational and centrifugal potentials valid for the whole volume $v(t)$ of the deformed body at time t. We first consider the energy balance of a body in an inertial frame subject to gravitational body force $-\rho \nabla V$ only, where V is the gravitational potential generated by the body. If the surface of the body is free,

$$\frac{\mathrm{d}}{\mathrm{d}t} \int_{v(t)} \left(\rho \epsilon + \tfrac{1}{2} \rho \boldsymbol{v} \cdot \boldsymbol{v} \right) \mathrm{d}v = - \int_{v(t)} \rho \nabla V \cdot \boldsymbol{v} \, \mathrm{d}v \,, \tag{2.77}$$

where the expression on the left-hand side corresponds to the time change of the internal and kinetic energies, ϵ denotes the internal energy density, and the integral on the right-hand side is the total power of the gravitational force. Using

the definition of material derivative eq. (2.77) can be rearranged as

$$\frac{\mathrm{d}}{\mathrm{d}t}\int_{v(t)}\left(\rho\epsilon+\tfrac{1}{2}\rho\boldsymbol{v}\cdot\boldsymbol{v}\right)\,\mathrm{d}v+\int_{v(t)}\rho\frac{1}{2}\frac{\mathcal{D}V}{\mathcal{D}t}\mathrm{d}v=\int_{v(t)}\rho\left(\frac{\partial V}{\partial t}-\frac{1}{2}\frac{\mathcal{D}V}{\mathcal{D}t}\right)\,\mathrm{d}v\,. \quad (2.78)$$

The time derivative in the second integral on the left-hand side of eq. (2.78) can be pulled in front of the integral using the modified Reynolds theorem, eq. (2.63), and the integrand on the right-hand side can be reformulated by substituting for the material derivative of V:

$$\rho\left(\frac{\partial V}{\partial t}-\frac{1}{2}\frac{\mathcal{D}V}{\mathcal{D}t}\right)=\rho\left(\frac{\partial V}{\partial t}-\frac{1}{2}\frac{\partial V}{\partial t}-\frac{1}{2}\nabla V\cdot\boldsymbol{v}\right)=\frac{1}{2}\rho\left(\frac{\partial V}{\partial t}-\boldsymbol{v}\cdot\nabla V\right)\,. \quad (2.79)$$

Eq. (2.78) then gives

$$\frac{\mathrm{d}}{\mathrm{d}t}\int_{v(t)}\left(\rho\epsilon+\tfrac{1}{2}\rho\boldsymbol{v}\cdot\boldsymbol{v}+\tfrac{1}{2}\rho V\right)\,\mathrm{d}v=\frac{1}{2}\int_{v(t)}\rho\left(\frac{\partial V}{\partial t}-\nabla V\cdot\boldsymbol{v}\right)\,\mathrm{d}v\,. \quad (2.80)$$

On the left-hand side we now have the sum of all energies in the system, including the gravitational energy. The total energy must be conserved which implies that the right-hand side of eq. (2.80) is equal to zero. Consequently,

$$\int_{v(t)}\rho\nabla V\cdot\boldsymbol{v}\,\mathrm{d}v=\int_{v(t)}\rho\frac{\partial V}{\partial t}\,\mathrm{d}v\,. \quad (2.81)$$

A similar formula can be derived for the centrifugal potential Ψ. In this case, however, we must consider the energy balance in a rotating frame which is fixed with respect to the body and consider all relevant forces that act in the rotating frame. In analogy to eq. (2.77), but this time not considering any gravitational forcing, we can write

$$\frac{\mathrm{d}}{\mathrm{d}t}\int_{v(t)}\left(\rho\epsilon+\tfrac{1}{2}\rho\boldsymbol{v}\cdot\boldsymbol{v}\right)\,\mathrm{d}v=\int_{v(t)}\left(-\rho\nabla\Psi-\rho\boldsymbol{\omega}\times\boldsymbol{v}-\rho\frac{\mathrm{d}\boldsymbol{\omega}}{\mathrm{d}t}\times\boldsymbol{r}\right)\cdot\boldsymbol{v}\,\mathrm{d}v, \quad (2.82)$$

where the terms in parentheses on the right-hand side represent the centrifugal, Coriolis and Euler body force, respectively. The scalar product of the Coriolis force with the velocity vector is zero. The power of the Euler force can be rearranged using the vector algebra identity $\boldsymbol{a}\cdot(\boldsymbol{b}\times\boldsymbol{c})=\boldsymbol{b}\cdot(\boldsymbol{c}\times\boldsymbol{a})$:

$$\int_{v(t)}\left(-\rho\frac{\mathrm{d}\boldsymbol{\omega}}{\mathrm{d}t}\times\boldsymbol{r}\right)\cdot\boldsymbol{v}\,\mathrm{d}v=-\frac{\mathrm{d}\boldsymbol{\omega}}{\mathrm{d}t}\cdot\int_{v(t)}\boldsymbol{r}\times(\rho\boldsymbol{v})\,\mathrm{d}v=-\frac{\mathrm{d}\boldsymbol{\omega}}{\mathrm{d}t}\cdot\boldsymbol{h}\,, \quad (2.83)$$

where $\boldsymbol{h}$ is the relative angular momentum. In the Tisserand frame (Munk & MacDonald, 1960), $\boldsymbol{h}$ is equal to zero by definition, and the total power of the Euler force is thus zero in such frame. Following the same procedure as above

(eqs 2.78 – 2.80 where V is replaced by Ψ), we obtain

$$\frac{\mathrm{d}}{\mathrm{d}t}\int_{v(t)}\left(\rho\epsilon+\tfrac{1}{2}\rho\boldsymbol{v}\cdot\boldsymbol{v}+\tfrac{1}{2}\rho\Psi\right)\,\mathrm{d}v=\frac{1}{2}\int_{v(t)}\rho\left(\frac{\partial\Psi}{\partial t}-\nabla\Psi\cdot\boldsymbol{v}\right)\,\mathrm{d}v\,. \tag{2.84}$$

On the left-hand side we have the sum of all energies of the now considered system, when viewed from the inertial reference frame. The time derivative of this sum must again be zero, giving

$$\int_{v(t)}\rho\nabla\Psi\cdot\boldsymbol{v}\,\mathrm{d}v=\int_{v(t)}\rho\frac{\partial\Psi}{\partial t}\,\mathrm{d}v\,. \tag{2.85}$$

2.A.5 Term $-(\rho_0\nabla\Phi)\cdot\boldsymbol{v}$

We first evaluate the integral of $-(\rho_0\nabla\Phi)\cdot\boldsymbol{v}$ over the volume $v(t)$ of the deformed body and then we transform it into an integral over the computational domain $\mathrm{S}_a-\mathrm{S}_b$.

The potential V in auxiliary formula (2.81) can be expressed as the sum of the reference potential V_0, independent of time, and the increment Φ due to the deformation, $V(t)=V_0+\Phi(t)$. Considering that $\partial V_0/\partial t=0$,

$$\int_{v(t)}\rho\nabla(V_0+\Phi)\cdot\boldsymbol{v}\,\mathrm{d}v=\int_{v(t)}\rho\frac{\partial\Phi}{\partial t}\,\mathrm{d}v\,. \tag{2.86}$$

The term $\rho\nabla V_0\cdot\boldsymbol{v}$ can be moved to the right-hand side and replaced by $\rho\mathcal{D}V_0/\mathcal{D}t$:

$$\int_{v(t)}\rho\nabla\Phi\cdot\boldsymbol{v}\,\mathrm{d}v=\int_{v(t)}\rho\left(\frac{\partial\Phi}{\partial t}-\frac{\mathcal{D}V_0}{\mathcal{D}t}\right)\,\mathrm{d}v\,. \tag{2.87}$$

Adding $\int_{v(t)}\rho\nabla\Phi\cdot\boldsymbol{v}\,\mathrm{d}v$ to both sides of eq. (2.87), dividing the equation by 2 and invoking the expression for the material derivative of Φ, we obtain

$$\int_{v(t)}\rho\nabla\Phi\cdot\boldsymbol{v}\,\mathrm{d}v=\frac{1}{2}\int_{v(t)}\rho\frac{\mathcal{D}}{\mathcal{D}t}\left(\Phi-V_0\right)\,\mathrm{d}v\,, \tag{2.88}$$

where the time derivative on the right-hand can be pulled in front of the integral using the Reynolds theorem (2.63):

$$\int_{v(t)}\rho\nabla\Phi\cdot\boldsymbol{v}\,\mathrm{d}v=\frac{1}{2}\frac{\mathrm{d}}{\mathrm{d}t}\int_{v(t)}\rho\left(\Phi-V_0\right)\,\mathrm{d}v\,. \tag{2.89}$$

The integral on the right-hand side of eq. (2.89) is formally the same as in eq. (2.38) except that the sign of V_0 is opposite. Thus, the integral can be evaluated in an analogous manner as described in section 2.2.4.1, giving

$$\int_{v(t)}\rho\nabla\Phi\cdot\boldsymbol{v}\,\mathrm{d}v=\frac{1}{2}\sum_{i=1}^{N}\frac{\mathrm{d}}{\mathrm{d}t}\int_{h_i}[\rho_0]_i\Phi\mathrm{d}v\cong\frac{\mathrm{d}}{\mathrm{d}t}\left[\frac{1}{2}\sum_{i=1}^{N}[\rho_0]_i\int_{\partial\mathrm{S}_i}\Phi u_r\,\mathrm{d}s\right] \tag{2.90}$$

for a layered model and

$$\int_{v(t)} \rho \nabla\Phi \cdot \boldsymbol{v}\, \mathrm{d}v \cong \frac{\mathrm{d}}{\mathrm{d}t}\left[\frac{1}{2}\left([\rho_0]_a \int_{\partial \mathrm{S}_a} u_r \Phi \mathrm{d}s + [\rho_0]_b \int_{\partial \mathrm{S}_b} u_r \Phi \mathrm{d}s - \int_b^a \frac{\mathrm{d}\rho_0}{\mathrm{d}r} \int_{\partial \mathrm{S}_r} u_r \Phi \,\mathrm{d}s\,\mathrm{d}r\right)\right] \tag{2.91}$$

for a continuous density profile. The terms on the right-hand sides of eqs (2.90) and (2.91) correspond to the gravitational energy due to potential Φ induced by the deformation (cf. eqs 2.47, 2.50 and 2.51).

Now we transform the integral on the left-hand side of eq. (2.89) into an integral over the computational domain $\mathrm{S}_a - \mathrm{S}_b$:

$$\int_{v(t)} \rho \nabla\Phi \cdot \boldsymbol{v}\, \mathrm{d}v \cong \int_{\mathrm{S}_a - \mathrm{S}_b} \rho_0 \nabla\Phi \cdot \boldsymbol{v}\, \mathrm{d}v + \rho_\mathrm{c} \int_{\mathrm{S}_b} \nabla\Phi \cdot \boldsymbol{v}\, \mathrm{d}v\,. \tag{2.92}$$

where we omitted the second order term $-\delta\rho\nabla\Phi$ (cf. eq. 2.24) and neglected the contributions of $\rho\nabla\Phi\cdot\boldsymbol{v}$ within the small volumes corresponding to topographic anomalies. The volume integral over S_b can be transformed into a surface integral using the Gauss theorem. Considering that $\nabla\Phi\cdot\boldsymbol{v} = \nabla\cdot(\Phi\boldsymbol{v})$ for an incompressible body, we get

$$\int_{v(t)} \rho \nabla\Phi \cdot \boldsymbol{v}\, \mathrm{d}v \cong \int_{\mathrm{S}_a - \mathrm{S}_b} \rho_0 \nabla\Phi \cdot \boldsymbol{v}\, \mathrm{d}v + \rho_\mathrm{c} \int_{\partial\mathrm{S}_b} (\Phi\boldsymbol{v}) \cdot \boldsymbol{e}_r\, \mathrm{d}v\,. \tag{2.93}$$

Combining eqs (2.93) and (2.90) provides the sought relation between the power of $\rho_0\nabla\Phi$ over the computational domain and the associated energy rate:

$$\int_{\mathrm{S}_a - \mathrm{S}_b} \rho_0 \nabla\Phi \cdot \boldsymbol{v}\, \mathrm{d}v + \rho_\mathrm{c} \int_{\partial\mathrm{S}_b} (\Phi\boldsymbol{v}) \cdot \boldsymbol{e}_r\, \mathrm{d}v \cong \frac{\mathrm{d}}{\mathrm{d}t}\left[\frac{1}{2}\sum_{i=1}^{N} [\rho_0]_i \int_{\partial\mathrm{S}_i} \Phi u_r\, \mathrm{d}s\right]. \tag{2.94}$$

An analogous expression is obtained for body with a continuous density profile by combining eqs (2.93) and (2.91). The validity of eq. (2.94) is numerically demonstrated by curve 4 in Fig. 2.13b.

2.A.6 Term $-(\rho_0\nabla\Psi)\cdot\boldsymbol{v}$

Using eq. (2.85) and following the analogous procedure as above, we get

$$\begin{aligned}\int_{v(t)} \rho \nabla\Psi \cdot \boldsymbol{v}\, \mathrm{d}v = \int_{v(t)} \rho \frac{\partial\Psi}{\partial t}\, \mathrm{d}v = \frac{1}{2}\int_{v(t)} \rho \left(\frac{\partial\Psi}{\partial t} + \nabla\Psi\cdot\boldsymbol{v}\right) \mathrm{d}v = \\ = \frac{1}{2}\int_{v(t)} \rho \frac{\mathcal{D}\Psi}{\mathcal{D}t}\, \mathrm{d}v = \frac{\mathrm{d}}{\mathrm{d}t}\int_{v(t)} \frac{1}{2}\rho\Psi\, \mathrm{d}v = \frac{\mathrm{d}}{\mathrm{d}t}\left(\frac{1}{2}\boldsymbol{\omega}\cdot\boldsymbol{I}\cdot\boldsymbol{\omega}\right).\end{aligned} \tag{2.95}$$

The integral of $\rho\nabla\Psi\cdot\boldsymbol{v}$ over $v(t)$ can be expressed as (cf. eq. 2.92)

$$\int_{v(t)} \rho \nabla\Psi \cdot \boldsymbol{v}\, \mathrm{d}v \cong \int_{\mathrm{S}_a - \mathrm{S}_b} \rho_0 \nabla\Psi \cdot \boldsymbol{v}\, \mathrm{d}v + \rho_\mathrm{c} \int_{\mathrm{S}_b} \nabla\Psi \cdot \boldsymbol{v}\, \mathrm{d}v\,. \tag{2.96}$$

Combining eqs (2.95) and (2.96) we obtain

$$\int_{\mathrm{S}_a-\mathrm{S}_b} \rho_0 \nabla\Psi\cdot\boldsymbol{v}\,\mathrm{d}v + \rho_\mathrm{c}\int_{\mathrm{S}_b}\nabla\Psi\cdot\boldsymbol{v}\,\mathrm{d}v = \frac{\mathrm{d}}{\mathrm{d}t}\left(\frac{1}{2}\boldsymbol{\omega}\cdot\boldsymbol{I}\cdot\boldsymbol{\omega}\right)\,, \tag{2.97}$$

see also Fig. 2.13b, curve 2.

Note that the derivations of eqs (2.94) and (2.97) rely on the auxiliary formulae from Appendix 2.A.4, and as such they are only valid if the energy of the studied system is conserved. In energetically ill-posed problems eqs (2.94) and (2.97) must not be satisfied, as illustrated in Section 2.2.4.5 in the main text (cf. Fig. 2.11).

2.A.7 Term $\rho_0\boldsymbol{g}_0\cdot\boldsymbol{v}$

Since ρ_0 and $\boldsymbol{g}_0$ are spherically symmetric and the body is incompressible ($\int_{\partial\mathrm{S}_r}\boldsymbol{v}\cdot\boldsymbol{e}_r\,\mathrm{d}s=0$), the integral of the last term in eq. (2.61) over the computational domain is equal to zero:

$$\int_{\mathrm{S}_a-\mathrm{S}_b}\rho_0\boldsymbol{g}_0\cdot\boldsymbol{v}\,\mathrm{d}v = -\int_{\mathrm{S}_a-\mathrm{S}_b}\rho_0 g_0\boldsymbol{v}\cdot\boldsymbol{e}_r\,\mathrm{d}v = -\int_b^a \rho_0 g_0\int_{\partial\mathrm{S}_r}\boldsymbol{v}\cdot\boldsymbol{e}_r\,\mathrm{d}s\,\mathrm{d}r = 0\,. \tag{2.98}$$

Note, however, that the integral of $\rho\boldsymbol{g}_0\cdot\boldsymbol{v}$ over the real volume of the body $v(t)$ is non-zero, even if the density is constant within the mantle shell. For a body with $\nabla\rho_0$ equal to zero within the shell the integral is equal to the right-hand side of eq. (2.70):

$$\int_{v(t)}\rho\boldsymbol{g}_0\cdot\boldsymbol{v}\,\mathrm{d}v \cong \int_{\partial\mathrm{S}_a}\boldsymbol{v}\cdot(u_r[\rho_0]_a\boldsymbol{g}_0)\,\mathrm{d}s + \int_{\partial\mathrm{S}_b}\boldsymbol{v}\cdot(u_r[\rho_0]_b\boldsymbol{g}_0 + p_\mathrm{c}\boldsymbol{e}_r)\,\mathrm{d}s\,. \tag{2.99}$$

This is because in this integral there are contributions from the non-zero Eulerian density increments $\delta\rho = \pm[\rho_0]_{a,b}$ in the vicinity of the boundaries (see Fig. 2.4). If the computational domain is chosen regular ($\mathrm{S}_a - \mathrm{S}_b$) as in the present study, these volumetric density increments are condensed into surface densities and we encounter them in Appendix 2.A.2 in the form of boundary tractions (2.25) and (2.26). For a body with $\nabla\rho_0 \neq 0$ inside the mantle shell the term $\rho\boldsymbol{g}_0\cdot\boldsymbol{v}$ also includes a contribution from the internal Eulerian density increment $-\boldsymbol{u}\cdot\nabla\rho_0$, which was discussed in Appendix 2.A.3.

2.A.8 Remark

Inspection of the left-hand side of Fig. 2.13a suggests that the formulae used to evaluate the energy balance in the main text can be replaced by the corresponding formulae for the rates of the mechanical work evaluated over the computational domain $\mathrm{S}_a - \mathrm{S}_b$. However, there are three integrals over $\partial\mathrm{S}_b$ on the right-hand side of Fig. 2.13a which are related to the body force $-\rho_\mathrm{c}\nabla(V_0+\Phi+\Psi)$ in the

core. The sum of these terms is equal to zero,

$$-\int_{\partial \mathrm{S}_b} (\rho_\mathrm{c} \Psi \boldsymbol{v}) \cdot \boldsymbol{e}_r \,\mathrm{d}s - \int_{\partial \mathrm{S}_b} p_\mathrm{c} \boldsymbol{v} \cdot \boldsymbol{e}_r \,\mathrm{d}s - \int_{\partial \mathrm{S}_b} (\rho_\mathrm{c} \Phi \boldsymbol{v}) \cdot \boldsymbol{e}_r \,\mathrm{d}s = 0\,, \tag{2.100}$$

since $p_\mathrm{c} = -\rho_\mathrm{c}(V_0 + \Phi + \Psi)$ and

$$\int_{\partial \mathrm{S}_b} \rho_\mathrm{c} V_0 \boldsymbol{v} \cdot \boldsymbol{e}_r \,\mathrm{d}s = \rho_\mathrm{c} V_0 \int_{\partial \mathrm{S}_b} \boldsymbol{v} \cdot \boldsymbol{e}_r \,\mathrm{d}s = 0\,. \tag{2.101}$$

2.B Second order correction to LLE

The third component of the NLE is

$$0 = \frac{\mathrm{d}}{\mathrm{d}t} \left(\boldsymbol{I} \cdot \boldsymbol{\omega}\right)_3 + \varepsilon_{3jk} \omega_j \left(\boldsymbol{I} \cdot \boldsymbol{\omega}\right)_k \,, \tag{2.102}$$

where ε is the Levi-Civita symbol. Using the traditional notation,

$$\boldsymbol{\omega} = \boldsymbol{\omega}_0 + |\boldsymbol{\omega}_0| \boldsymbol{m} \quad \text{and} \quad \boldsymbol{I} = \begin{pmatrix} A + c_{11} & c_{12} & c_{13} \\ c_{12} & A + c_{22} & c_{23} \\ c_{13} & c_{12} & C + c_{33} \end{pmatrix}, \tag{2.103}$$

with $\boldsymbol{\omega}_0$ equal to $[0, 0, \omega_0]$ and c_{ij}, m_i denoting small quantities, and inserting from eq. (2.103) to eq. (2.102), we obtain

$$\begin{aligned} 0 &\cong \frac{\mathrm{d}}{\mathrm{d}t}[c_{33} + c_{13}m_1 + c_{23}m_2 + c_{33}m_3 + Cm_3] + \omega_0 m_1 c_{23} - \omega_0 m_2 c_{13} \\ &= (\dot{c}_{33} + \dot{c}_{13}m_1 + \dot{c}_{23}m_2 + \dot{c}_{33}m_3 + c_{13}\dot{m}_1 + c_{23}\dot{m}_2 + c_{33}\dot{m}_3 + C\dot{m}_3) \\ &\qquad + \omega_0(m_1 c_{23} - m_2 c_{13}), \end{aligned} \tag{2.104}$$

where third order terms are neglected, the dot abbreviates time derivative and $\dot{C}$ and $\dot{\omega}_0$ are zero, since both C and ω_0 are constants. Recalling the LLE for m_1 and m_2 (Munk & MacDonald, 1960):

$$\omega_0(C - A)\left(m_1 - \frac{A\,\dot{m}_2}{(C - A)\omega_0}\right) = \omega_0 c_{13} + \dot{c}_{23} \tag{2.105}$$

$$\omega_0(C - A)\left(m_2 + \frac{A\,\dot{m}_1}{(C - A)\omega_0}\right) = \omega_0 c_{23} - \dot{c}_{13}, \tag{2.106}$$

we can insert for $\dot{c}_{23}$ and $\dot{c}_{13}$ in eq. (2.104) from eqs (2.105) and (2.106), introducing only a third order error, because $\dot{c}_{23}$ and $\dot{c}_{13}$ are both multiplied by a small quantity in eq. (2.104). This leads to

$$\begin{aligned} 0 \cong \dot{c}_{33} + C\dot{m}_3 - Am_1\dot{m}_1 - Am_2\dot{m}_2 + \dot{c}_{33}m_3 + \omega_0(m_1 c_{23} - m_2 c_{13}) \\ + \omega_0[c_{23}m_1 - (C - A)m_1 m_2 - c_{13}m_2 + (C - A)m_1 m_2 + c_{13}\dot{m}_1 + c_{23}\dot{m}_2 + c_{33}\dot{m}_3]\,. \end{aligned} \tag{2.107}$$

The fifth term on the first line of eq. (2.107) can be expressed using the LLE for m_3, $\dot{c}_{33} = -C\dot{m}_3$, introducing only a third order error:

$$\begin{aligned} 0 \cong\ & \dot{c}_{33} + C\dot{m}_3 - Am_1\dot{m}_1 - Am_2\dot{m}_2 - C\dot{m}_3 m_3 \\ & + \omega_0[2c_{23}m_1 - 2c_{13}m_2 + c_{13}\dot{m}_1 + c_{23}\dot{m}_2 + c_{33}\dot{m}_3]\,. \end{aligned} \tag{2.108}$$

This can be rewritten as

$$\begin{aligned} 0 \cong\ & \dot{c}_{33} + C\left(m_3 - \frac{m_1^2 + m_2^2 + m_3^2}{2}\right)^{\cdot} + \\ & + \omega_0[2c_{23}m_1 - 2c_{13}m_2 + c_{13}\dot{m}_1 + c_{23}\dot{m}_2 + c_{33}\dot{m}_3] + (C - A)(\dot{m}_1 m_1 + \dot{m}_2 m_2), \end{aligned} \tag{2.109}$$

which provides a second-order correction to the vertical component of the LLE. The second equality in eq. (2.58) is obtained when the relative importance of the second-order terms in eq. (2.109) are assessed: the terms on the second line are negligible due to the multiplication by factors ω_0 and $C - A$, which are both much smaller than factor C.

3. Stress memory effect in viscoelastic stagnant lid convection

"*But I should be very sorry if an interpretation founded on a most conjectural scientific hypothesis were to get fastened to the text in Genesis... The rate of change of scientific hypothesis is naturally much more rapid than that of Biblical interpretations, so that if an interpretation is founded on such an hypothesis, it may help to keep the hypothesis above ground long after it ought to be buried and forgotten.* "
– James Clerk Maxwell, Letter to Rev. C. J. Ellicott (22 Nov 1876)

The following chapter was published in Geophysical Journal International, Volume 209(3), p. 1462-1475, doi: 10.1093/gji/ggx102, 2017

V. Patočka[1], O. Čadek[1], P. J. Tackley[2], and H. Čížková[1]

[1]Department of Geophysics, Faculty of Mathematics and Physics, Charles University, Prague, Czech Republic
[2]Institute of Geophysics, Department of Earth Sciences, ETH Zurich, Switzerland

Summary

Present thermo-chemical convection models of planetary evolution often assume a purely viscous or visco-plastic rheology. Ignoring elasticity in the cold, outer boundary layer is, however, questionable since elastic effects may play an important role there and affect surface topography as well as the stress distribution within the stiff cold lithosphere. Here we present a modelling study focused on the combined effects of Maxwell viscoelastic rheology and a free surface in the stagnant lid planetary convection. We implemented viscoelastic rheology in the StagYY code using a tracer-based stress advection scheme that suppresses subgrid oscillations. We apply this code to perform thermal convection models of the cooling planetary mantles and we demonstrate that while the global characteristics of the mantle flow do not change significantly when including viscoelasticity, the stress state of the cold lithosphere may be substantially different. Transient cooling of an initially thin upper thermal boundary layer results in a complex layered stress structure due to the memory effects of viscoelastic rheology. The stress state of the lid may thus contain a record of the planetary thermal evolution.

3.1 Introduction

Mantle dynamics of terrestrial planets is traditionally modelled using viscous or viscoplastic rheology with viscosity strongly dependent on temperature and pressure. High viscosity contrasts typical for present day temperatures result in stagnant lid convection (Solomatov, 1995), which can explain the tectonic style of most terrestrial planets. Surface topography and gravitational field are the primary constraints on the internal structure and dynamics of terrestrial planets and both are strongly affected by the properties of the lid. A commonly used assumption that this lid is purely viscous or viscoplastic is, however, questionable. There are multiple lines of evidence that planetary lithospheres show elastic behaviour on geological time scales. For example, the height and width of a forebulge associated with subduction and the response of a sedimentary basin to surface loading can be successfully explained by the deflection of a thin elastic plate (Turcotte & Schubert, 2002). Numerous studies have thus addressed the effects of elasticity on the topography and geoid induced by internal dynamics of a planet.

Zhong (2002) calculated the topography and geoid of a 3-D spherical viscoelastic shell with static internal loading, where this loading was derived from the distribution of thermal buoyancy computed with a viscous flow solver. A different approach for combining the calculation of small deformations of an elastic or viscoelastic spherical shell with a viscous mantle convection code is presented by Golle et al. (2012), who used normal tractions from the mantle convection simulation at a given depth as the boundary condition for the deformation of a thin elastic shell. A more advanced approach involves the fully viscoelastic treatment of mantle convection within the whole domain including the stagnant lid. Such an approach allows the inclusion of lateral variations in the thickness of the lithosphere and accounts for the possible feedback between viscoelastic features in the lithosphere and sublithospheric internal dynamics.

Convection of a viscoelastic material on a planetary mantle scale was first addressed by Ivins et al. (1982). Later, Harder (1991) performed numerical experiments with a Maxwell medium with constant viscosity, the main focus being on stationary solutions of thermal convection in a box with free slip boundaries. More elaborate models that could include pressure and temperature induced lateral variations of viscosity, nonlinear stress-dependent rheologies and variable thickness of the lithosphere emerged about a decade later. Muhlhaus et al. (2006) found no significant deviations of statistical steady states in convection models with nonlinear rheology; only the transient phase was influenced by considering viscoelasticity. Beuchert & Podladchikov (2010) demonstrated how elasticity broadens the region of effective stress associated with a cold temperature anomaly prescribed within the lithosphere. They also studied statistical steady state convection. All of the above studies assumed a free-slip surface. Thielmann et al. (2015) addressed the effects of viscoelasticity and a free surface

on stagnant lid convection with temperature dependent viscosity. Their target parameters were mean stress in the lithosphere and thickness of the stress boundary layer. While the significance of a free surface was clearly demonstrated, the effect of viscoelasticity seemed to be negligible for planetary parameters, as the resulting dependencies of target parameters were rather flat for Deborah numbers up to 1. The above mentioned works focus on the effect of viscoelasticity on the horizontally averaged stress profile or on global characteristics of convection such as the bottom and top Nusselt numbers. Little attention is paid to the effect of stress memory, initial thermal conditions and topography.

The main focus of this study is to provide a detailed analysis of the effects of viscoelasticity on surface topography and stress evolution within the parameter range characteristic of planetary mantles. We will introduce a new viscoelastic flow solver based on the formulation by Moresi et al. (2002), implemented in StagYY (Tackley, 2008). With this tool we will first employ a simple compositional model of a cylinder (representing plume head) rising below a stiff lithosphere to evaluate the response of a viscoelastic lid to convective loading. This part is an extension of the viscous model introduced by Crameri et al. (2012) and it demonstrates what are the combined effects of elasticity and a free surface on the developed surface topography. We will compare the free surface topography of the viscoelastic models to the topography calculated using the traditional instantaneous viscous flow (IVF) approach (e.g. Kiefer et al. (1996)), in which dynamic topography is assumed to be proportional to the normal component of surface traction. After examining the effects of elasticity on lithospheric deformation in this basic model we will move to a more elaborate description of the cooling of a planetary mantle. We will construct a model of thermal convection in a planetary mantle with a free surface and evaluate the effects of viscoelastic rheology on lithospheric stresses. We will focus on temporal changes in the stress distribution during planetary cooling and we will demonstrate how the stress memory of the lithosphere affects the formation of stress distribution in planetary mantles.

3.2 Governing equations and numerical methods

We employ two types of models. First, we perform models of purely composition driven convection with a simple density load (labeled as RC). A compositionally buoyant cylinder represents a rising plume head and we evaluate the effects of elasticity and surface boundary condition on the topography. In the second group of numerical experiments (labeled TC) we use viscoelastic thermal convection models and concentrate on the stress evolution within the lithosphere.

3.2.1 Governing equations

We assume an incompressible fluid with infinite Prandtl number with following equations describing conservation of mass and momentum:

$$\nabla \cdot \boldsymbol{v} = 0, \tag{3.1}$$

$$-\nabla p + \nabla \cdot \boldsymbol{\tau} + \rho \boldsymbol{g} = 0. \tag{3.2}$$

Here $\boldsymbol{v}$ is the velocity, ρ density, p pressure, $\boldsymbol{g}$ gravitational acceleration and $\boldsymbol{\tau}$ deviatoric stress. In case of the compositional models (RC) we further require the conservation of composition:

$$\frac{\partial c_k}{\partial t} + \boldsymbol{v} \cdot \nabla c_k = 0, \tag{3.3}$$

where c_k is the concentration (either 0 or 1) of kth material with the density ρ_k.

In the thermal convection models (TC), eqs (3.1) and (3.2) are supplemented by conservation of energy in the Boussinesq approximation:

$$\frac{\partial T}{\partial t} = \kappa \triangle T - \boldsymbol{v} \cdot \nabla T, \tag{3.4}$$

and a linearized equation of state:

$$\rho = \rho_0 (1 - \alpha (T - T_0)). \tag{3.5}$$

where T is the temperature, κ is the diffusivity, α is the thermal expansivity and ρ_0 is the density at reference temperature T_0. Both thermal expansivity and diffusivity are assumed constant.

3.2.2 Maxwell viscoelastic rheology

The rheological description of a Maxwell viscoelastic material is given by

$$\mathbb{D} = \mathbb{D}_{\text{viscous}} + \mathbb{D}_{\text{elastic}} = \frac{1}{2\eta(p_0, T)} \boldsymbol{\tau} + \frac{1}{2G} \frac{\mathcal{D}\boldsymbol{\tau}}{\mathcal{D}t}, \tag{3.6}$$

where $\mathbb{D}$ is the deviatoric part of the strain rate tensor, $\eta(p_0, T)$ is the viscosity dependent on temperature and hydrostatic pressure p_0, and G is the shear modulus. $\frac{\mathcal{D}}{\mathcal{D}t}$ denotes an objective tensor rate (e.g. Liu & Sampaio (2014)). Here we adopt the Jaumann rate that is traditionally used in viscoelastic convection (see appendix A in Thielmann et al. (2015) and Muhlhaus & Regenauer-Lieb (2005) for a discussion of objective rates in geodynamical context):

$$\frac{\mathcal{D}\boldsymbol{\tau}}{\mathcal{D}t} := \frac{\partial \boldsymbol{\tau}}{\partial t} + \boldsymbol{v} \cdot \nabla \boldsymbol{\tau} + (\boldsymbol{\tau}\mathbb{W} - \mathbb{W}\boldsymbol{\tau}), \tag{3.7}$$

where $\mathbb{W}$ is the antisymmetric part of the velocity gradient (spin tensor)

$$\mathbb{W} = \frac{1}{2}\left(\nabla \boldsymbol{v} - (\nabla \boldsymbol{v})^{\mathrm{T}}\right). \tag{3.8}$$

The corotational term $(\boldsymbol{\tau}\mathbb{W} - \mathbb{W}\boldsymbol{\tau})$ accounts for rotation of a volume element within the flow. Inserting (3.7) into (3.6) gives the following form of the constitutive equation:

$$2\eta\mathbb{D} = \boldsymbol{\tau} + \frac{\eta}{G}\left(\frac{\partial \boldsymbol{\tau}}{\partial t} + \boldsymbol{v}\cdot\nabla\boldsymbol{\tau} + \boldsymbol{\tau}\mathbb{W} - \mathbb{W}\boldsymbol{\tau}\right). \tag{3.9}$$

We consider an Arrhenius viscosity that depends exponentially on temperature and hydrostatic pressure p_0:

$$\eta(p_0, T) = \eta_0 \cdot \exp\left(\frac{E_{\mathrm{act}} + p_0 V_{\mathrm{act}}}{RT}\right), \tag{3.10}$$

where η_0 is set such that η is the reference viscosity at $T = 1600$ K and $p_0 = 0$ Pa, E_{act} is the activation energy, V_{act} is the activation volume and R is the gas constant. In viscous models that will be used as a reference to evaluate elasticity effects, $G \to \infty$ in Eq. (3.9) and viscosity follows the same pressure and temperature dependency (Eq. (3.10)).

Following Moresi et al. (2002) we discretize Eq. (3.9) with a mixed Euler first-order accurate scheme (implicit with respect to $\mathbb{D}$, $\boldsymbol{\tau}$ and viscosity, explicit with respect to advectional and corotational terms) and obtain the equation for stress in the nth time step:

$$\boldsymbol{\tau}^{\mathrm{n}} = 2\mathrm{Z}\eta\mathbb{D}^{\mathrm{n}} + (1-\mathrm{Z})\tilde{\boldsymbol{\tau}}^{\mathrm{n}-1}, \tag{3.11}$$

$$\tilde{\boldsymbol{\tau}}^{\mathrm{n}-1} := \boldsymbol{\tau}^{\mathrm{n}-1} - \triangle t\left(\boldsymbol{v}\cdot\nabla\boldsymbol{\tau} + \boldsymbol{\tau}\mathbb{W} - \mathbb{W}\boldsymbol{\tau}\right)^{\mathrm{n}-1}, \tag{3.12}$$

$$\mathrm{Z} = \frac{\triangle t}{\triangle t + \eta/G}. \tag{3.13}$$

The implementation of viscoelasticity into a viscous flow code thus consists of replacing viscosity by numerical viscosity $\eta_{\mathrm{num}} := \mathrm{Z}\eta$ and evaluating an extra term $\nabla\cdot[(1-\mathrm{Z})\tilde{\boldsymbol{\tau}}^{\mathrm{n}-1}]$, which accounts for the effect of stress that did not fully relax within one time step. The importance of elastic effects is measured by viscoelasticity parameter Z that is closely related to the Maxwell relaxation time $t_{\mathrm{M}} = \eta/G$ ($\mathrm{Z} \to 1$ when $\eta/G \ll \triangle t$). In nondimensional studies, the role of t_{M} is played by the Deborah number, $De := \eta\kappa G^{-1}D^{-2}$, with D denoting the domain's depth.

Let us consider a constant value of the shear modulus, $G = 7\cdot 10^{10}$ Pa (representative of the Earth's uppermost mantle). Then, for viscosity (in the mantle) equal to 10^{22} Pa s the relaxation time η/G is ~ 4.5 kyr. With a typical computational time step of 100 kyr more than 95% of stress is relaxed within one time step and the material behaves effectively as a viscous fluid. However, if the viscosity

(in the lithosphere) is $\eta = 10^{27}$ Pa s, the relaxation time is ~ 450 Myr and for the same computational time step only 0.02% of stress is relaxed within one time step. Consequently, the material remembers its stress state from thousands of previous time steps.

In order to evaluate the differences between different viscous and viscoelastic models we introduce a scalar measure of stress, the second invariant of the stress tensor, which we will refer to as the effective stress:

$$\tau_{\text{eff}} := \sqrt{\frac{\tau_{xx}^2 + \tau_{zz}^2}{2} + \tau_{xz}^2}\,, \tag{3.14}$$

with τ_{xx}, τ_{zz} and τ_{xz} denoting the Cartesian components of $\boldsymbol{\tau}$.

Time derivative of $\boldsymbol{\tau}$ in Eq. (3.9) implies the need for an initial condition on the deviatoric stress. In all viscoelastic models we assume $\boldsymbol{\tau}(t = 0)$ equal to zero.

3.2.3 Numerical implementation

Numerical solution of the governing equations is performed using the code StagYY (Tackley, 2008), which has been extended to include viscoelastic rheology by following the method described in Moresi et al. (2002) and Gerya & Yuen (2007). The method introduced by Moresi et al. (2002) and Moresi et al. (2003) was originally designed for finite elements. Here we apply it to a finite volume discretization (some aspects of stress evaluation accuracy in context of finite volume discretizations of elastic plate bending problems are discussed in Vaz et al. (2009)). Benchmarks used to test the viscoelastic part of the code are presented in Appendix 3.A. For technical details regarding the implementation we refer the reader to Gerya & Yuen (2007), deviations from their approach are described below.

We implemented both a grid-based and tracer-based advection of stress. Using particles for advecting a quantity is optimal when the quantity remains constant on each particle throughout the simulation. If so, only interpolation from tracers to grid is needed. This is not the case with the stress tensor in viscoelastic media: the first term on the right hand side of Eq. (3.11) is a contribution that is computed each time step on the grid and is interpolated from grid to tracers. The convenience of tracer-based advection thus depends on the relative importance of the terms on the right hand side of Eq. (3.11). It performs slightly better than the grid-based donor cell method when simulating the recovery of the original shape of an elastic slab (see Appendix 3.A.2), as the stresses only gradually build up in the slab and do not change much over computational time steps. The opposite is true when simulating the flow described in Appendix 3.A.1, especially for advecting stresses in regions of high vorticity on a sparse mesh. While the donor cell method leads to a satisfactory fit to the reference stationary flow described in Harder (1991), with tracer-based advection over a thousand tracers per cell are required to reach comparable solution quality. In the thermal convection simula-

tions reported below we use tracers to advect stress tensor components, but we obtained qualitatively the same results with the donor cell advection scheme as well.

Our implementation of the tracer-based variant differs from Gerya & Yuen (2007) in the way the second term on the right hand side of Eq. (3.11) is treated. In thermal convection simulations, subgrid oscillations of stress can occur in advection dominated regions. When the stress change is computed in a volume integrated sense (i.e. on the nodes of the mesh) and subsequently interpolated to tracers, then two tracers with a different stress history that at certain moment are very close to each other can unphysically retain a mutual stress jump even when entrained to an effectively viscous part of the domain (see App. 3.B and Fig. 3.13 for more details). The problem is similar to the problem of subgrid oscillations of temperature when this quantity is carried on tracers but diffusion is computed on the mesh.

In order to reduce these oscillations Gerya & Yuen (2007) use subgrid diffusion, controlled by additional numerical parameters (see their Eq. (24) and the preceding paragraph). Here we introduce a novel approach that performs the relaxation procedure, that is, multiplication by factor $(1-\mathrm{Z})$ in Eq. (3.11), directly on tracers and not on the grid. Only then is the second term in Eq. (3.11) interpolated to the respective positions on the staggered grid. In effectively viscous regions this procedure leads to individually zeroing out the stress from the previous time step on each tracer, regardless of the value of stress on neighbouring tracers. As a result, the stress field is smooth and determined solely by $2\mathrm{Z}\eta\mathbb{D}^{\mathrm{n}}$ in these regions. No additional (numerical) diffusion parameters are needed in our simulations.

Another important issue that determines numerical stability is the choice of time step. In the time-averaging approach of Moresi et al. (2003) the elastic time step $\triangle t$ in equations (3.12) and (3.13) can in general be chosen independently on the advectional time step controlled by CFL condition. If one sets a lower bound on $\triangle t$ it means that material with relaxation time smaller than this limit value $\triangle t_{\min}$ behaves effectively as viscous medium (c.f. Eq. (3.11)). This can help to stabilize the numerical simulations in certain cases (see section "Elastic Timestep" in Moresi et al. (2002) for details). Here we however did not need to apply a lower bound $\triangle t_{\min}$ and use only one time step both in the constitutive equation and for advecting the tracers (see the discussion in Appendix 3.A.1). This time step is dictated by the CFL condition with Courant number equal to 0.5.

The tracers are advected using the fourth-order spatially accurate Runge-Kutta method. We use linear tracer to node interpolation for the diagonal components of the deviatoric stress (located at cell centres) and cell averaging interpolation for the off-diagonal components (located at grid vertices, resp. edge centres in 3-D).

To conclude this section, a note should be made of a positive side effect that

comes with implementing viscoelasticity. The numerical viscosity, which numerically plays the role of physical viscosity when solving the Stokes equation, has much smaller spatial contrasts than the physical one (see Beuchert & Podladchikov (2010) for details). The prefactor Z in eq. (3.13) is from the interval $(0, 1)$, and decreases with increasing viscosity for a given time step. Thus $Z \doteq 0.95$ for mantle material with viscosity $\eta = 10^{22}$ Pa s and shear modulus $G = 7 \times 10^{10}$ Pa if the computational time step is 100 kyr, while $Z \doteq 0.0002$ for lithosphere with $\eta = 10^{27}$ Pa s and the same shear modulus, that is, reducing the viscosity contrast by four orders of magnitude. This improves the convergence of multigrid iterations when solving the resulting system of linear equations.

3.3 Rising cylinder (RC models)

3.3.1 Model setup

We use the same model setup as Crameri et al. (2012), designed to mimic the interaction of the stiff lithosphere with a rising plume head. Our model domain is an isothermal 2-D box (2800 km $\times$ 700 km) with a no-slip bottom boundary and impermeable free-slip side boundaries (Fig. 3.1). Viscous mantle (600 km deep) with a viscosity of 10^{21} Pa s and density of 3300 kg m^{-3} is overlain by a 100 km thick, neutrally buoyant, viscoelastic lithosphere. We test three values of lithospheric viscosity: $10^{23}, 10^{25}$ and 10^{27} Pa s. The rising plume head is modelled as a less dense cylinder initially located in the middle of the mantle layer. The diameter of the cylinder is 100 km and it is characterized by a density of 3200 kg m^{-3} and a relatively low viscosity of 10^{20} Pa s. Viscoelastic models have shear modulus $G_{\mathrm{L}} = 7 \times 10^{10}$ Pa in the viscoelastic lithosphere and their mantle is kept viscous (which is numerically achieved by using a high value of the shear modulus in the mantle, $G_{\mathrm{M}} = 10^{20}$ Pa). We use a regular grid resolution with 256×1024 points and 100 particle tracers per cell.

Our models have either a free surface implemented using the sticky-air approach (Matsumoto & Tomoda, 1983; Schmeling et al., 2008) or an impermeable free-slip surface. Sticky air is modelled as a 100 km thick layer of a very weak material ($\eta_A = 10^{18}$ Pa s) with negligible density ($\rho_{\mathrm{A}} = 10^{-3}$ kg m^{-3}). Surface topography in the free surface models is calculated by tracking the interface between the lithosphere and sticky-air. In free-slip models the surface topography is assumed to be proportional to the normal component of surface traction (e.g. Kiefer et al. (1996)) – we denote this here as the IVF response. For each lithospheric viscosity we run four models – with purely viscous or viscoelastic rheology and with a free surface or a free-slip surface. We use very fine time steps here, $20\times$ smaller than the values dictated by the CFL stability condition, in order to resolve the initial evolution of topography.

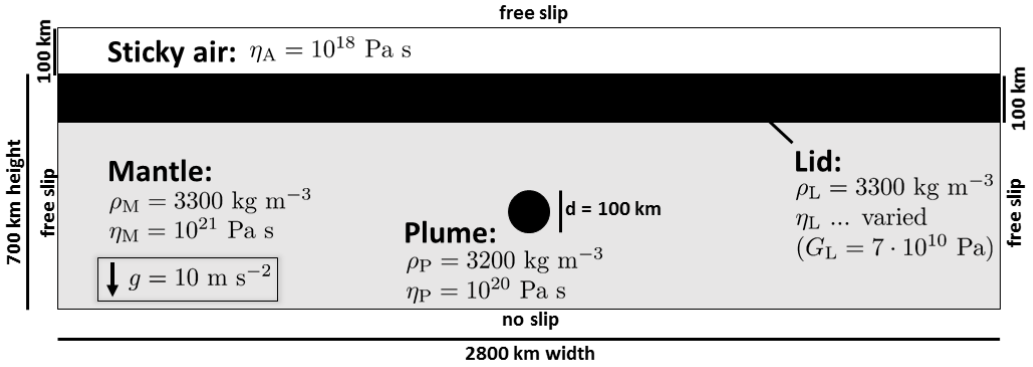

Figure 3.1: Model setup used in Section 3.3. Viscosity of the lid is varied. Simulations with viscoelastic rheology have constant shear modulus $G_L = 7 \times 10^{10}$ Pa. For free surface simulations sticky air layer of thickness 100 km and viscosity 10^{18} Pa s is employed.

3.3.2 Results: topography above a rising cylinder

First, let us discuss the topography developing above a cylinder rising through the mantle towards the stiff lithosphere (Fig. 3.1). We use this simple model to demonstrate the basic features of stress and topography development in a stiff layer loaded by a viscous upwelling. We vary the viscosity of the stiff lithosphere ($10^{23}, 10^{25}$ and 10^{27} Pa s) and for each viscosity we perform both the IVF model (with impermeable free-slip surface) and the free surface model, and compare the resulting topographies.

The buoyant cylinder needs about 10 Myr to rise from its initial position towards the base of the lithosphere. During this time the traction acting at the bottom of the lid due to the load steadily increases. Figure 3.2 depicts the maximum topography reached in the middle of the box above the rising cylinder as a function of time. Solid lines show the viscoelastic models while dashed lines are for corresponding viscous models ($G_L \to \infty$). The IVF topographies are insensitive to lithospheric viscosity and almost identical for viscous and viscoelastic models. Viscoelastic material transfers stresses to the top free slip boundary in a similar way to viscous material when flexure is not allowed by the top boundary condition. The IVF topographies gradually increase as the load becomes closer to the surface and reach their maximum of about 800 m when the cylinder reaches the base of the lithosphere. Free-surface topographies (red, blue and black lines), on the other hand, do depend on the lithospheric viscosity and vary between the viscous and viscoelastic models. In case of the lowest lid viscosity (10^{23} Pa s, red line) the Maxwell relaxation time is ~ 45 kyr and viscoelasticity thus plays little role. At the beginning both topographies quickly increase (time is displayed on logarithmic scale) and after few hundreds of kyr they get close to the IVF value, which they follow afterwards because the Stokes time scale is larger than the isostatic relaxation time of the lid (see Crameri et al. (2012) for details). Higher viscosity lids (10^{25} and 10^{27} Pa s; blue and black lines) already cause visible

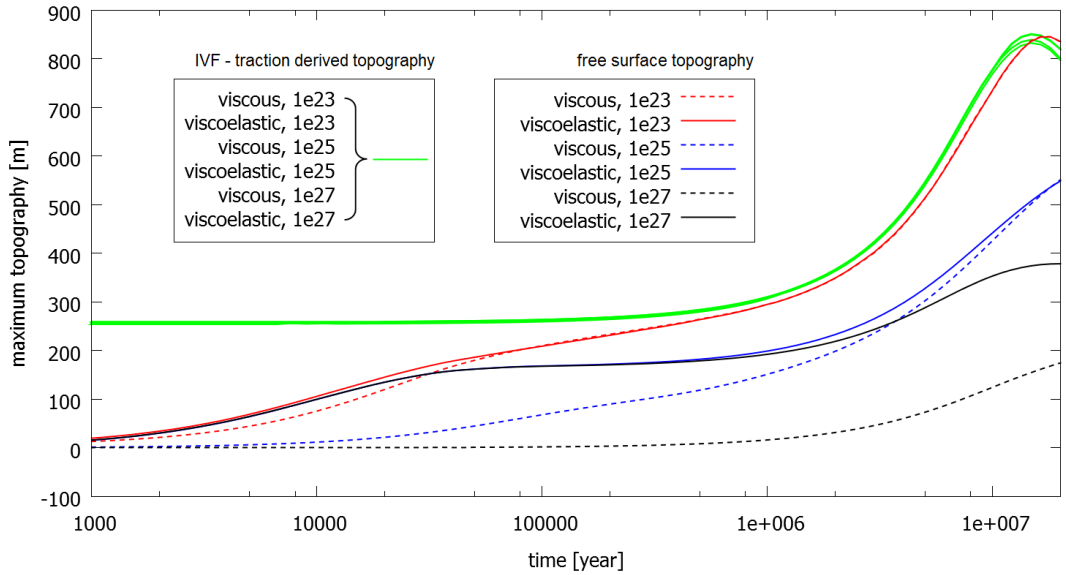

Figure 3.2: Topographic response to a rising cylinder, different colours stand for different values of η_{L} in Pa s. Solid lines show the evolution of maximum topography when viscoelastic rheology is employed, dashed lines are for viscous rheology. Red dashed curve is the response to Case 2 in Crameri et al. (2012). Green lines represent the overlapping, traction derived topographies.

differences between viscous and viscoelastic models in topography development. Topographies in viscous models are significantly reduced with respect to the IVF response due to the resistance of a stiff lid to bending. Viscoelastic material on the other hand responds with elastic deformation as well and developed topography is higher (closer to IVF values). The large difference between the IVF and free-surface topography of purely viscous models demonstrates a drawback of the IVF approach: it yields topographies that are almost independent of the lid's viscosity, whereas free surface topographies differ significantly for lithospheric viscosities which are commonly used as cut-off values in geodynamical models.

The evolution of topography formed by the viscoelastic lids is determined by their respective Maxwell relaxation times ($\sim$ 45 kyr for the solid red line, $\sim$ 4.5 Myr for the solid blue line, $\sim$ 450 Myr for the solid black line), with the exception of the initial rise, which is controlled by viscosity of the mantle. The viscous deformation of the mantle delays the (otherwise instantaneous) elastic flexure of the lid (cca 160 m for the initial position of the load). Weak lithosphere (solid red line) is characterized by a short Maxwell relaxation time, smaller than both the Stokes time scale of the rising cylinder and the isostatic relaxation time of a viscous lithosphere (for the given viscosity). The evolution of topography in viscoelastic cases with higher lithospheric viscosity (solid blue and solid black lines) is identical as long as the dominant deformation mechanism is the purely elastic one (i.e. mechanism insensitive to η_{L}). The lines separate as soon as viscoelastic relaxation starts to be significant for $\eta_{\mathrm{L}} = 10^{25}$ Pa s, slowly increasing the observed topography by shifting from the elastic to the viscous limit. With

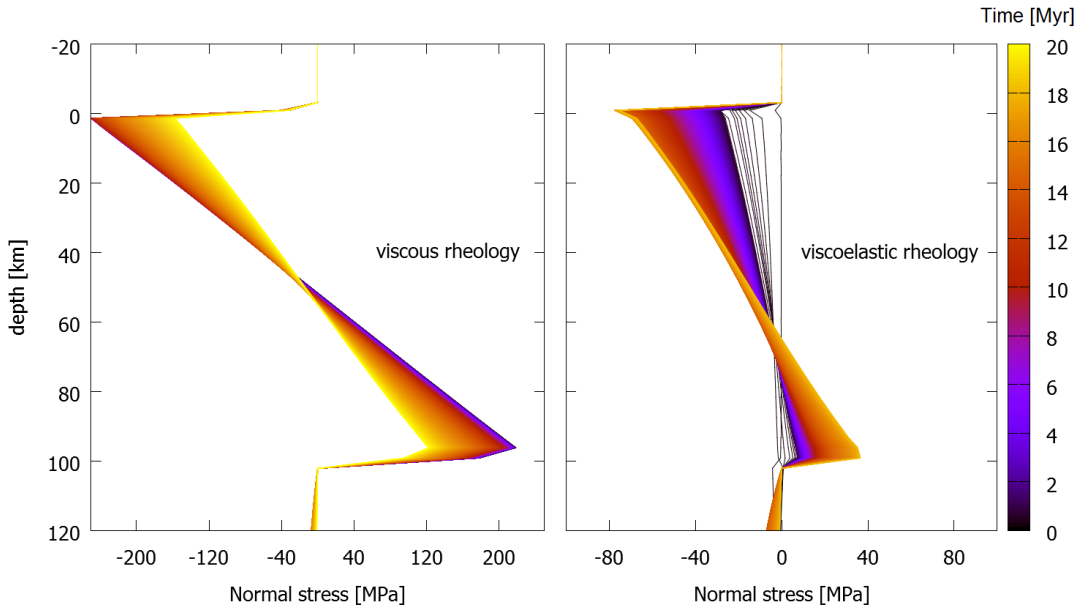

Figure 3.3: Temporal evolution of vertical deviatoric stress τ_{zz} in models with a free surface and η_{L} equal to 10^{27} Pa s. Left panel shows viscous model, right panel is for viscoelastic model. Stress is plotted as a function of depth along a vertical line located above the centre of the rising cylinder. Colour represents time in Myr.

$\eta_{\mathrm{L}} = 10^{27}$ Pa s the Maxwell relaxation time is much larger than the duration of the simulation, and the solid black line thus represents a purely elastic response ($\eta_{\mathrm{L}} \to \infty$). The effect of elastic filtering, described in Golle et al. (2012), addresses the difference between such response and a traction derived topography.

Figure 3.3 demonstrates stress evolution within the lithosphere with a free surface. It shows the vertical deviatoric stress τ_{zz} as a function of depth plotted above the centre of the rising cylinder in a model with the strongest lithosphere ($\eta_{\mathrm{L}} = 10^{27}$ Pa s). Colour represents time: black and dark colours are for the beginning of the calculation, while orange and yellow are for the time when the cylinder reaches the bottom of the lid. The left panel shows the viscous model, whereas the right panel is for the viscoelastic model. The initial stress in the viscous model is large ($\sim$ 200 MPa) and the pattern corresponds to bending. The amplitude decreases as the cylinder rises and topography grows – the elevated surface of the lid counteracts the effect of the upward push of the cylinder.

In the viscoelastic lid the stresses are significantly smaller and they simply increase as the topography increases, because the stresses are fully determined by the total strain in the effectively elastic lid.

3.4 Thermal convection (TC models)

3.4.1 Model setup

After examining the basic characteristics of a viscoelastic response in free-slip and free-surface models, we now proceed towards the convection models, in which the flow is driven by thermal buoyancy and the viscosity is controlled by the temperature distribution and the depth.

We concentrate on the effects of viscoelasticity on the transient behaviour of the stiff lid and demonstrate how viscoelasticity affects stress evolution in the lithosphere during its cooling and thickening. To that end we perform models of two planetary bodies with different reference viscosities and thus different vigour of convection in the transient phase. The first one is an Earth-sized body (E-models) with a relatively high η_{ref} and model parameters based on Crameri & Tackley (2014). The other one is a Mars-sized body (M-models) with lower η_{ref} and parameters taken from Golle et al. (2012). For each planet we test two scenarios – one with an initially thin lithosphere (controlled by the initial thermal boundary layer thickness $d_{\mathrm{TB}} = 30$ km) and the other one with an initially 300 km thick lithosphere.

We assume basally heated convection with constant temperature top and bottom boundaries, while the sides are insulating with zero normal heat flux. The initial temperature distribution follows the relation:

$$T(z) = T_0 + (T_{\mathrm{surf}} - T_0) \exp\left(\frac{-z}{d_{\mathrm{TB}}}\right) + (T_{\mathrm{CMB}} - T_0) \exp\left(\frac{z - D}{d_{\mathrm{TB}}}\right), \qquad (3.15)$$

where $T_0 = 1900$ K is the temperature at the mid-depth, T_{surf} and T_{CMB} are surface and core-mantle boundary temperatures, d_{TB} is the initial thickness of the thermal boundary layer, D is the mantle thickness and z is the depth. Random temperature perturbations with amplitude 20 K are used to initiate convection. The model parameters are summarized in Table 3.1.

Each convection simulation starts with a transient stage in which the sublithospheric flow evolves and the cold, stiff lithosphere gradually changes its thickness. Then, a statistically steady state is reached and the lithospheric thickness remains constant. The temperature T_0 in the mid-mantle is initially set to 1900 K. For E-models this is less than the statistically steady state mid-mantle temperature, thus the central part of the model heats up during transient phase and the vigour of convection increases. For the Mars-like parameter set, on the other hand, 1900 K represents an overheated mantle, mainly because of the smaller temperature drop between the core-mantle boundary and surface. Due to the lower reference viscosity, a vigorous, downwelling dominated convection initially develops in the model and is gradually quelled as the mid-mantle temperature decreases down to cca. 1700 K.

The model domain is a 2-D Cartesian box with aspect ratio 1 and a mantle

Table 3.1: Parameters used in the convection calculations

Parameter	Symbol	Model E_{el}	Model M_{el}	Units
Mantle depth	D	2890	1666	km
Gravitational acceleration	g	9.81	3.7	m s^{-2}
Reference density	ρ_0	3300	3300	kg m^{-3}
Temperature drop	$\triangle T$	2500	1500	K
Reference viscosity	η_{ref}	10^{23}	$9.316 \cdot 10^{19}$	Pa s
Upper viscosity cut-off	η_{max}	10^{28}	10^{28}	Pa s
Thermal diffusivity	κ	$7.6 \cdot 10^{-7}$	$7.6 \cdot 10^{-7}$	m^2 s^{-1}
Thermal expansivity	α	$3 \cdot 10^{-5}$	$3 \cdot 10^{-5}$	K^{-1}
Activation energy	E_{act}	240	346	kJ mol^{-1}
Activation volume	V_{act}	$8.9 \cdot 10^{-7}$	$2 \cdot 10^{-7}$	m^3 mol
Surface temperature	T_{surf}	289	230	K
Shear modulus[a]	G	$7 \cdot 10^{10}$	$7 \cdot 10^{10}$	Pa

[a]Models E_{vis} and M_{vis} are obtained by setting $G \to \infty$

depth of 2890 km for E-models and 1666 km for M-models. Impermeable free slip boundaries are assumed at the bottom and sides of the box. The top boundary is either assumed to be impermeable free slip, or similarly to the RC models, a free surface using the sticky-air approach. Following Crameri & Tackley (2014) we use a 150 km thick sticky-air layer with viscosity $\eta_{\mathrm{A}} = 10^{21}$ Pa s (given our upper viscosity cut-off, this choice provides a reasonable balance between obtained accuracy and the length of computational time step necessary to avoid the "drunken seaman" instability described by Kaus et al. (2010) and Duretz et al. (2011)). The mesh resolution is 256×256 nodes.

3.4.2 Results: free-slip surface

First let us discuss the Earth-size models with an impermeable free-slip surface and initially thin lithosphere. Figure 3.4 shows a snapshot of viscosity in the whole model domain (left column), effective stress in the upper half of the model domain (middle column) and vertical deviatoric stress (right column), all taken after 4.6 Gyr. The upper row is for a purely viscous model E_{vis}, while bottom row is for a viscoelastic one E_{el}. Below the lithosphere the flow pattern is almost identical for both rheologies (see Fig. 3.5) and we can thus compare responses to almost identical loading. The viscous model results in a relatively simple smooth stress distribution within the stiff lithosphere that reflects the distribution of upwelling and downwelling features.

The viscoelastic model, on the other hand, shows a rather complex layered stress pattern in the lower part of the lithosphere in the middle between the two downwellings. The depth of the first "layer" indicates the thickness to which the lithosphere cooled conductively with no accompanying deformation. The stress layers themselves formed during the thickening period and reflect the lateral movement of upwellings and downwellings during the history of the thickening lithosphere. In general, when viscoelastic lithosphere grows, the accretionary edge records the stresses caused by the upwelling and downwelling features active

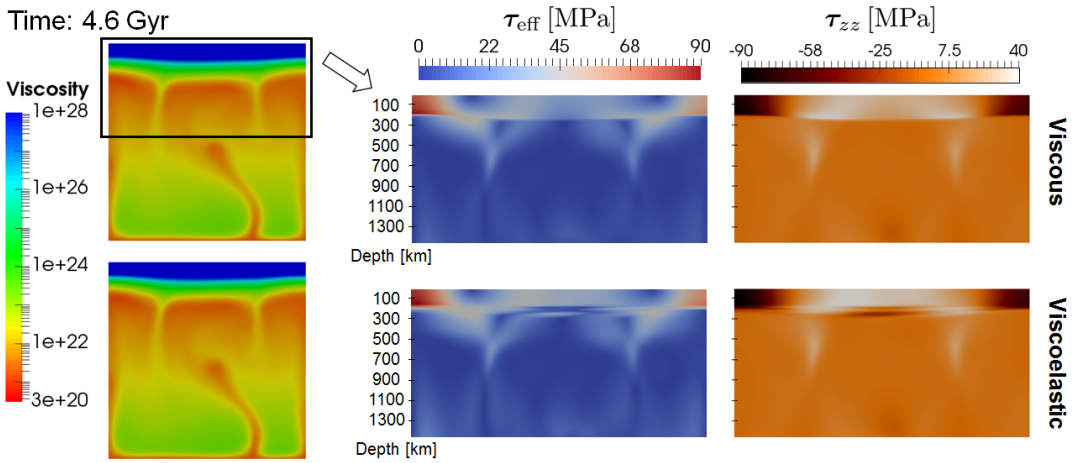

Figure 3.4: Model E with aspect ratio 1, $T_0 = 1900$ K, $d_{\mathrm{TB}} = 30$ km and a free slip upper boundary after approximately 4.6 Gyr. Top row shows the viscosity, effective stress and vertical deviatoric stress τ_{zz} of model $\mathrm{E_{vis}}$, bottom row shows the simulation with vicoelastic rheology ($\mathrm{E_{el}}$). Stresses are shown in upper part of the domain only, depth is in km.

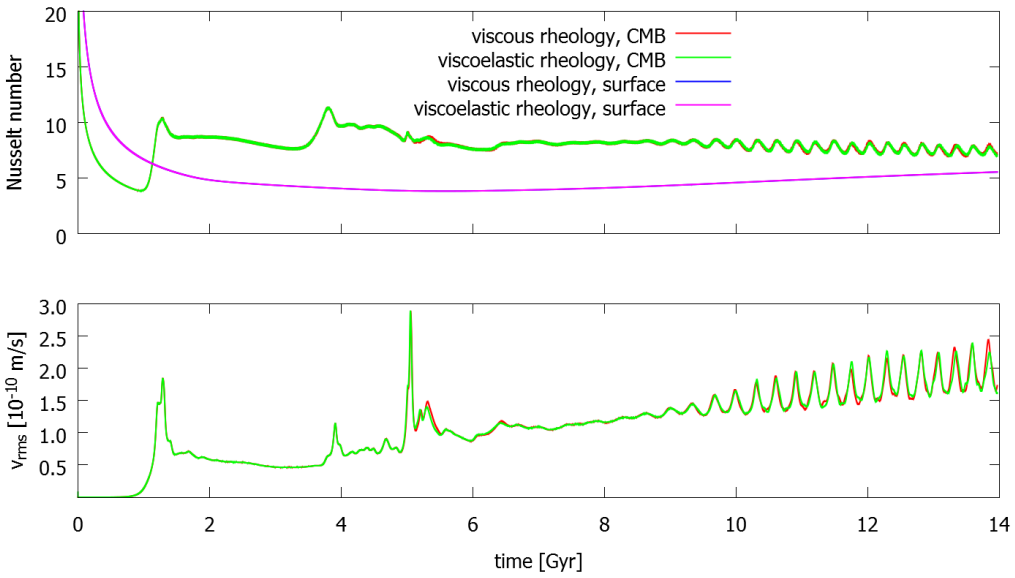

Figure 3.5: Top and bottom Nusselt numbers and mean velocities in models $\mathrm{E_{vis}}$ and $\mathrm{E_{el}}$ with aspect ratio 1, $T_0 = 1900$ K, $d_{\mathrm{TB}} = 30$ km and a free-slip upper boundary.

at the time of the accretion. These stresses are remembered, but they are also gradually altered as they relax and as new downwellings pull and new plumes push throughout the entire thickness of the lid. The thickness and lateral extent of the stress layers is determined by the spatial stability of the dynamical features relative to the characteristic time of the cooling.

In case of the Mars-like body more vigorous convection develops during the transition phase. The shorter wavelength structure of the downwellings in the sublithospheric mantle is also reflected in the stress pattern in the lithosphere, in both viscous and viscoelastic models. Figure 3.6(a) shows the vertical stress component τ_{zz} at two snapshots taken during transient cooling and thickening of the lithosphere at 1 Gyr and at 2 Gyr. Clearly, a complex layered lithospheric stress pattern due to memory effects in a viscoelastic model (as described above) is much more pronounced here. This is due to the relative instability and characteristic wavelength of the downwellings. Additionally, the region of smooth stresses is significantly reduced when compared to the less vigorous Earth-sized model as the downwellings quickly develop in the early stages of the model evolution. When a steady state is reached and lithospheric thickness does not increase further, frozen stress structures relax and within several Gyr this shallow, layered stress structure resulting from memory effects of viscoelastic rheology is no longer present. Viscoelastic models then have comparable stress magnitude and pattern as viscous ones. The time that the structure needs to disappear is related to the Maxwell relaxation time of the lithosphere (4.5 Gyr for the upper viscosity cut-off 10^{28} Pa s).

So far we have discussed the results of the models with an initially thin lithosphere. If we instead initially prescribe a thick lithosphere ($d_{\mathrm{TB}} = 300$ km) we observe none of the above described effects on stress development and the behaviour of viscoelastic models is the same as that of viscous models (see Fig. 3.6b).

3.4.3 Results: free surface

In the previous paragraph we described the results of the models with a free-slip surface. Now let us focus on the models with a free surface. Based on the results of our numerical experiments with a rising cylinder, we may expect much stronger effects of elasticity, as the lithospheric flexure can now fully develop.

Fig. 3.7 shows the stress evolution in the smaller Mars-like mantle models $\mathrm{M_{vis}}$ and $\mathrm{M_{el}}$ – with initially thin lithosphere $d_{\mathrm{TB}} = 30$ km. In a purely viscous model (left column) the stress pattern in the lithosphere reflects its bending due to the pull of the sublithospheric downwellings (no plumes are initially present due to the fact that the mantle is overheated). The wavelength of the lithospheric undulations is controlled by the temporary distribution of the downwellings and by the actual thickness of the lithosphere. As the lithosphere cools and thickens, the wavelength of the undulations generally increases. In a viscoelastic case (right column) the stress pattern is again much more complex. Stresses obtained during

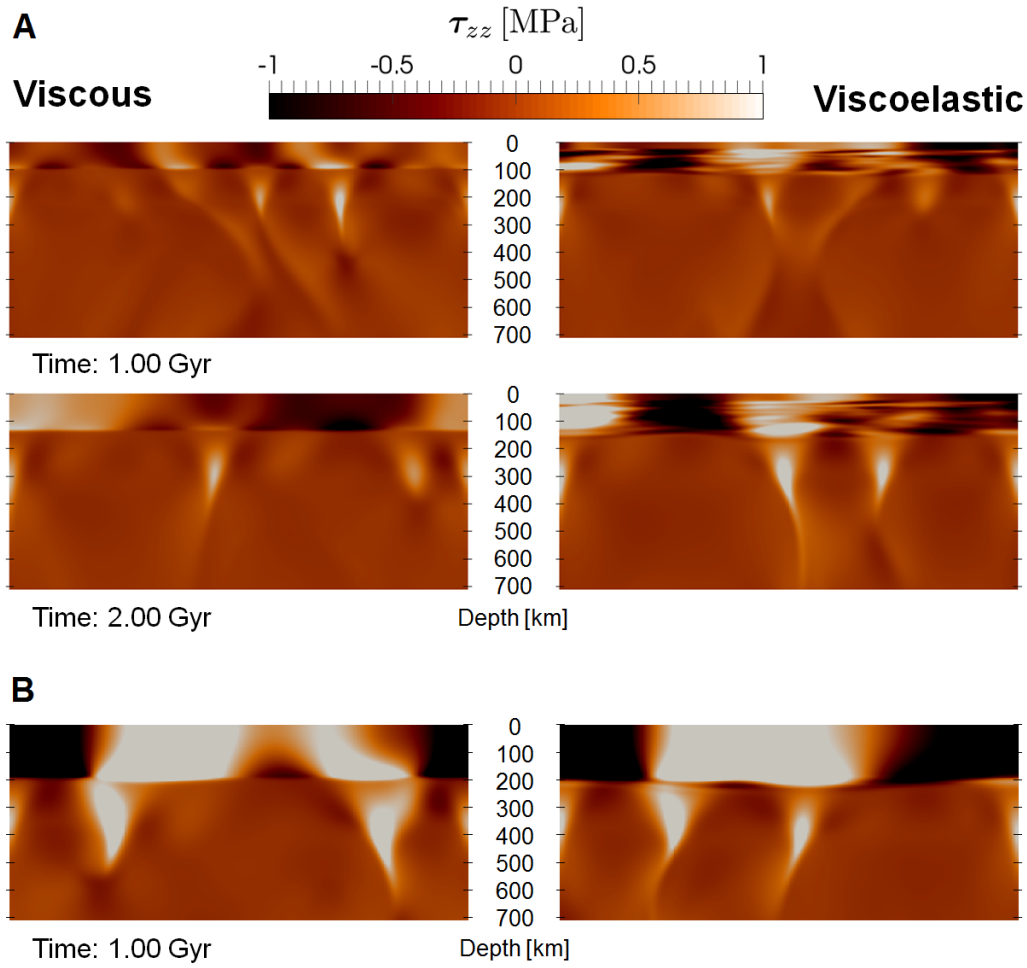

Figure 3.6: Normal stress component τ_{zz} in model M_{vis} (left column) and model M_{el} (right column) after cca. 1 Gyr (top row) and 2 Gyr (second row). Both models have aspect ratio 1, $T_0 = 1900$ K and a free-slip surface. Depths only down to 700 km are shown. Stress scale is clipped for better visibility of the memory effect. (a) Initially thin lithosphere is prescribed, with $d_{TB} = 30$ km. (b) The case with initially thick lithosphere, $d_{TB} = 300$ km.

the bending of initially thin plate (easy to bend and thus reaching relatively large strains) are remembered ('frozen') until cca. 4 Gyr and during cooling and thickening of the lid its deeper parts adopt and remember the stresses due to later bending. The amplitude of the stress in the deeper layers is smaller than the amplitude of the initial surface stress layer due to the fact that the colder and thicker lid becomes increasingly difficult to bend. These large stresses are preserved on time scales comparable to the surface value of t_{M} (4.5 Gyr). After 3 Gyr mantle has cooled down enough and plumes start to develop. Large stresses associated with strong plumes pushing at the base of the lithosphere then overprint the stress pattern associated with the cooling and early bending. Note that the lithospheres of the models with a free surface exhibit bending stresses that are order of magnitude larger than in the previously discussed simulations with a free slip upper boundary.

Figure 3.8 shows vertical profiles of effective stress (horizontally averaged) in both models $\mathrm{M_{vis}}$ and $\mathrm{M_{el}}$, evenly sampled over the first 3 Gyr. It demonstrates thickening of the viscous lithosphere with a typical bending/unbending pattern (left panel) while the viscoelastic lithosphere with generally lower stresses shows preservation of the bending pattern of the initially thin lithosphere (right panel). Note that the stresses associated with bending of the 30 km thick lithosphere are in tens of MPa, while we observed stresses of only a few MPa in the free-slip surface simulations. In the viscoelastic model, the stresses below the 30 km depth are similar as in the free-slip case.

After examining the effects of lithospheric thickening, let us now look at the models in which the lithosphere is initially thick ($d_{\mathrm{TB}} = 300$ km). Such models display no differences between viscous and viscoelastic rheology, in case that a free slip condition is prescribed at the top (Section 3.4.2 above). In free surface models we do observe differences, but of a different nature than the stress memory effect described above.

In these models, the lithosphere is thinning and the layered stress structures thus could not develop here. The stress patterns are dominated by the bending stresses, and these are significantly smaller for the viscoelastic simulations (see the last paragraph of Section 3.3.2 and Fig. 3.3). We demonstrate this in Figure 3.9, which shows the time evolution of the effective stress in E-models within a 3 Gyr long time window taken 12 Gyr after the initiation of the simulation.

Further evolution of the models is characterized by similar stress profiles as depicted in Fig. 3.9 – the stress reduction is a general characteristic of statistically steady state viscoelastic convection with a free surface (i.e. regardless of the value of d_{TB}), as long as the lithosphere is bending and unbending in the reached statistically steady state.

For the M-models the statistically steady states are almost stationary, with a stable plume in the centre and downwellings at the sides. Due to this steady loading the lithosphere is permanently bent, and not flexing up and down as in the previous case. It then reaches the viscous limit and the effects of viscoelasticity

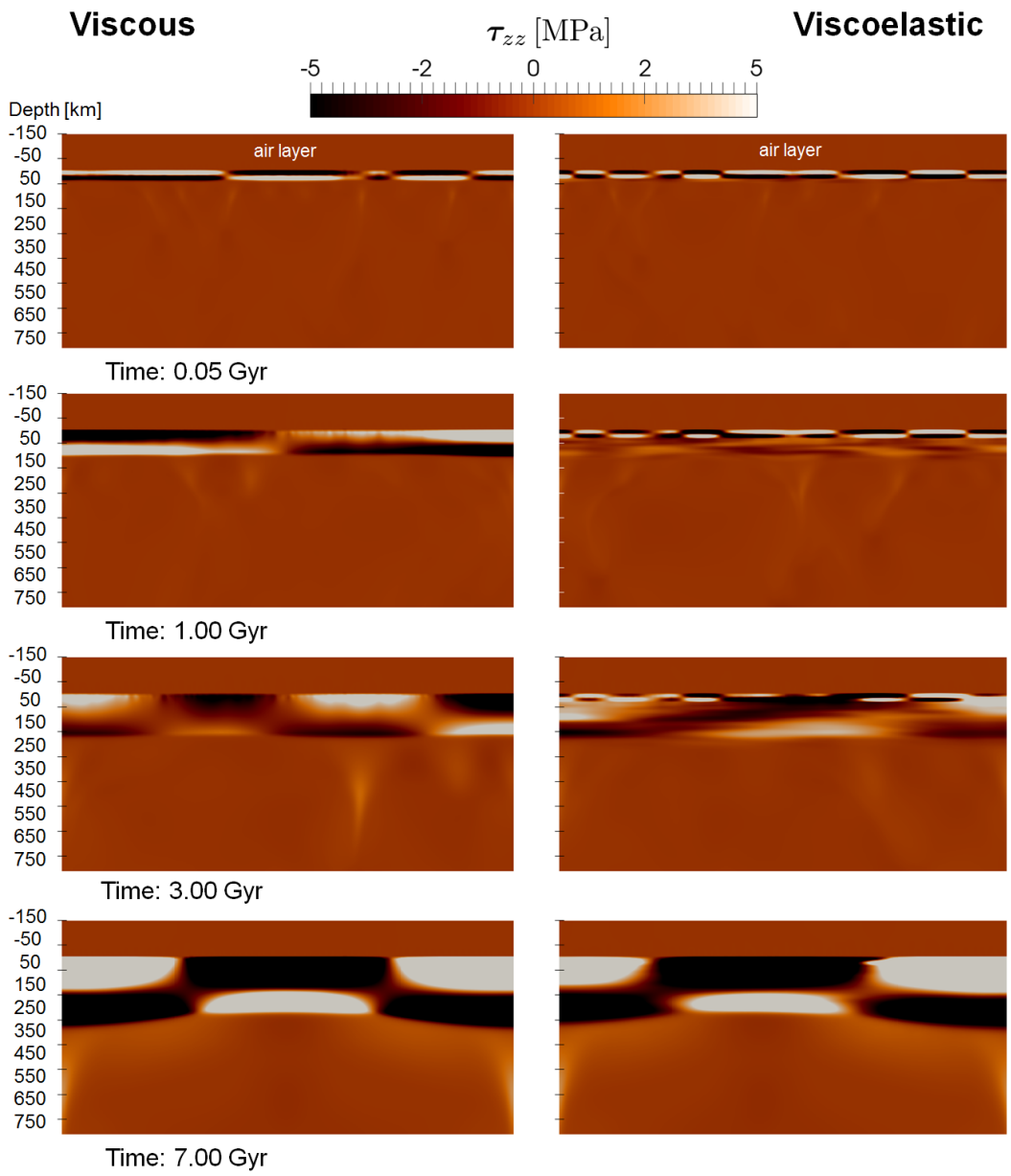

Figure 3.7: Vertical component of deviatoric stress τ_{zz} in model M with aspect ratio 1, $T_0 = 1900$ K, $d_{\mathrm{TB}} = 30$ km and a free surface. Stress scale is clipped for better visibility of the memory effect. Negative depths (in km) show the sticky air layer.

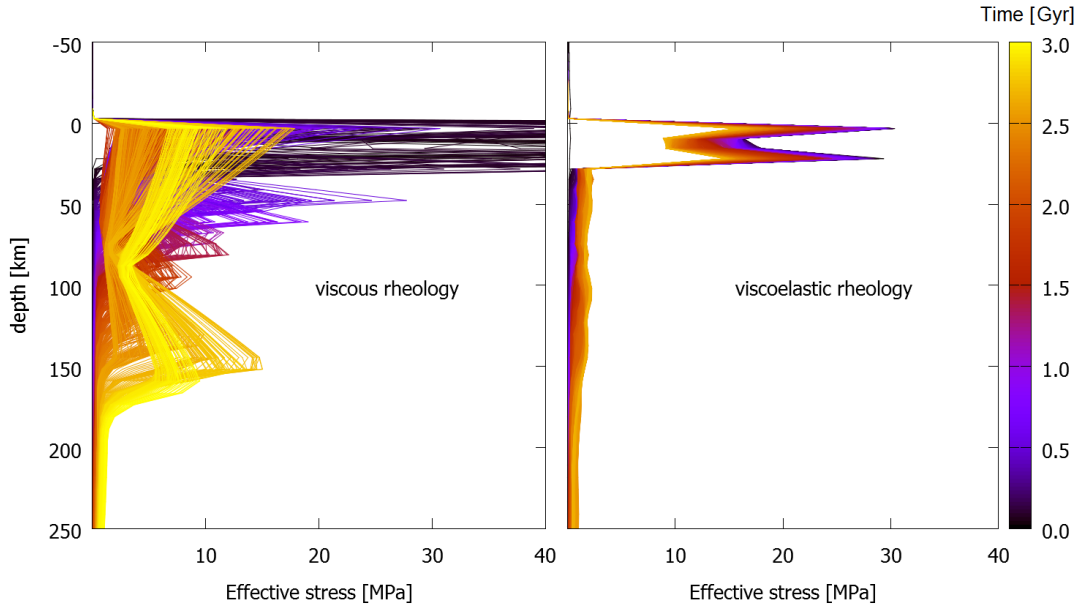

Figure 3.8: Temporal evolution of effective stress τ_{eff} in models M_{vis} and M_{el} with the same parameters as in Figure 3.7. We show horizontally averaged radial profiles that are evenly sampled in time. Colour represents the time in Gyr, only the transient behaviour is shown.

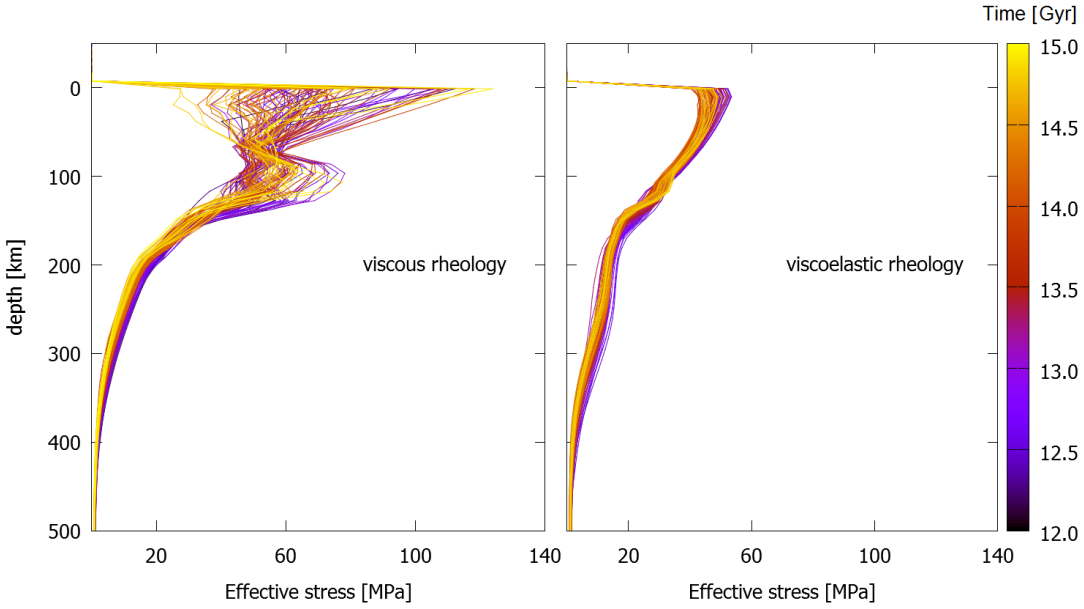

Figure 3.9: Temporal scatter of effective stress τ_{eff} in models E_{vis} and E_{el} with aspect ratio 1, $T_0 = 1900$ K, $d_{\text{TB}} = 300$ km and a free surface. We show 100 horizontally averaged depth profiles that are evenly sampled in time. Colour represents the time in Gyr.

Table 3.2: Summary of the viscoelastic effects in stagnant lid convection

Model characteristics	"Frozen-in" stresses	Stress reduction
Free-slip, initially thick lithosphere	No	No
Free-slip, initially thin lithosphere	Yes	No
Free surface, initially thick lithosphere	No	Yes
Free surface, initially thin lithosphere	Yes	Yes

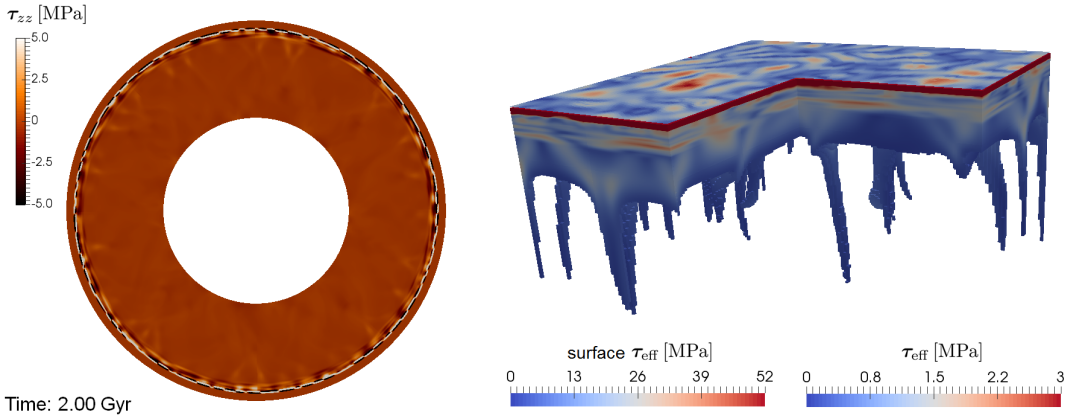

Figure 3.10: Model M_{el} with $T_0 = 1900$ K, $d_{TB} = 30$ km and a free surface after 2 Gyr, computed in 2-D spherical annulus (left) and 3-D Cartesian (right) geometries. Air is not shown in the 3-D model in order to reveal the surface stresses and the model domain is thresholded by an isotherm of 1670 K to show the spatial distribution of the downwellings. The stress scale is clipped in both cases to enhance the visibility of the subsurface layered structures, with the exception of the surface stresses in the 3-D simulation that are shown in their full range.

disappear (c.f. the last snapshot in Fig. 3.7).

Table 3.2 summarizes how the viscoelastic effects depend on the initial and boundary conditions. Both effects are stronger when the vigour of convection is higher.

3.4.4 Robustness of the results

The results presented above were obtained in a 2-D Cartesian geometry with aspect ratio 1. In order to estimate the effects of model geometry we repeated some of the simulations also in aspect ratio 4, 2-D spherical annulus (Hernlund & Tackley, 2008), and 3-D Cartesian box. Based on these tests we can conclude that the stress memory and the stress reduction effects discussed in previous sections are robust, though the stress amplitudes differ in different geometries (c.f. Figure 3.10).

In agreement with studies by Thielmann et al. (2015) and Muhlhaus & Regenauer-Lieb (2005) the sublithospheric mantle convection was hardly affected by viscoelasticity or a free surface in our simulations. This does not imply that the internal dynamics were equivalent for each pair (viscous vs. viscoelastic) of the simulations we performed. Due to the chaotic nature of thermal convection we

observed that some models get locked into a quasi-stable statistically steady state for up to billions of years (e.g. having more, or distorted, convection cells when compared to the stable statistically steady state). To our experience the likelihood of such behaviour was not affected by the inclusion of viscoelasticity and we avoided such cases in the presented work.

3.5 Discussion

We present here the results of numerical experiments focused on the effects of viscoelasticity on the stress and surface topography development of internally loaded lithosphere. First, we use the compositional model of a cylinder rising below the stiff lithosphere introduced by Crameri et al. (2012) and we extended their analysis for a viscoelastic stiff lid and also for higher lithospheric viscosities. We demonstrate that while for lower lithospheric viscosity (10^{23} Pa s) the IVF topography (from a free-slip model) is in good agreement with free surface topography, for higher lid viscosities the differences between free-slip and free-surface models significantly increase. These differences, that is, the error of the instantaneous IVF approach, are largely reduced if the lid is viscoelastic. Similar conclusions were made by Zhong (2002) for stationary loading.

Second, we performed thermal convection models focused on the evolution of planetary mantles. Lithospheric stresses were shown to differ considerably. If a free surface is prescribed and stiff lithosphere is thus able to bend and build topography, then viscoelastic models generally show lower stress amplitudes than purely viscous models. If a planetary mantle is cooling from an initially hot state with a thin lithosphere, then the memory effects associated with viscoelastic deformation result in a complex layered stress pattern, in which the shallower layers reflect preceding sublithospheric convective features active during the earlier stages of the model evolution. These frozen-in stresses remain visible on a time scale comparable to the Maxwell relaxation time of the lithosphere. The described phenomenon is thus a transient feature and depends on the initial temperature distribution. It is clearly favoured by the initially thin thermal boundary layer that may result from cooling of a magma ocean (Solomatov, 2007). The vigour of the initial convection increases the observed complexity of the stress structure that is being recorded in the cooling and thickening lithosphere.

Thielmann et al. (2015) also observe non-smooth deviatoric stresses, while presenting simulations with surface Deborah numbers up to $De_s = 10^5$. Since the Deborah number is given by the ratio of the lithosphere's viscoelastic relaxation time to the diffusion time, it takes approximately De_s diffusion times for the stresses to relax from a certain state. The simulations presented in Thielmann et al. (2015) do not last multiples of the diffusion times, thus it is likely that the stress state of the lithosphere is largely influenced by the initial conditions, even though it cannot be seen from the Nusselt numbers or average velocity of the flow.

The key parameter controlling the importance of the memory effect is the Maxwell relaxation time of the lithosphere. The viscosity of the crust and lithosphere that determines the relaxation time is, however, largely unknown. Its estimates based on postglacial rebound inversions only give a lower bound, since the glacial cycle occurs on a time scale of about 100 kyr. Layers with t_{M} larger than 100 kyr behave effectively as an elastic material to such loading (see Section 3.3) and GIA (glacial isostatic adjustment) inversions are thus insensitive to higher viscosities. The fact that subduction or loading due to sedimentation are successfully modelled using a thin elastic plate theory again provides only the lower bound on the viscosity, in the sense that that t_{M} must be larger than the characteristic time of these phenomena.

In our simulations the Maxwell relaxation time of the lithosphere was determined by the upper viscosity cut-off. Lowering its value directly decreases the importance of the medium's memory. The ability to quickly deform in an elastic manner remains intact. One may thus expect the stress reduction effect to be independent on cut-off viscosity. However, less stiff purely viscous lids show smaller resistance when compared to more stiff purely viscous ones, and decreasing the cut-off value thus reduces the importance of both the stress memory and the stress reduction when comparing viscous and viscoelastic models with the same lithospheric viscosities. In a limited extent we still observed both effects when lowering η_{max} down to 10^{25} Pa s in thermal convection simulations with a free surface.

The models presented here were designed to investigate the basic effects of viscoelasticity on the evolution of a stiff planetary lid. As such they suffer from several simplifying assumptions. The first and probably major one is that the rheological description does not include any form of plastic yielding, even though the brittle failure and ductile yielding are important deformation mechanisms in the lithosphere and limit the resulting stresses. The second one is the simple Boussinesq approximation of the energy equation that does not account for shear heating. Viscous dissipation could play an important role in strain localization in a visco-elasto-plastic model (e.g. Schmalholz & Duretz (2015)). In particular, it was recently shown by Jaquet et al. (2016) that the release of elastic energy promotes faulting induced by thermal softening. On the basis of our results we may speculate that yielding or thermal softening would occur on shorter wavelengths in the models that include viscoelasticity. Especially in the early stages of planetary evolution, when their thermal boundary layer is thin, viscoelasticity in combination with plasticity could dramatically affect lithospheric deformation or regime of convection. Indicative in this regard may be the results by Muhlhaus et al. (2006), who demonstrate an increase in the frequency of overturns in the episodic lid regime due to elasticity. Such a scenario should in future be tested in visco-elasto-plastic models in three-dimensional spherical geometry.

Despite the above mentioned simplifications we believe that our models demonstrate that including viscoelasticity is important if stress evolution and deforma-

tion of the lithosphere in models of planetary mantles are addressed.

Acknowledgments

VP acknowledges the support from the Sciex project No. 13.250 and the Charles University grant SVV260327/2016. We thank Louis Moresi, Thibault Duretz and an anonymous reviewer for helpful comments that significantly improved the manuscript.

3.A Benchmark tests

Our implementation of viscoelasticity was verified using two benchmark tests: (i) a stationary viscoelastic flow in a 2-D box with aspect ratio 1 (Harder, 1991) and (ii) the deformation of an elastic slab embedded in a viscous medium (Gerya, 2010).

3.A.1 Thermal convection of an isoviscous Maxwell fluid

In this benchmark we test the implementation of the advection and corotation of the stress. We perform the simulation of thermal convection of an isoviscous Maxwell fluid in a 1×1 Cartesian box. We assume the Boussinesq approximation and reproduce results of Harder (1991) for Rayleigh number 9487 and Deborah number 1.5×10^{-3} (Fig. 3.11) on a mesh with 40×40 grid points. We make a visual comparison of the isolines of vorticity, temperature, deviatoric shear stress and normal stress difference (the exact values of isolines are stated in Harder (1991)).

In reproducing the stationary flow it is important to realize that the Weissenberg number, $W_{ei} := 2De\|\mathbb{D}\|D^2/\kappa$, is close to 1 for $De = 1.5 \times 10^{-3}$ and the given model setup. A Maxwell body with Jaumann's rate chosen as the stress rate (i.e. the medium we study) exhibits shear softening in a simple shear flow for Weissenberg number greater than 1 (see Muhlhaus & Regenauer-Lieb (2005) for details) and shear softening leads to numerically unstable solutions. The viscoelastic convection simulation thus needs to be started from a state which is close to the stationary solution (e.g. from the viscous stationary solution), in order not to exceed the critical Weissenberg number when reaching the final state.

For Deborah numbers higher than 1.5×10^{-3} we no longer reach a stationary solution and the simulations become numerically unstable (the velocities go to infinity). Setting a lower bound on the time step used in the rheological equations (3.11) – (3.13) prevents such instabilities, largely extending the range of Deborah numbers that can be modelled. Detailed analysis of the problem is beyond the scope of this paper – in the convection simulations of planetary bodies presented in the main text we are far from the critical Weissenberg number.

In this benchmark test we used a grid-based donor cell advection technique instead of the tracer based advection scheme applied in all other calculations.

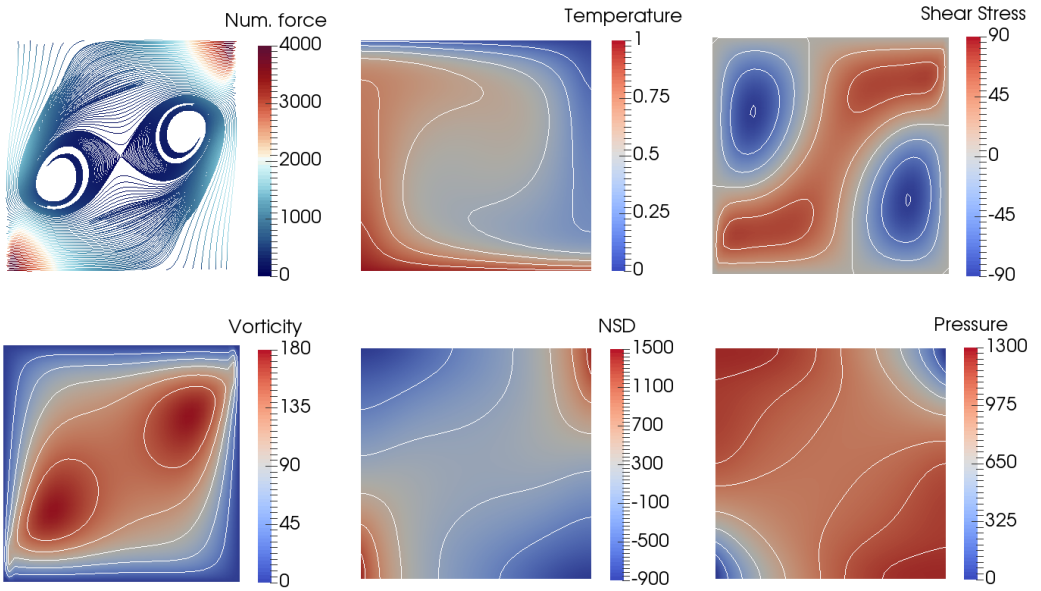

Figure 3.11: Stationary flow of an isoviscous fluid in a 40 × 40 box with free slip boundaries, $De = 0.0015$. See Harder (1991) for comparison with a viscous solution and for exact values of the isolines. Left top picture shows streamlines of the extra force term $\nabla \cdot [(1 - \mathrm{Z})\tilde{\boldsymbol{\tau}}^{\mathrm{n}-1}]$, middle picture in the bottom row displays normal stress differences.

Tracer based advection of stress does not perform well in this case, due to the high vorticity gradient in the corners of the box (in combination with the low resolution of the mesh). The number of tracers per cell needed to produce results comparable to the grid-based approach is over 1000 here. The time step was governed by the CFL stability criterion.

3.A.2 Recovery of the original shape of an elastic slab

Following Gerya (2010) we further examine the deformation of a hanging slab due to gravitational force. An effectively elastic slab, attached to the left boundary, is being steadily deformed over 20 kyr by gravity ($g = 10$ m s^{-2}). After 20 kyr gravity is switched off and the original shape of the slab is recovered. The slab viscosity is 10^{27} Pa s and its shear modulus is 10^{10} Pa. The effectively viscous medium that surrounds the slab has a viscosity of 10^{21} Pa s and a shear modulus of 10^{20} Pa. The density of the slab is 4000 kg m^{-3} while the surrounding material has a density of 1 kg m^{-3}. Extreme discontinuities in material parameters are treated using harmonic averaging of the shear modulus in order to avoid high numerical viscosity on the interfaces (Gerya, 2010). A resolution of 128 × 128 nodes with 100 particles per cell was used, time step of 2 yr was being gradually increased after reaching 30 kyr. Results are summarized in Fig. 3.12(a). The elastic (relaxation time ∼ 3 Gyr) slab fully recovered its shape while the viscous medium sustained permanent deformation.

This particular example is rather challenging as the model includes sharp

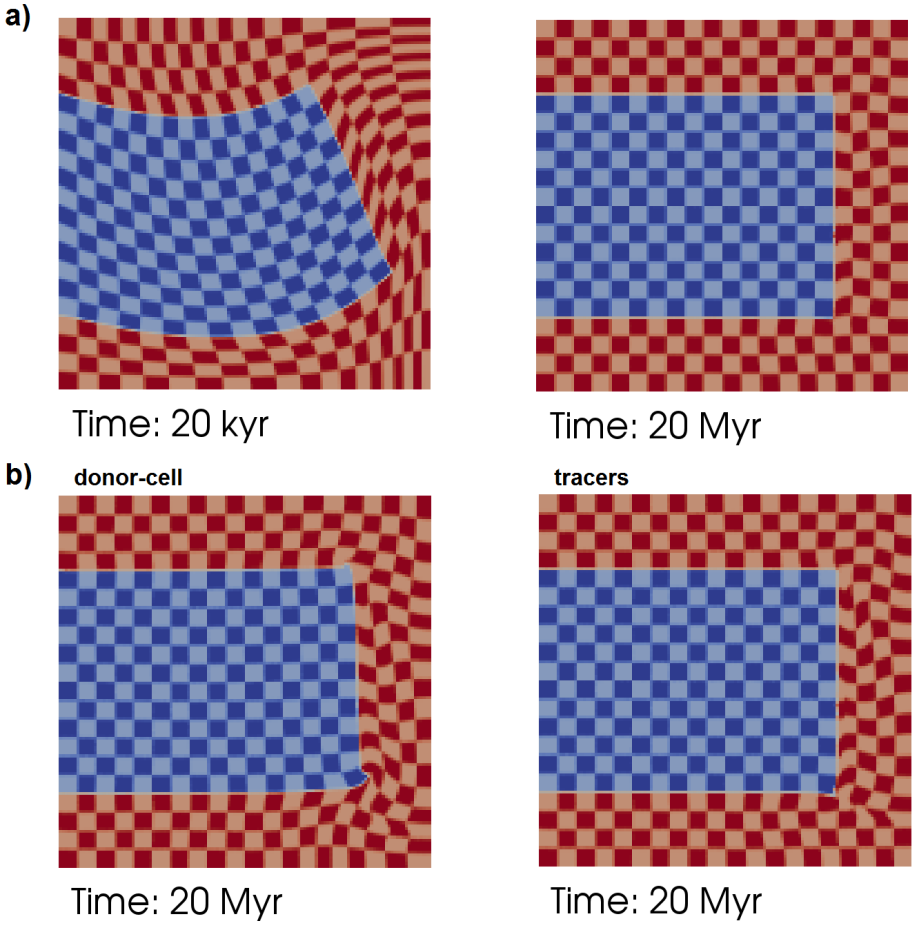

Figure 3.12: (a) Reproduction of numerical experiment by Gerya (2010). A slab with high viscosity of 10^{27} Pa s and shear modulus 10^{10} Pa is attached to the left boundary and surrounded by a weak viscoelastic medium with viscosity 10^{21} Pa s and shear modulus 10^{20} Pa. Density of the slab is 4000 kg m^{-3}, density of the surroundings is only 1 kg m^{-3}. (b) Comparison of the numerical methods used for advection of stresses. Gravity is switched off after 35 kyr and not 20 kyr as in the upper case, left panel shows the recovery when grid-based donor cell method is applied, right panel shows the recovery when tracers are used to advect the stresses.

interfaces with strongly varying properties. Numerical diffusion has to be kept to a minimum when treating advection of quantities, including the stresses, in order to retain clear interfaces as the slab is being deformed and then relaxed to its original position. While both methods that we tested, that is, donor cell scheme and storing stress on tracers, lead to a perfect recovery of the slab for the case described above, the methods begin to differ if gravity is applied longer than for 20 kyr. Fig. 3.12(b) compares the recovery obtained when the gravity was switched off only after 35 kyr (still a negligible time with respect to the relaxation time of the slab). We see that numerical diffusion has slightly distorted the recovery when grid-based donor cell method was used, especially near the unattached corners of the slab. Quantities other than the stress (η, μ and ρ) were carried on tracers in both cases.

Parts of the slab experience significant rigid body rotation during the studied process and the corotational term in eq. (3.7) is thus crucial – omitting it would lead to distorted recovery of the slab.

3.B Subgrid oscillations of stress

Similarly to advection of the temperature field, the problem with treating advection of stresses using the incremental update scheme by Gerya & Yuen (2007) is that stress jumps on adjacent markers, resulting from flow-induced stirring, cannot be damped out by grid-scale corrections.

Fig. 3.13 shows an example of such oscillations in a thermal convection simulation. The viscoelasticity parameter Z is close to one (cca. 0.8) in the circled region and the stress should thus be governed by the viscous creep, forming relatively smooth patterns. However, tracers with a different stress history are transported close to each other in the selected region. The grid-scale updates of stresses (eqs 22 and 23 in Gerya & Yuen (2007)) cannot relax such subgrid stress differences and result in the depicted unphysical oscillations of the stress field. The likelihood of such oscillatory behaviour increases with increasing resolution and with the number of tracers per cell.

In our modification of the algorithm designed by Gerya & Yuen (2007), we use directly Eq. (3.11) to evaluate the stress tensor on each tracer. First, the tracers are advected and the corotational term, computed on the grid, is interpolated to them. Then, the value of the viscoelasticity parameter is computed on the grid and interpolated to each tracer, so that we can multiply the stress on each tracer by $(1 - \mathrm{Z})$. Finally, the term $2\mathrm{Z}\eta\mathbb{D}^{\mathrm{n}}$ is computed on the grid and interpolated to each tracer.

In regions with Z close to 1, the procedure leads to practically re-setting the value of stress on each tracer to $2\mathrm{Z}\eta\mathbb{D}^{\mathrm{n}}$ at each time step, and two adjacent tracers will thus carry similar stress tensors after the procedure, even if before there was a mutual stress jump (consequently, the oscillations as depicted in Fig. 3.13 are not observed). In regions with Z close to 0, the procedure behaves

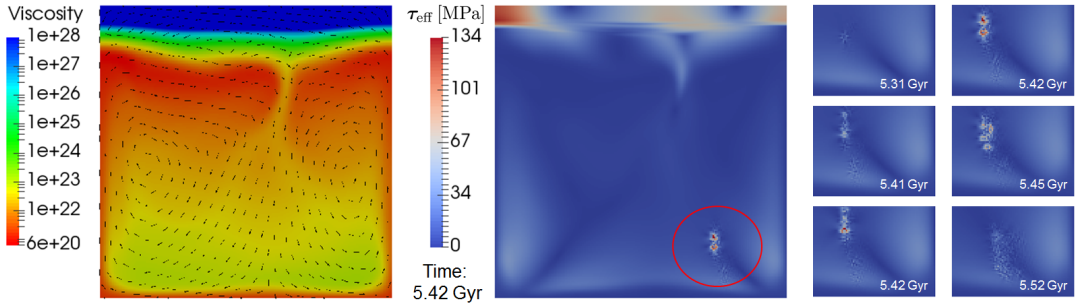

Figure 3.13: Stress oscillations in a viscoelastic thermal convection. Red circle points to the oscillatory behaviour, right panel zooms in the respective part of the model domain in a sequence of time steps. Model parameters are the same as in Fig. 3.4 from the main text.

as an incremental update scheme: the stress tensor changes only slightly on each tracer and mutual stress differences among the tracers are preserved. This is important as interpolating the entire stress (instead of the stress change) from grid to tracers would lead to spurious numerical diffusion in such regions.

4. Spontaneous initiation of subduction in mantle convection models with elasticity and a free surface

4.1 Introduction

The onset of plate tectonics on Earth is not well understood. For how long has the Earth's surface been covered by mutually colliding and subducting plates is unknown – the geochemical and geological data provide only limited constraint, with most estimates ranging from cca. 600 Myr to about 3.5 Gy (e.g. Dhuime et al., 2015). Various mechanisms have been proposed to weaken the existing plate boundaries and thus to allow for subductions to proceed, but only a few of these can act to form a new lithosphere-scale shear zone inside of an unbroken plate. In other words, many mechanisms that localize deformation within a narrow zone and make the sliding of one plate under another possible require already ongoing plate tectonics. This is the case for grain size reduction (e.g. Rozel et al., 2011), shear heating (e.g. Thielmann & Kaus, 2012), hydration of the subducted crust and mantle (Regenauer-Lieb et al., 2001), or sedimentary loading (Cloetingh & Wortel, 1982). However, most of terrestrial bodies are currently in a stagnant lid regime of convection (Moresi & Solomatov, 1995) and also the early Earth's mantle was likely to convect below a stagnant lid after the freezing of its primordial magma ocean (Solomatov, 2007). Investigating the transition from a stagnant lid to a plate-like mode of convection is thus of primary interest when trying to explain the fundamental differences between tectonic behaviors of terrestrial planets, or when deciphering the onset of plate tectonics on Earth.

There are two primary sources of forces acting to break a stagnant lid: lateral variations of pressure resulting from the variations in lid thickness and basal traction due to convection of the underlying mantle (e.g. Solomatov, 2004a). The stresses that develop in the lithosphere due to these forces are much smaller than the experimentally determined values of yield strengths of rocks (Kohlstedt et al., 1995). In order to "break the lid" (form more plates out of one) in a numerical model, one may assume that over geological time scales the strength of the lithosphere is actually small, and parametrize its brittle and ductile yielding by a much smaller friction angle and yield stress value than measured in the laboratory. The critical yield stress value (the maximum strength one can prescribe and still obtain lid failure) was found only very small (a few MPa) in models of upper mantle, downwelling dominated convection (Solomatov, 2004a). Somewhat stronger lithosphere may be assumed when plate-like behaviour is to be reached

in a global-scale model of mantle convection (Tackley, 2000). More recently, Lu et al. (2015) initiated subduction in a model that employed laboratory values of rock strength, but the temperature anomaly driving the flow (and controlling the amplitude of lithospheric basal traction) was imposed rather than self-consistently developed in a convection simulation.

Once a subduction forms it may lead to a global overturn of the mantle, completely resurfacing the planet and sweeping away any geological evidence of the former lithosphere. The only method with a potential to see inside a planet throughout such events is numerical modelling. However, the focus of global-scale geodynamical models has traditionally been on the deeper parts of the mantle rather than near its surface, and for this reason the codes developed in the community have long suffered from two simplifications: 1) approximating outer surface by a free-slip boundary, and 2) neglecting the elastic properties of the lithosphere by assuming that it behaves as viscous rather than viscoelastic fluid on geological time scales.

Recently, it was shown by Crameri & Tackley (2016) that initiating subduction is easier when the traditional free-slip surface is replaced by a more realistic, free surface upper boundary condition. Owing to the ability to build topography and bend the lithosphere, stresses are much higher in models with a free surface, raising the critical value of yield stress by tens of percent. While considering a free surface increases the lithospheric stresses, considering viscoelasticity, on the other hand, significantly reduces these. It is because accounting for elastic in addition to viscous deformation lowers the lithospheric resistance to bend, making it depend not only on the value of the plate's viscosity but also on the value of its shear modulus. As a result, one may easily exaggerate lithospheric stresses by considering a free surface and neglecting elasticity, as was shown in models of stagnant lid convection by Thielmann et al. (2015) and Patočka et al. (2017). Here we test whether this also applies in models that include plasticity: we systematically study the effects of a free surface and elasticity on the critical value of yield stress defining the transition between stagnant lid and plate-like mantle convection.

The outline of the chapter is as follows. First, we focus on small-scale, internally heated convection in the upper mantle, following the works of Solomatov (2004a) and Crameri & Tackley (2016). We repeat a set of viscoplastic models from Crameri & Tackley (2016) and extend it by performing also simulations with visco-elasto-plastic rheology. Next we turn to global-scale models with hot plumes rising up to the lithosphere-astenosphere boundary (LAB) where they produce a strong basal drag on the lithosphere. Initiating subduction by a strong plume is more probable than doing so by the small-scale convection, and such events have already been reported both in numerical and analogue models (e.g. Davaille et al., 2017; Lu et al., 2015; Crameri & Tackley, 2016). We evaluate the influence of free surface and elasticity on such plume-induced subduction within a model that contains many of the complexities present to the real Earth – phase

transitions, compositional dependence of physical properties, and a combination of internal and basal heating.

Parametric studies of mantle flow, such as the one presented here, have to deal with the intrinsic chaoticity of thermal convection. Since two simulations with identical parameters and only slightly different initial conditions may result in quite different internal dynamics, it may be difficult to distinguish between an effect of a varied parameter and mere randomness. In this paper we discuss how comparing two sets of simulations, each set having identical initial conditions, can lead to a misleading conclusion about the role of the parameter whose influence is being tested.

4.2 Model setup

We test here two scenarios of subduction initiation – by small-scale convection and by plume-lithosphere interaction. Each of these scenarios has somewhat different model setup. In the first group we repeat and extend the regional, 2-D Cartesian models addressed in table 2 of Crameri & Tackley (2016). These assume an incompressible, internally heated upper mantle and apply the Boussinesq approximation. Their aspect ratio is 4. Viscosity is only temperature dependent and follows Frank-Kamenetskii approximation:

$$\eta(T) = \frac{\rho_0^3 g \alpha H D^5 C_p}{k^2 Ra_H} \exp\left(-\frac{k\theta T}{\rho H D^2}\right). \tag{4.1}$$

The meaning of symbols is summarized in Table 4.1. The values of these model parameters are obtained by dimensionalization (for details see Crameri & Tackley (2016), only here we set the surface temperature to 0 K) of the original non-dimensional models by Solomatov (2004a). In the original models only two parameters are needed to describe the $\eta(T)$ relationship: the heating-based Rayleigh number Ra_H and Frank-Kamenetskii parameter θ. For the simulations presented here $Ra_H = 0.1$ and $\theta = 60$. The regional models are designed to assess lithospheric stresses resulting from small-scale convection, which may be occurring in the upper mantle.

The second group of models is designed for investigating plume-induced subductions. We perform 2-D spherical models with parameters adopted from Lourenco et al. (2016). These incorporate realistic parameter values descriptive of the planet Earth and thus include compressibility, phase transitions, shear heating, diffusion creep with pressure and temperature dependent viscosity, and are heated both internally and from the bottom. Values of model parameters are summarized in Tables 4.2 and 4.3 and are identical to the ones in Lourenco et al. (2016), with the exception of internal heating rate and the half-life of radioactive elements. Here we study statistically steady states of convection and so we assume a much lower and time-constant value than Lourenco et al. (2016) used in their

evolutionary model. We use reference viscosity of 10^{21} Pa s – the relatively high value allows for a clearer identification of regime boundaries (cf. fig. 1 in Lourenco et al. (2016)).

The physical model assumes truncated anelastic Boussinesq approximation:

$$\nabla \cdot (\rho \boldsymbol{v}) = 0, \tag{4.2}$$

$$-\nabla p + \nabla \cdot \boldsymbol{\tau} + \rho \boldsymbol{g} = 0, \tag{4.3}$$

$$\rho C_p \left(\frac{\partial T}{\partial t} + \boldsymbol{v} \cdot \nabla T \right) = -\alpha T \rho |\boldsymbol{g}| v_z + \nabla (k \nabla T) + \rho H + \boldsymbol{\tau} : \mathbb{D}_{\text{vis}}, \tag{4.4}$$

with $\boldsymbol{\tau}$ being the deviatoric Cauchy stress tensor, p is the pressure, $\boldsymbol{v}$ is the velocity, v_z its radial component (z is the depth), T is the temperature, ρ is the density, and $\mathbb{D}_{\text{vis}}$ is the viscous part of the strain-rate tensor (full strain-rate tensor in non-elastic cases). The meaning of other symbols and their values are given in Table 4.2.

The density ρ is equal to $\bar{\rho}(z)(1 - \alpha(T - \bar{T}(z))$, where $\bar{\rho}(z)$ and $\bar{T}(z)$ are the depth-dependent reference density profile and reference adiabat respectively. The reference density is computed using the third-order Birch-Murnaghan equation of state along the reference adiabat with a potential temperature of 1600 K. We assume two mineralogical systems, labeled as "Olivine" and "Pyroxene-garnet". Each system corresponds to several (3 resp. 4 – see Table 4.3) mineral phases that change with the depth z. For details and parameters used to compute the reference state we refer to Lourenco et al. (2016) and the references therein. In Fig. 4.1 we show the resulting reference density profile for both mineralogical systems and the combined adiabat representative of the entire model, which is obtained by assuming that the fraction of the "Olivine" system is 0.6 of total.

Rocks in the cold lithosphere have a finite strength which may be exceeded due to the convective forces, resulting in brittle failures of the rocks. At higher temperatures and pressures, that is, in the deeper parts of the lithosphere, a ductile creep may similarly be activated. Both these mechanisms are parametrized by a plastic flow rule with pressure dependent yield stress

$$\tau_{\text{y}} = \tau_0 + \mu\, p, \tag{4.5}$$

where τ_{y} is the yield stress, τ_0 is its surface value, μ is the friction coefficient and p is the pressure. In the first group of models, repeating Crameri & Tackley (2016), both τ_0 and μ are varied. In the second group of models only τ_0 is varied and μ is fixed at the value of 0.0024. In both cases the tested values of rock strength are generally much lower than laboratory measurements would suggest. In view of this fact, the role of the friction coefficient is primarily to avoid yielding in the deep mantle rather than to represent a realistic Byerlee's friction law. It is essentially the integrated strength of the lithosphere that matters when the failure of a stagnant lid is investigated, as pointed out by Solomatov (2004a). We

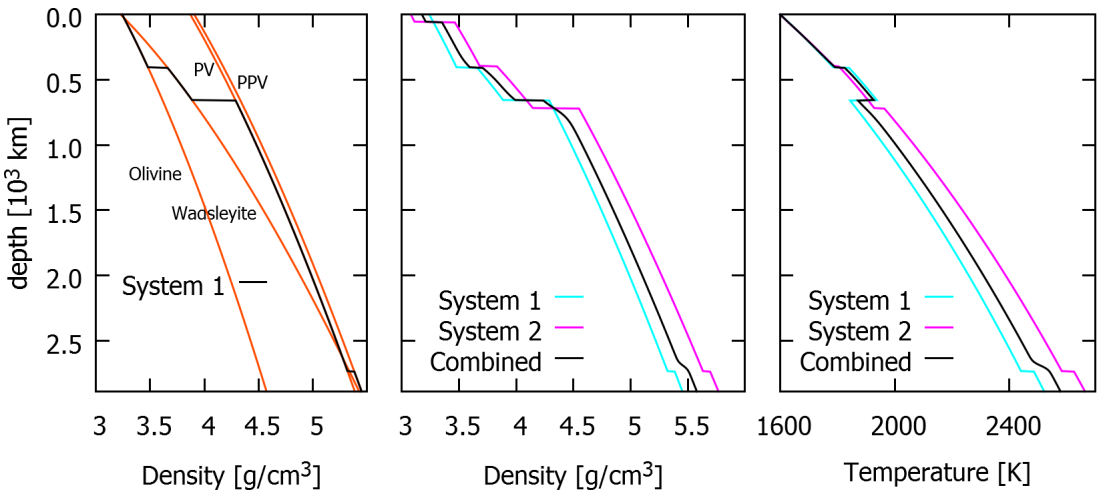

Figure 4.1: Reference density profile (center) and reference adiabat (right) for the two considered mineral systems: "Olivine" (light blue) and "Pyroxene-garnet" (magenta). Black lines are the combined profiles $\bar{\rho}(z)$ and $\bar{T}(z)$ respectively. Left panel illustrates how the profiles for each system are constructed: for each mineral phase we compute the third-order Birch-Murnaghan equation of state along an adiabat (also computed separately for each mineral phase) and combine these into one curve to match the mineral phases with their respective depth ranges.

pay further attention to the parametrization of plasticity in the discussion.

For each tested value of τ_0 and μ we perform three simulations: 1) with visco-plastic (VP) rheology and a free-slip upper boundary (represented by red colour); 2) with VP rheology and a free surface (green); and 3) with visco-elasto-plastic (VEP) rheology and a free surface (blue). Within this framework, the effects of elasticity and free surface are systematically studied. Numerical solutions are obtained with the code StagYY (Tackley, 2008), enhanced to model the flow of VEP instead of VP material using the method originated by Moresi et al. (2002). The details of the implementation of elasticity into StagYY and numerical benchmarks are described in Patočka et al. (2017).

To approximate a free surface we use a sticky-air layer (Matsumoto & Tomoda, 1983; Schmeling et al., 2008). For our global-scale models the air layer has thickness of 150 km and viscosity 10^{19} Pa s, for regional-scale models we follow Crameri & Tackley (2016) and set these values to 30 km and 6.92×10^{19} Pa s. In both cases the C-condition, determining whether the channel flow in the air layer is putting up only little resistance to the mantle flow and thus a good approximation of a free surface is achieved, is well satisfied. In order to avoid the 'drunken sailor effect' a stabilization algorithm by Kaus et al. (2010) is employed (see also Duretz et al., 2011).

In the first group of models the initial temperature distribution follows the relation:

$$T(z) = T_0 \left(1 - \exp\left(\frac{-z}{d_{\mathrm{TB}}}\right)\right), \tag{4.6}$$

Table 4.1: Parameters used in the regional-scale models

Parameter	Symbol	Value	Units
Mantle depth	D	600	km
Gravitational acceleration	g	9.81	m/s^2
Reference density	ρ_0	3300	kg/m^3
Surface temperature	T_{surf}	0	K
Internal heating rate	H	6.31×10^{-12}	W/kg
Thermal expansivity	α	3×10^{-5}	K^{-1}
Thermal conductivity	k	3	W/K/m
Heat capacity	C_p	1200	J/kg/K
Shear modulus	G	7×10^{10}	Pa

where T_0 is the initial internal temperature (temperature below the thermal boundary layer), $d_{TB} = 180$ km is the initial thickness of the thermal boundary layer, $D = 600$ km is the thickness of the upper mantle and z is the depth. We perform three sets of simulations that differ by the value of T_0, with its value set to 650, 700 and 750 K, and label these sets r650, r700, and r750 respectively. The symbol "r" stands for reflective side boundaries. In another set of simulations, labeled w700, we deviated from Solomatov (2004a) and Crameri & Tackley (2016) and set the side boundaries so that the model domain is wrapped around at its sides (material leaving the right boundary appears on the left side and vice versa). Random temperature perturbations with amplitude 25 K are used to initiate convection. The values of d_{TB} and T_0 are such that convection only gradually develops slowly thins the lithosphere. We aim to asses the critical value of yield stress in statistically steady state of convection for each model – breaking the lid in the initial transient stage of model evolution is not desired in the first group of models.

In the second group of models the initial temperature distribution follows the relation:

$$T(z) = T_0 + (T_{surf} - T_0)\exp\left(\frac{-z}{d_{TB}}\right) + (T_{CMB} - T_0)\exp\left(\frac{z-D}{d_{TB}}\right), \qquad (4.7)$$

where $T_0 = 1800$ K is the temperature at the mid-depth, $T_{surf} = 300$ K and T_{CMB} are surface and core-mantle boundary temperatures, $d_{TB} = 100$ km is the initial thickness of the thermal boundary layer, $D = 2890$ km is the mantle thickness and z is the depth. In accord with the time-constant internal heating we also assume a time-constant T_{CMB} and set it so that the superadiabatic temperature difference is 2500 K across the entire mantle (unlike in the evolutionary model by Lourenco et al. (2016), where core cooling is taken into account).

Table 4.2: Parameters used in the global-scale models (UM = upper mantle (dry olivine); PV = Perovskite; PPV = Post-Perovskite)

Parameter	Symbol	Value	Units
Mantle depth	D	2890	km
Gravitational acceleration	g	9.81	m/s^2
Reference density	ρ_0	3300	kg/m^3
Surface temperature	$T_{\rm surf}$	300	K
Super-adiabatic temp. diff.	$\triangle T$	2500	K
Reference viscosity	$\eta_{\rm ref}$	10^{21}	Pa s
Upper viscosity cut-off	$\eta_{\rm max}$	10^{27}	Pa s
Thermal diffusivity	κ	7.6×10^{-7}	m^2/s
Thermal expansivity	α	3×10^{-5}	K^{-1}
Heat capacity	C_p	1200	J/kg/K
Gas constant	R	8.3145	J/K/mol)
Internal heating rate	H	5.2×10^{-12}	W/kg
Half-life	$t_{\rm half}$	∞	Ga
Activation energy - UM	$E_{\rm ol}$	300	kJ/mol
Activation volume - UM	$V_{\rm ol}$	5.00	cm^3/mol
$p_{\rm decay}$ - UM	$p_{\rm decay_{ol}}$	∞	GPa
Activation energy - PV	$E_{\rm pv}$	370	kJ/mol
Activation volume - PV	$V_{\rm pv}$	3.65	cm^3/mol
$p_{\rm decay}$ - PV	$p_{\rm decay_{pv}}$	200	GPa
Activation energy - PPV	$E_{\rm ppv}$	162	kJ/mol
Activation volume - PPV	$V_{\rm ppv}$	1.40	cm^3/mol
$p_{\rm decay}$ - PPV	$p_{\rm decay_{ppv}}$	1610	GPa
Shear modulus	G	7×10^{10}	Pa

Table 4.3: Phase change parameters $\rho_{\rm surf}$ stands for surface density, $\Delta\rho_{\rm pc}$ is the desity jump across a phase transition and γ is the Clapeyron slope.

Depth (km)	Temperature (K)	$\Delta\rho_{\rm pc}$ (kg/m^3)	γ (MPa/K)
	Olivine ($\rho_{\rm surf}$=3240 kg/m^3)		
410	1600	180	2.5
660	1900	400	-2.5
2740	2300	61.6	10.0
	Pyroxene-garnet ($\rho_{\rm surf}$=3080 kg/m^3)		
60	1000	350	0.0
400	1600	150	1.0
720	1900	400	1.0
2740	2300	61.6	10.0

4.3 Results: small-scale convection

4.3.1 Influence of elasticity and a free surface on the critical value of yield stress

At the beginning of our simulations the upper mantle is rather cold and the thermal boundary layer thick. The conductive heat flux near the surface does not balance out the internal heat production and the internal temperature is rising in effect. Downwellings (sinking plumes) develop and get stronger as the temperature difference across the thermal boundary layer is increasing. As a result, gradually deeper plastic yielding gets triggered in the thinning lithosphere, eventually reaching the LAB in some of the simulations. The formation of lithospheric-scale shear zones may cause the entire lid to "break" and sink into the mantle. We adopt the notation by Solomatov (2004a) and call these subduction events, even though they are missing some of the defining features of Earth-like subductions as discussed below.

In Table 4.4 we show the time that elapsed before the first subduction event occurred in each of the performed simulations. If failure of the lid did not occur within 10 Gy we mark the time as infinity. In Table 4.5 we summarize the results from Table 4.4 and compare them with the previous results by Crameri & Tackley (2016). For each yield stress profile we show two numbers, the first one is the percentage of simulations that experienced a subduction event within the first 10 Gy and the second number (in parentheses) is the harmonic mean of the first-event times from Table 4.4.

Table 4.4: Time (in Gy) of the first subduction event for each performed simulation

τ_y profile																
Byerlee	$\mu = 0.003$				$\mu = 0.004$				$\mu = 0.005$				$\mu = 0.006$			
$\tau_y = \mu p$	r650	r700	r750	w700	r650	r700	r750	w700	r650	r700	r750	w700	r650	r700	r750	w700
	3.7	3.6	5.4	3.3	5.1	4.3	9.6	4.4	∞	∞	∞	∞	9.6	6.0	∞	∞
	4.2	3.4	1.8	4.0	9.4	5.2	2.6	5.2	∞	∞	2.9	∞	∞	∞	3.8	∞
	4.6	3.4	2.4	4.2	6.0	3.6	3.2	4.1	∞	∞	4.2	5.6	∞	∞	4.7	∞
constant	$\tau_0 = 4.4$ MPa				$\tau_0 = 5.8$ MPa				$\tau_0 = 7.3$ MPa							
$\tau_y = \tau_0$	r650	r700	r750	w700	r650	r700	r750	w700	r650	r700	r750	w700				
	3.1	3.0	5.8	3.0	7.3	4.6	5.0	3.5	∞	∞	∞	∞				
	5.0	4.1	1.7	3.8	8.2	4.9	2.6	8.8	∞	∞	3.3	∞				
	3.6	3.1	2.2	3.4	4.8	3.4	3.2	5.6	∞	∞	4.5	∞				
composite	$\tau_0 = 7.3$ MPa, $\mu = 0.0045$				$\tau_0 = 8.7$ MPa, $\mu = 0.0054$				$\tau_0 = 10.2$ MPa, $\mu = 0.0063$							
$\tau_y = \min[\tau_0, \mu p]$	r650	r700	r750	w700	r650	r700	r750	w700	r650	r700	r750	w700				
	4.4	3.9	4.7	4.1	∞	9.3	∞	4.4	∞	7.6	∞	∞				
	∞	4.8	2.5	4.0	∞	6.9	2.8	8.2	∞	∞	3.0	∞				
	3.7	3.2	3.3	3.9	4.5	4.3	4.0	5.0	∞	∞	3.8	∞				

Legend
red: VP, free-slip
green: VP, free surface
blue: VEP, free surface

Table 4.5: Likelihood of subduction initiation for each tested yield stress profile

τ_y profile									
Byerlee	$\mu = 0.003$		$\mu = 0.004$		$\mu = 0.005$		$\mu = 0.006$		
$\tau_y = \mu p$	this study	CT2016	this study	CT2016	this study	CT2016	this study	CT2016	
	100% (3.9)	yes	100% (5.3)	no	0% (∞)	no	50% (14.4)	no	
	100% (3.0)	yes	100% (4.6)	yes	25% (11.6)	yes	25% (15.2)	no	
	100% (3.4)		100% (4.0)		50% (9.6)		25% (18.8)		
constant	$\tau_0 = 4.4$ MPa		$\tau_0 = 5.8$ MPa		$\tau_0 = 7.3$ MPa				
$\tau_y = \tau_0$	this study	CT2016	this study	CT2016	this study	CT2016			
	100% (3.4)	yes	100% (4.8)	no	0% (∞)	no			
	100% (3.1)	yes	100% (4.9)	yes	25% (13.2)	no			
	100% (3.0)		100% (4.0)		25% (18.0)				
composite	$\tau_0 = 7.3$ MPa, $\mu = 0.0045$		$\tau_0 = 8.7$ MPa, $\mu = 0.0054$		$\tau_0 = 10.2$ MPa, $\mu = 0.0063$				
$\tau_y = \min[\tau_0, \mu p]$	this study	CT2016	this study	CT2016	this study	CT2016			
	100% (4.3)	yes	50% (11.9)	no	25% (30.4)	no			
	75% (4.7)	yes	75% (6.4)	yes	25% (12.0)	no			
	100%(3.5)		100% (4.4)		25% (15.2)				

Legend
red: VP, free-slip
green: VP, free surface
blue: VEP, free surface

As expected, the results show that increasing the average strength of the lithosphere makes subduction events less likely. However, they also suggest that neither free surface nor elasticity have significant influence on the likelihood of subduction initiation. This is surprising for two reasons. First, it contradicts the previous findings by Crameri & Tackley (2016) who observed a free surface boundary condition to result in an increase of the critical yield stress for all three types of considered yield stress profiles (Byerlee-type, depth-constant, composite). Second, a significant increase of lithospheric stresses was reported in numerical experiments of stagnant lid convection with a free surface when compared to the free-slip surface, this increase being much smaller when also elasticity was included (Thielmann et al., 2015; Patočka et al., 2017) – a shift in the critical yield stresses defining the stagnant lid to plate-like behaviour is likely to be expected for both features.

In order to explain the negative results we analyze stress profiles and their fluctuations. Let us start by analyzing cases with no plastic yielding – we extend the set r700 by computing three additional simulations with $\tau_y = \infty$, that is, with no plastic yielding. Fig. 4.2 depicts the depth profile of the deviatoric part of the Cauchy stress tensor in these additional simulations. Each line is the horizontal average of stress for a given time and we show all the recorded profiles from the time window of 5 to 6 Gy to display the fluctuations once a statistically steady state is reached. We see that, when viscous rheology is assumed, the simulation with a free surface shows higher near-surface stresses when compared to the simulation with a free-slip surface. This increase is reduced upon employing viscoelastic rheology and a region of increased stresses appears deeper in the lithosphere. Such findings are consistent with previous studies by (Beuchert & Podladchikov, 2010; Thielmann et al., 2015; Patočka et al., 2017), but they are less pronounced. Due to the rapid exponential decrease of viscosity right below the surface (cf. left panel of Fig 4.9) the mutual differences between the three stress profiles are confined mostly to the very narrow near-surface stress boundary layer. In the previous studies a relatively large upper viscosity cut-off was controlling the value of viscosity in a layer of certain finite thickness, and the stress differences could display more fully within such layer.

Nevertheless, the stress profiles do respond to changing the upper boundary condition and including elasticity. However, these differences are much smeared out when the deviatoric stress is integrated over the entire stagnant lid – see Fig. 4.3. The lid is defined by a 750 K isotherm, approximately matching the velocity-based definition by Solomatov & Moresi (2000) in the statistically steady state of the simulation. Solomatov (2004a) derives and validates a scaling law that relates the integral of the vertical component of deviatoric stress in the stress boundary layer with stresses caused by sinking plumes in the simulation. Such theory neglects stresses caused by bending of the lithosphere. The fact that volume averages of stress in the lid are not much influenced by either the upper boundary condition or elasticity, demonstrated in Fig. 4.3, implies that bending

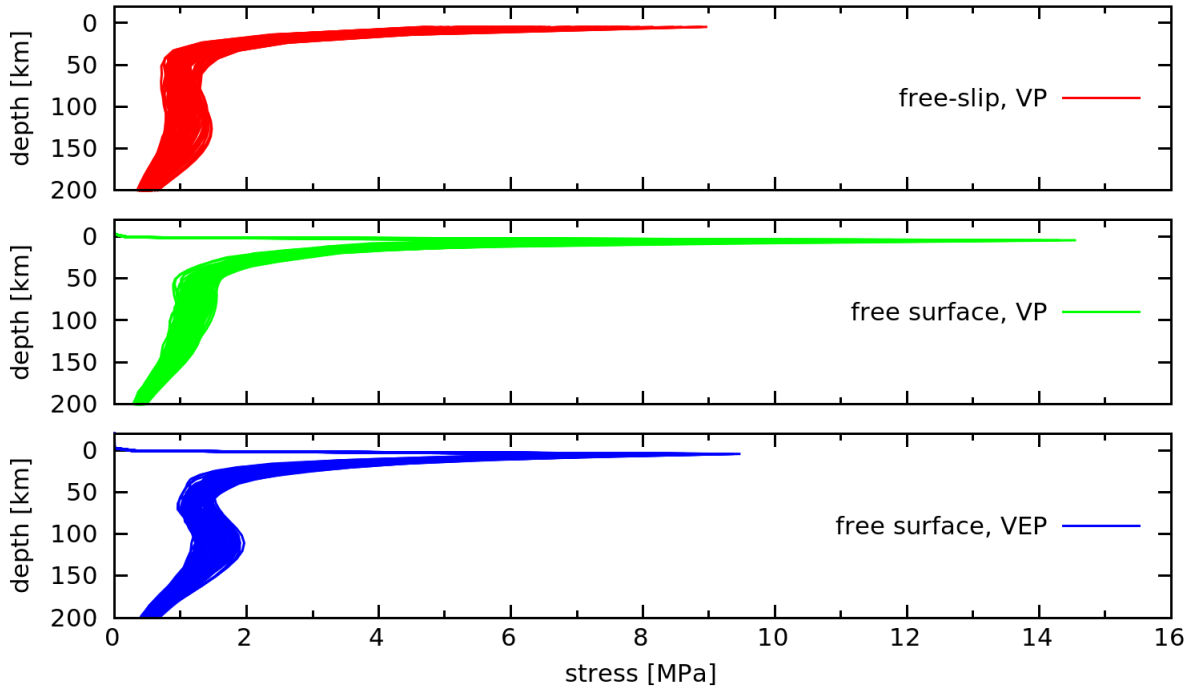

Figure 4.2: Depth profiles of horizontally averaged deviatoric stress. We show profiles recorded within one 1 Gy after reaching a statistically steady state in simulations r700 without plastic yielding. Red colour stands for the numerical experiment with a free-slip surface and VP rheology, green colour is for a free surface and VP rheology, and blue colour stands for a free surface and VEP rheology. Only the top 200 km are shown. The negative depths of -30 to 0 km correspond to the sticky air layer when a free surface is employed.

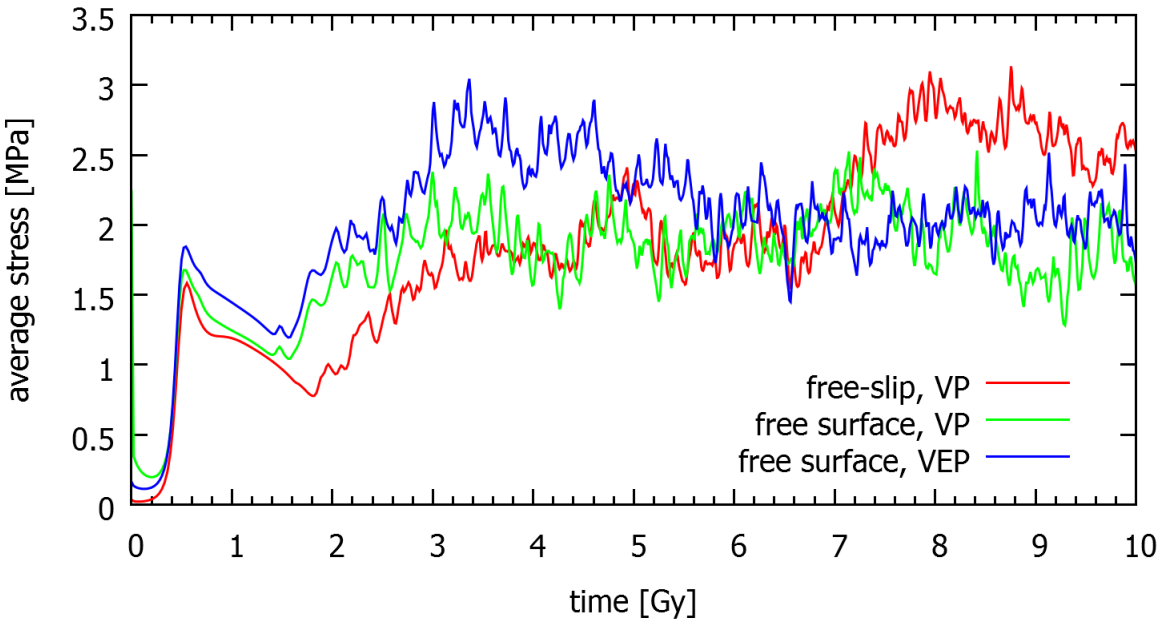

Figure 4.3: Temporal evolution of the deviatoric stress integrated over the lid (defined by 750 K isotherm) and divided by the area of the lid. We show the reference simulations (i.e. without plastic yielding) for the set r700. Red curve is the numerical experiment with a free-slip surface and VP rheology, green curve is with a free surface and VP rheology, and blue colour stands for a free surface and VEP rheology.

does not play a significant role in these simulations.

When plastic yielding is allowed the stress boundary layer disappears as stresses are spread over a larger volume of the lithosphere due to the presence of yielding. Since the volume averages of stress are comparable for the three investigated scenarios (VP with free-slip surface, VP with a free surface, VEP with a free surface), also the maximum depths of yielding are similar, as already suggested by the results in Tables 4.4 and 4.5. We illustrate the yielding depths and their fluctuations in Fig. 4.4, plotted are the maximum stresses for simulations r700 with $\tau_0 = 7.3$ MPa. The figure is obtained similarly as Fig. 4.2, only instead of the horizontal mean for each depth we show the maximum value of stress for each depth.

4.3.2 Short-term fluctuations and locked convection cells

In Fig. 4.5 we show the mean velocities of the flow for the simulations analyzed in Figs 4.3 and 4.2. The statistically steady state is reached after cca. 5 Gy and only short-term fluctuations are observed afterwards, corresponding to the birth of new downwellings, their sinking down the upper mantle, and the lateral movement of their roots along the LAB. When comparing the time window of 5-10 Gy in Figs. 4.5 and 4.3 one can see that the time evolution of the average lithospheric stresses is dominated by these short-term fluctuations, but that also some longer-lasting phenomena are present.

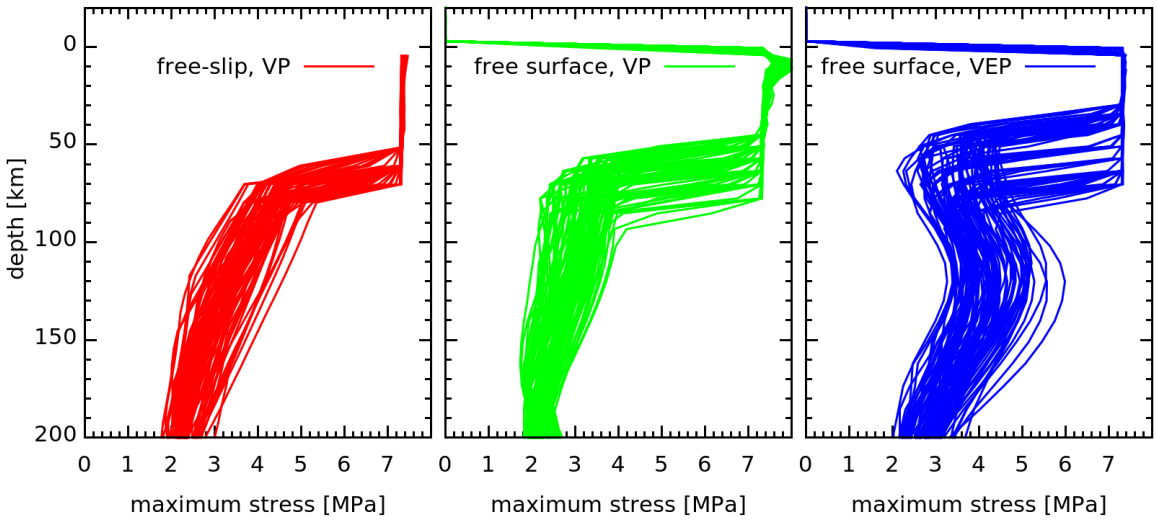

Figure 4.4: Depth profiles of maximum deviatoric stress. We show profiles recorded within one 1 Gy after reaching a statistically steady state in simulations r700 with constant yield stress $\tau_0 = 7.3$ MPa. Red colour stands for the numerical experiment with a free-slip surface and VP rheology, green colour is for a free surface and VP rheology, and blue colour stands for a free surface and VEP rheology. Only the top 200 km are shown, negative depths correspond to the sticky air layer.

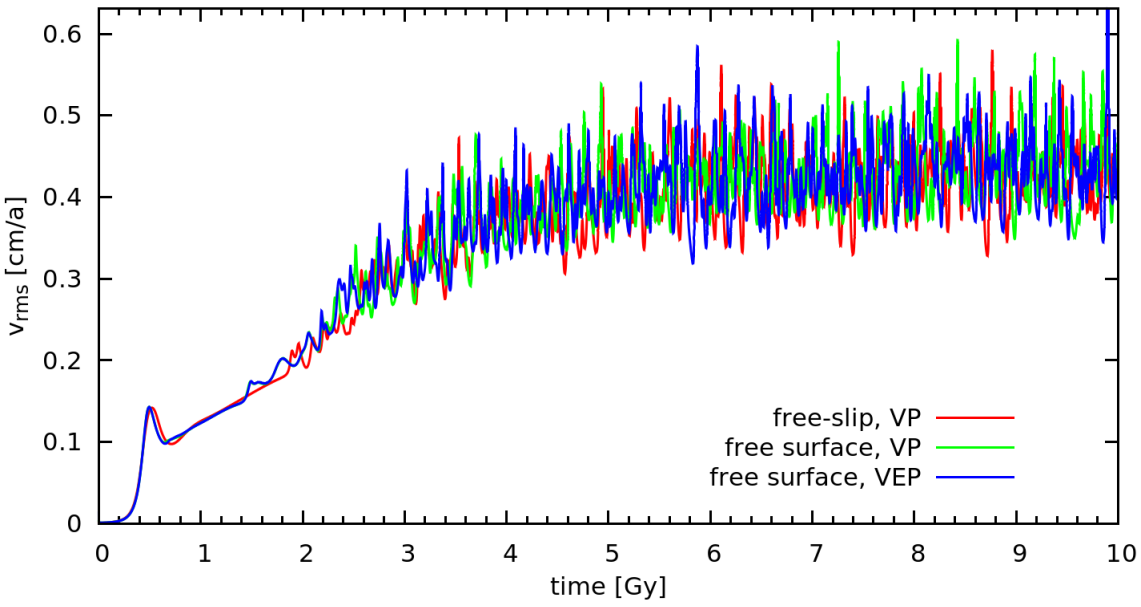

Figure 4.5: Temporal evolution of the average flow velocity in the simulations from Fig. 4.3.

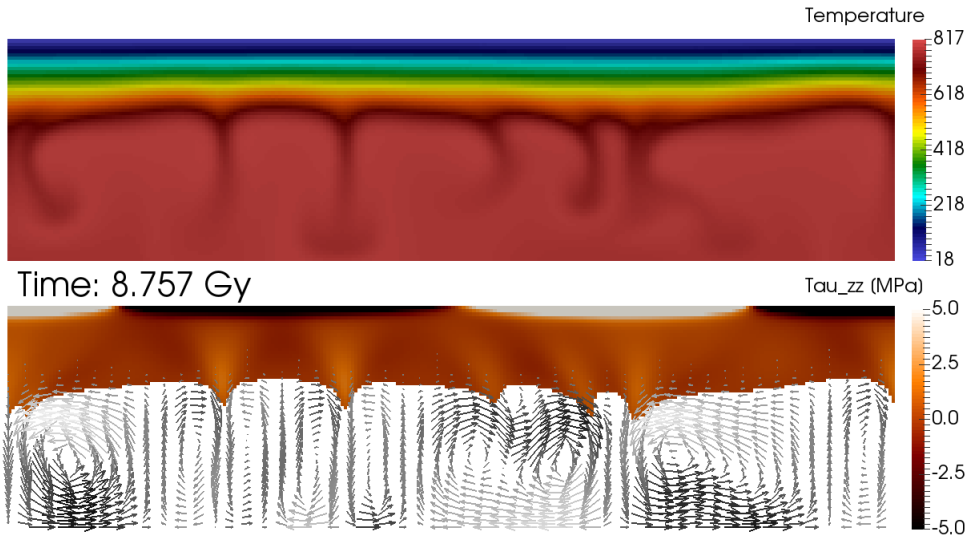

Figure 4.6: Temperature field (top) and τ_{zz} component of the deviatoric stress (bottom) in a simulation with no plastic yielding and a free-slip surface, taken from the set r700. A locked convection cell appears near the right boundary, where a downwelling forms below a regio with positive topography (see the negative values of τ_{zz} in the right upper corner of the model domain). Arrows indicate the velocity field and the model domain is thresholded by an isotherm when plotting τ_{zz} in order to reveal the roots of downwellings.

For instance, the red curve in Fig. 4.3 rises by over 2 MPa after 6 Gy and stays elevated for several Gy until its mean gradually returns to the value it had around 6 Gy. Careful analysis of the respective simulation reveals that the increase of the mean stress is related to the spatial organization of downwellings near the right edge of the model domain. When free-slip is assumed at the sides, the position of a sinking plume that gets pushed to an edge is locked in one direction, making such downwelling much more spatially stable when compared to other downwellings which are not constrained in their lateral movement. Thus, the observed increase of stress is generated by a downwelling getting pushed to the right edge of the model domain and being locked there for several Gy. The velocity field suggests that without the side wall the sinking plume would move further to the right. Since it cannot go there, a smaller than usual convection cell develops and the stresses are increased.

The "locked states" appear randomly and they increase the amplitude of stress fluctuations in the simulations, making the value of critical yield stress less constrained. In order to avoid them (and also to avoid subduction events in which the lid is broken along a side boundary of the model domain – see below), we perform the set w700, in which sides of the model domain are wrapped around. The lid stresses for simulations with such permeable sides and no plasticity are depicted in Fig. 4.7. Their mean seems more steady when compared to Fig. 4.3, but some long-term fluctuations are still present. It is because the average stress depends on the number of convection cells and their size, and these characteristics

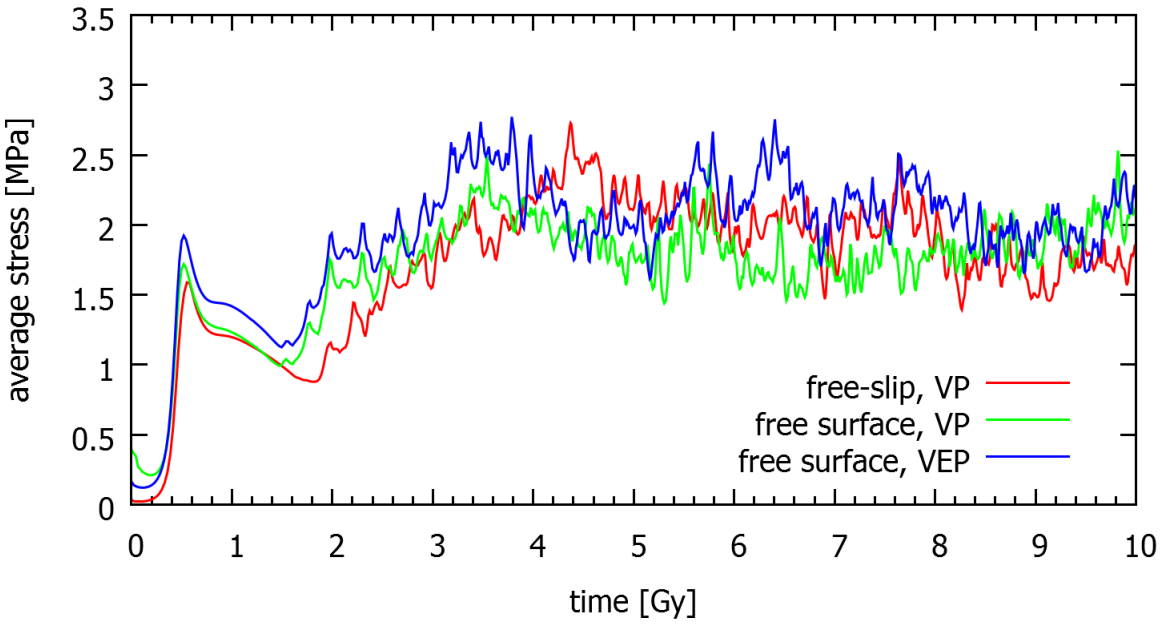

Figure 4.7: Same as Fig. 4.3, only for the set w700, that is, for the simulations without reflective side boundaries.

vary in time even when no side walls confine the flow.

4.3.3 Role of the initial temperature perturbation

Since we do not observe a systematic increase of the critical yield stress value due the effect of a free surface in Table 4.5, how come it was observed by Crameri & Tackley (2016)? Note that if only one set of simulations was considered, for example the set r700, we would record a systematic effect of a free surface, but an exactly opposite to the one reported by Crameri & Tackley (2016) – we would conclude that in simulations with a free surface the lid is less likely to break. However, if the only set at hand was the set r750, we could systematically confirm the findings of Crameri & Tackley (2016), the lid being easier to break due to a free surface for all the three tested yield stress profiles.

To explain the apparent controversy one must realize the role of the initial perturbation of temperature that is used to initiate convection in our simulations (and in the simulations by Crameri & Tackley (2016)). When a parametric study of mantle convection is performed, typically the only parameters changed in the input files to run the code are the ones whose effect is being investigated. Thus, the only numbers changed in the input files that were used to run the simulations with a free-slip surface and viscoplastic rheology labeled as r700 (all the red numbers in Table 4.4) were the values of τ_0 and μ. In all these simulations the initial temperature field is exactly the same because the initial geometry and position of tracers is the same (most programming languages take random numbers from a predefined set of numbers that follows a desired probability distribution). In effect, the first downwellings develop at the very same positions in space and time

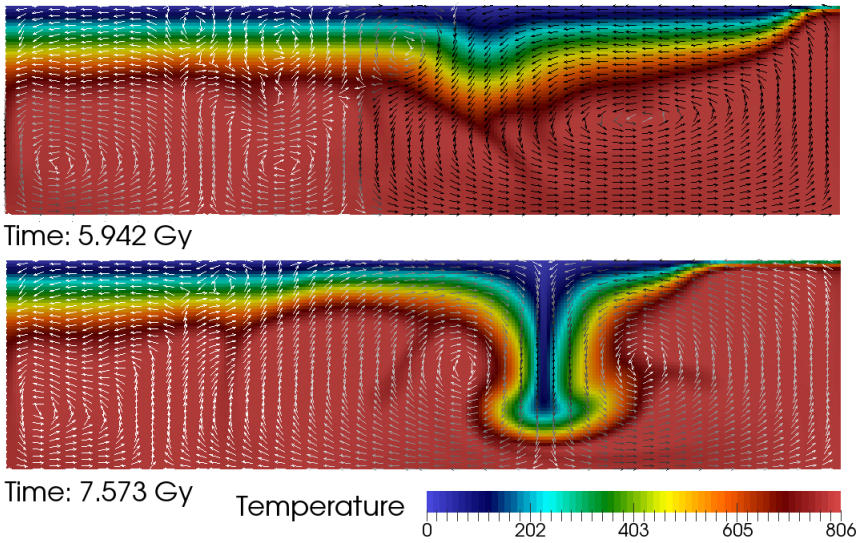

Figure 4.8: Temperature field in a simulation with Byerlee-type yield stress profile (top), $\mu = 0.006$, and with a composite yield stress profile (bottom), $\tau_0 = 10.2$ MPa $\mu = 0.0063$. Both cases have a free-slip surface and are taken from the set r700. Subduction event occurrs after lithosphere-deep yielding takes place in the right upper corner of the model domain (cf. also Fig. 4.6).

and since the interplay between the stagnant lid and sublithospheric dynamics is limited, the internal dynamics in all the simulations is nearly identical for several Gy, unless of course a subduction event occurs, which dramatically disrupts internal dynamics.

The trend observed for the set r700, that is, the "red" simulations being more likely to result in a subduction initiation, is a result of these simulations falling into the locked state discussed above. In Fig. 4.8 we compare the simulations that appear anomalous in Table 4.4 (composite and Byerlee-type yield stress profiles, with the highest of the tested values of τ_0 and μ) and show how the lid gets broken near the right edge of the model domain due a locked convection cell. When a free surface is employed, the initial geometry is different due to the presence of a sticky-air layer and the spatial position of the first downwellings is different to the one observed in the simulations with a free-slip surface. It is, however, the same for all the "green" and "blue" simulations with the same initial temperature T_0, that is, for each of the performed sets of simulations.

In order to obtain results that are independent on a particular initial configuration we performed at least three sets of simulations with different initial temperature field (r650, r700, r750). Another option would be to perform several sets in which the initial temperature T_0 was the same but a different seed for random numbers was chosen for each set. Note also that no systematic increase or decrease of the critical yield stress is observed for the set w700, as "locked" states seem to be related to the side boundary conditions, with open walls being more convenient in this regard (and are also more realistic).

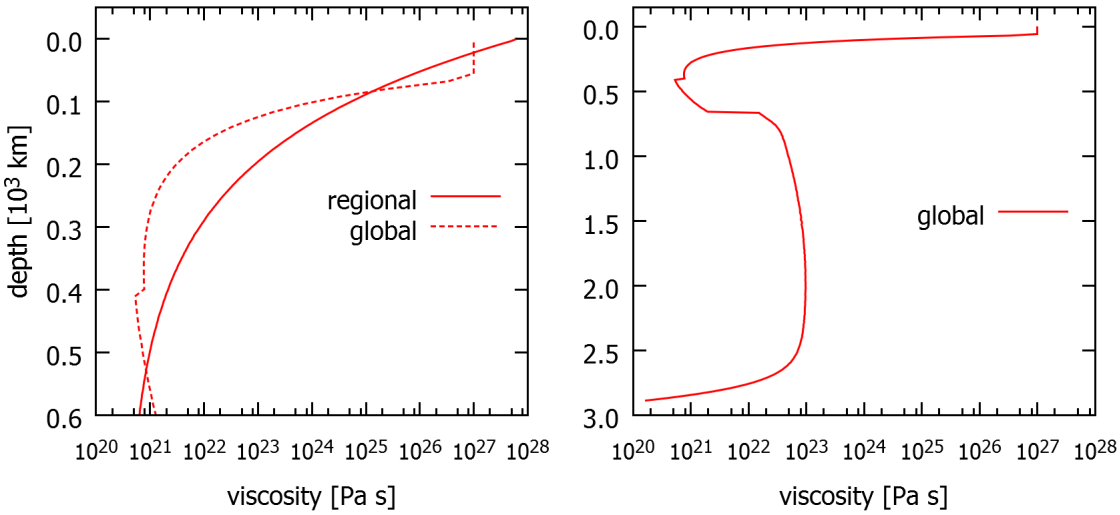

Figure 4.9: Viscosity profile corresponding to the initial temperature profile in the regional-scale (left) and the global-scale (right) models. We show part of the global viscosity profile also in the left panel for comparison.

4.4 Results: global-scale convection

4.4.1 Plume-induced subduction

The lithospheric stresses resulting from small-scale convection, discussed above, are much smaller than the strength of rocks determined in laboratory measurements. In effect, downwelling dominated convection in the upper mantle is not very likely to initiate subduction on the real Earth if a pre-existing weak zone is not prescribed (Solomatov, 2004b). However, when mantle flow is dominated by a strong upwelling, the basal drag acting on the bottom of the lithosphere builds significantly larger lithospheric stresses, and can result in initiation of subduction even for realistic rock strengths (Lu et al., 2015). In this section we test such a scenario in Earth-like models, with rising plumes being self-consistently developed in the simulations.

Similarly as in the previous section, we vary the value of τ_0, and for each value we compare three cases: 1) with visco-plastic (VP) rheology and free-slip upper boundary (represented by red colour), 2) with VP rheology and a free surface (green), and 3) with visco-elasto-plastic (VEP) rheology and a free surface (blue). In this section we test much larger values of τ_0, ranging from 20 to 200 MPa, with a step of 20 MPa. The friction coefficient μ is set to 0.0024 in all 30 cases.

In Fig. 4.9 we show the initial viscosity profile in these global-scale experiments and compare it to the initial viscosity profile in the regional-scale models. We see that the global-scale models have a few tens of km thick layer near the surface where viscosity reaches its maximum allowed value, making their dynamics more likely to be affected by considering a free surface and elasticity. Due to its pressure and compositional dependence, the sub-lithosphere viscosity is lower in the transition zone than in the lower mantle. In effect, the first convectional

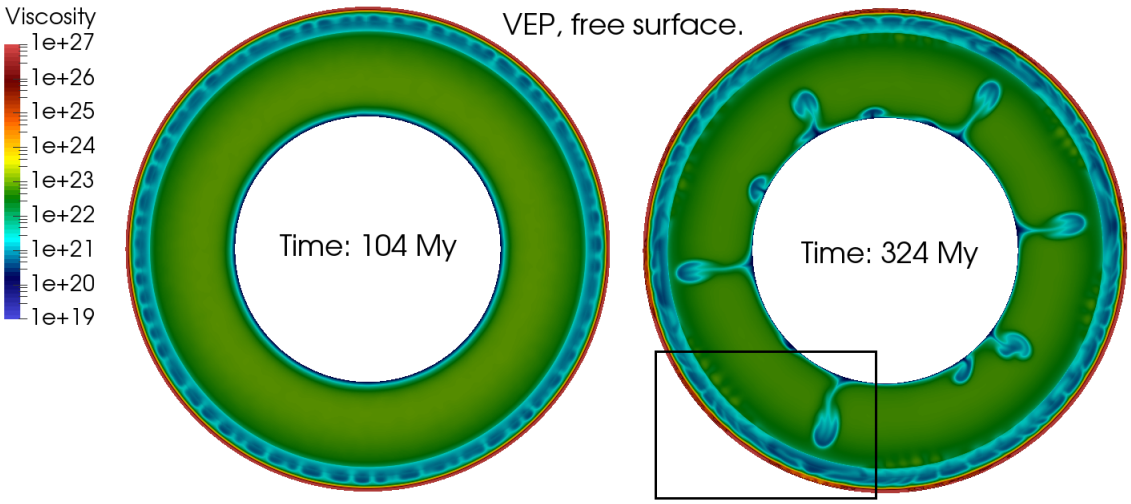

Figure 4.10: (left) The formation of small-scale convection in the upper mantle of our global-scale models. (right) Strong plumes form and rise through the mantle, dominating the global pattern of the studied flow. Black rectangle marks the area to which is zoomed in the following figures.

instabilities that develop in the model are sub-lithospheric downwellings, resulting after few tens of My in the formation of small convection cells in the upper mantle (see left panel of Fig. 4.10). Shortly after, plumes develop near the CMB and start rising, reaching the transition zone after a few hundreds of My (cf. right panel of Fig. 4.10). We depict only the VEP model with a free surface, but the initial evolution is identical for the VP model with a free surface and very similar to the initial evolution of the VP model with a free-slip upper boundary.

The initial temperature of the mantle is chosen so that the relative temperature difference (and thus the relative buoyancy) of the first plumes is rather large, making them ideal candidates for initiating subduction. High stresses (up to 160 MPa in absence of a predefined yield stress) develop in the lithosphere above the plume head and plastic yielding is activated, allowing for the plume to push the softened lithosphere to the sides and rise nearly to the outer surface (Fig. 4.11a). At this point the situation resembles the initial set-up considered by Lu et al. (2015). The stresses are low in the region of elevated temperatures and the convection cell is producing a basal drag on the lithosphere, building-up lithospheric stresses in the direction away from the center of the former plume head (Fig. 4.11b, see also Fig. 4 in Lu et al. (2015) for a comparison). For low friction angles Lu et al. (2015) reported a "symmetric" subduction mode and since the friction angle considered here is very low, we also observe this mode of subduction in our simulations – see Fig. 4.12.

When the value of τ_0 is sufficiently high, the plume cannot penetrate into the lithosphere, reducing the basal drag it produces, and it is also harder to form the shear zones that are necessary for the symmetric subduction to take place. Thus, for a certain critical value of τ_0 the lid does not fail and stagnant lid is maintained throughout the simulation. When free-slip upper boundary is

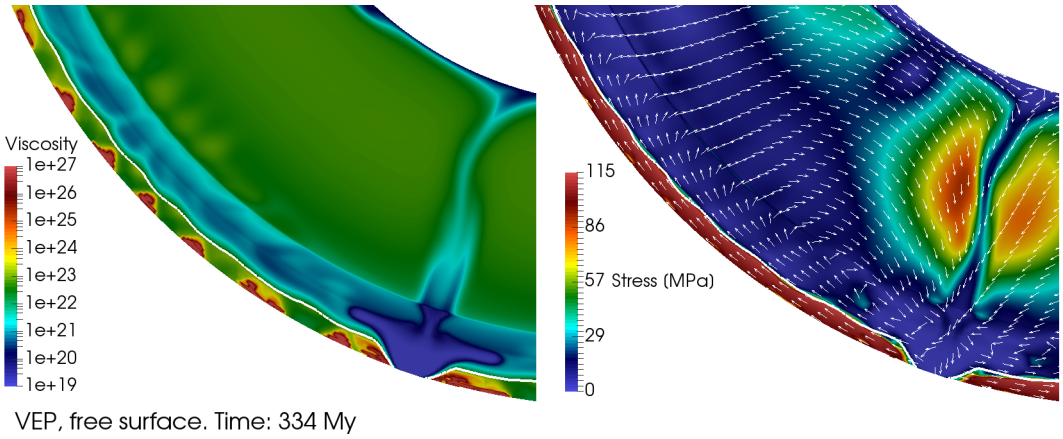

Figure 4.11: Penetration of a rising plume into the lithosphere in our global-scale model with $\tau_0 = 100$ MPa, only the region selected in Fig. 4.10 by a rectangle is shown. Stresses are low in the region of the former plume head and build up away from it due to the basal drag. As a result, shear zones with lower viscosities, dominated by plastic yielding, develop in the lithosphere. (a) Viscosity field (b) Second invariant of the deviatoric stress. White line is the isotherm denoting the LAB, small vectors display the velocity field.

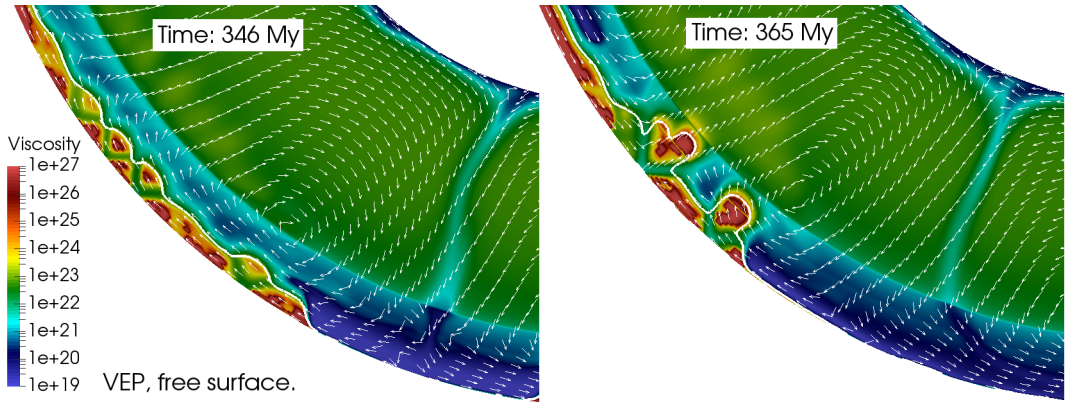

Figure 4.12: The formation of of "symmetric subduction", similar to the one described by Lu et al. (2015). After the "un-necking" phase, displayed on the left panel of the figure, the lithosphere accummulates and starts sinking into the deep mantle (right). We show the simulation with visco-elasto-plastic rheology and a free surface, $\tau_0 = 100$ MPa, only the region selected in Fig. 4.10 by a rectangle is shown.

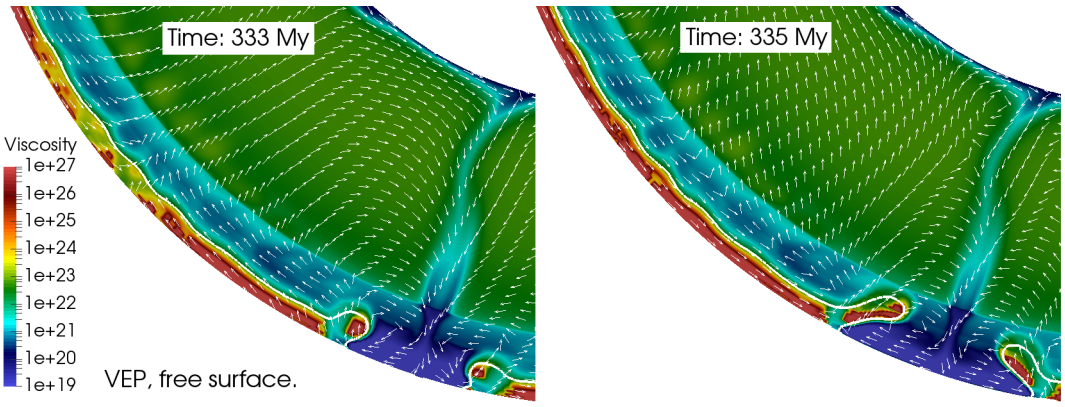

Figure 4.13: Plume-induced asymmetric subduction, similar to that described by Crameri & Tackley (2016). For lower values of rock strength the hot material from the plume spreads above the lithosphere, forming the wedge necessary for asymmetric subduction to start. We show the simulation with visco-elasto-plastic rheology and a free surface, $\tau_0 = 80$ MPa, only the region selected in Fig. 4.10 by a rectangle is shown.

assumed and elasticity is neglected, we observe this transition to be somewhere between 80 and 100 MPa, that is, for 80 MPa the lid fails and for 100 MPa does not. When a free surface is assumed the stresses above plumes are larger because the lid can bend. As a result, for $\tau_0 = 100$ MPa we still observe the lid to fail, but already for 120 MPa stagnant lid is maintained, placing the critical value of yield stress somewhere between 100 and 120 MPa. When elasticity is included, the bending stresses are reduced (e.g. Kaus & Becker, 2007; Patočka et al., 2017), which could potentially decrease the critical value of τ_0. However, within the framework presented here, that is, when τ_0 is sampled rather coarsely by 20 MPa, we do not record such phenomena: for 100 MPa the lid still fails and for 120 MPa stagnant lid is maintained.

The "symmetric" subduction mode, discussed above, was only observed for near-critical values of τ_0. For lower values of yield stress the material from the rising plume pushes the lithosphere not only to the sides but also downwards, as it tends to accumulate near the surface. In effect, we observe an asymmetric subduction for lower values of τ_0, similar to the one reported in the numerical experiment of a global overturn event in Crameri & Tackley (2016) – see Fig. 4.13. This mode of plume-induced subduction is recently gaining attention, as it may be currently happening on Venus (e.g. Davaille et al., 2017), or may have triggered plate tectonics on Earth (Gerya et al., 2015).

4.5 Discussion

The models of small-scale convection presented here are rather simplified when compared to state-of-the-art regional-scale modelling of subduction, partly because they lack compositional variation of physical properties of rocks and phase transitions of minerals. However, the goal of this study is to systematically evalu-

ate the effect of elasticity and a free surface on the stresses built in the lithosphere by small-scale convection and for this purpose the models are instructive. They also have the advantage of having been used by a previous parametric study by Crameri & Tackley (2016) to which we can make comparisons.

The global-scale models shown in Section 4.4 are, on the other hand, much more complex in terms of compositional dependence of physical properties. But there is one simplification that remains in all of the presented models – the way brittle and ductile yielding is parametrized. We tested only very low (when compared to laboratory measurements) values of friction angles to simulate the plastic yielding. It is a common approach in many geodynamical simulations where spontaneous formation of deep shear zones is sought. Some advocate the use of low friction angles on the grounds of averaging rapid events into the geological time frames but it is viewed as controversial within the community. Moreover, using low friction angles results in poorly localized shear-zones, with yielding activated in much larger volumes of the lithosphere than observed in nature, where relatively narrow zones of localized shearing are found. Interesting methods have been proposed in the last decade to overcome the discrepancy, either through a strain-rate dependence of the friction angle (e.g. van Dinther et al., 2013), or by considering structural inheritance of the lithosphere (Duretz et al., 2016). We note that the effects of viscoelasticity in these new models may be more dramatic than in the traditional models presented here, especially when elastic energy from a large volume of the model domain gets released within a narrow shear zone as observed in a numerical experiment of lithospheric shortening by Jaquet et al. (2016).

The technique used here to approximate a free surface is to prescribe a low-viscosity, low-density layer of "sticky-air" on top of the model domain. Its viscosity is chosen so that the C-condition (Crameri et al., 2012) is well satisfied in the stagnant-lid regime. In the global-scale models, once the lid is broken and hot material from the deep mantle rises right below the new and very thin thermal boundary layer, the viscosity contrast between the sticky-air and the hot mantle material may be too small for the sticky-air to approximate a free surface well. For this reason we, with the exception of the paragraph below, refrain from commenting on the entire evolution of our models and focus on the initiation of subduction only.

When lid failure does occur in our models, it usually results in an overturn of the entire lid. Such event cools the mantle down and curbs convection – it takes several Gy before convective stresses are strong enough to result in another lid overturn in such episodic-lid regime. A more continuous, mobile-lid regime was obtained only for low values of τ_0 up to 40 MPa. In the regional-scale models lid overturns often occur in an unphysical manner. Due to the low values of yield stress that are being tested it is often large portions of the model domain where the critical stress is reached during a subduction event, triggering very distributed and domain-deep yielding rather than narrow localized shear zones.

Such behaviour is often related to some material being locked by a side wall – domain-deep yielding does not occur in the set w700, confirming that periodic sides are a better choice for these type of simulations.

4.6 Conclusions

We investigated the effects of a free surface and viscoelasticity on the value of yield stress that is necessary to break a stagnant-lid and initiate subduction. First we performed models of the upper mantle that originate from the work of Solomatov (2004a). Contrary to previous findings of Crameri & Tackley (2016), in these models of small-scale convection we found no significant shift of the critical yield stress due to a free surface. When plastic deformation is suppressed, the radial profiles of stress are to some extent affected by considering a free surface and elasticity, but once plastic yielding is allowed the differences are smeared out and the maximum depths of yielding are similar. In other words, the critical yield stress does not depend on the upper boundary condition or the consideration of elasticity in these models.

Short-term and long-term fluctuations, intrinsic to thermal convection simulations, can complicate the evaluation the critical yield stress in a numerical model of given parameters. Short-term fluctuations are caused by the lateral movement and formation of sinking and rising plumes. Long-term fluctuations are related to the existence of locked, or meta-stable, convective states. We illustrated how the occurrence of a locked convective state can lead to observing a false trend in a parametric study: what appears to be the effect of the studied parameter can in fact result from the formation of meta-stable convective state in a particular set of simulations.

In global-scale models with Earth-like parameters we observed two types of plume-induced subduction. One is the symmetric subduction described by Lu et al. (2015) and the other is asymmetric subduction that originates directly above a plume head, recently reported by Crameri & Tackley (2016); Gerya et al. (2015); Davaille et al. (2017). We found the lid failure to be more likely in models with a free surface than with a free-slip surface, but the shift of the critical yield stress value was no more than 20 MPa in our simulations.

Whether or not the average lithospheric stresses are significantly influenced by a free surface and/or elasticity depends primarily on how much bending can occur, which is governed by the viscosity profile. Profiles with a thick high-viscosity layer of essentially rigid (or elastic) material favor bending, while profiles with viscosity exponentially decaying directly below the surface do not.

Conclusions and perspectives

Numerical models that evaluate the internal deformation of planetary mantles are important for various applications. Perhaps the most unknown parameter entering such calculations is the rock rheology, with the two end-member material models being the elastic solid and viscous fluid. In the traditional view, elastic models describe the short-term behaviour and viscous models the long-term behaviour of rocks. However, there are observations implying that elasticity plays an important role in the lithosphere even on very long time scales (for a review, see Watts et al., 2013).

The medium that combines both models in a simple way – by assuming that both mechanisms are connected in series – is referred to as Maxwell-type viscoelastic material. The general idea on which the rheology is based was proposed in the 19th century, but the exact form of its constitutive equation is still subject to an open debate (see e.g. Málek & Průša, 2016). The traditional formula that appears in the literature has only the partial time derivative standing for the stress rate. However, such formula is applicable only to problems dealing with small deformations of a body. For a general deformation it is physically inconsistent because it violates the condition of material objectivity. Several objective tensor rates have been proposed to complete the traditional formula, but one is usually left without any physical argument that could help to choose a particular one, leaving the choice to experimental means. In Chapter 1 we review the physical interpretation of the commonly assumed objective tensor rates. Based on geometrical considerations, we argue that the so-called lower convected tensor rate fits the original idea of Maxwell material the best.

In studies of glacial isostatic adjustment the use of viscoelastic models has always prevailed. Postglacial rebound of the Earth's surface is essentially caused by a viscoelastic relaxation of its interior, and Maxwell model seems to provide a good first-order fit to the observed data (e.g. Sabadini et al., 2016). In Chapter 2 we investigate GIA from a rather overlooked perspective – its energetical balance. We derive a numerical tool for analyzing the changes in the rotational, gravitational, and elastic energies of a rotating planet that is subject to surface loads. The tool is used to test the accuracy of the linearized Liouville equation in determining the changes in Earth's rotation induced by GIA. We show that the predicted changes in the magnitude of the angular velocity vector are significantly affected by the linearization of the Liouville equation.

Earth's deformation associated with postglacial rebound is very small and there is no need for other than the traditional Maxwell constitutive formula. In mantle convection this is no longer the case. Chapters 3 and 4 are devoted to numerical modelling of mantle convection and assume the mantle rocks to behave as Maxwell viscoelastic fluid with the constitutive relation containing an objective stress rate. This is a step towards more realistic mantle convection models, as

present-day simulations usually ignore elasticity.

One of the primary constraints on the internal structure and dynamics of terrestrial planets is given by their surface topography. At the same time, surface topography is an observable that is likely to be affected by considering elasticity in the lithosphere, and so a number of studies have already addressed its potential effects. In Chapter 3 we compute lithospheric flexure above a rising plume in a fully viscoelastic model with a free surface and observe an elastic filtering of the resulting topography, consistently with previous findings by authors who used more simplified approaches (e.g. Golle et al., 2012).

We also observed an unforeseen effect in our mantle convection simulations. While in GIA modelling it is obvious that current deformation depends on the past (the observed uplift is caused by glaciers that no longer exist), in mantle convection this is usually not assumed. Two common exceptions, in which the internal dynamics at a given moment depend on the history of preceding flow, are simulations with grain size evolution and simulations with a predefined weak zones. In the first case, shearing can reduce the grain size in some regions, forming zones of low viscosity that further localize deformation (e.g. Rozel et al., 2011). In the latter case, predefined weak zones are supposed to represent some structural inheritance, that is, material that got weakened by deformation that preceded the numerical experiment (recently e.g. Duretz et al., 2016). We observe a new type of history dependence. When a planet cools down from its initially hot state, its lithosphere is thin at the beginning and gradually grows in thickness. Due to convective forcing, the thin lithosphere undergoes severe bending resulting in large stresses. In Chapter 3 we describe how these bending patterns can "freeze" into the growing lithosphere and are remembered there long after the sinking and rising plumes that caused the bending have disappeared. The relaxation of these features is governed by the Maxwell relaxation time of the lithosphere, which depends on the poorly constrained value of lithospheric viscosity, and can be comparable with the geological time scales.

We merely provide a proof of concept for the stress memory effect. 3-D spherical simulations that would confirm our hypothesis in a model with realistic parameters suited for a particular planet or moon are yet to be done. Especially interesting may be to study how the different spatial wavelengths of surface topography evolve throughout viscoelastic convection of a cooling planet. An ideal stagnant lid candidate seems to be the planet Mars, where the effective elastic thickness T_e of the lithosphere is observed to decrease with increasing age of surface loads (e.g. McGovern et al., 2002). This may either indicate "frozen-in" topography, consistent with the memory effect described here, or it can simply be the result of viscoelastic relaxation under the surface loads (i.e. not related to the changes of lithospheric thickness). Another open question is how much of the stress that accumulates in the initially thin lid in our simulations would get released if a realistic description of brittle and ductile yielding was involved. To answer the question, global-scale numerical simulations with complex lithospheric

rheology and high near-surface resolution must be performed.

While the behaviour of the lithosphere is altered substantially by including elasticity into mantle convection simulations, sub-lithospheric dynamics seem to be unaffected. The ability of our models to quickly build surface topography, the resistance of this process being governed by the elastic shear modulus (and not by the high value of lithospheric viscosity as in purely viscous runs), could potentially stabilize or destabilize mantle upwellings and downwellings in their spatial position, or change the number and stability of convection cells. However, we have not observed any such changes in the internal dynamics, at least for convection experiments in stagnant lid regime.

A convective regime that exhibits stronger interaction of the deep mantle with the lithosphere is the one observed on Earth. In a plate-like regime the thermal boundary layer breaks into plates which are being continuously created and subducted. One of the outstanding problems of numerical simulations of plate tectonics is that the highest possible (critical) value of yield stress that one may prescribe and still obtain a plate-like regime is much lower than the values suggested by laboratory measurements. This problem could be even worse when elastic properties of rocks are accounted for. Considering an additional deformation mechanism lowers the lithospheric resistance, reducing the convective stresses that develop in the lithosphere (to some extent, though in different settings, the effect is observed in the works of Kaus & Becker, 2007; Beuchert & Podladchikov, 2010; Thielmann et al., 2015; Patočka et al., 2017). In Chapter 4 the critical yield stress value is analyzed in a parametric study. We compare sets of visco-plastic and visco-elasto-plastic simulations with a free surface and with a free-slip surface. We find that the importance of elasticity and a free surface depends on the viscosity profile. If low viscosity is assumed, or if the viscosity exponentially decreases right below the surface (i.e. without forming an effectively elastic layer of non-negligible thickness), then little to no shift of the critical yield stress is observed. A shift appears when a high-viscosity layer several tens of km thick is assumed – the critical yield stress is higher in cases with a free surface when compared to the cases with free-slip surface. However, no first-order differences are observed between the visco-plastic and visco-elasto-plastic simulations with a free surface. This may seem surprising, because in models with comparable internal dynamics, presented in Chapter 3, the horizontally averaged lithospheric stresses differed by up to tens of MPa between viscous and viscoelastic models.

To fully understand the role of elasticity in numerical models of planetary evolution, it is necessary to perform global-scale experiments that employ complex treatment of brittle and ductile yielding in the lithosphere. The pseudoplastic yielding, commonly used to generate plate-like behaviour in global-scale convection models (e.g. Tackley, 2000), which is also used here in Chapter 4, is not suitable to capture the complexities of lithospheric deformation. Especially when low values of surface yield stress and low friction angles are employed the resulting yielding is distributed into relatively large volumes of the lithosphere instead of

forming narrow shear zones. Such behaviour disfavors the display of viscoelastic effects. These can fully develop only in settings in which elastic stresses build up in a large portion of the model domain and are subsequently released within a localized shear zone – significantly promoting the extent of deformation accommodated therein. An example of such setting was demonstrated by Jaquet et al. (2016), who performed simulations of continental collision.

The methodological division between regional and global geodynamical modelling is slowly falling apart. In numerical studies of single regions the boundary conditions are often critically questioned. It is becoming increasingly obvious that for many segments of Earth we cannot cut out a part of the mantle and model its deformation without considering the feedback from the rest of the mantle. That is, without considering how the region's boundary conditions change in reaction to what is happening inside the region. On the other hand, in global simulations of plate-like or episodic lid convection it is the lid behaviour that has first-order influence on the internal dynamics. However, regional modelling implies that a high-resolution lithosphere with non-linear, composition dependent rheology that combines various creep mechanisms is necessary to capture the lid behaviour correctly. One can thus expect the future models to be global-scale, but with complexities typical for regional-scale models. The enhancement of StagYY presented in this thesis is one of the necessary steps towards such models.

Bibliography

Afonso, J. & Ranalli, G., 2004. Crustal and mantle strengths in continental lithosphere: is the jelly sandwich model obsolete?, *Tectonophysics*, **394**(3-4), 221–232.

Armann, M. & Tackley, P. J., 2012. Simulating the thermochemical magmatic and tectonic evolution of Venus's mantle and lithosphere: Two-dimensional models, *J. Geophys. Res.*, **117**.

Benjamin, D., Wahr, J., Ray, R. D., Egbert, G. D., & Desai, S. D., 2006. Constraints on mantle anelasticity from geodetic observations, and implications for the J(2) anomaly, *Geophys. J. Int.*, **165**(1), 3–16.

Beuchert, M. J. & Podladchikov, Y. Y., 2010. Viscoelastic mantle convection and lithospheric stresses, *Geophys. J. Int.*, **183**(1), 35–63.

Burov, E., 2010. The equivalent elastic thickness (T-e), seismicity and the long-term rheology of continental lithosphere: Time to burn-out "creme brulee"? Insights from large-scale geodynamic modeling, *Tectonophysics*, **454**(1-4), 4–26.

Cambiotti, G., Ricard, Y., & Sabadini, R., 2010. Ice age True Polar Wander in a compressible and non-hydrostatic Earth, *Geophys. J. Int.*, **183**(3), 1248–1264.

Cambiotti, G., Ricard, Y., & Sabadini, R., 2011. New insights into mantle convection true polar wander and rotational bulge readjustment, *Earth Planet. Sic. Lett.*, **310**(3-4), 538–543.

Cathles, L., 2015. *Viscosity of the Earth's Mantle*, Princeton Legacy Library, Princeton University Press.

Choblet, G., Cadek, O., Couturier, F., & Dumoulin, C., 2007. OE DIPUS: a new tool to study the dynamics of planetary interiors, *Geophys. J. Int.*, **170**(1), 9–30.

Cloetingh, S. & Wortel, R., 1982. Finite-element models of passive continental margins with implications for the initiation of subduction zones, *Geol. Mijn.*, **61**(3), 281–292.

Contreras-Reyes, E., Grevemeyer, I., Watts, A. B., Planert, L., Flueh, E. R., & Peirce, C., 2010. Crustal intrusion beneath the Louisville hotspot track, *Earth Planet. Sic. Lett.*, **289**(3-4), 323–333.

Crameri, F. & Tackley, P. J., 2014. Spontaneous development of arcuate single-sided subduction in global 3-D mantle convection models with a free surface, *J. Geophys. Res.*, **119**(7), 5921–5942.

Crameri, F. & Tackley, P. J., 2016. Subduction initiation from a stagnant lid and global overturn: new insights from numerical models with a free surface, *Pro. Earth Planet. Sci.*, **3**.

Crameri, F., Schmeling, H., Golabek, G. J., Duretz, T., Orendt, R., Buiter, S. J. H., May, D. A., Kaus, B. J. P., Gerya, T. V., & Tackley, P. J., 2012. A comparison of numerical surface topography calculations in geodynamic modelling: an evaluation of the sticky air' method, *Geophys. J. Int.*, **189**(1), 38–54.

Davaille, A., Smrekar, S. E., & Tomlinson, S., 2017. Experimental and observational evidence for plume-induced subduction on Venus, *Nat. Geo.*, **10**(5), 349+.

Dhuime, B., Wuestefeld, A., & Hawkesworth, C. J., 2015. Emergence of modern continental crust about 3 billion years ago, *Nat. Geo.*, **8**(7), 552–555.

Duretz, T., May, D. A., Gerya, T. V., & Tackley, P. J., 2011. Discretization errors and free surface stabilization in the finite difference and marker-in-cell method for applied geodynamics: A numerical study, *Geochem. Geophys. Geosyst.*, **12**.

Duretz, T., Petri, B., Mohn, G., Schmalholz, S. M., Schenker, F. L., & Muntener, O., 2016. The importance of structural softening for the evolution and architecture of passive margins, *Scientific Reports*, **6**.

Floberghagen, R., Fehringer, M., Lamarre, D., Muzi, D., Frommknecht, B., Steiger, C., Pineiro, J., & da Costa, A., 2011. Mission design, operation and exploitation of the gravity field and steady-state ocean circulation explorer mission, *J. Geodesy*, **85**(11), 749–758.

Gerya, T., 2010. *Introduction to Numerical Geodynamic Modelling*, Cambridge University Press.

Gerya, T. & Yuen, D., 2003. Characteristics-based marker-in-cell method with conservative finite-differences schemes for modeling geological flows with strongly variable transport properties, *Phys. Earth Planet. Inter.*, **140**(4), 293–318.

Gerya, T. V. & Yuen, D. A., 2007. Robust characteristics method for modelling multiphase visco-elasto-plastic thermo-mechanical problems, *Phys. Earth Planet. Inter.*, **163**(1-4), 83–105.

Gerya, T. V., Stern, R. J., Baes, M., Sobolev, S. V., & Whattam, S. A., 2015. Plate tectonics on the Earth triggered by plume-induced subduction initiation, *Nature*, **527**(7577), 221+.

Golle, O., Dumoulin, C., Choblet, G., & Cadek, O., 2012. Topography and geoid induced by a convecting mantle beneath an elastic lithosphere, *Geophys. J. Int.*, **189**(1), 55–72.

Gurnis, M., Eloy, C., & Zhong, S., 1996. Free-surface formulation of mantle convection .2. Implication for subduction-zone observables, *Geophys. J. Int.*, **127**(3), 719–727.

Gurtin, M., 1982. *An Introduction to Continuum Mechanics*, Mathematics in Science and Engineering, Elsevier Science.

Gurtin, M., Fried, E., & L, A., 2010. *The Mechanics and Thermodynamics of Continua*, Cambridge University Press.

Hall, C. & Gurnis, M., 2005. Strength of fracture zones from their bathymetric and gravitational evolution, *J. Geophys. Res.*, **110**(B1).

Harder, H., 1991. Numerical-simulation of thermal-convection with Maxwellian viscoelasticity, *J. Non-Newton. Fluid Mech.*, **39**(1), 67–88.

Harris, A., 1994. Tumbling asteroids, *Icarus*, **107**(1), 209–211.

Hernlund, J. W. & Tackley, P. J., 2008. Modeling mantle convection in the spherical annulus, *Phys. Earth Planet. Inter.*, **171**(1-4), 48–54.

Horgan, C. & Saccomandi, G., 2004. Constitutive models for compressible nonlinearly elastic materials with limiting chain extensibility, *J. Elasticity*, **77**(2), 123–138.

Ivins, E., Unti, T., & Phillips, R., 1982. Large Prandtl number finite-amplitude thermal-convection with Maxwell viscoelasticity, *Geophys. Astrophys. Fluid Dyn.*, **22**(1-2), 103–132.

Jaquet, Y., Duretz, T., & Schmalholz, S. M., 2016. Dramatic effect of elasticity on thermal softening and strain localization during lithospheric shortening, *Geophys. J. Int.*, **204**(2), 780–784.

Jones, M., 1985. *Spherical harmonics and tensors for classical field theory*, Electronic & electrical engineering research studies: Applied and engineering mathematics series, Research Studies Press.

Joseph, D., 2013. *Fluid Dynamics of Viscoelastic Liquids*, Applied Mathematical Sciences, Springer New York.

Kaus, B. J. P. & Becker, T. W., 2007. Effects of elasticity on the Rayleigh-Taylor instability: implications for large-scale geodynamics, *Geophys. J. Int.*, **168**(2), 843–862.

Kaus, B. J. P., Muehlhaus, H., & May, D. A., 2010. A stabilization algorithm for geodynamic numerical simulations with a free surface, *Phys. Earth Planet. Inter.*, **181**(1-2), 12–20.

Kiefer, W., Bills, B., & Nerem, R., 1996. An inversion of gravity and topography for mantle and crustal structure on Mars, *J. Geophys. Res.*, **101**(E4), 9239–9252.

Kite, E. S., Matsuyama, I., Manga, M., Perron, J. T., & Mitrovica, J. X., 2009. True Polar Wander driven by late-stage volcanism and the distribution of paleopolar deposits on Mars, *Phys. Earth Planet. Inter.*, **280**(1-4), 254–267.

Kohlstedt, D., Evans, B., & Mackwell, S., 1995. Strength of the lithosphere - constraints imposed by laboratory experiments, *J. Geophys. Res.*, **100**(B9), 17587–17602.

Lau, H. C. P., Mitrovica, J. X., Austermann, J., Crawford, O., Al-Attar, D., & Latychev, K., 2016. Inferences of mantle viscosity based on ice age data sets: Radial structure, *J. Geophys. Res.*, **121**(10), 6991–7012.

Leeds, A., Knopoff, L., & Kausel, E., 1974. Variations of Upper Mantle Structure under Pacific Ocean, *Science*, **186**(4159), 141–143.

Lefftz, M., Legros, H., & Hinderer, J., 1991. Non-linear equations for the rotation of a viscoelastic planet taking into account the influence of a liquid core, *Celest. Mech. Dyn. Astron.*, **52**(1), 13–43.

Liu, I.-S. & Sampaio, R., 2014. Remarks on material frame-indifference controversy, *Acta Mechanica*, **225**(2), 331–348.

Lourenco, D. L., Rozel, A., & Tackley, P. J., 2016. Melting-induced crustal production helps plate tectonics on Earth-like planets, *Earth Planet. Sic. Lett.*, **439**, 18–28.

Lu, G., Kaus, B. J. P., Zhao, L., & Zheng, T., 2015. Self-consistent subduction initiation induced by mantle flow, *Terra Nova*, **27**(2), 130–138.

Málek, J. & Průša, V., 2016. *Derivation of Equations for Continuum Mechanics and Thermodynamics of Fluids*, pp. 1–70, Springer International Publishing, Cham.

Málek, J. & Rajagopal, K., 2005. Chapter 5 - mathematical issues concerning the navier-stokes equations and some of its generalizations, in *Handbook of Differential Equations Evolutionary Equations*, vol. 2, pp. 371 – 459, eds Dafermos, C. & Feireisl, E., North-Holland.

Martinec, Z., 2011. *Continuum Mechanics*, Charles University in Prague 2011.

Martinec, Z. & Hagedoorn, J., 2014. The rotational feedback on linear-momentum balance in glacial isostatic adjustment, *Geophys. J. Int.*, **199**(3), 1823–1846.

Matsumoto, T. & Tomoda, Y., 1983. Numerical-simulation of the initiation of subduction at the fracture-zone, *J. Phys. Earth*, **31**(3), 183–194.

Maxwell, J., 1871. Theory of heat, *Longmans, Green, and Co.*.

McGovern, P., Solomon, S., Smith, D., Zuber, M., Simons, M., Wieczorek, M., Phillips, R., Neumann, G., Aharonson, O., & Head, J., 2002. Localized gravity/topography admittance and correlation spectra on Mars: Implications for regional and global evolution, *J. Geophys. Res.*, **107**(E12).

Milne, G. & Mitrovica, J., 1998. Postglacial sea-level change on a rotating Earth, *Geophys. J. Int.*, **133**(1), 1–19.

Minshull, T. A., Ishizuka, O., & Garcia-Castellanos, D., 2010. Long-term growth and subsidence of Ascension Island: Constraints on the rheology of young oceanic lithosphere, *Geophys. Res. Let.*, **37**.

Mitrovica, J. & Peltier, W., 1991. A complete formalism for the inversion of postglacial rebound data - resolving power analysis, *Geophys. J. Int.*, **104**(2), 267–288.

Mitrovica, J., Milne, G., & Davis, J., 2001. Glacial isostatic adjustment on a rotating earth, *Geophys. J. Int.*, **147**(3), 562–578.

Moresi, L. & Solomatov, V., 1995. Numerical investigation of 2D convection with extremely large viscosity variations, *Phys. Fluids*, **7**(9), 2154–2162.

Moresi, L., Dufour, F., & Muhlhaus, H., 2002. Mantle convection modeling with viscoelastic/brittle lithosphere: Numerical methodology and plate tectonic modeling, *Pure Appl. Geophys.*, **159**(10), 2335–2356.

Moresi, L., Dufour, F., & Muhlhaus, H., 2003. A Lagrangian integration point finite element method for large deformation modeling of viscoelastic geomaterials, *J. Comput. Phys.*, **184**(2), 476–497.

Muhlhaus, H. & Regenauer-Lieb, K., 2005. Towards a self-consistent plate mantle model that includes elasticity: simple benchmarks and application to basic modes of convection, *Geophys. J. Int.*, **163**(2), 788–800.

Muhlhaus, H.-B., Davies, M., & Moresi, L., 2006. Elasticity, yielding and episodicity in simple models of mantle convection, *Pure Appl. Geophys.*, **163**(9), 2031–2047.

Munk, W. H. & MacDonald, G. J. F., 1960. *Rotation of the Earth*, Cambridge University Press.

Nakada, M. & Karato, S.-i., 2012. Low viscosity of the bottom of the Earth's mantle inferred from the analysis of Chandler wobble and tidal deformation, *Phys. Earth Planet. Inter.*, **192**, 68–80.

Oldroyd, J., 1950. On the formulation of rheological equations of state, *Proc. R. Soc. A*, **200**(1063), 523–541.

Patočka, V., 2013. *Polar wander prediction based on the solution of the Liouville equation*, Master's thesis, Charles University in Prague, Czech Republic, http://geo.mff.cuni.cz/theses/2013-Patocka-Mgr.pdf.

Patočka, V., Čadek, O., Tackley, P. J., & Čížková, H., 2017. Stress memory effect in viscoelastic stagnant lid convection, *Geophys. J. Int.*, **209**(3), 1462–1475.

Peltier, W., 1998. Postglacial variations in the level of the sea: Implications for climate dynamics and solid-earth geophysics, *Rev. Geophys.*, **36**(4), 603–689.

Peltier, W., 2004. Global glacial isostasy and the surface of the ice-age earth: The ice-5G (VM2) model and grace, *Ann. Rev. Earth Planet Sci.*, **32**, 111–149.

Peltier, W. R., 1974. The impulse response of a Maxwell Earth, *Rev. Geophys. Space Phys.*, **12**, 649–669.

Rajagopal, K. & Srinivasa, A., 2004. On thermomechanical restrictions of continua, *Proc. R. Soc. Lond.*, **460**(2042), 631–651.

Ranalli, G., 1995. *Rheology of the Earth*, Springer Netherlands.

Regenauer-Lieb, K., Yuen, D., & Branlund, J., 2001. The initiation of subduction: Criticality by addition of water?, *Science*, **294**(5542), 578–580.

Ricard, Y., Spada, G., & Sabadini, R., 1993. Polar wandering of a dynamic earth, *Geophys. J. Int.*, **113**(2), 284–298.

Rozel, A., 2012. Impact of grain size on the convection of terrestrial planets, *Geochem. Geophys. Geosys.*, **13**.

Rozel, A., Ricard, Y., & Bercovici, D., 2011. A thermodynamically self-consistent damage equation for grain size evolution during dynamic recrystallization, *Geophys. J. Int.*, **184**(2), 719–728.

Runcorn, S., 1984. The primeval axis of rotation of the moon, *Phil. T. R. Soc.*, **313**(1524), 77+.

Sabadini, R., Vermeersen, B., & Cambiotti, G., 2016. *Global Dynamics of the Earth: Applications of Viscoelastic Relaxation Theory to Solid-Earth and Planetary Geophysics*, Modern Approaches in Geophysics, Springer Netherlands.

Sabadini, R., Yuen, D., & Boschi, E., 1982. Polar wandering and the forced responses of a rotating, multilayered, viscoelastic planet, *J. Geophys. Res.*, **87**(NB4), 2885–2903.

Schaeffer, A. J., Lebedev, S., & Becker, T. W., 2016. Azimuthal seismic anisotropy in the Earth's upper mantle and the thickness of tectonic plates, *Geophys. J. Int.*, **207**(2), 901–933.

Schmalholz, S. M. & Duretz, T., 2015. Shear zone and nappe formation by thermal softening, related stress and temperature evolution, and application to the Alps, *J. Metamorphic Geol.*, **33**(8, SI), 887–908.

Schmeling, H., Babeyko, A. Y., Enns, A., Faccenna, C., Funiciello, F., Gerya, T., Golabek, G. J., Grigull, S., Kaus, B. J. P., Morra, G., Schmalholz, S. M., & van Hunen, J., 2008. A benchmark comparison of spontaneous subduction models-Towards a free surface, *Phys. Earth Planet. Inter.*, **171**(1-4, SI), 198–223.

Shapiro, N. & Ritzwoller, M., 2002. Monte-Carlo inversion for a global shear-velocity model of the crust and upper mantle, *Geophys. J. Int.*, **151**(1), 88–105.

Solomatov, V., 1995. Scaling of temperature-dependent and stress-dependent viscosity convection, *Phys. Fluids*, **7**(2), 266–274.

Solomatov, V., 2004a. Initiation of subduction by small-scale convection, *J. Geophys. Res.*, **109**(B1).

Solomatov, V., 2004b. Initiation of subduction by small-scale convection (vol 109, art no B01412, 2004), *J. Geophys. Res.*, **109**(B5).

Solomatov, V., 2007. 9.04 - magma oceans and primordial mantle differentiation, in *Treatise on Geophysics*, pp. 91 – 119, ed. Schubert, G., Elsevier, Amsterdam.

Solomatov, V. & Moresi, L., 2000. Scaling of time-dependent stagnant lid convection: Application to small-scale convection on Earth and other terrestrial planets, *J. Geophys. Res.*, **105**(B9), 21795–21817.

Souček, O., Hron, J., Běhounková, M., & Čadek, O., 2016. Effect of the tiger stripes on the deformation of Saturn's moon Enceladus, *Geophys. Res. Let.*, **43**(14), 7417–7423.

Spada, G., Barletta, V. R., Klemann, V., Riva, R. E. M., Martinec, Z., Gasperini, P., Lund, B., Wolf, D., Vermeersen, L. L. A., & King, M. A., 2011. A benchmark study for glacial isostatic adjustment codes, *Geophys. J. Int.*, **185**(1), 106–132.

Tackley, P., 2000. Mantle convection and plate tectonics: Toward an integrated physical and chemical theory, *Science*, **288**(5473), 2002–2007.

Tackley, P. J., 2008. Modelling compressible mantle convection with large viscosity contrasts in a three-dimensional spherical shell using the yin-yang grid, *Phys. Earth Planet. Inter.*, **171**(1-4, SI), 7–18.

Tagawa, M., Nakakuki, T., & Tajima, F., 2007. Dynamical modeling of trench retreat driven by the slab interaction with the mantle transition zone, *Earth Planets Space*, **59**(2), 65–74.

Tanaka, Y., Klemann, V., & Okuno, J., 2009. Application of a Numerical Inverse Laplace Integration Method to Surface Loading on a Viscoelastic Compressible Earth Model, *Pure Appl. Geophys.*, **166**(8-9), 1199–1216.

Tapley, B., Bettadpur, S., Watkins, M., & Reigber, C., 2004. The gravity recovery and climate experiment: Mission overview and early results, *Geophys. Res. Let.*, **31**(9).

Thielmann, M. & Kaus, B. J. P., 2012. Shear heating induced lithospheric-scale localization: Does it result in subduction?, *Earth Planet. Sic. Lett.*, **359**, 1–13.

Thielmann, M., Kaus, B. J. P., & Popov, A. A., 2015. Lithospheric stresses in Rayleigh-Benard convection: effects of a free surface and a viscoelastic Maxwell rheology, *Geophys. J. Int.*, **203**(3), 2200–2219.

Tobie, G., Cadek, O., & Sotin, C., 2008. Solid tidal friction above a liquid water reservoir as the origin of the south pole hotspot on Enceladus, *Icarus*, **196**(2), 642–652.

Turcotte, D. & Schubert, G., 2002. *Geodynamics*, Cambridge University Press.

van Dinther, Y., Gerya, T. V., Dalguer, L. A., Corbi, F., Funiciello, F., & Mai, P. M., 2013. The seismic cycle at subduction thrusts: 2. Dynamic implications of geodynamic simulations validated with laboratory models, *J. Geophys. Res.*, **118**(4), 1502–1525.

Vaz, Jr., M., Munoz-Rojas, P. A., & Filippini, G., 2009. On the accuracy of nodal stress computation in plane elasticity using finite volumes and finite elements, *Computers & Structures*, **87**(17-18), 1044–1057.

Čížková, H., van Hunen, J., & van den Berg, A., 2007. Stress distribution within subducting slabs and their deformation in the transition zone, *Phys. Earth Planet. Inter.*, **161**(3-4), 202–214.

Vermeersen, L., Sabadini, R., Devoti, R., Luceri, V., Rutigliano, P., Sciarretta, C., & Bianco, G., 1998. Mantle viscosity inferences from joint inversions of Pleistocene deglaciation-induced changes in geopotential with a new SLR analysis and polar wander, *Geophys. Res. Let.*, **25**(23), 4261–4264.

Watts, A. & Zhong, S., 2000. Observations of flexure and the rheology of oceanic lithosphere, *Geophys. J. Int.*, **142**(3), 855–875.

Watts, A. B., Zhong, S. J., & Hunter, J., 2013. The Behavior of the Lithosphere on Seismic to Geologic Timescales, in *Annual Review of Earth and Planetary Sciences, Vol 41*, vol. 41, pp. 443+, ed. Jeanloz, R.

Wu, P. & Peltier, W., 1982. Viscous gravitational relaxation, *Geophysical J. R. astr. Soc.*, **70**(2), 435–485.

Wu, P. & Peltier, W., 1984. Pleistocene deglaciation and the Earth's rotation - a new analysis, *Geophysical J. R. astr. Soc.*, **76**(3), 753–791.

Zhong, S., 2002. Effects of lithosphere on the long-wavelength gravity anomalies and their implications for the formation of the Tharsis rise on Mars, *J. Geophys. Res.*, **107**(E7).

List of Figures

1 Bathymetric profile across the Mariana trench 5
2 Flexure of seafloor loaded by a seamount chain 7
3 Flexure of subducted continental lithosphere 10

1.1 Mechanical analogue for Maxwell viscoelastic body 14
1.2 Two observers of a material body 17
1.3 The concept of natural configuration 33

2.1 Small deformation of a sphere 47
2.2 Numerical validation of the Eulerian formulation 56
2.3 Polar motion induced by imposing a spherical ice cap on Earth's surface 57
2.4 Deformation of N-layer sphere 60
2.5 Energy balance on a non-rotating Earth 64
2.6 Energy balance of Chandler wobble 65
2.7 Energy balance of a loaded, rotating Earth 66
2.8 Time evolution of LOD and displacement for a loaded Earth . . . 68
2.9 Energy balance of a constantly rotating Earth 70
2.10 Energetic inconsistency of constantly rotating models 71
2.11 Energetic term by term analysis 1 72
2.12 Energetic term by term analysis 2 73
2.13 Energy balance and the rate of mechanical work 76

3.1 Model setup for a rising cylinder 93
3.2 Topographic response to a rising cylinder 94
3.3 Deviatoric stress above a rising cylinder 95
3.4 Viscosity and stress field in convection model E 98
3.5 Top and bottom Nusselt numbers and mean velocities in model E 98
3.6 Vertical component of deviatoric stress in viscoelastic and viscous convection models 100
3.7 Vertical component of deviatoric stress in viscoelastic and viscous convection models with a free surface 102
3.8 Horizontally averaged deviatoric stress in viscous and viscoelastic convection models with initially thin lithosphere 103
3.9 Horizontally averaged deviatoric stress in viscous and viscoelastic convection models with initially thick lithosphere 103
3.10 Stress memory effect in 3-D convection models 104
3.11 Benchmark comparison: isoviscous viscoelastic flow 108
3.12 Benchmark comparison: elastic slab in viscous medium 109
3.13 Subgrid oscillations of stress 111

4.1 Reference state of the global-scale models 116

4.2 Stress profiles in simulations r700 without plastic yielding 122
4.3 Average stress in the lithosphere in simulations r700 without plastic yielding 123
4.4 Stress profiles in simulations r700 without plastic yielding 124
4.5 Mean velocities in simulations r700 without plastic yielding 124
4.6 Locked convection cell in a simulation with free-slip sides 125
4.7 Average stress in the lithosphere in simulations w700 without plastic yielding 126
4.8 Subduction events occurring near a side boundary 127
4.9 Comparison of the viscosity profile in the global-scale and regional-scale models 128
4.10 Initial evolution of the global-scale models 129
4.11 Penetration of a rising plume into the lithosphere 130
4.12 Formation of "symmetric subduction" 130
4.13 Plume-induced asymmetric subduction 131

List of Tables

3.1 Parameters used in the convection calculations 97
3.2 Summary of the viscoelastic effects in stagnant lid convection . . . 104

4.1 Parameters used in the regional-scale models 117
4.2 Parameters used in the global-scale models 118
4.3 Phase change parameters used in the global-scale models 118
4.4 Time of the first subduction event for each simulation 120
4.5 Likelihood of subduction initiation 120